

2017 Project Abstract

For the Period Ending June 30, 2020

PROJECT TITLE: Moose Calf Surveys and Monitoring

PROJECT MANAGER: Dr. James D. Forester

AFFILIATION: University of Minnesota – Twin Cities

MAILING ADDRESS: 2003 Upper Buford Circle, Suite135

CITY/STATE/ZIP CODE: St. Paul/MN/55108

TELEPHONE NUMBER: 612-626-6721

EMAIL ADDRESS: jdforest@umn.edu

FUNDING SOURCE: Environment and Natural Resources Trust Fund

LEGAL CITATION: M.L. 2017, Chp. 96, Sec.2, Subd. 03j

APPROPRIATION AMOUNT: \$ 348,000

AMOUNT SPENT: \$ 348,000

AMOUNT REMAINING: \$ 0

Sound bite of Project Outcomes and Results

New techniques were developed to allow Unmanned Aerial Vehicles (UAVs) to efficiently home in on radio-collared animals and collect images of surrounding landscapes at multiple angles. UAVs, equipped with thermal and multi-spectral cameras, were then used to determine moose calving success and survival, characterize moose habitat, and estimate deer populations.

Overall Project Outcome and Results

Broad-scale monitoring of populations and ecosystems is needed to improve wildlife conservation and management efforts; however, the required data are often expensive and time consuming to collect. The overall goals of the project were to develop Unmanned Aerial Vehicle (UAV) capabilities to collect novel and important data on wildlife and ecosystems using methods that reduce or eliminate negative impacts on wildlife by removing the need to closely approach or handle them.

We developed new methods to home in on radio-collared animals and collect fine-scale imagery from multiple angles to improve our ability to count wildlife and characterize their habitat. We equipped UAVs with thermal and multi-spectral cameras to test whether UAVs can: 1) remotely confirm moose calving success or mortality events, 2) identify fine-scale habitat selection behavior of moose (e.g., locations of calving, foraging, and mortality), and 3) estimate population densities of white-tailed deer in forested natural areas.

We found that UAVs are a promising tool for quantifying moose calving success, twinning rate, and calf survival. We also determined that analysis of UAV-derived imagery can produce reliable estimates of forage availability and horizontal visibility. Our results indicate that female moose choose calving sites with relatively low visibility (subsequent calf mortality events appear to be associated with large, high-visibility forest patches). In our survey of the deer population at the Cedar Creek Ecosystem Science Reserve, we found that automatic detection of deer using software was not feasible, given the flight elevation required for the survey; however, we developed a methodology in which researchers count animals in a subset of images from the survey area to produce a repeatable count estimate. Overall, our methods provide safe, relatively inexpensive alternatives to traditional approaches of collecting critical data on wildlife populations.

Project Results Use and Dissemination

This project resulted in four scientific presentations, two published conference papers, three accepted journal papers and one submitted journal article; the CSE graduate student working on developing an aerial robotic

system and strategy to approach a radio signal beacon from a high altitude was awarded the UMII MnDrive fellowship award from the University of Minnesota. Our research into field applications of thermal imagery for assessing moose calving and mortality events was conducted in close collaboration with researchers from the Grand Portage Band of Lake Superior Chippewa and the MNDNR; we are continuing these collaborations and expect to submit another paper (detailing the calving habitat results) later this year. Our work to develop a new approach to sample deer populations using UAVs and thermal sensors grew out of a need at Cedar Creek to better understand their deer population. We tested our approach in the Cedar Creek Ecosystem Science Reserve and compared population estimates generated from UAV data to those from more traditional pellet-count approaches; we are now working with researchers at Cedar Creek to validate their camera-trap estimates of deer population density. Finally, three undergraduate students, three graduate students, and two postdoctoral researchers received training as part of this project; results from this research have been added into teaching materials in two required Fisheries, Wildlife, and Conservation Biology courses at UMN.



Environment and Natural Resources Trust Fund (ENRTF) M.L. 2017 LCCMR Work Plan Final Report

Date of Submission: 06/03/2021

Date of Next Status Update Report: Final Report

Date of Work Plan Approval: 06/07/2017

Project Completion Date: 4/30/2020

PROJECT TITLE: Moose Calf Surveys and Monitoring

Project Manager: Dr. James D. Forester

Organization: University of Minnesota – Twin Cities

Mailing Address: 2003 Upper Buford Circle, Suite135

City/State/Zip Code: St. Paul/MN/55108

Telephone Number: 612-626-6721

Email Address: jdforest@umn.edu

Web Address:

Location:Statewide

Total ENRTF Project Budget:

ENRTF Appropriation: \$348,000

Amount Spent: \$348,000

Balance: \$0

Legal Citation: M.L. 2017, Chp. 96, Sec. 2, Subd. 03j

Appropriation Language:

\$348,000 the first year is from the trust fund to the Board of Regents of the University of Minnesota to assess the use of unmanned aerial vehicles in natural resource monitoring of moose populations and changes in ecosystems.

I. PROJECT TITLE: Non-invasive Moose Calf Surveys and Ecosystem Monitoring with Unmanned Aerial Vehicles

II. PROJECT STATEMENT:

Many species and ecosystems in Minnesota are facing a variety of threats ranging from changing patterns of natural disturbance and human land use to alteration in the timing and amount of precipitation. Broad-scale monitoring of populations and ecosystems is needed to improve conservation and management efforts; however, the required data are often expensive and time consuming to collect. Fortunately, technological advances in the fields of robotics and data processing are opening up new capabilities for natural resource biologists to better identify and understand when and where changes in management strategies are needed. Specifically, Unmanned Aerial Vehicles (UAVs) improve on current technologies and methodologies because they can access remote or difficult terrain, collect large amounts of data for lower cost with reduced risk for humans, and facilitate observations of species that are wary of human presence. The use of UAVs has tremendous potential to advance the quality, scale, and frequency of aerial imagery collection and will enable researchers to better monitor landscapes as they change through time and then understand how wildlife species respond to these changes.

The overall **GOALS** of the project are to develop UAV capabilities to **1) collect novel and important data on wildlife and ecosystems** using methods that **2) reduce or eliminate negative impacts on wildlife** by removing the need to drug and handle them. Specifically, we will attempt to develop novel UAV capabilities to home in on VHF signals from collared animals to collect fine-scale habitat use and behavior data without the need to approach or re-handle the individual. We will also develop survey methodologies to utilize UAVs equipped with infrared cameras to count and track the survival of the moose calves without ever needing to handle them; fixed-wing UAVs will fly at high altitudes to avoid affecting moose behavior. We will also produce easy to use software that works with a simple UAV system for the monitoring and analysis of imagery over threatened or sensitive ecosystems such as wetlands and areas experiencing encroaching invasive species. This project will directly lead to better management and conservation **OUTCOMES** for **i) the MN moose population** without needing to collar calves, and **ii) better monitoring and management action for natural areas** by providing an approach that could be adopted by natural resource managers to collect finer temporal scale and higher quality land-cover data, enable a fast and effective way to assess results of management actions, and provide a user friendly means of processing the imagery data. These outcomes will provide a set of tools that will help advance conservation in Minnesota and will eventually save taxpayer dollars while simultaneously reducing risk to biologists and pilots.

III. OVERALL PROJECT STATUS UPDATES:

Project Status as of 01/01/2018: Now combined in 07/01/2018 status update per instructions from LCCMR staff: "In an effort to manage staff and project manager work load and resources, LCCMR staff is requesting you disregard your first scheduled update. Past history shows there is usually very little activity in the first six months of a new work plan. Please combine your first update status with your second project status update submission. If you have an amendment request, then submit your update as planned. Any amendment request must include an update."

Project Status as of 07/01/2018:

We had a busy fall of 2017 where we spent a good deal of time researching unmanned aerial vehicles and sensors for purchase to help us accomplish our goals. We worked with a local Minnesota company, Sentera (<https://sentera.com>), to purchase our fixed-wing aircraft and to obtain flight lessons for use in our ungulate surveys. We needed a place to easily test all of our cutting-edge equipment and methodologies prior to moose-calf surveys, so the Fisheries, Wildlife and Conservation Biology (FWCB) graduate student added on an additional component to this project, comparing the efficacy of different methods for determining the abundance of white-tailed deer. We believe this addition will be of great use for research and management in MN as well. During this time, the Computer Science and Engineering (CS&E) team has started to help us create computer code to automatically identify and count the number of deer in a thermal image collected by the UAV.

The CS&E team have been testing custom-built UAVs that can home in on a VHF signal emitted from a collar. While they have had some good success in the lab, more field testing will be required this year before it can be implemented to help us find collared moose. These experiments will be performed at the Cedar Creek Wildlife reserve throughout the summer of 2018.

Some preliminary results have been presented at the Multi-Robots Systems Conference in December. Further results on the algorithm to localize the target has been submitted to IROS 2018 (one of the top two robotics conferences).

Throughout the fall we collected aerial imagery from several locations, often multiple times per week, with our UAV quadcopter. We picked these sites in order to work with imagery and do analyses that would be similar to situations where Minnesota land managers might find UAVs very useful. We are currently using the latest software to analyze this imagery to better understand how UAVs can be incorporated into everyday work for Minnesota land managers.

Currently, the FWCB graduate student along with an FWCB undergraduate student, are in Grand Portage working with the tribal biologists for the initial moose survey season. They have had some success collecting thermal imagery of adults and calves, but importantly, we are learning many ways in which we can improve our methods and success for our second season in 2019. All successes and failures that we encounter in developing these new methodologies will be assessed to determine their utility for future research, conservation and management work. The CS&E graduate student is working to make software that can automatically detect and count the moose in thermal videos.

Amendment Request 04/26/2019: Amendment Approved by LCCMR 6/13/2019

Because we were able to save travel funding due to inexpensive rent found in Grand Portage, and because we paid our field techs salary instead of per diem, we are asking to shift \$12,520 from Travel and \$2,566 from Capital Expenditures to personnel. This will cover the increased need for graduate students and undergraduate assistants to collect and process the large amount of image data we have stored. To cover repair of our two UAVs that were damaged in crashes, we need to retroactively transfer \$2,111 from Capital Expenditures to Other (service contracts for repair costs from Sentera and DJI) and \$2,287 to Equipment/Tools/Supplies to cover replacement batteries, props.

A trip outside of Minnesota was made by the Volkan Isler lab (June 28-July 2 DC trip) to present the findings of our radio tracking approach at a national meeting. At this conference, they were able to get valuable insights from colleagues on how to refine their approach so we are requesting a retroactively requesting \$770.40 to be allowed for out of state travel.

Because we are still collecting data now, we are requesting an extension of our completion date (recognizing that the budget will be spent out by 1 July 2019) to 1/30/2020. This will give us the opportunity to complete our analysis and provide a more comprehensive final report. We will provide a progress report on 7/1/2019.

Amendment Request 04/26/2019: Amendment Approved by LCCMR 6/13/2019

The remaining \$6,348 in Capital Expenditures will be used for a combined Thermal/Color camera that will allow for more accurate temperature measurements, simultaneously collected color imagery, all of which is geotagged. In our initial year of sampling, we found that the largest roadblock we had to identifying moose calves was not having geotagged color and thermal imagery. This camera will be purchased according to UMN purchasing guidelines; although UMN does not require an official bidding process for material < \$10k, we have received three bids for the camera. At the completion of the project, the camera will continue to be used to further develop our wildlife detection techniques and habitat surveys. If this use changes, we will pay back the ENTRF equal to the residual value as approved by the director of the LCCMR.

Project Status as of 04/26/2019:

During the fall of 2018 we collected a second year of landscape imagery at Cedar Creek Ecosystem Science Reserve (CCESR). We collected data over the same forested areas as during the fall of 2017 and over the same wetland and lake shore as was collected in the spring of 2018. During these flights we utilized our multi-spectral sensor which collects several types of additional spectral bands that enabled us to calculate and quantify several metrics such as the normalized difference vegetation index (NDVI); a measure of the greenness or productivity. We have processed the imagery from these flights, calculated various metrics and are currently in the process of analyzing the results.

Students from both the FWCB and CS&E teams went to multiple locations with captive ungulates for the purposes of advancing our methodologies when conducting flights over wild moose. These data are especially useful for furthering the development of algorithms to automatically detect and correctly identify the presence and species of large mammals from thermal surveys. The data collected from both bison at CCESR and white-tailed deer from a deer farm near Bethel, MN will be instrumental in honing our methods for the 2019 field season and final products. Michael McMahon is currently in the field collecting sightability data on collared deer (these animals are similar in body size to moose calves) while he is searching for calving moose in Grand Portage.

Project Status as of 07/01/2019:

In the last two months, we completed the collection of field data. Based on our preliminary analysis, we were able to thermally detect cows with 85% success and correctly identified the presence of one or more calves with 79% success. By adjusting our methodology based on our initial detection model findings, we increased our moose detection success from 25% our first season, to 85% during our second season. We are currently analyzing these results and expect to submit a manuscript in early 2020. The CS&E team continues to work on how to optimize radio tracking from the UAS, and how to process efficiently the imagery we collect.

Amendment Request 01/30/2020:

Because the data analysis has taken longer than expected due to the processing time required for large image files, we are requesting an extension of our completion date (recognizing that the budget was spent out on 1 July 2019) to 4/30/2020. This will give us the opportunity to complete our analysis and provide a more comprehensive final report. We are doing all work after 30 June 2019 on our own time and using non-sponsored funding sources.

In the last months of the project, we needed additional personnel and computer network support to finish the data collection. We are retroactively asking to move \$2,285 to Personnel from Equipment and Tools, and \$1,020 to Other (Networking and Computer Services) from Other (Repair Fees, \$227) and Equipment/Tools (\$789). In the last month of funding, a subcontract reallocated funds to complete the project but did not know that an amendment was required. This happened because they realized the need to have more personnel and computer support on the project as they finalized their portion of the analysis of radiotelemetry and image data.

Overall Project Outcomes and Results:

Broad-scale monitoring of populations and ecosystems is needed to improve wildlife conservation and management efforts; however, the required data are often expensive and time consuming to collect. The overall goals of the project were to develop Unmanned Aerial Vehicle (UAV) capabilities to collect novel and important data on wildlife and ecosystems using methods that reduce or eliminate negative impacts on wildlife by removing the need to closely approach or handle them.

We developed new methods to home in on radio-collared animals and collect fine-scale imagery from multiple angles to improve our ability to count wildlife and characterize their habitat. We equipped UAVs with thermal and multi-spectral cameras to test whether UAVs can: 1) remotely confirm moose calving success or mortality

events, 2) identify fine-scale habitat selection behavior of moose (e.g., locations of calving, foraging, and mortality), and 3) estimate population densities of white-tailed deer in forested natural areas.

We found that UAVs are a promising tool for quantifying moose calving success, twinning rate, and calf survival. We also determined that analysis of UAV-derived imagery can produce reliable estimates of forage availability and horizontal visibility. Our results indicate that female moose choose calving sites with relatively low visibility (subsequent calf mortality events appear to be associated with large, high-visibility forest patches). In our survey of the deer population at the Cedar Creek Ecosystem Science Reserve, we found that automatic detection of deer using software was not feasible, given the flight elevation required for the survey; however, we developed a methodology in which researchers count animals in a subset of images from the survey area to produce a repeatable count estimate. Overall, our methods provide safe, relatively inexpensive alternatives to traditional approaches of collecting critical data on wildlife populations.

IV. PROJECT ACTIVITIES AND OUTCOMES:

ACTIVITY 1: Non-invasive methods to monitor the MN moose population

Description:

For this activity, we will utilize UAVs with thermal imaging to better monitor the MN moose population without the need to re-handle adults or collar calves. We will utilize the collars already on adult moose in the Grand Portage Reservation. We will fly our UAV above the adults and utilize thermal imagery to determine the number and survivorship of calves. Data collected non-invasively on moose calves is critical because moose cannot be handled or collared in MN and the methods and technologies pioneered here may be later used in other areas of the state. This activity has two discrete components: **i) a lab component** where a graduate research assistant in the Department of Computer Science & Engineering (CS&E) at the University of Minnesota will work with Dr. Volkan Isler and his lab to develop new UAV capabilities to home in on the location of a VHF signal and, **ii) a field component**, where a graduate research assistant in the Department of Fisheries, Wildlife, and Conservation Biology (FWCB) at the University of Minnesota working with Dr. Mark Ditmer and Dr. James Forester collect data on moose calves. The FWCB graduate research assistant will fly the UAV with thermal and regular (RGB) imagery over the locations of adult moose with GPS-collars and count the number of calves born, track their survival over time, and capture additional data about the habitat selected by the adult moose for giving birth and areas used after the calves are mobile. This data will be processed by the CS&E graduate research assistant and analyzed for ecological and biological interpretation by the FWCB graduate research assistant.

i) For this activity, Dr. Isler and the CS&E graduate research assistant will develop robot control software to autonomously home in on a signal source (i.e. the collar) of an adult moose. First, a multi-rotor aerial vehicle will be fitted with a small computer, a UHF radio signal receiver and a sound card. The characteristics of the signal and its relationship to the source-receiver geometry (in particular with respect to distance and bearing) will be investigated. Second, the flight controller will be modified so that it can take commands from an onboard computer. Third, a “home-in” behavior will be developed so that the UAV can approach the signal source. In ideal conditions, this could be achieved by following the gradient of the signal. However, preliminary tests indicated that due to obstacles such as trees as well as noise from the environment (including the rotors), signal strength is not a reliable indicator of distance. We will develop more sophisticated search behaviors which guarantee successful approach to the target. This capability will be demonstrated in field experiments using a collar and a multi-rotor vehicle near campus.

ii) Prior to developing survey methodologies for conducting UAV flights to collect data on moose calves, the FWCB graduate research assistant will obtain training on UAV flying during August or September of 2017. Following training, the FWCB graduate research assistant will first test out the capabilities of the UAV coupled with a thermal camera by doing field testing on the University of Minnesota’s property during October of 2017. This testing will allow us to make any changes to the camera or UAV settings and determine the best altitude for collecting thermal data on large-bodied mammals. To collect data on moose calves, the FWCB graduate research assistant will fly the UAV over the locations of adult moose in the Grand Portage Reservation in northeastern MN, that were previously collared, after they have given birth (typically May through early June). The graduate student will work with the resident wildlife biology for the Grand Portage band, Dr. Seth Moore. We will know

when an adult collared moose gave birth because moose based on an existing statistical model that identifies characteristic movement behavior that usually occurs just prior to giving birth. This specific movement, evident from GPS locations transmitted from the moose’s GPS-collar via satellite to our computer, consists of a long distance movement away from the individual’s usual home range, followed by relatively little movement for several days. Once the calving movement is identified, the FWCB graduate research assistant will fly the UAV to the location of the moose at the highest altitude that can be safely flown in the conditions that allows us to successfully capture thermal imagery for the moose and the calves. The Univ. of Minnesota has a Certificate of Authorization (2016-CSA-63-COA-R) provided by the Federal Aviation Administration that outlines all of the safety requirements and rules that all of our flights will adhere to. Along with the thermal imagery of the moose and the calves, the UAV will also collect regular aerial imagery of landscape using an RGB camera. Data from the cameras will be downloaded and stored on a Cloud-based system and later analyzed by the FWCB graduate research assistant to determine the habitat characteristics selected for by the adult moose for calving relative to the habitat in the surrounding area. During October and December of 2018, both the FWCB and CS&E graduate research assistants will test out the newly developed homing capabilities of the UAV using a similar VHF collar. During May through June of 2019, the same flights over moose in Grand Portage will be conducted by the FWCB graduate research assistant. The second season may involve alterations in methodologies to improve on the outcomes from Season 1 (2018).

Summary Budget Information for Activity 1:

ENRTF Budget: \$187,810
Amount Spent: \$ 187,810
Balance: \$ 0

Outcome	Completion Date
1. Testing of UAV and thermal camera at captive animal facility to determine optimal settings for moose surveys.	11/01/2017
2. Conducting moose survey and habitat flights in Grand Portage collecting counts and survival data using thermal imagery. – Season 1.	07/01/2018
3. Alteration of UAS system to include the capability of tracking VHF collar and field tests with unused VHF collars on campus.	01/01/2019
4. Testing of newly engineered homing technology of VHF collars.	05/01/2019
5. Conducting moose survey and habitat flights in Grand Portage collecting counts and survival data using thermal imagery. – Season 2.	07/01/2019

Activity 1 Status as of 01/01/2018: Now combined in 07/01/2018 status update.

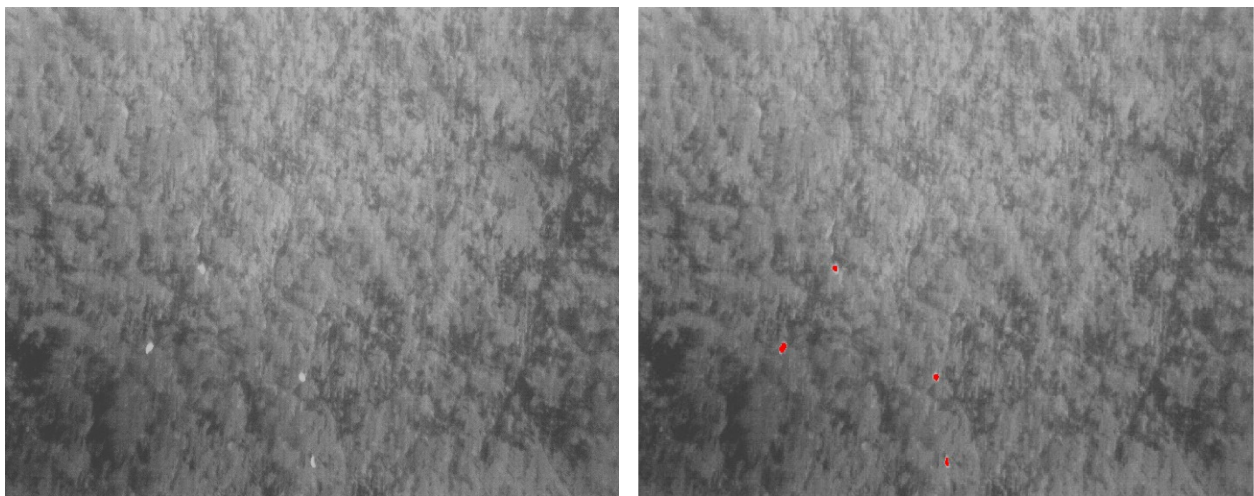
Activity 1 Status as of 07/01/2018:

Dr. Volkan Isler and his engineering students have made great strides in developing a UAV that can automatically detect and localize VHF signals for purposes of automated tracking of wildlife. They have overcome many hurdles in terms of developing a search algorithm, processing information while in flight, and the creation of user friendly software. They have built a custom-made quadcopter with an attached traditional Yagi antenna (used for wildlife studies; see image 1A below) and we have tested it out at the University of Minnesota’s Cedar Creek Ecosystem Science Reserve (CCESR; see image 1B). The initial tests, while promising, point to a lack of range that the VHF collar can be detected. Currently, Dr. Isler’s team is working on a solution to the limited range and will continue field testing later this year.



Images 1A (left) and 1B (right): 1A-Development of a custom-made UAV for the tracking of VHF signals utilizing a traditional wildlife Yagi. 1B-Testing the VHF-homing UAV at Cedar Creek Ecosystem Science Reserve. We placed VHF transmitters throughout the area and tested the ability of the UAV to detect, collect data, and search out the location of the transmitters.

Because our moose field work in Grand Portage can only occur during the spring, and we are employing new methodologies, we tested our abilities to use UAVs with thermal sensors for ungulate population counts locally. The FWCB graduate student conducted 22 UAV surveys over 5 different areas within CCECSR aiming to record and count white-tailed deer. The student is also analyzing data from a camera-trap grid within CCECSR and has conducted hundreds of deer pellet count surveys (a traditional approach of estimating deer abundance) in order to compare the estimates of relative abundance and determine the efficacy of these methods for estimating deer populations. The CS&E graduate student is developing computer code to automatically determine and count the deer from these thermal flights. See image 2 for an example.



Images 2A (left) and 2B (right): 2A-Raw thermal imagery from flights over the CCESR. The bright white spots are those of white-tailed deer. 2B-The same image processed with code developed by the CS&E graduate researcher that automatically detects (red) the likely locations of deer from within a series of thermal images.

Currently in Grand Portage, the FWCB graduate student is conducting thermal surveys over moose in the hopes of detecting calves and monitoring their survival throughout the spring season (**Image 3** below). Because of the remote nature of the area, and the thick vegetation, the team has had to work incredibly hard to get the UAV over the current locations of adult female moose who potentially have calves. To date, they have attempted ~40 flights thus far, and based on initial inspection of the thermal data, have only been able to positively identify moose in less than 10 sets of imagery. However, a more formal and thorough search will occur after the field season and will be enhanced with analysis from the CS&E team. We have already learned important lessons from this field season that will increase our success in 2019. For instance, we initially worried that coniferous trees and shrubs would prevent us from sighting the moose, but the conifers do not block our sighting of moose, it has been thick deciduous cover that has created most of the issues. Next year, our student will head into the field a month earlier (mid-April) in order to conduct more surveys prior to deciduous leaf-out in the spring. Additionally, we are conducting surveys of moose calving locations with our multi-spectral sensor to better understand the habitat conditions where moose select to give birth.

Despite some of the initial logistical hurdles, the tribal biologists in Grand Portage are extremely excited by the work and are looking for ways to incorporate UAVs into many more aspects of their wildlife management work. They have asked us to come back in the winter to conduct thermal surveys. This will allow us to further detect survival of moose calves after a summer and fall. They also have interest in using the UAV with thermal capacity for conducting wolf pack counts.



Image 3: Raw thermal imagery from a flight over the location of a collared adult female moose with calf. Thermal video makes this detection even more apparent and we will conduct a more formal analysis of imagery after the field season.

Activity 1 Status as of 04/26/2019:

We used the fall of 2018 to collect imagery, often several times a week at different altitudes, of captive bison at CCESR (**Image 4** below) and also captive deer at a farm near Bethel, MN (**Images 5A & 5B** below). We collected this data for several important reasons: 1) This data was requested by the CS&E team to refine their computer programs that can auto-detect mammals from thermal imagery. By flying the drone at several altitudes,

times of day, and with varying levels of ground obstruction (e.g., trees, rocks), the engineers are able to refine their algorithm for detection which accounts for the altitude of the UAV and the size of the species being surveyed. 2) By working with our thermal imagery, the CS&E team have provided updated recommendations for the altitude to that best maximize survey cover and increase the probability that large-bodied mammals can be detected with the thermal camera. 3) Finally, working with captive animals allows us to understand how well the thermal sensor can detect individual animals because we know the exact number of individuals in captivity. We can then compare how detection is influenced on the altitude of the flight, ambient temperature, and types of ground cover.

During our 2018 moose field season (May and June), we flew 26 UAV grid surveys over GPS-collared cow-calf groups and confirmed 7 calf detections (27% success for detecting at least one calf present). We believe that by improving our auto-detection software and flying the surveys earlier in the season, we can improve on our detection rates in 2019.



Image 4: Raw thermal imagery from a flight over a captive bison herd at the Cedar Creek Ecosystem Science Reserve. By collecting imagery in areas where we know the number of individuals present, we can improve on our understanding of detection and further refine field and analytical methods.



Image 5A: RGB imagery from flights over a deer farm near Bethel, MN. Collecting RGB imagery in conjunction with thermal helps to understand how vegetation impacts our thermal detection rates.



Image 5B: A screenshot from thermal video collected during drone flights over a deer farm near Bethel, MN. Collecting both thermal and RGB imagery at various altitudes, times of day, and various vegetation coverage helps us understand our ability to detect mammals and improve our auto-detection software.

Activity 1 Status as of 07/01/2019:

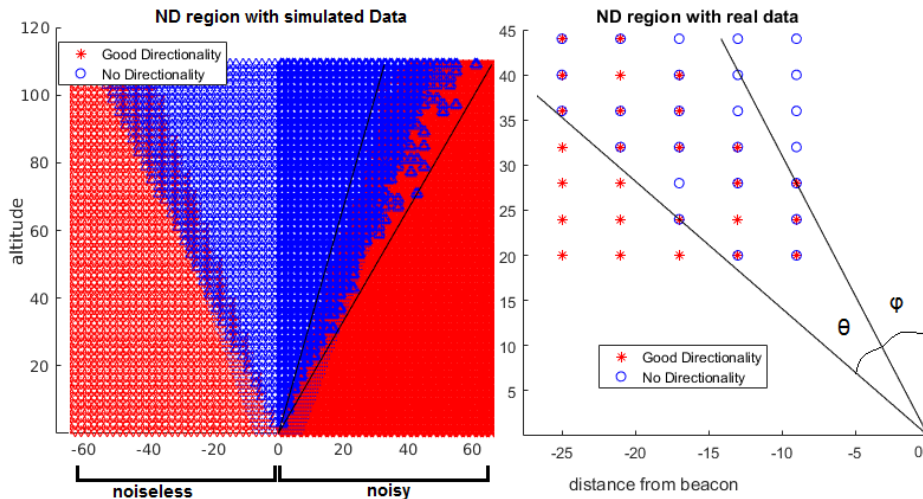
During 2018 our detection success of adult moose was 25%. After making adjustments to our field methodologies based on preliminary graphical analyses, adult cow moose detection improved substantially to 85% during 2019. We discovered that cloud cover and the amount the vegetation had leafed out were two factors that were extremely important to account for with respect to detections. Overcast skies led to far better detections and late-season flights (when the deciduous vegetation had started to leaf out) were much less successful. We are beginning to work on statistical models that will formally quantify these results.

Final Report Summary:

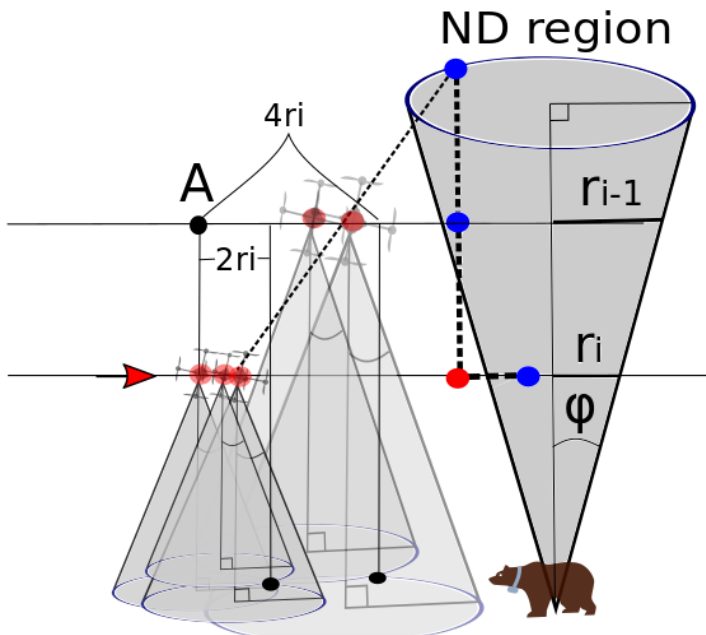
i) For this activity, Dr. Isler and the CS&E graduate research assistant worked on utilizing VHF radio tags with a UAV. First, we fitted a multi-rotor UAV system with a small on-board computer and a directional antenna that can detect the signal source. We developed control software that allows the UAV system to communicate with the autopilot and perform commands from the on-board computer.



Second, we modeled the area around the signal source based on our antenna radiation field and classify the locations in which we can or cannot obtain reliable directionality measurements (a.k.a. bearing measurements). The results of this modeling resemble a cone-like region above the signal source inside of which bearing measurements lose directionality. In order to verify that our modeling is realistic, we also collected data with a real UAV system.

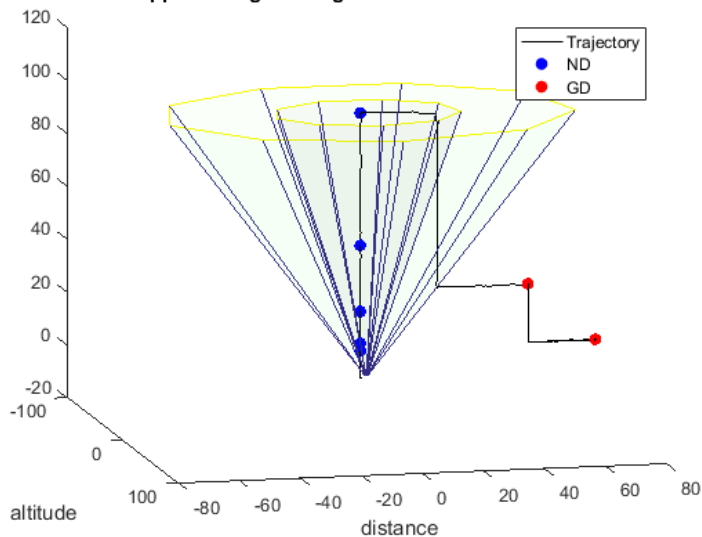


Finally, we developed a “home-in” strategy that takes advantage of a UAV’s ability to change altitude and exploits the special structure of the modeled conic-like region in order to approach the signal source from above.



We analyzed the performance of our strategy and demonstrated through simulations and field experiments that by exploiting this structure we can achieve short flight times. Initial tests and proof of concept experiments were conducted on the UMN campus and at the Cedar Creek Ecosystem Science Reserve.

Approaching the target with ND measurements



We found that by using the UAV's ability to change altitude, we could process the radio signal in a way that allowed for reduced flight time required to home in on the beacon. The results of this work were published with the IEEE International Conference on Intelligent Robots and Systems (IROS), 2019 under the title "UAV Landing at an Unknown Location Marked by a Radio Beacon" (Stefas et al. 2020).

ii) To study the signals of moose and their calves in the forest using thermal imaging devices, we first tested our equipment and tested the feasibility of using automated detection to identify animals (**Protocol Development and Image Processing**). We then applied the thermal camera approach to identify whether female moose had successfully calved (**Evaluating Unmanned Aerial Systems for the Detection and Monitoring of Moose in Northeastern Minnesota**). Finally, we flew our UAV over areas of moose habitat that were associated with important life history events (calving sites, peak lactation sites, mortality sites, and areas of recent concentrated use) and collected fine-scale multi-spectral data (**Linking multi-spectral vegetation data with moose habitat**).

Protocol Development and Image Processing

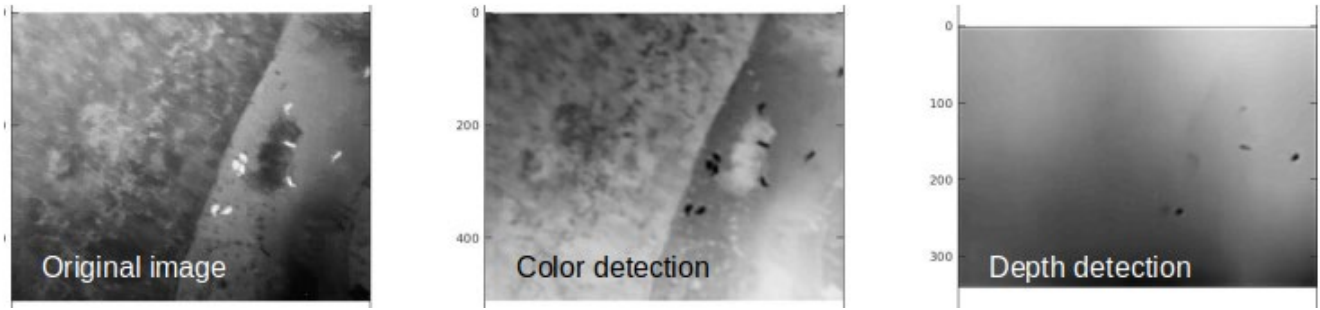
We first took thermal image data from a local deer farm where the locations and number of animals can be easily acquired. One of the images is shown in here.



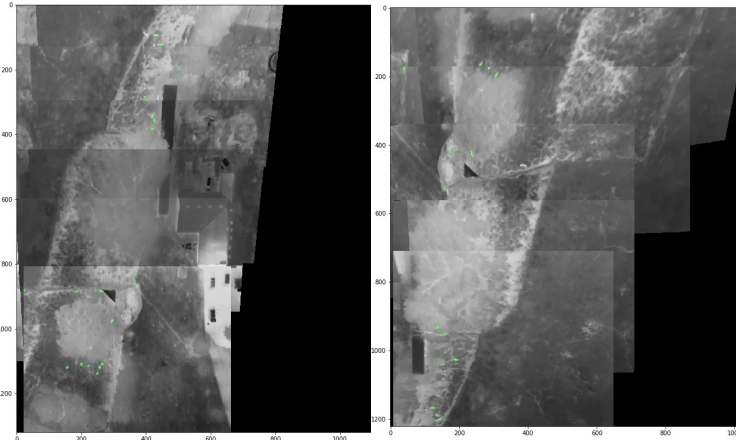
To see the thermal response, images at different altitudes were taken. We then developed a blob detection algorithm to detect the hotspot response from the animals in the thermal images. We analyzed the performance of the algorithm on a set of thermal images, which is able to successfully extract the animals as shown here.



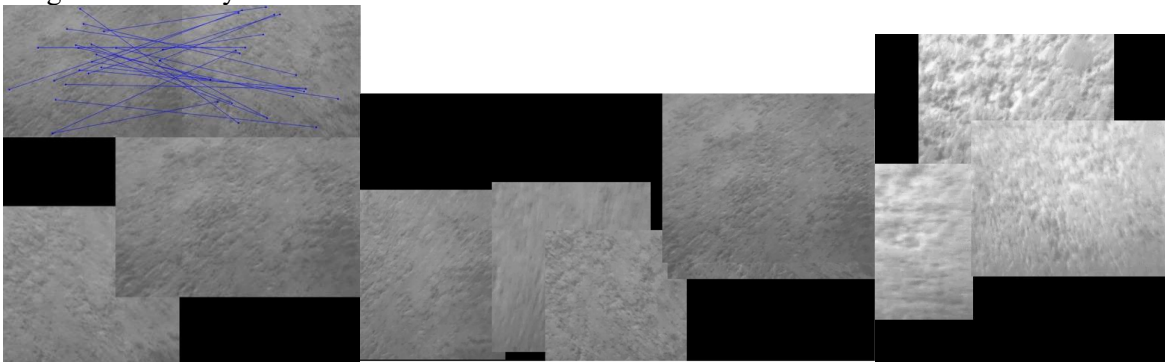
The number of animals extracted from the image and the corresponding black mask is 9. We also tested depth extraction to validate if the hotspot is above the ground with a certain distance. The purpose is to distinguish the animal from other anomalies such as branches or rocks. The results are shown here.



After detecting and counting the animal for each image, the next step is to detect and count the animals across different images. The stitched mosaic across multiple images from one of the footage is shown here.



However, due to the lack of features in many areas, it is difficult to find the correct correspondences and stitch the images successfully.



When the scene has distinguished features, we developed an algorithm to select less views for ground imagery mosaicking and it is published in *Robotics: Sciences and Systems 2017*. Despite the difficulties in automatically processing thermal images, we were able to successfully home in on collared moose and determine whether there were calves present.

Evaluating Unmanned Aerial Systems for the Detection and Monitoring of Moose in Northeastern Minnesota

Overview:

Our study population consisted of 22 cow moose fitted with GPS-collars with Iridium-satellite relay capabilities (VECTRONIC Aerospace, Berlin, Germany). Capture and handling of moose was conducted by the Grand Portage Natural Resources Management Department (IACUC Protocol# 1812-36635A). Moose locations were recorded and stored every 30 minutes to GPS collars, with GPS coordinates transmitted to satellites every two hours. We analyzed cow moose movements multiple times a day to identify locations and times for safe and

efficient UAV deployment to detect cow moose and calves. Prior to conducting flight missions above cow-calf pairs, we conducted initial test flights over GPS-collared bull moose in May of 2018 to gauge levels of disturbance from UAV flights. We would classify a disturbance if there were any erratic movements (i.e., fleeing from an area) that corresponded in time to UAV launch and flight times. Although none of these initial flights led to a behavioral disturbance, we took precautions in our surveys of cow moose and calves to reduce the risk of disturbance, and continued monitoring movement behavior to identify potential disturbance responses.

We used a DJI Inspire 2 quadcopter equipped with a FLIR Vue Pro 640 for the 2018 surveys and a FLIR Duo Pro R for 2019 surveys. Both thermal sensors were one-band sensors with a spectral interval that measured 7.5 to 13.5 μm . The FLIR Duo Pro R used in 2019 also featured an RGB sensor (4000 x 3000 pixels, 56° x 45° FOV) that allowed us to capture color imagery simultaneously with thermal imagery. Survey flights were planned and conducted using the Pix4Dcapture app (Pix4D, Prilly, Switzerland). Thermal infrared and RGB footage were recorded and stored onboard the UAV for review post flight. Flights occurred from 25 May 2018 to 28 June 2018 (n = 44 flights) and 25 April 2019 to 30 May 2019 (n = 48 flights) at varying times between morning and evening civil twilight (Figure 1.1). Surveys were flown in rectangular grid transects centered over the most recently updated GPS locations of cows. Rectangular grids were used to maximize our coverage in the event that the cow moved off of the last known location prior to launching the UAV, and to minimize the risk of animal disturbance. To minimize animal disturbance from our presence on the ground, we launched the UAV from reservation and county roads or trails that were between 300-m and 600-m Euclidean ground distance from updated moose locations. This distance also allowed us to maintain visual contact of the UAV, and sufficient radio communication between the remote and quadcopter. Additionally, we flew at altitudes that were near the maximum allowable 122 m (~400 ft) above ground level; altitudes ranged from 75 m to 121 m depending on terrain elevations relative to launch points.

Moose Demographic Data and Predation Events:

Thermal infrared video footage was reviewed manually post flight by human observers. Observers were trained to detect living animals in thermal video by viewing sample footage collected over domestic animals (e.g., domestic bison, cows, and captive deer) of known location and abundance, to develop a sight picture for large-bodied mammals in thermal imagery (Fig 1.2). The same observers reviewed thermal video footage for both seasons. Adult moose and calves were visually identified from the video footage by their shape and brightness in the footage, the latter also by their proximity with the cow. Detections of target moose (i.e., bright white silhouettes that often resembled a large animal body with a head) were confirmed by updated cow GPS locations collected during and post UAV survey times. We attempted to utilize object-based image analysis (OBIA) to quantify moose detections from our thermal video footage. However, we would have needed to greatly increase the resolution of our FLIR sensors, or fly the UAV at lower altitudes, increasing the risk of disturbing moose and striking hazards (e.g., tall trees), to effectively apply OBIA methods to discern moose from other objects.

For 2018 flights, moose detections were verified by matching the position of the UAV on the flight transect where a thermal detection was observed (based on flight time) to the location and time stamp from the collared moose that corresponded to that time in the flight. In 2019, detections were verified by matching GPS coordinates of the UAV and of the moose at given flight times. This was possible because the FLIR Duo Pro R used in 2019 featured geotagged video footage that provided GPS coordinates for the UAV every second of survey time, whereas the FLIR Vue Pro used in 2018 did not. Color (RGB) footage was also reviewed for flights with positive thermal detections as an additional verification throughout the 2019 season. Thermal detections of cows and counts of calves were recorded for each flight.

We investigated suspected calf predation events by flying over known collared cow-calf pairs after large movements occurred in a short period of time, with the cow commonly circling back to the suspected predation location. We considered a predation event to be positively confirmed if we could detect the cow without the previously detected calf. Conversely, we concluded that a predation event was unsuccessful or did not occur by thermally detecting the calf with its mother. Our conclusions about predation events through remote sensing were corroborated by subsequent on-foot investigations.

Results and Conclusions:

We successfully applied UAV technology and FLIR sensors to detect collared adult cow moose and calves in a heavily forested region of northeastern Minnesota (Fig 1.4). The increase in detection success from our first to our second field season was a result of developing preliminary relationships between adult moose detection and environmental and temporal covariates. This improvement provides validation that our final detection model (which incorporated both years of flight data) captured useful relationships for researchers planning to conduct ungulate surveys with UAV and FLIR technology. We maximized detection success during our second season by conducting survey flights earlier in the calving season to take advantage of leaf-free conditions. We also concentrated our flight efforts within the early morning hours when temperatures were coolest, and less thermal energy was being emitted from ground objects. Snow cover present in our second season (2019) during the early spring also improved thermal detection by covering ground objects and maximizing the thermal contrast between moose and their environment. Importantly, this research provides a valuable method for determining ungulate reproductive success and calf survival using a less invasive method than handling and collaring calves, which may induce additional stressors.

Our FLIR-equipped UAV demonstrated clear advantages over conventional methodology for monitoring moose calving success by increasing animal detectability while reducing survey cost and effort. The inclusion of FLIR sensing with UAV was crucial for detecting cow-calf pairs in forested environments. Moose were often obscured by canopy cover in RGB footage, whereas FLIR footage allowed for easy detection (Figure 1.3). Challenges of visual detection without FLIR are also reflected in the state-wide aerial counts conducted by the MNDNR. The MNDNR reported an average estimated detection probability of 61% for their 2018 aerial survey using conventional aircraft and visual observation, compared to our detection probability of 85% using UAV and FLIR technology (N.B., the area we surveyed was much smaller than the units surveyed by the MNDNR across moose range). Further, unmanned aerial systems offered a relatively cheap method to collect aerial data and following the initial financial investment for UAV equipment, our operating costs were minimal, with ground transportation being our largest field expenditure.

We intended to integrate object-based image analysis (OBIA) methods for detecting moose in aerial imagery. However, because we employed an economical FLIR sensor with relatively low resolution (640 x 512), we experienced challenges using OBIA. Flying the UAV at lower altitudes may have compensated for low resolution but would have increased the potential to disturb moose and have been problematic for terrain avoidance. Dense forest further convoluted the OBIA process because of the many bright returns caused by heated, non-living ground objects among the trees. These objects sometimes resembled moose in brightness and shape (e.g., vegetation would distort the recognizable silhouette of a moose), greatly decreasing the ability of OBIA software to accurately classify objects. Instead, we opted to manually review the video footage, which served to be a simple and efficient way to identify collared moose, and was especially effective for identifying calves present with cows (distinguishing different sized targets with OBIA adds further complexity). Manual detection required ~ 16 combined hours per observer over our two seasons, averaging ~ 10 min per UAV flight for each observer. Based on our results, we conclude that until sensors with higher resolution become more economical, or OBIA methods overcome lower resolution limitations, the technical hurdles of implementing OBIA may only be worthwhile for researchers with access to high-resolution sensors and those attempting to detect non-collared animals, especially over large spatial extents.

This work served to hone UAV methodology for the application of wildlife research. We found that a readily available off-the-shelf UAV equipped with FLIR technology was an effective platform for detecting collared moose and counting and monitoring calves in a densely forested environment. We identified several ongoing environmental challenges and technical limitations, but we also realized significant improvement in detection success from one season to the next. Our efforts to model factors driving moose detectability allowed us to establish best practices for maximizing UAV efficacy with FLIR sensing for surveys of forest-dwelling animals. It is likely that the continued improvement and reduced costs of UAV and associated sensors, will open new doors to the types of data collection possible and expand on potential target species. We postulate that FLIR sensor-equipped UAV—especially with the capability to collect geo-tagged thermal imagery—could be effective for monitoring reproductive success (e.g., birthing success, twinning rate, and young survival) of other GPS-collared, large-bodied mammals.

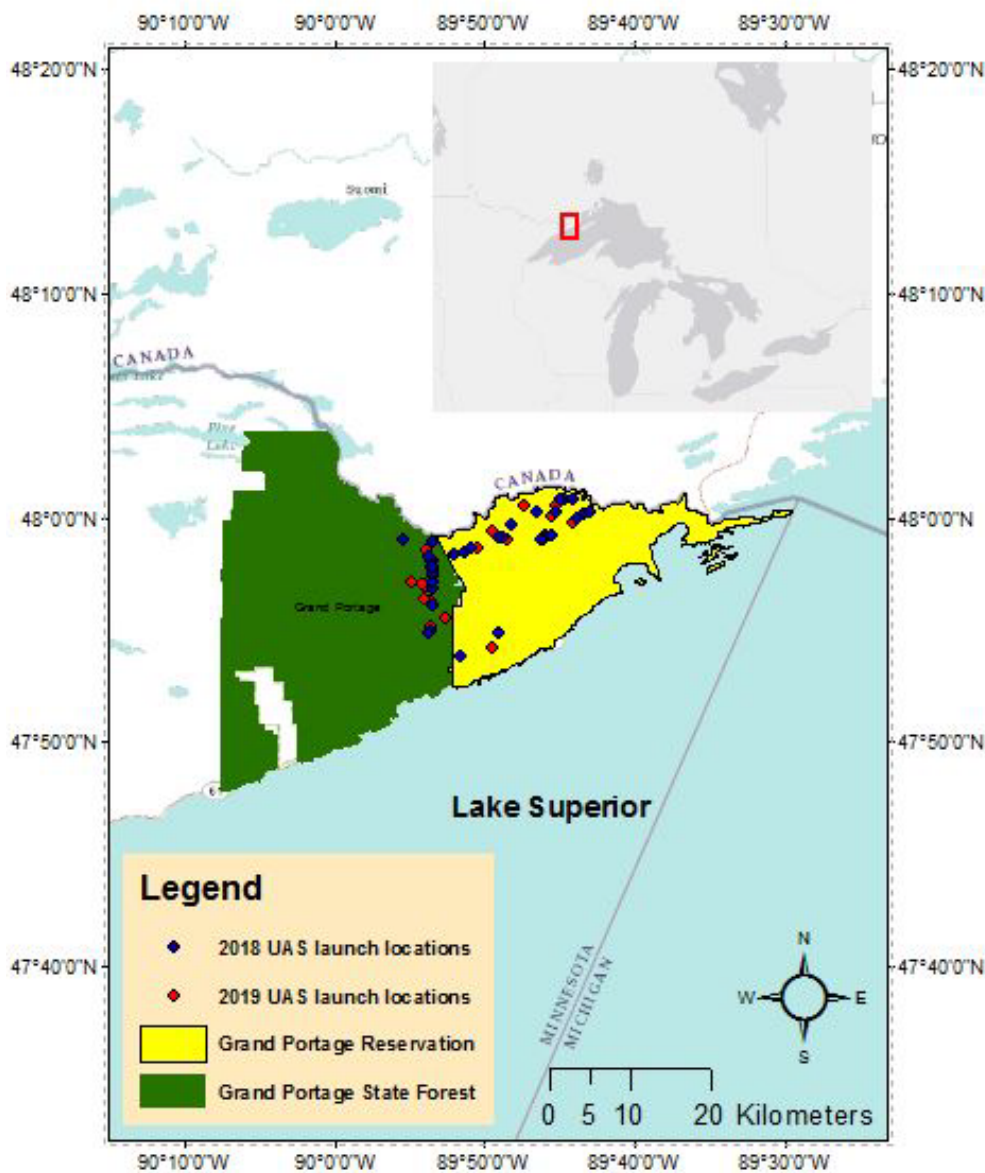


Figure 1.1 Study area of Grand Portage Reservation and eastern Grand Portage State Forest, in northeastern Minnesota, USA. Unmanned aerial system (UAV) launches are shown across the study area for the 2018 and 2019 field seasons.

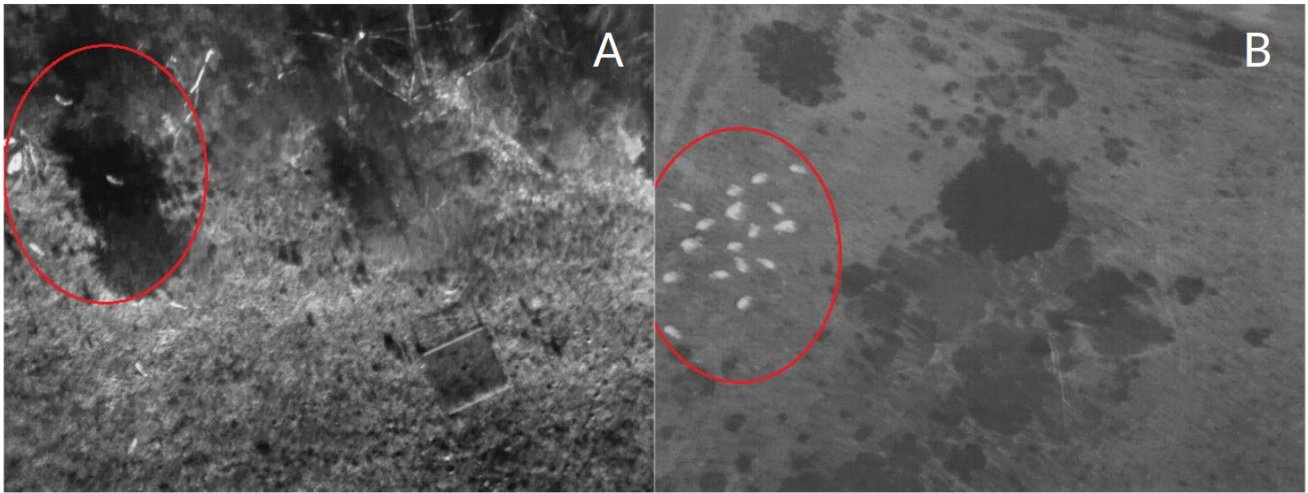


Figure 1.2 Side-by-side comparison of thermal infrared photos of a captive bison herd captured during clear sky conditions (A) and overcast sky conditions (B). Imagery was collected at the University of Minnesota’s Cedar Creek Ecosystem Science Reserve during July 2018. This contrast demonstrates the positive effect that overcast sky conditions have on thermal detection.

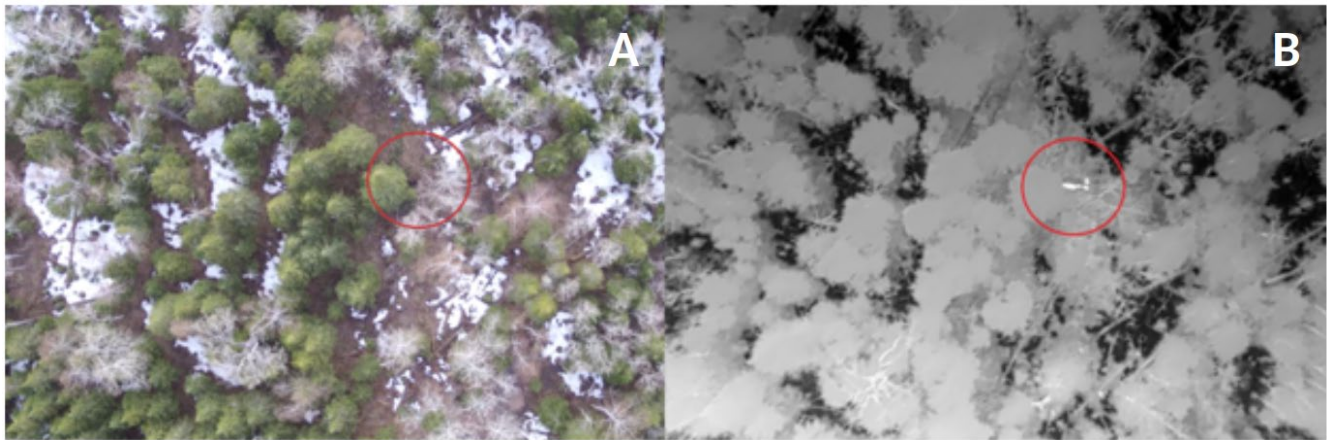


Figure 1.3 Comparison of UAV-gathered RGB imagery (A) and thermal infrared imagery (B) of a cow moose with two calves in northeastern Minnesota during spring of 2018-2019. These photos were captured at the same time and location over this cow and her calves, which demonstrates the advantage of increased detection success from thermal infrared technology over RGB photography.

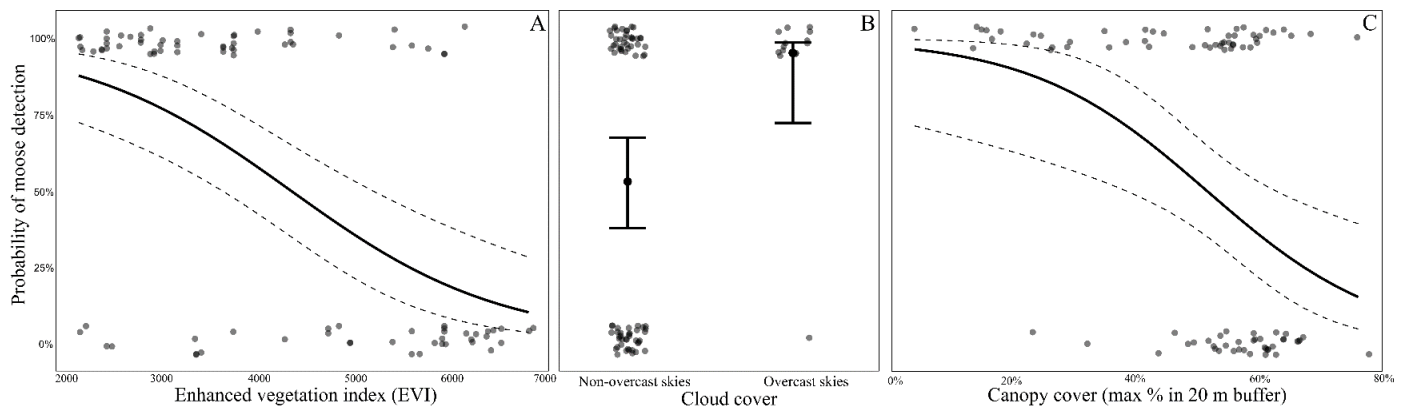


Figure 1.4 Detection success of GPS-collared adult cow moose in northeastern Minnesota during spring of 2018-2019 using thermal technology mounted on a UAV. Moose detections are plotted as raw values on the y-axis as either 100% (present and detected) or 0% (present but not detected). The predicted mean and 95% confidence intervals are based on the best-supported model for detection. We predicted moose detection for all sampled values of A) the remotely-sensed enhanced vegetation indices (EVI) over the moose’s location, B) whether or not the sky was overcast during the flight (field-observation) while holding the other values in the best-supported model at their means, and C) maximum canopy cover around the moose’s GPS location during the time of the flight.

Linking multi-spectral vegetation data with moose habitat

Overview:

During spring 2019 we flew our quadcopter UAV over areas of moose habitat that were associated with important life history events and collected fine scale multi-spectral data (Figure 1.5). We flew over four types of locations: 1) moose calving sites, 2) moose peak lactation sites (defined as 26 days post-parturition), 3) mortality sites where it was confirmed that moose calves had been killed, and 4) locations where living moose had been recently. Moose calving sites, calf mortality sites, and peak lactation sites were provided to us by Dr. William Severud and Dr. Glenn DelGiudice of the Minnesota Dept. of Natural Resources. Drs. Severud and DelGiudice were interested in collaborating with us for the moose habitat component of our research after we gave a presentation of our capabilities with the UAV and associated thermal and multi-spectral sensors. Most of the sites we flew over were a result of the MN DNR’s efforts to understand the causes of moose calf mortality in northeastern MN (Severud et al. 2015). Our aim was to determine if the data from our multi-spectral sensor could collect vegetation data that would allow us to discern patterns in the vegetation density and vegetative productivity that might be related to the type of event that had occurred at the location (e.g., calving site vs. mortality cite). We also assessed whether patterns of vegetation and vegetative productivity differed from the location of the event (e.g., peak lactation site) relative to the surrounding area based on our flight (an area ~ 290,000 – 785,000 m² around each location).

To make a more meaningful connection between patterns of vegetative greenness captured by our multi-spectral sensor and moose habitat at these locations, we also flew over sites where Dr. DelGiudice’s team collected detailed vegetation data and related the vegetation patterns to neonate moose survival (Severud et al. 2019). Connecting patterns from data collected by our multi-spectral sensor to on-the-ground vegetation surveys would allow us to then relate vegetation patterns at other sites where important moose events occurred but on-the-ground vegetation surveys were not conducted. Data collected at these sites was based on moose ecology in order to assess how well a site provided forage and protective cover from potential predators. Forage was assessed at an 11 m² area around the location by counting saplings and shrubs that may provide forage for moose. Calf-visibility (horizontal visibility) was assessed at a 15 m² radius around the site by counting the observed visible percentage of a life-size cardboard cut-out of a standing moose calf silhouette from each of the cardinal directions.

UAV Flight Data:

Flights were conducted over 30 moose event sites (calf mortality/predation = 16; calving = 8; living = 5; peak lactation = 4) including five sites that contained on-the-ground vegetation surveys. Flights were conducted in the

spring of 2019 as close to the date of historical moose event (all events occurred in the spring of 2015). Our UAV allowed us to collect data over each event site and the surrounding 300-500 m area. The UAV was equipped with our Parrot Sequoia multi-spectral sensor and an RGB camera. Flights were conducted between 300 – 500 feet above ground level depending on tree canopy and other safety precautions.

We processed and ortho-rectified both multi-spectral and RGB data using Pix4D software in Dr. Joseph Knight's remote sensing lab at the University of Minnesota. The multiple bands collected by Parrot Sequoia were used to estimate Normalized Difference Vegetation Index (NDVI), a metric of greenness or plant health at a resolution of $\sim 1/8^{\text{th}} - 1/5^{\text{th}}$ of a meter depending on the flight altitude (Figure 1.6). For each location we downloaded both current and historical satellite-based estimates of NDVI from NASA's MODIS sensor (Didan 2015) because it provides coarse estimates of NDVI that allow us to compare among sites instead of only within sites (i.e., data from our multi-spectral sensor provides relative estimates of NDVI only).

Analysis:

To assess how moose are using the landscape, we quantified values of NDVI both within a 30 m² area of the event location and within areas of increasing distance from the event location (buffered rings at: 30-50 m, 50-100 m, 100-150 m, 150 – 200 m, 200 – 250m, 250 – 300 m, 300 – 350 m, 350 – 400 m; Figure 1.7). We hypothesized that the amount of NDVI alone may not allow us to discern differences among and within our sites. We believed that the configuration of the vegetation may play a strong role in providing both moose forage and cover/protection for moose and calves. To connect our vegetation data with the on-the-ground measurements of moose forage and visibility, we sampled both the center location (where the event occurred) along with randomly located points within each buffer ring (Figure 1.7; Figure 1.8-A). The locations were then buffered by both 11 m and 15 m (Figure 1.8-B), which correspond to the on-the-ground field measurements collected for calf visibility (15 m) and forage (11 m) by Severud et al. (2019). To calculate a variety of landscape metrics associated with the configuration of NDVI in the landscape, we first converted the NDVI into three classes (classified factors are required for analysis) representing the lowest third, middle third, and highest third of NDVI values (Figure 1.8-C). We then calculated over 30 spatial configuration metrics for each 11 m and 15 m location (30 location sites and > 200 random locations within buffered rings). These data were analyzed using the “landscapemetrics” package (Hesselbarth et al. 2019) in program R (R Core Team 2019). Linear models assessing the relationships between our sampled data and both on-the-ground measurements and within site variability were also conducted using program R.

Results:

Overall, we did not find consistent patterns of changes in mean NDVI levels collected from our multi-spectral sensor and the distance to the event site for any category of event (e.g., calf predation [Figure 1.9], calving). However, using NASA's satellite-derived estimates of NDVI we found differences among the site types (Figure 1.10). Locations with living moose had higher overall values of NDVI compared to calving and mortality sites.

We found strong correlations between our estimates of vegetation configuration and on-the-ground moose habitat sampling (Figure 1.11). A landscape metric that estimates the edge and interior shape index of our NDVI classifications had a positive correlation with on-the-ground estimates of moose forage (adjusted $R^2 = 0.92$; Figure 1.11-A). Calf visibility was strongly associated with several landscape metrics and a metric describing NDVI patch heterogeneity had a strong negative correlation with calf visibility (adjusted $R^2 = 0.97$; Figure 1.11-B).

Because of the strong correlations between these aspects of moose habitat and the metrics we calculated, we then used the two most correlated metrics to assess changes in moose forage and visibility at locations where no on-the-ground vegetation sampling was conducted. Among sites, we found estimated moose forage was higher at moose calving, peak lactation, or where moose were currently found (GPS-collared) compared to mortality sites (Figure 1.11-A). Modeled relationships showed that within sites, living moose were found in areas with more available moose forage (relative to calving and mortality sites) and that the living moose were often found in the area of highest estimated forage availability compared to the surrounding area (negative relationship between forage and distance; Figure 1.12-B).

We found significantly lower amounts of estimated horizontal visibility at calving sites relative to calf mortality and living sites using the best landscape configuration metric from our UAV-collected NDVI values. Calving sites had a significant negative relationship between inverse horizontal visibility and distance from the calving site suggesting moose seek out areas with the lowest visibility to give birth at relatively fine spatial scales (300 – 500 m; Figure 1.13).

Conclusions:

- We found strong correlations with on-the-ground measurements of vegetation (based on both NASA satellite-derived overall greenness and relative metrics of NDVI from our UAV-based multi-spectral sensor).
- Sites that had locations associated with living moose demonstrated that moose sought out the greenest patches at a fine spatial scale.
- Moose sought out calving sites in locations with the relatively lowest levels of horizontal visibility; calf mortality sites appear to be associated with areas of higher visibility.
- Our ability to link landscape metrics with important moose resources (forage and horizontal cover) demonstrated that the use of UAV-collected moose habitat data provides efficiency and much larger extents for capturing how moose make fine-scale decisions about foraging and calving.
- Use of UAVs to collect fine scale habitat data, especially when it can be linked with on-the-ground measurements, provides a potentially powerful and time saving tool for managers hoping to understand wildlife-habitat relationships in critical areas.
- Our findings will be further refined and shared with Dr. Glenn DelGiudice of the DNR for further consideration.

Citations:

- Didan, K. (2015). MOD13A2 MODIS/Terra Vegetation Indices 16-Day L3 Global 1km SIN Grid V006 [Data set]. NASA EOSDIS Land Processes DAAC. Accessed 2019-03-01 from <https://doi.org/10.5067/MODIS/MOD13A2.006>
- Hesselbarth, M.H.K., Sciaini, M., With, K.A., Wiegand, K., Nowosad, J. 2019. landscapemetrics: an open-source R tool to calculate landscape metrics. - *Ecography* 42:1648-1657(ver. 0).
- R Core Team. 2019. R: A language and environment for statistical computing. R Foundation for Statistical Computing, Vienna, Austria. <<https://www.R-project.org/>>.
- Severud, W. J., G. D. DelGiudice, and T. R. Obermoller. 2019. Association of moose parturition and post-parturition habitat with calf survival. *The Journal of Wildlife Management* 83:175–183.
- Severud, W. J., G. D. Giudice, T. R. Obermoller, T. A. Enright, R. G. Wright, and J. D. Forester. 2015. Using GPS collars to determine parturition and cause-specific mortality of moose calves. *Wildlife Society Bulletin* 39:616–625.

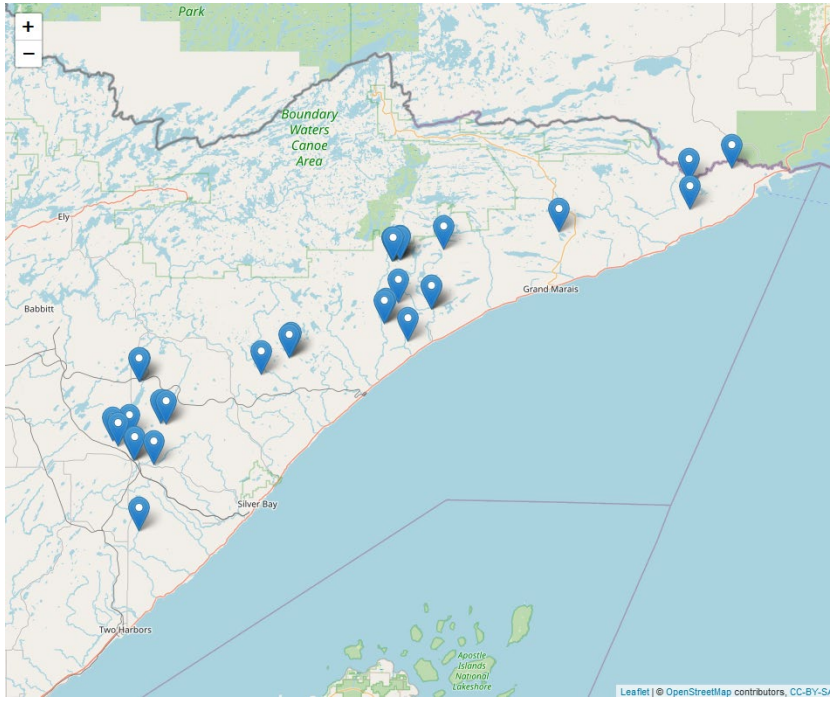


Figure 1.5) Locations of UAV flights in northeastern Minnesota where multi-spectral data was collected at locations associated with critical moose-related events.

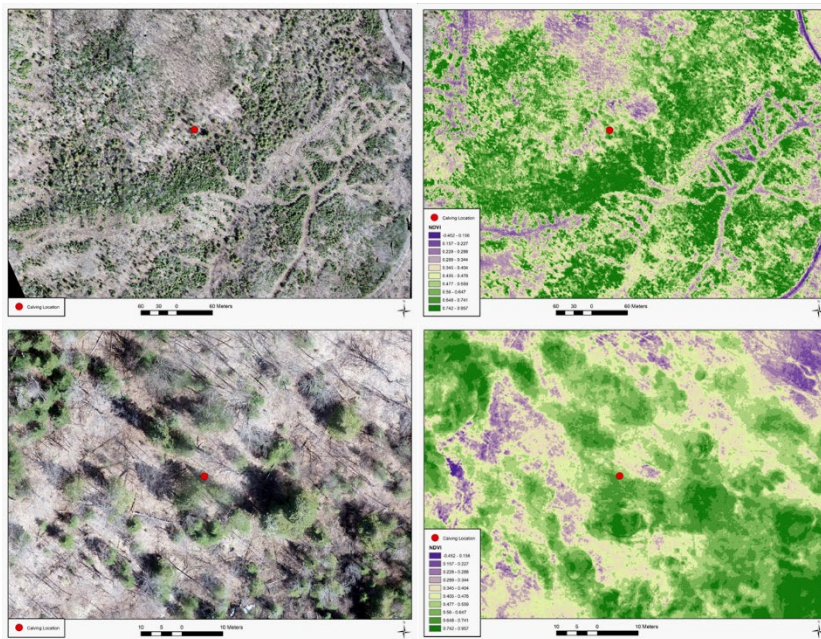


Figure 1.6) RGB (left panels) and estimates of relative NDVI (“greenness”; right panels; purple = lowest, dark green = greatest) at two moose calving sites in 2015.

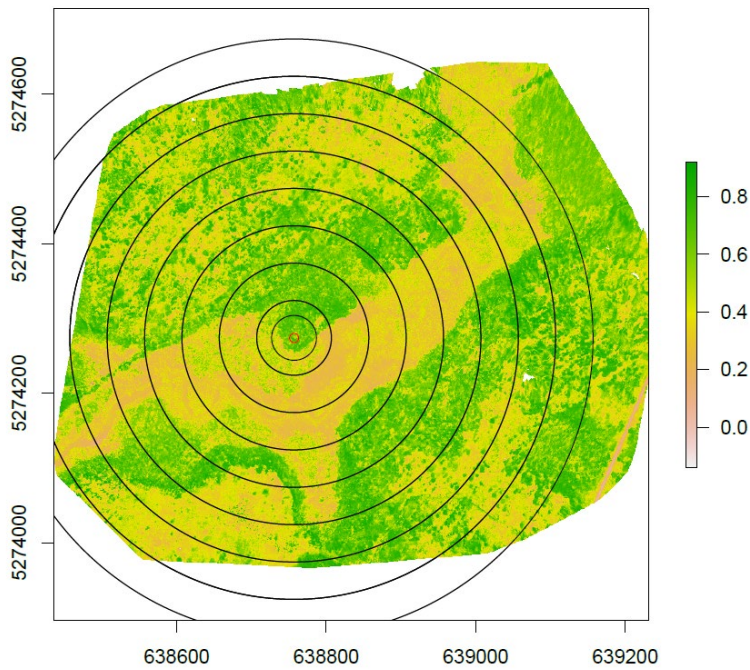


Figure 1.7) Example of the buffered rings used to assess changes in NDVI at each of the 30 moose event sites. The red point in the center is calving location.

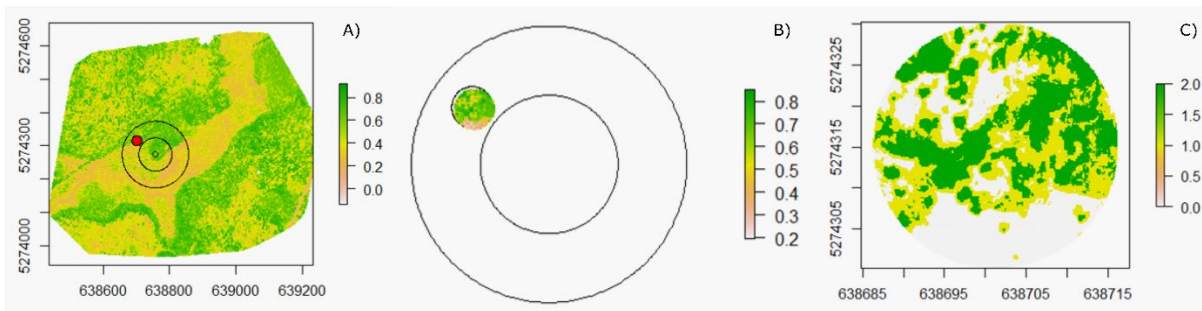


Figure 1.8) 4A: The 50-100 m buffered ring from Figure 3 with an associated random location (red point) inside. Locations were buffered at both 11 and 15 m and we analyzed the UAV-collected NDVI data within those buffered areas (4B). Within those areas we converted the NDVI estimates into low, medium, and high values in order to create landscape configuration metrics associated for each location (4C).

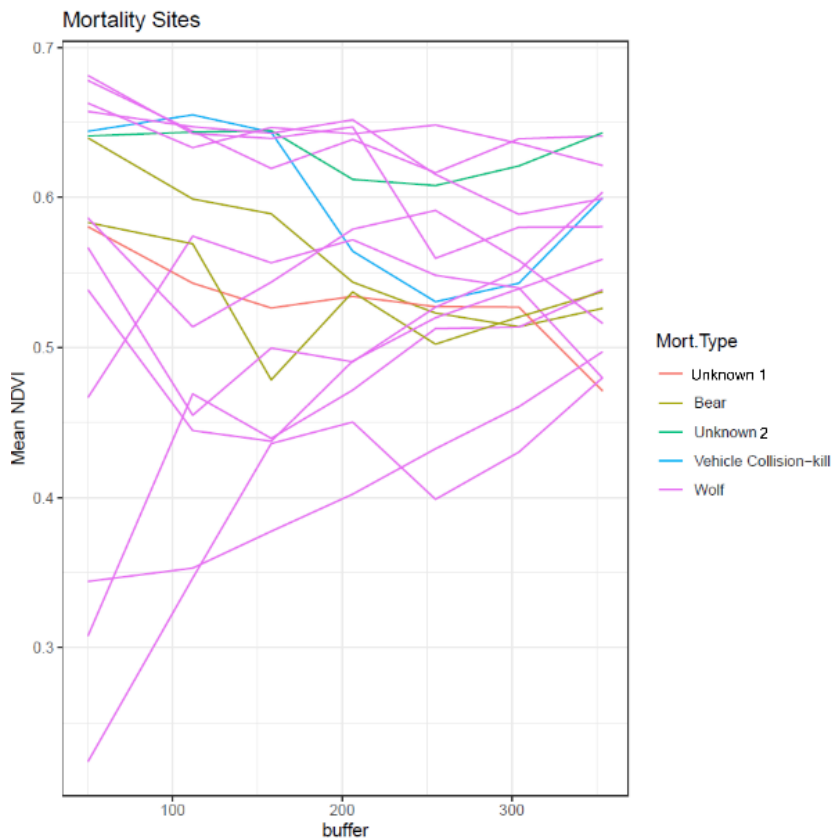


Figure 1.9) Relationship between mean NDVI (Y-axis) at the center of each location and among equal size rings (X-axis; units in meters) for moose calf mortality event sites. Mortality types are designated in the legend. Types were determined by researchers investigating kill sites of GPS-collared calves in 2015.

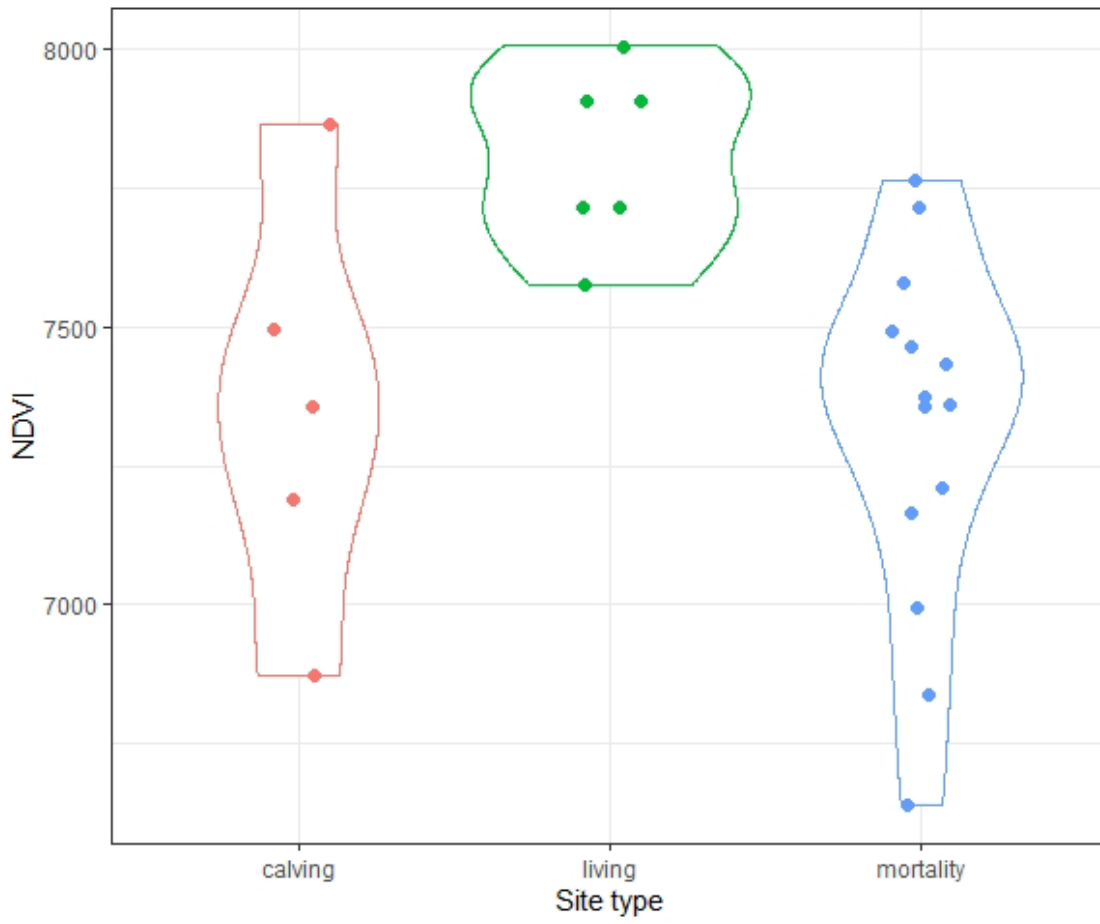


Figure 1.10) Satellite-derived estimates of NDVI (greenness) among different moose event sites.

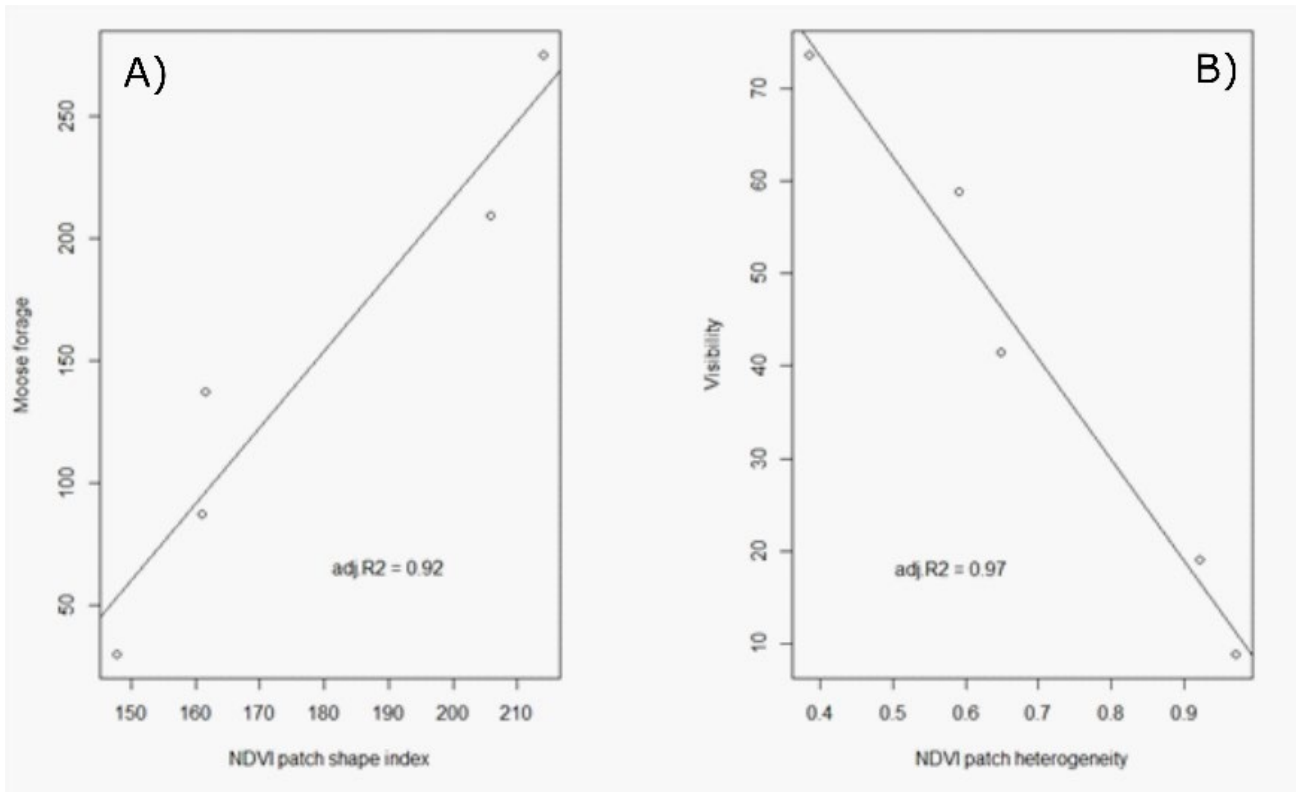


Figure 1.11) Linear relationships between landscape configuration metrics of NDVI from our multi-spectral sensor and on-the-ground estimates of moose forage (A) and calf visibility (B).

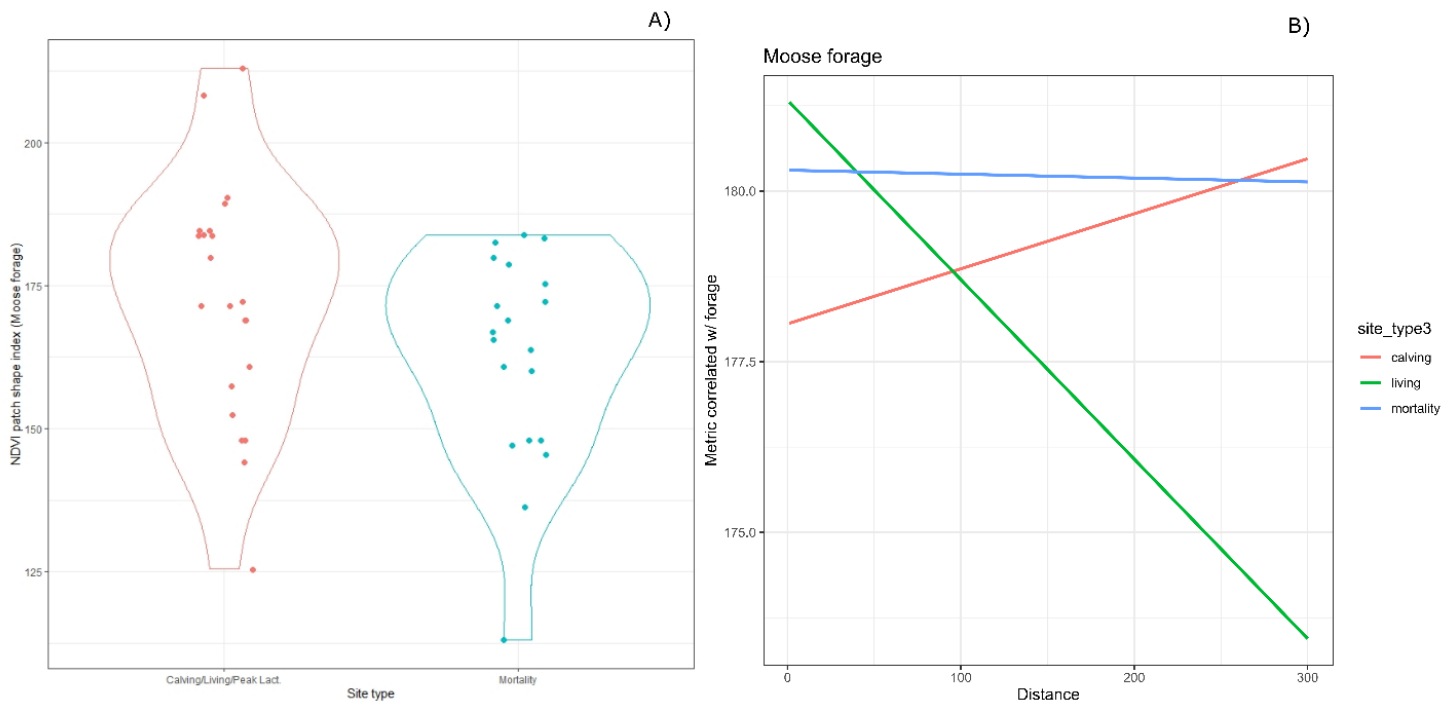


Figure 1.12) Using our landscape configuration metric of NDVI from our UAV-collected data that was most associated with moose forage, we examined the relationship among sites and the amount of estimated

moose forage at the central location for each type of site (calving, etc.; A). We modeled the relationship between distance from the central location and estimates of moose forage within the surrounding landscape (B).

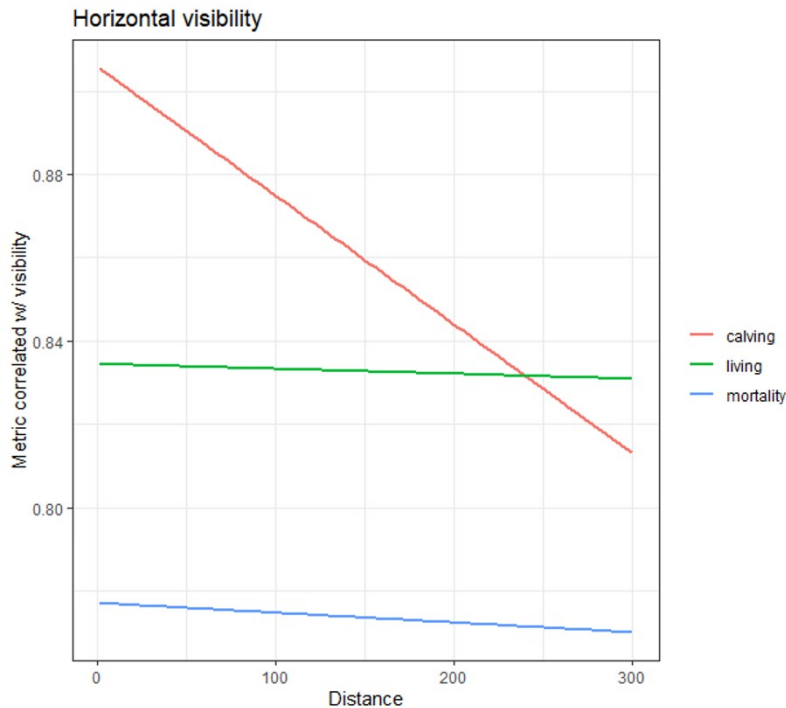


Figure 1.13) Using our landscape configuration metric of NDVI that is negatively associated with calf/horizontal visibility, we examined the relationship among sites and the amount of estimated visibility at the central location for each type of site (calving, etc.). Here we show the modeled the relationship between distance from the central location and estimates of inverse visibility within the surrounding landscape.

Summary (Activity 1)

- Using UAVs to automatically home in on VHF-collared individuals is feasible; however, it still requires custom-built hardware and software. We have made important strides towards making this a viable research technique.
- Small thermal cameras deployed on UAVs can produce images that identify medium to large-bodied mammals. Although the characteristics of these images lack enough unique features to reliably stitch them into large aerial images, we found that individual animals could be manually identified and counted within single images or frames of video.
- Automated processing of thermal images (to identify and count individual animals) is possible; however, it requires a very high-resolution image. We found that that the only way to produce such images was to fly our cameras very low to the ground (thus increasing potential impact on the study animals and also reducing the area that can be surveyed per flight). As thermal camera technology improves, the resolution of collected images will be greater and thus allow for automated ID of animals at higher flight elevations.
- We found that UAVs with FLIR sensing is a promising tool for quantifying moose calving success, twinning rate, and calf survival, and may be effective for monitoring the reproductive success and survival of other wildlife species in densely forested regions.

- We show that UAVs equipped with a multi-spectral camera can produce reliable estimates of forage availability and horizontal visibility. We found that female moose chose calving sites with lower visibility while adult moose usually chose areas with greater visibility yet more forage. Calf mortality sites tended to be in large patches of relatively high visibility habitat.

ACTIVITY 2:

Description: System to monitor and identify changes to sensitive ecosystems

We will utilize an existing UAV system, but develop a user friendly flight planning system that will maximize visual coverage, imagery collection, and post-processing capabilities to summarize collected data across space and through time. We will demonstrate this ability across several ecosystem types. The methods and software we develop for this activity can serve a wide array of ecological research questions, monitoring of the health of ecosystems, the effectiveness of management actions, the spread of disease or invasive species and potentially spills in waterways. This activity also has: **i) a lab component led by the Dr. Isler's graduate research assistant** that focuses on the development of the software and **ii) a field component, conducted by Dr. Forester's graduate research assistant**, to collect aerial imagery across a variety of ecosystems at the Cedar Creek Ecosystem Science Reserve (owned by the University of Minnesota).

i) The CS&E graduate research assistant will consider a number of trade-offs that need to be addressed to effectively use autonomous aerial vehicles in surveying and ecosystem monitoring tasks. The first one is the trade-off between coverage and resolution. Because an aerial vehicle has a downward looking camera, as the altitude of the vehicle increases, so does the camera footprint on the ground (i.e., the vehicle can cover larger areas by flying higher). However, this increased footprint comes at the expense of resolution (the number of pixels occupied by an object of interest in the image). Depending on the task and sensing requirements, the optimal altitude must be determined. Second, the amount of data collected by imaging sensors can easily overwhelm the storage and computation requirements of many systems. Most UAVs have limited storage and computation capabilities. Videos collected over time across multiple surveys can be hard to access and manage for users even after they are copied over to a workstation.

We will develop image processing software to summarize imagery collected in a single flight. This will be in the form of a 2.5 dimensional reconstruction of the environment. We will generate a mosaic corresponding to the (roughly flat) ground plane along with objects such as trees sticking out as convex polyhedral objects. Although existing software can mosaic aerial imagery, the programs usually fail when data are collected at low-altitudes. Therefore a new mosaic software will be developed. The map will be geotagged and aligned so that changes across time can be easily observed by going back and forth in time. We will demonstrate the effectiveness of the software by processing the imagery collected and stored from the UAV surveys conducted by the FWCB graduate research assistant at the Cedar Creek Ecosystem Science Reserve (CCESR). Time and resources permitting, we will investigate automated detection of major changes.

ii) The FWCB graduate research assistant will fly a UAV over areas of CCESR that experience ecosystem change through time. Based on where we have permission to fly transects, we will conduct case studies by collecting data over: 1) oak forests experiencing oak wilt, 2) fields where invasive plant species are spreading (*Elymus repens*), and 3) wetlands where cattails are highly prevalent. We will capture imagery from our UAV system equipped with multiple sensors (RGB and thermal imagery cameras) of these areas during September through October 2017. We chose oak wilt because it is a serious concern in Minnesota. This disease is caused by the non-native fungus *Ceratocystis fagacearum*, and is responsible for killing large numbers of oaks annually in Minnesota. Our second case study, focused on capturing the prevalence and spread of *Elymus repens*, is relevant because it will test our ability to identify the spread of terrestrial invasive plants. Finally, with our third case study, we will test the ability of our platform to map the extent of aquatic invasive species; cattails are of particular interest because the removal of the invasive cattail species often requires large expenditures or intensive management efforts. Collectively, our demonstrations of how UAV's can be utilized to quickly determine the extent and spread of disease and invasive species will be of great use to natural resource managers and researchers. Flights and

corresponding safety precautions will follow rules and regulations set forth in the Federal Aviation Administration’s Certificate of Authorization granted to the University of Minnesota. The altitude of the flights is will vary for each example, but all will be below 400 feet above ground level and likely about 200-300 feet above ground level. We have been granted access to fly over these areas by the Associate Director (Dr. Forest Isbell) of CCECSR.

The aerial imagery provided from these flights will be utilized by the CS&E graduate research assistant to develop the software and provide data to researchers working at CCECSR who have an interest in these questions. The FWCB graduate research assistant will conduct more flights at CCECSR during 2018 (July- September). We will work with CCECSR staff after 2017 to determine if the areas of image collection should change during the following year to answer new questions and also to test our newly developed software with different aerial imagery.

Summary Budget Information for Activity 2:

ENRTF Budget: \$ 160,190
Amount Spent: \$ 160,190
Balance: \$ 0

Outcome	Completion Date
1. UAV flights to collect data over different ecosystems in the Cedar Creek Ecosystem Science Reserve (CCECSR).	12/01/2017
2. Development of capabilities for geo-referencing imagery, comparing changes in the images, and creating a user-friendly interface for the software designed to handle aerial imagery from flights.	07/01/2018
3. Second year of flights at CCECSR during a slightly different time of year (and potentially over different area in CCECSR) to collect more imagery and further test the software developed in Outcome 2.	09/01/2018

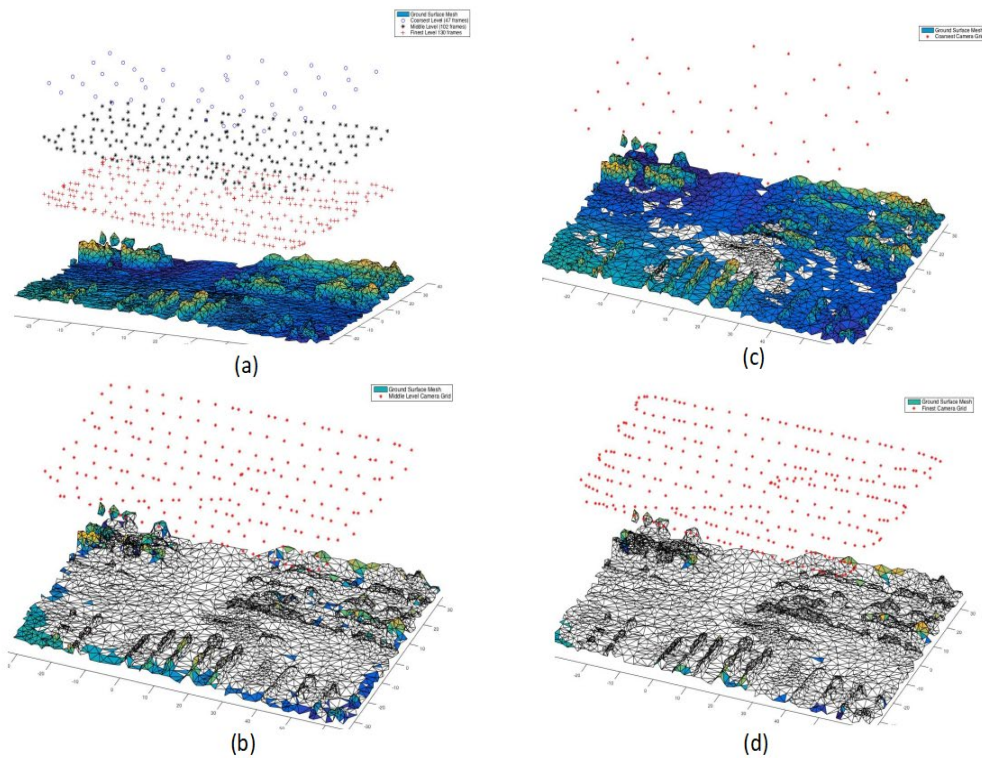
Activity 2 Status as of 01/01/2018: Now combined in 07/01/2018 status update.

Activity 2 Status as of 07/01/2018:

To date, we have collected UAV imagery from three locations that mimic potential management situations for MN land managers. In the first, we partnered with Dr. Rebecca Montgomery in the Forestry Dept. (UMN) to understand how canopy phenology may be linked to oak wilt, a disease killing oak trees in MN (**Image 5**). We conducted flights over an area CCECSR where every tree has been catalogued on a twice-weekly basis during four weeks in the fall to identify patterns of leaf senescence. We will repeat these surveys again this fall (2018).

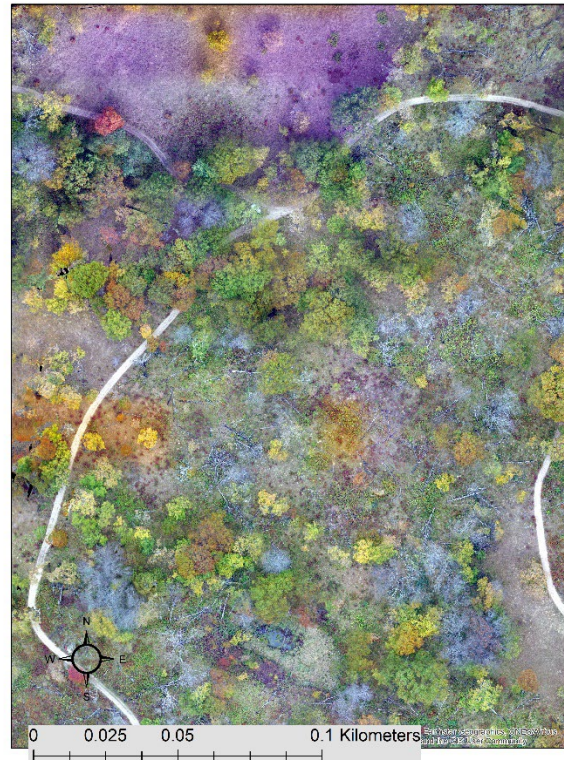
We also conducted flights before and after grass transect harvesting on experimental plots (**Image 6**) at CCECSR. The purpose was to understand if we can identify landscape change at a fine scale and determine the size of the change in biomass. Developing protocols like these will help land managers test the efficacy of prescribed burns or invasive species removal.

Finally, we used a multi-spectral sensor to collect imagery along a lakeshore in CCECSR. We will repeat this flight again during summer to demonstrate the abilities of the multi-spec to catalog and delineate vegetative changes in aquatic systems.



Dr. Isler and his graduate student Cheng Peng developed a view selection methodology, which can be used to select informative views from an image sequence which can be used as input to off the shelf image reconstruction software such as AgiSoft and Pix4D. With our view selection mechanism, reconstruction and image mosaic creation can be reduced from multiple hours to a few minutes. These results will be presented at a highly selective robotics conference at the of June.

We are currently collaborating with Dr. Joseph Knight (unpaid personnel on this project) who runs a remote sensing lab at the Univ. of Minnesota. We are utilizing the latest software (e.g. Pix 4D, Erdas) to geo-reference and stitch imagery and conduct analyses of landscape change from our thousands of collected images. We will continue to work on ways in which this can be made a more user-friendly experience for MN land managers who wish to incorporate drones to improve management actions and better quantify the efficacy of the results.



Images 5A and 5B: Fall flights over a forest at the CCESR where every tree is catalogued. We are recording changes in fall foliage and comparing them with patterns of oak wilt within the forest.



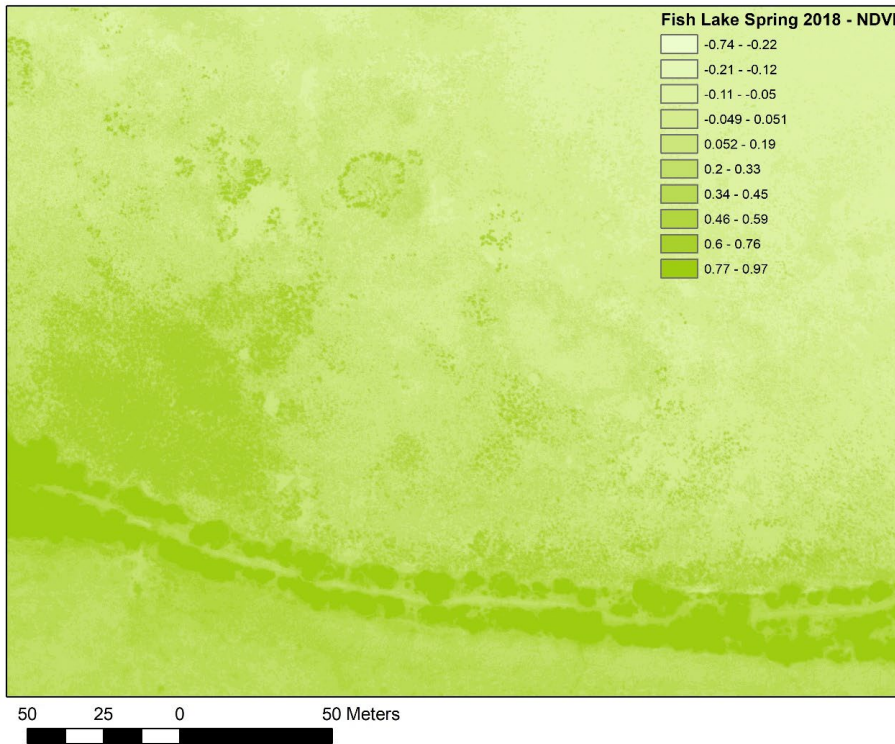
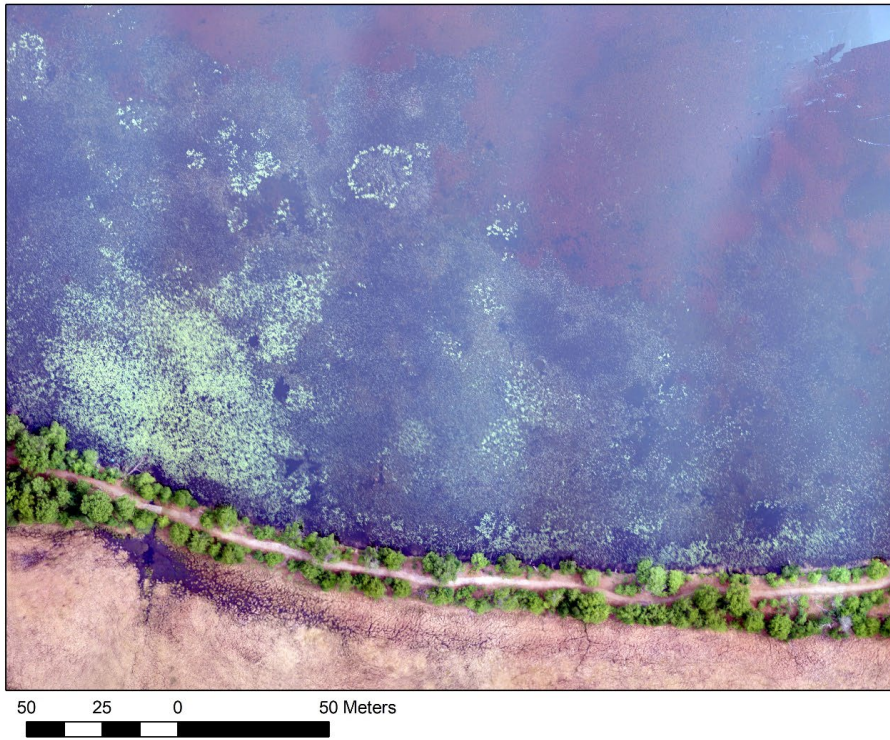
Image 6: Flights over a grassland in the Cedar Creek Ecosystem Reserve where small strips of grass were cut. We are identifying the change in the imagery from before and after the harvest.

Activity 2 Status as of 04/26/2019:

As part of our continuing partnership with Dr. Rebecca Montgomery in the Forestry Dept. (UMN), to understand how canopy phenology may be linked to oak wilt, a disease killing oak trees in MN, we repeated our forest surveys in the fall of 2018. This year our twice-weekly flights not only collected RGB imagery, but we estimated NDVI (normalized difference vegetation index), a measure of the greenness or productivity, using our multi-spectral sensor to track changes in leaf senescence during a 4-week period (see Image 7B below for an example at

another location). The resulting RGB and multi-spectral layers have been stitched together and we are working on the analysis.

We also repeated our flights over a wetland and lakeshore in the CCEsr. We chose to fly over this area in the spring and summer to collect imagery that shows a large amount of change in the aquatic vegetation community from one season to the next. We again used our RGB (**Image 7A** below) and multi-spectral sensors and estimated NDVI (**Image 7B** below). Utilizing this imagery in our automatic change detection software (under development) will highlight to managers the incredible usefulness of drones for identifying changes in invasive species, the efficacy of management actions, or simply the vegetative productivity of an area. Typically, vegetation/habitat data are only available at a resolution of either 15 m² or 30 m², which is often too coarse and collected too infrequently to inform management of the effectiveness of their actions or changes in the management area. Our imagery allowed us to quantify NDVI at a resolution of one-eighth (1/8th) m² which can provide very detailed and accurate estimates of change.



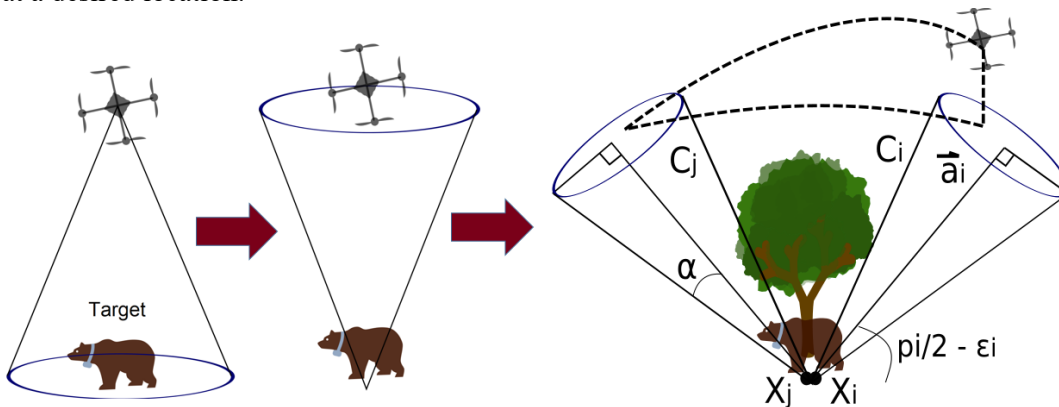
Images 7A and 7B: Flights over a lakeshore within CCSR during the fall using RGB (Image 7A) and multi-spectral imagery that can be converted into NDVI (Image 7B). Our multi-spectral imagery can be used to quantify NDVI at a very fine scale (resolution in image $\sim 1.8^{\text{th}}$ m²).

Activity 2 Status as of 07/01/2019:

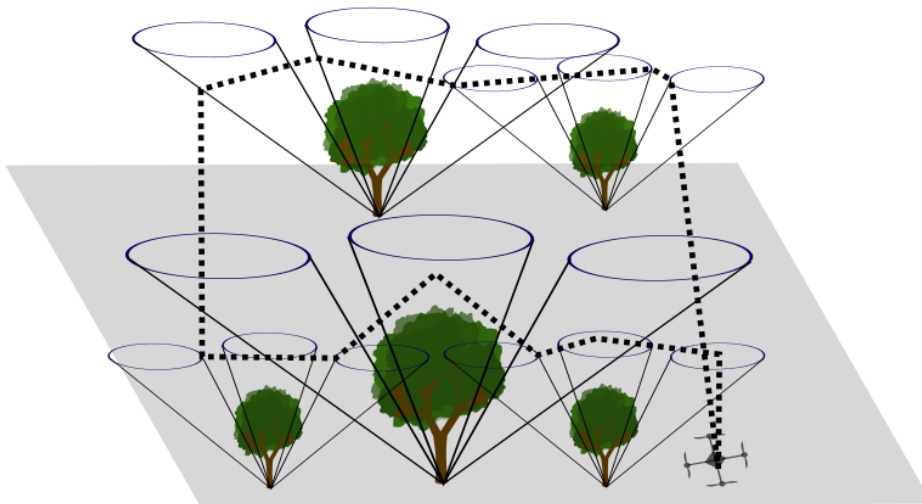
In the last two months, we have continued to analyze these data and will be continuing to work with them over the rest of the year.

Final Report Summary:

i) For this activity, Dr. Isler and the CS&E graduate research assistant considered a number of trade-offs and proposed solutions for related ecosystem monitoring tasks. First, we considered the relation between the camera resolution and UAV altitude. We associated each camera image with an inverted cone apexed at the location of the interest. The height of the cone is associated with the desired resolution and the apex angle corresponds to camera field of view. In other words, each cone encodes the set of view points from which a target can be imaged at a desired location.

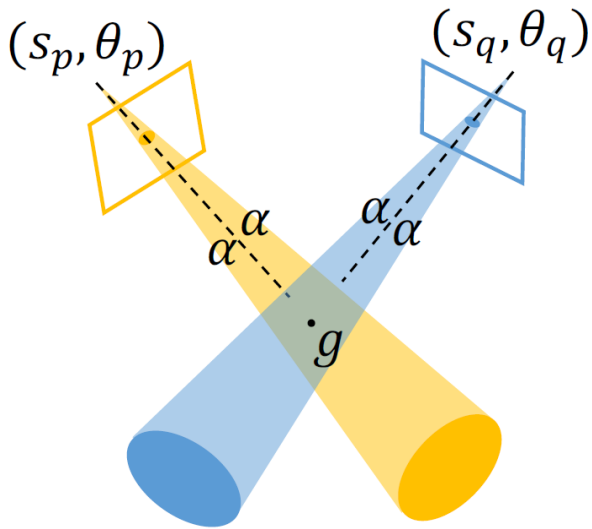


Second, we developed a strategy to efficiently visit a large number of such view cones in order to capture image footage.

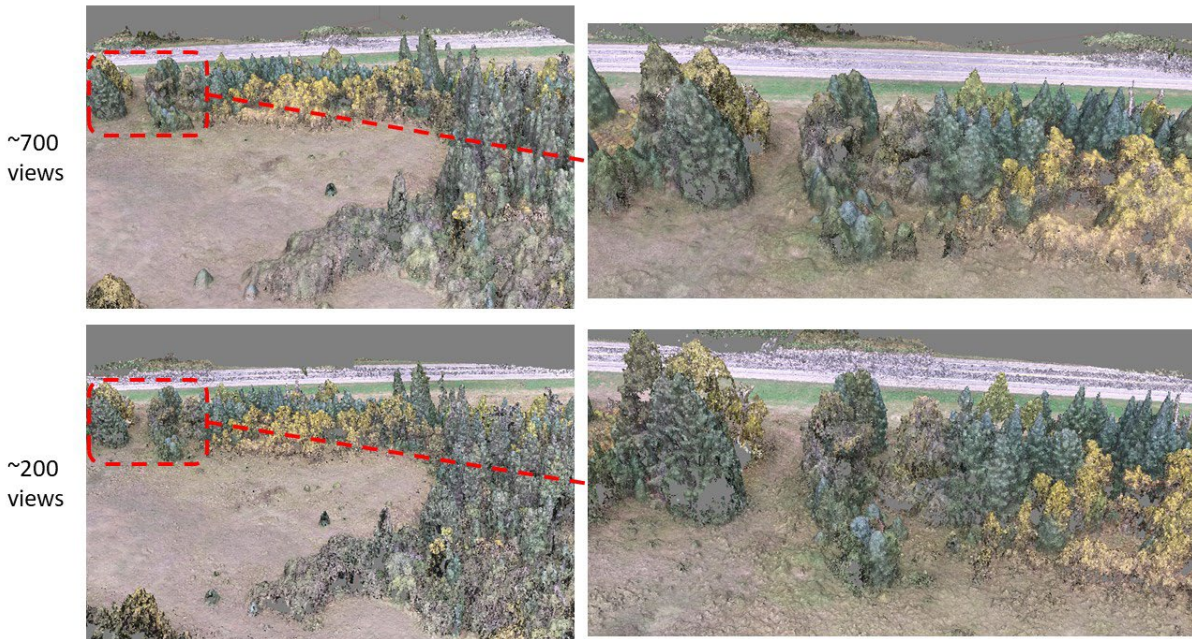


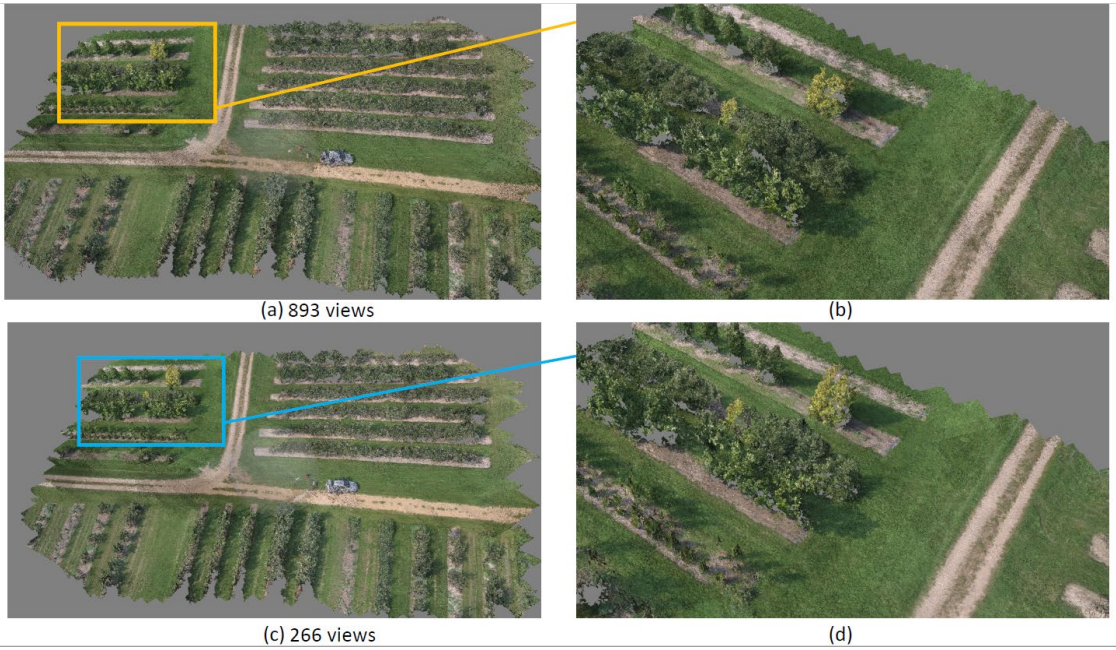
We analyzed the performance of our strategy and demonstrated through simulations and field experiments that by exploiting the special structure of the cones we can achieve shorter flight times than any other available solution. The strategy can be used with any number of cones and split coverage into multiple flights in order to account for limited battery power or image storage. The results of this work was published in IEEE International Conference on Robotics and Automation (ICRA), 2018 under the title “Approximation Algorithms for Tours of Orientation-varying View Cones”.

To minimize the number of views selected to build mosaic, we modeled image feature triangulation uncertainties during mosaicking process as intersections of right circular cones. We then analyze the worst case uncertainty behavior with only two views.

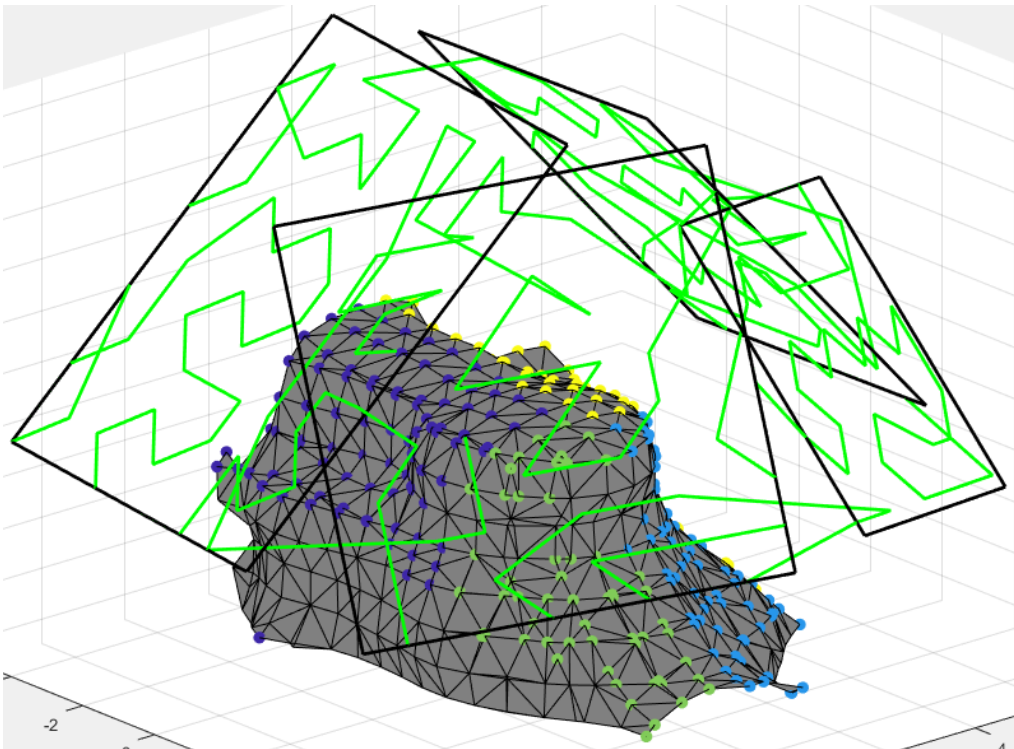


The result claims near-optimal performance given orthogonal viewing angles. Therefore, using this insight, we developed a coarse-to-fine strategy to select a subset of views such that the mosaic and reconstruction quality of a field is almost as good as that from using all images. The resulting processing time can be reduced from 12 hours to less than 1 hour. The result is published in Robotics: Science and Systems 2017.





When a scene has significant height variations and the planar assumption no longer holds. We also developed a method to reconstruct 3D geometry by dividing the scene into multiple planes. Our results extend the previous work to cover a broader range of geometry and is published in International Conference on Robotics and Automation 2019.



ii) For the second part of this activity, we first conducted a pilot study at Cedar Creek in which our graduate student learned how to collect multi-spectral data on areas with oak wilt and aquatic vegetation growth. Although the researchers involved with the oak-wilt study determined that hyper-spectral data (i.e., another sensor) was

more appropriate for their application, we were able to use the images to refine approaches for mosaic optimization (Stefas et al. 2018, 2020). We decided to use our experience with the multi-spectral camera to better understand fine-scale moose habitat selection (this study is detailed under Activity 1). When we consulted with managers at Cedar Creek about their potential needs for aerial image collection, they indicated that one of their concerns was being able to estimate how their white-tailed deer population changes through time. They are in the process of collecting camera trap data on deer, but had no other way to estimate population densities. We leveraged our experience with thermal imagery from Activity 1 to develop a sampling protocol that we ground-truthed with pellet counts.

Comparing unmanned aerial systems to conventional methodology for surveying a wild white-tailed deer population

Overview:

Here, we compare population density estimates derived from a UAV with a mounted FLIR sensor to estimates based on fecal (pellet-group) surveys, a method frequently used to estimate the density of ungulate populations. Pellet-group counts have been used for decades, and are still in use today, because of their cost effectiveness and ease of implementation. A major drawback of the approach is the requirement to estimate deer defecation and pellet decay rates, which can be difficult to obtain due to seasonal variation in diet and environmental conditions.

Our objectives were to: 1) examine the feasibility of using a fixed-wing UAV for detecting wild white-tailed deer (hereafter referred to as deer) in a forest-prairie interface, 2) determine deer population density from counts of deer in FLIR imagery, and 3) compare deer density estimates from UAV-gathered data to deer density estimates from pellet-group counts. We aim to provide information to wildlife professionals about whether UAV technology provides a significant advantage over cheaper and simpler conventional methodology, and how wildlife managers can most efficiently employ UAV technology to achieve research and management goals.

UAV surveys:

Surveys were conducted at the Cedar Creek Ecosystem Science Reserve (CCESR); located ~50 km north of Saint Paul, Minnesota, USA, near Bethel, Minnesota, in Anoka and Isanti counties (Figure 2.1). This is a 2,200 ha experimental ecological reserve that the University of Minnesota operates in cooperation with the Minnesota Academy of Science. We conducted UAV thermal surveys across the CCESR property from March to April of 2018 and from January to March of 2019. We used a Sentera PHX Pro fixed-wing UAV equipped with a FLIR Vue Pro 640 (640 x 512 pixel resolution, 32° FOV, 19 mm lens, 30 Hz) thermal sensor to detect white-tailed deer. We identified eight survey plots ranged in size from 46.29 ha to 119.82 ha and encompassed 30.69% of the CCESR property in total (Figure 2.1).

We pre-programmed the PHX to fly parallel transects at 121 m above ground level (AGL) over each survey plot using the laptop-based Sentera Ground Control program. We flew each plot at least twice per survey season, for a grand total of 35 survey flights, at various times of day from morning until evening. Parallel transects were used for efficiency and to minimize wildlife disturbance, and we did not observe any behavioral reactions during the course of our study. The onboard thermal sensor was automatically triggered by the PHX's flight computer to achieve the pre-programmed image overlap. Thermal imagery was captured as still photos with 70 to 80% front overlap and 30% side overlap. Each image covered an average ground area of 3,948 m² (approximately 60 x 70 m ground distance). Images were geo-referenced from the PHX's GPS system and included data on altitude, speed, and bank angle of the UAV at the time of image capture. Imagery was saved on a mini SD card onboard the UAV, and was transferred post flight to an external hard drive and cloud-based storage system for post-processing.

UAV data analysis

We removed any imagery that was captured with UAV bank angles (amount of side-to-side roll) of >10° because imagery captured at greater angles of bank (e.g., during turn-arounds when the UAV was realigning to start new

transects) would show inconsistent ground areas depending on bank angle, and would likely include space outside of our defined survey plots. We considered any bank angles of $<10^\circ$ to be products of ordinary wind turbulence during flight, based on observing the flight characteristics of the PHX and the distribution of bank angles in our data. We subsampled our thermal imagery for each plot by randomly selecting starting images and successively keeping any image with a centroid that was ≥ 80 m apart from any previously retained image's centroid, using program R. This process yielded a subsample of thermal imagery with a ground distance of 10 m to 24 m between the edges of thermal images to be analysed. This ensured that we did not analyse overlapping imagery, potentially recounting individual deer, and reduced the workload of reviewing the $\sim 22,600$ total thermal images collected.

We randomly subsampled the images under the constraint that any given sampled image was ≥ 80 m from the centroid of all other sampled images (i.e., no overlap was allowed). We manually reviewed the subsampled imagery from each plot and recorded counts of deer observations that we classified as either 'certain' or 'potential' detections. Certain detections were recorded when we had no doubt that a deer was in the image based on the shape, size, and relative brightness of the thermal heat signature. Potential detections were less certain detections that may have only met some, but not all of our shape, size, and brightness search criteria. Deer were distinguished from other wildlife by relative size and shape, as they were the only animal of their size present (e.g., bears were in dens, and wolves are rarely found in the study area). Coyotes, which were present in the study area, could potentially be misidentified as deer but are generally smaller and less common than deer. Prior to the start of the study, we recorded thermal imagery from a captive deer farm with a known number of deer. We used the imagery from the deer farm for training observers prior to reviewing field data. Imagery of the captive deer was taken with the same FLIR sensor at varying altitudes, angles, and amounts of vegetative cover to provide examples of how deer might appear in thermal imagery.

UAV deer density modeling:

We modeled deer counts (i.e., the number of deer observed in a thermal image) using the glmmTMB package in program R because it allowed for the inclusion of zero-inflated models and random effects. This approach also allows for different model structures in the zero inflation and conditional components. We included in our models the variables of sky cover (0 = clear sky, 1 = overcast sky) and the proportions of habitat cover type as possible fixed effects; a maximum of one cover type proportion was included per model component (i.e., each of the two component models could have at most sky cover and one land-cover proportion as a fixed effect). We used sky cover instead of ambient temperature because sky cover was previously shown to improve models of moose (*Alces alces*) detection over ambient temperature in forested habitats (Activity 1). Ground area (i.e., the spatial area observed within each thermal picture) was added as an offset to the conditional model based on our *a priori* reasoning that a greater area observed would result in a greater probability of deer detection. Survey flight ID and survey year (0 = 2018, 1=2019) were included as crossed random intercepts to account for variation among survey flights and years.

We determined the proportion of cover types within each image by clipping land cover data (MN Land Cover Classification, 2013) with a 35-m buffer around the centroid of each thermal image using ArcMap 10.5.1 (Environmental Systems Research Institute, Inc., Redlands, CA, USA). The radius of 35 m was chosen so that the buffer area around each image centroid equaled the mean ground area captured in the thermal imagery. We calculated the ground area of the thermal imagery for each image from flight altitude data using the Pythagorean Theorem and then averaged across all images. Proportions of each land-cover class (developed, conifer forest, deciduous forest, forested wetland, emergent wetland, grassland, agriculture, and open water [i.e., snow-covered ice]) were considered individually and in meaningful groups: forested upland (conifer + deciduous), open upland (agriculture + grassland), wetland (forested wetland + emergent wetland), non-wetland open area (grassland + agriculture + developed + open water), and no cover (emergent wetlands + grass + water + agricultural + developed). The composite variables were chosen based on the type of resources they might provide in winter (e.g., food, cover) and whether a given vegetation type would likely be tall or dense enough to obscure a deer from aerial thermal detection.

To predict the deer population size across the entirety of the CCSR property using our top-supported models of deer abundance (based on high and low count data), we created a virtual grid in Program R that covered the entire

area. Each cell of the grid was 3,948 m² (62.83 m x 62.83 m), which equaled the mean ground area captured in the individual thermal images. We calculated the proportion of each land-cover type and composite cover-type variable within every grid cell using the land-cover data set and binning scheme described above. To generate a point estimate of the deer population size, we used the predict function in program R to estimate the number of deer present in each cell; the predictions for all cells were summed to provide an estimate of the deer population within the CCESR property (we use a parametric bootstrap approach to estimate uncertainty in the point estimate).

Pellet-group count surveys:

We arranged pellet-group survey transects within the established UAV survey plots using a stratified random approach. We clipped land-cover data (MN Land Cover Classification, 2013) by the boundaries of the eight UAV survey plots and randomly inserted ~ 20 survey points proportionately with the availability of each cover type within the plot. Our habitat cover types for conducting pellet-group counts included deciduous forest, forested wetland, emergent wetland, grass, and row crops. Transects were planned prior to fieldwork by using our stratified random points as starting locations and laying out a 100-m line in a direction from the starting point that would allow the surveyors to remain in the same habitat cover type for the entirety of the transect.

Pellet-group counts were conducted during the months of April and May (2018 and 2019). We surveyed 133 transects in 2018 and resurveyed 120 of the same transects during 2019. Thirteen of the 2018 transects were not available for resurveying in 2019 due to prescribed burning on the CCESR property. Deer droppings were considered a pellet-group if there were at least 4 pellets of similar size, shape, and color within close proximity (pellets within 30 cm of each other). Pellet-groups were only counted if ≥50% of the pellet-group was within 1 m of the transect centerline, and they were determined to have been deposited after leaf-off the previous fall. Deciduous leaf litter falling between survey periods (2018 and 2019) eliminated the need to age or clear away pellet-groups, as only pellet-groups that had been deposited from fall to spring would be visible above the leaf litter. Where leaf litter was not present (e.g., open habitat types), we examined pellet-groups and determined deposition timing based on the presence of weather exposure, moss, and insect damage. Pellet-groups deposited post fall leaf-off would not likely show any such damage from exposure.

Pellet-group count data analysis and density modeling:

We estimated deer density from pellet count data in two ways. In the first, we used a simple equation (Gable et al. 2017): Deer density (deer/km²) = pellet groups counted / (pellet group deposition rate * deposition period * sampling unit area [km²]). We considered the pellet deposition rate to be 25 pellet-groups/deer/day based on pellet count surveys from a study near International Falls, MN (Gable et al. 2017). This value is based on the mean values for deposition rate from two other studies; Rogers (1987) used a deposition rate of 34 and Patterson et al. (2002) used 16. We also calculated a low estimate using the value of 34 pellet-groups/deer/day and a high estimate using 16 pellet-groups/deer/day. Our pellet-group deposition period (time between mean leaf-off date and mean survey date) was 192 days for 2017–2018 and 209 days for 2018–2019. Density estimates were derived for forested (deciduous + forested wetland) and non-forested (emergent wetland + grass + row crops) habitat cover types by pooling count data from specific cover types for calculation, and averaging across survey years. Point estimates of deer density were predicted across CCESR by applying density estimates for forested and non-forested land cover to the proportion of forested and non-forested land cover of each grid cell in the virtual grid system described above in the UAV Deer Density Modeling section.

We also took a second approach, in which we fit a Poisson hurdle model to the number of pellet groups found per transect. We used the same potential covariates, random effects, and parametric bootstrapping approach that we used for the UAV models; we divided the total area of each land-cover type in the landscape into 200-m² transect units (i.e., equal in area to our sample transects). The result of predicting this model across each transect unit in the landscape was a “predicted number of pellets,” that we converted to “predicted number of deer” by assuming a 192-day deposition period and the same high, low, and average pellet deposition rates used in the above equation.

Results:

We conducted 2-3 replicate surveys over our eight UAV survey plots at CCESR during winter and spring of both 2018 and 2019, totaling 35 thermal UAV flights with analyzable data. Our thermal surveys required a total of 24.7 hours of flight time with the PHX. We captured a total of 22,626 thermal images and analyzed a subsample of 3,757 non-overlapping images. Of these images, 96.6% did not contain any potential deer detections. We classified 48 thermal images as containing certain deer detections (Figure 2.2-A) and an additional 95 with potential deer detections (Figure 2.2-B). Images with deer detections ranged in count from 1 to 9 individuals and we detected a total of 96 certain deer and an additional 135 potential deer within all survey images (Figure 2.3). Our top detection models predicted mean point estimates for deer density of 12.38 and 6.18 deer/km² for the high and low detection estimates, respectively. Point abundance estimates were 273.81 deer and 136.68 deer on the CCESR property (22.12 km², Figure 2.4, Table 2). Our bootstrapped estimates of deer density had a mean estimate of 13.77 deer/km² for the high detection model, and a mean of 9.40 deer/km² for the low detection model. These density estimates equated to a mean of 305 deer on the CCESR property for the high-detection model, and 208 deer for the low-detection model (Figure 2.4).

To ground-truth these estimates, we surveyed 133 pellet-group count transects covering 26,600 m² in 2018 and recorded 1,085 pellet-groups. In 2019, we completed 120 transects equating to 24,000 m² surveyed, recording 766 pellet-groups. Our predicted point estimates were 5.13, 6.98, and 10.91 deer/km² based on high (34 pellet groups/deer/day), mean (25 pellet groups/deer/day), and low (16 pellet groups/deer/day) deposition rates, respectively. Point estimates of abundance were 112.79 deer for high deposition, 153.39 deer for mean deposition, and 239.67 deer for low deposition on the CCESR property (Figure 2.4). The bootstrapped predictions resulted in a mean of 5.15 deer/km² for high deposition, a mean of 7.01 deer/km² for mean deposition, and a mean of 10.95 deer/km² for low deposition. The corresponding bootstrapped abundance estimates for CCESR from our bootstrapped prediction intervals were 113.25 deer, 154.02 deer, and 240.66 deer, respectively (Figure 2.4).

Conclusions:

We successfully applied UAV and FLIR technology to survey a wild population of white-tailed deer and compared the efficacy of this approach to pellet-group count surveys, a widely-used conventional method for surveying ungulate populations. Both of these methodologies yielded similar results for overall abundance estimates (between 200 and 300 animals; Figure 2.4) dependent on assumptions regarding the pellet deposition rates and detection rates, yet varied in levels of sampling effort, cost, and time. Despite increasing use of UAV in wildlife research, many studies rely on expensive UAV and sensors and do not assess how well the approach compares with established methods. However, understanding the logistical, financial and practical hurdles of incorporating UAV is especially important for wildlife managers with limited resources. Our findings provide insights into the process and utility of integrating UAV into monitoring ungulate populations in an efficient and temporally sensitive manner.

The most notable difference between pellet-group counts and UAV surveys was the amount of time and effort required for each approach. Pellet counts took approximately 160 hours (i.e., the time taken to count pellets and hike between survey transects) over both survey seasons, whereas the UAV surveys required only 24.7 hours of flight time in addition to approximately 30 minutes to one hour for set up and take down per launch site, totaling 17.5 to 35 hours of non-flight field effort. Time spent driving between UAV launch sites was negligible. An additional 25 to 35 hours of effort was required for manual review of thermal imagery. The physical effort required for pellet count surveys was greater, requiring large amounts of off-trail hiking to reach survey sites, relative to the majority of UAV launch sites off of drivable roads and trails. Pellet-group counts were also temporally restricted to just prior to spring green up, after all snow cover was melted, for maximum detectability of pellet-groups by human observers. Conversely, UAV FLIR surveys could be carried out with far greater flexibility and would have been feasible anytime from late November through April, which corresponded to leaf-off conditions for deciduous trees. The window of time for deciduous leaf-off conditions is relatively large at northern latitudes and is irrelevant for ungulate surveys in open grassland habitats. This wide temporal range allows researchers and managers greater operational flexibility for surveying ungulates, as compared to being seasonally restricted by pellet-group counts.

References:

Gable, T. D., Windels, S. K., and Olson, B. T. (2017). Estimates of white-tailed deer density in Voyageurs National Park: 1989–2016. Natural Resource Report NPS/VOYA/NRR—2017/1427. National Park Service, Fort Collins, Colorado.

Patterson, B. R., Macdonald, B. A., Lock, B. A., Anderson, D. G., and Benjamin, L. K. (2002). Proximate factors limiting population growth of white-tailed deer in Nova Scotia. *Journal of Wildlife Management* 66, 511-521.

Rogers, L. L. (1987). Seasonal changes in defecation rates of free-ranging white-tailed deer. *The Journal of Wildlife Management* 51(2), 330-333.

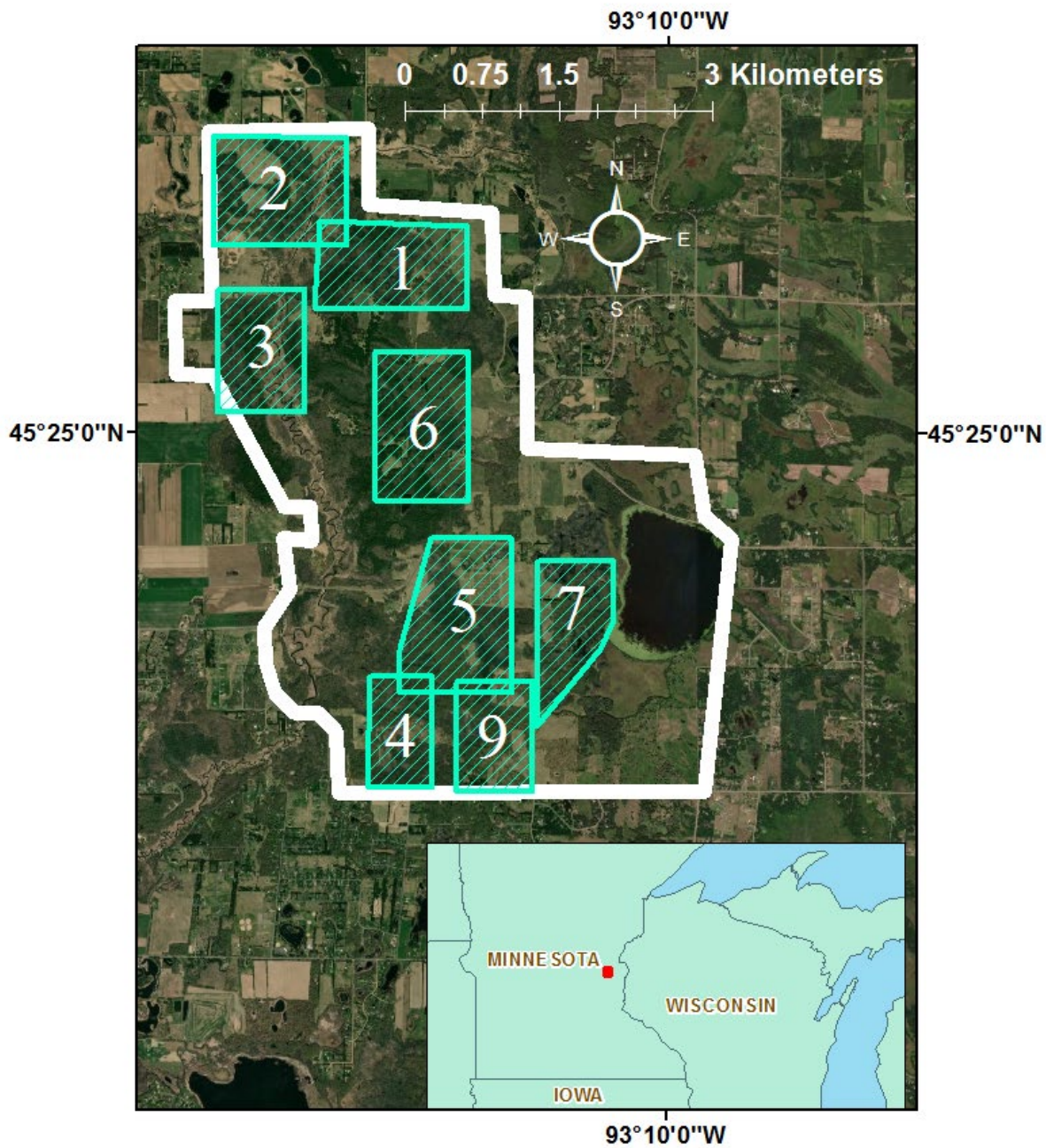


Figure 2.1: Cedar Creek Ecosystem Science Reserve (CCESR) study area, Minnesota, USA. Unmanned aerial system (UAV) survey plots are distinguished by the teal, numbered boundaries. Plot 8 was omitted from our study because of our inability to safely land the UAV at that site.

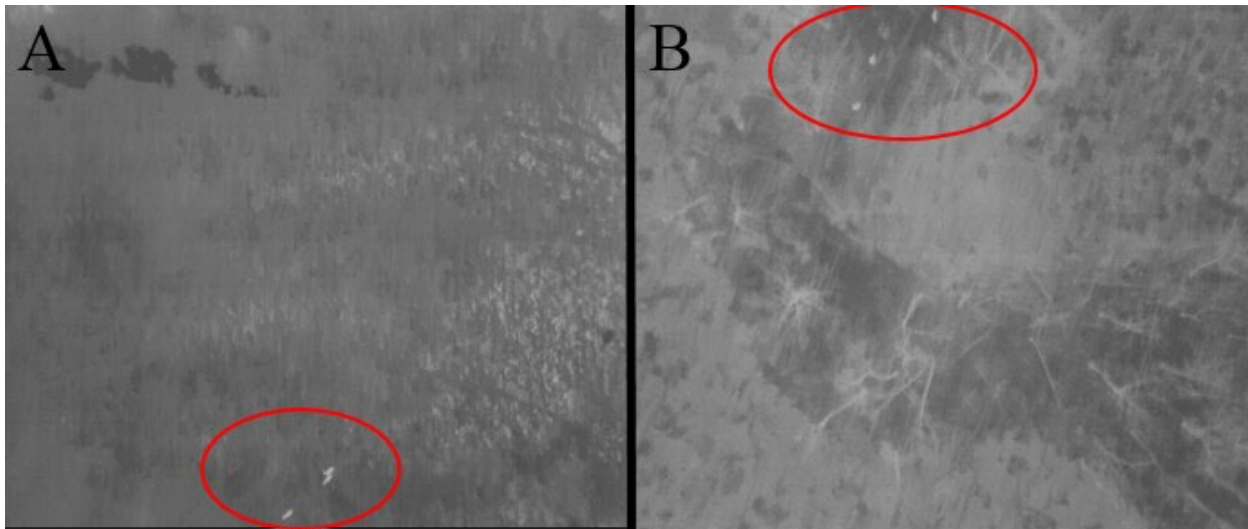


Figure 2.2: Thermal imagery of certain white-tailed deer (*Odocoileus virginianus*) detections (A) and potential deer detections (B) collected at Cedar Creek Ecosystem Science Reserve, Minnesota, USA during UAV surveys from March to April of 2018 and from January to March of 2019. We distinguished between certain and potential deer detections by shape, brightness, and size of thermal signatures. Figure 2A shows clear thermal signatures of deer based on these factors, while figure 2B contains less certainty based on shape. Such signatures were still counted as potential deer because shape can vary greatly in thermal imagery (e.g., when deer are bedded down versus standing/walking).

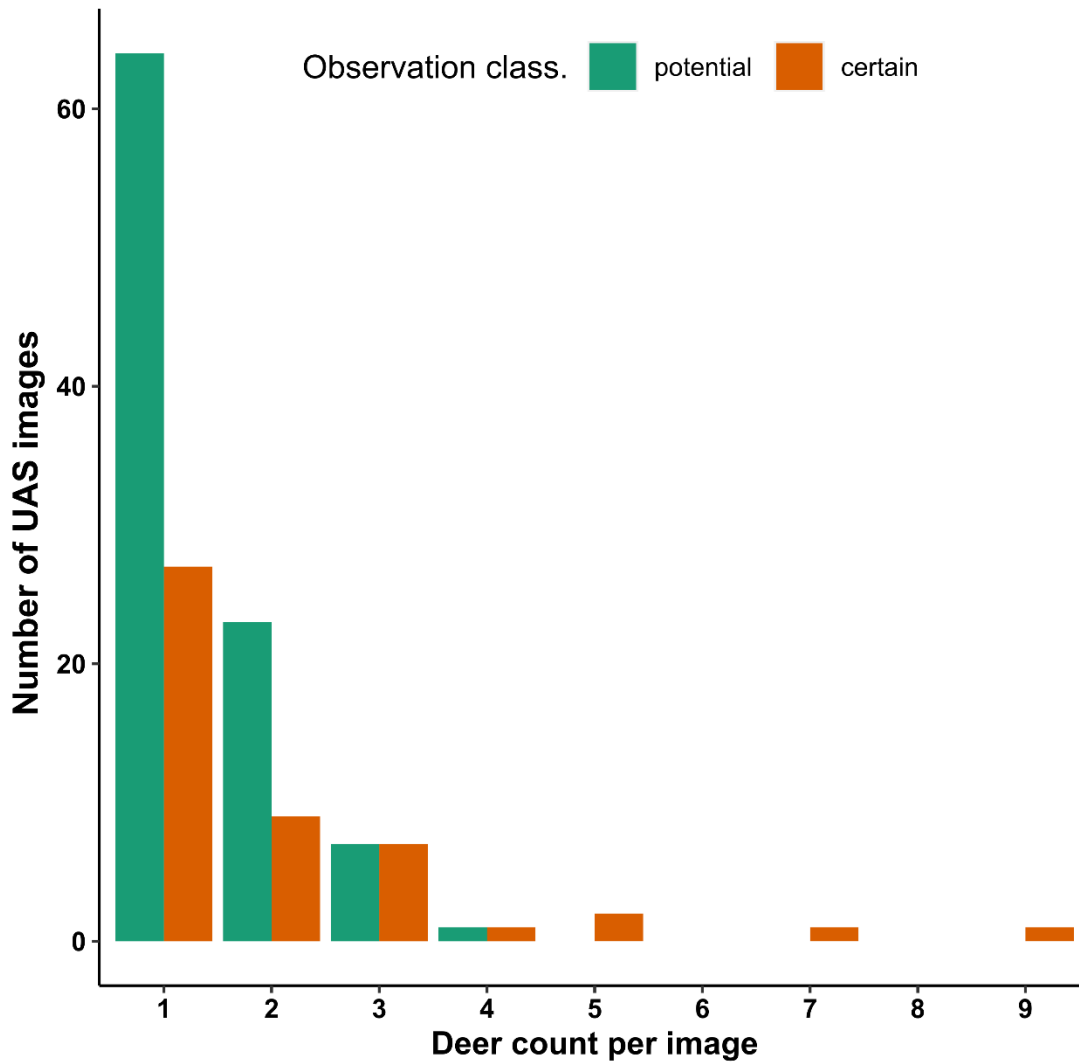


Figure 2.3: Histogram showing the number of UAV images with 1–9 certain or potential white-tailed deer (*Odocoileus virginianus*) detections from thermal imagery during unmanned aerial system surveys at the Cedar Creek Ecosystem Science Reserve, Minnesota, USA from March to April of 2018 and from January to March of 2019. Overall, deer counts per image ranged from 1 to 9 deer, with 3,631 images containing no detection. We distinguished between certain and potential deer detections by shape, brightness, and size of thermal signatures.

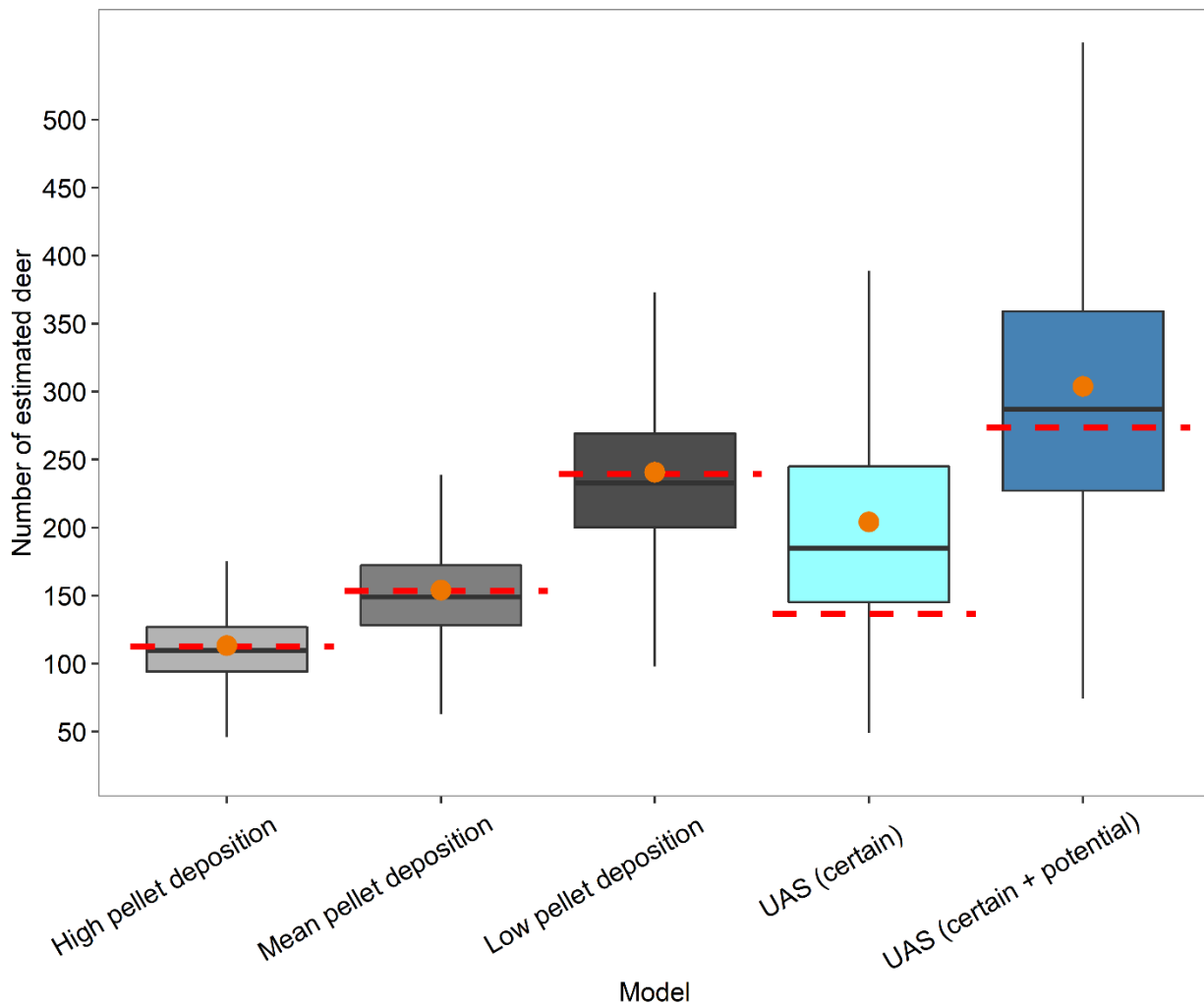


Figure 2.4: Boxplots of the bootstrapped predictions of the number of estimated deer in the Cedar Creek Ecosystem Science Reserve, Minnesota, USA based on pellet-group count models assuming high, mean, and low rates of pellet deposition (34, 25 & 16 pellets per deer per day, respectively) and UAV models using counts of certain and certain plus potential white-tailed deer in thermal images. Surveys were conducted from March to May of 2018 and from January to May of 2019. Orange points represent the means of the bootstrapped predictions. Red-dashed lines on each pellet-based model show the model-free point estimates. The red dashed-lines over the UAV model estimates represent mean point estimates from the top model for certain and certain plus potential deer detections.

Summary (Activity 2)

- We developed a new approach to optimize flight paths of UAVs so that optimal views of the target area could be achieved while avoiding undesirable artifacts such as glare on water or 3-D obstruction from trees.
- We conducted a pilot study in which we developed a workflow for multi-spectral data that allowed us to use a commercial UAV to collect fine-scale forage availability data for moose (for our application of this approach, see Activity 1).
- We used thermal cameras to repeatedly survey the deer population at Cedar Creek. Our approach can be easily applied in other areas and provides a repeatable, spatially explicit approach to estimating the abundance of mid-large sized mammals.

- We found that automatic detection of deer using software was not feasible, given the flight elevation required for the survey; however, we developed a methodology in which researchers manually counted animals in a random subset of images from the survey area. This approach is relatively fast and produces a repeatable count estimate.

V. DISSEMINATION:

Description:

Our development of technology and software, as well as our field methodologies and analyses of biological data, will result in several manuscripts written and submitted for publication in peer-reviewed journals. Findings will be presented at state and national wildlife and ecology conferences (e.g., the annual Minnesota Moose Meeting, state and national meetings of The Wildlife Society). All publications resulting from this project will be made available through the FWCB website or Open Access journal websites.

We expect that as our technologies and methodologies are proven in field tests, there will be a large amount of informal dissemination because we will be working closely with researchers at the University of Minnesota and the Grand Portage Band of the Lake Superior Chippewa. We also have a history of working with researchers and managers from the Department of Natural Resources, The Nature Conservancy, and the US Geological Survey. We have also been approached by Mike Schrage, the wildlife biologist for the Fond du Lac Band, about potential future collaboration and use of our UAV based on this proposal. We expect the MN Department of Natural Resources to have a strong interest in the UAV capabilities and specifically the effectiveness and data resulting from Activity 1 (moose calf surveys and VHF homing technologies). We hope that in the future, we can work closely with them to expand UAV moose surveys in other areas of the state and use UAVs to reduce the impact of studying other species of interest in MN. We will work openly with any of these groups to share our capabilities, software and equipment (as availability dictates), to ensure that our technological advancements and research papers reach a broad audience within their agencies.

Status as of 01/01/2018: Now combined in 07/01/2018 status update.

Status as of 07/01/2018:

We have worked extensively with the tribal biologists for the Grand Portage Band of Lake Superior Chippewa. Our work has sparked interest in additional surveys for other wildlife applications there and with the Fond du Lac Band tribal biologist. They have been impressed by the capabilities of the UAV and sensors and are looking into purchasing their own for management and wildlife monitoring. We plan to do additional surveys for them (wolves, moose in winter when we will likely improve sightability).

The FWCB graduate student is planning to give presentations at the upcoming Midwest Fish and Wildlife Conference and the Minnesota Fish and Wildlife Conference.

Once our methodologies are refined, we will reach out to several DNR collaborators (from previous research efforts) to share the results from this study.

Publications from the CS&E group:

Bayram, H., Stfas, N., Engin, K.S., & Isler, V. (2017). Tracking wildlife with multiple UAVs: System design, safety and field experiments. *2017 International Symposium on Multi-Robot and Multi-Agent Systems (MRS)*, 97-103.

<https://ieeexplore.ieee.org/abstract/document/8250937/>

Bayram, H., Stfas, N., & Isler, V. Aerial Radio-based Telemetry for Tracking Wildlife, submitted to IROS 2018

Peng, C & V. Isler (2018) View Selection with Geometric Uncertainty Modeling Robotics: Science and Systems, 2018. Accepted.

Status as of 04/26/2019:

The tribal biologists for the Grand Portage Band of Lake Superior Chippewa have been pleased with the FWCB student's first season and have invited him up during March to collect data about calf survival from spring (2018) through the winter of 2019. The early success of this field work has increased their interest in utilizing drone surveys to track moose and other wildlife in the future.

We are also reaching out to DNR researchers to show the capabilities of our drone flights with thermal and multi-spectral sensors. We are currently discussing working with Dr. Glenn DelGiudice and his former PhD student, Dr. Bill Severud to utilize our multi-spectral camera to determine fine-scale habitat components for moose calves that survived and those that were predated. This will help to advance part of this project's aim to "capture additional data about the habitat selected by the adult moose for giving birth and areas used after the calves are mobile". The master's student is already collecting this data in Grand Portage, but this collaboration would expand on it to areas further south of our current study area and offer sites to sample.

The master's student, Michael McMahon presented his research as a talk (w/ Dr. Ditmer and Dr. Forester as co-authors) entitled, "Find the Moose: Employing Unmanned Aerial Vehicles for the Detection of Moose in Northeastern Minnesota" at the upcoming Annual Meeting of Minnesota's The Wildlife Society (TWS) and the Society of American Foresters (SAF) in Duluth on February 19-21, 2019.

Status as of 07/01/2019:

No additional outreach activities have occurred in the last two months.

Final Report Summary:

This project resulted in four scientific presentations, two published conference papers, three accepted journal papers and one submitted journal article; the CSE graduate student working on developing an aerial robotic system and strategy to approach a radio signal beacon from a high altitude was awarded the UMII MnDrive fellowship award from the University of Minnesota. Our research into field applications of thermal imagery for assessing moose calving and mortality events was conducted in close collaboration with researchers from the Grand Portage Band of Lake Superior Chippewa and the MNDNR; we are continuing these collaborations and expect to submit another paper (detailing the calving habitat results) later this year. Our work to develop a new approach to sample deer populations using UAVs and thermal sensors grew out of a need at Cedar Creek to better understand their deer population. We tested our approach in the Cedar Creek Ecosystem Science Reserve and compared population estimates generated from UAV data to those from more traditional pellet-count approaches; we are now working with researchers at Cedar Creek to validate their camera-trap estimates of deer population density. Finally, three undergraduate students, three graduate students, and two postdoctoral researchers received training as part of this project; results from this research have been added into teaching materials in two required Fisheries, Wildlife, and Conservation Biology courses at UMN.

- We developed an aerial robotic system and strategy to approach a radio signal beacon from a high altitude with the purpose of obtaining image data at a desired resolution. This work resulted in a published conference paper [1] and a submitted journal paper [4].
- We developed a method to generate an optimal trajectory to obtain camera footage of difficult to see areas. This work resulted in a published conference paper [2] and a journal paper [3].
- We used UAV equipped with thermal sensors to estimate calving success for female moose in NE MN; this work resulted in a journal article [5].
- We also developed a new approach to sample deer populations using UAV and thermal sensors. We tested this approach in the Cedar Creek Ecosystem Science Reserve where we compared population estimates generated from UAV data to those from more traditional pellet-count approaches. This work has been accepted for publication in a journal [6].

[1] H. Bayram, N. Stefas, and V. Isler, "UAV Landing at an Unknown Location Marked by a Radio Beacon", IEEE International Conference on Intelligent Robots and Systems (IROS), 2019.

[2] N. Stefas, Patrick A. Plonski, and V. Isler, "Approximation Algorithms for Tours of Orientation-varying View Cones", IEEE International Conference on Robotics and Automation (ICRA), 2018.

[3] N. Stefas, Patrick A. Plonski, and V. Isler, 2020, "Approximation Algorithms for Tours of Orientation-varying View Cones", International Journal of Robotic Research 39(4):389-401.

[4] H. Bayram, N. Stefas, and V. Isler. "UAV Landing at an Unknown Location Marked by a Radio Beacon", IEEE Transactions on Robotics (T-RO) (submitted)

[5] McMahan, M. C., M. A. Ditmer, E. J. Isaac, S. A. Moore, J. D. Forester. 2021. Evaluating unmanned aerial systems for the detection and monitoring of moose in northeastern Minnesota. Wildlife Society Bulletin (in press). DOI: 10.1002/wsb.1167.

[6] McMahan, M. C., M. A. Ditmer, J. D. Forester. 2021. Comparing unmanned aerial systems to conventional methodology for surveying a wild white-tailed deer population. Wildlife Research (in press).

Presentations

McMahon, M.C., M. Ditmer, and J. Forester. Unmanned aerial vehicles for the detection and monitoring of moose calves in northeastern Minnesota. The Wildlife Society Annual Conference. Reno, NV. September 29-October 3, 2019.

Ditmer, M. Quantitative methods in wildlife research. WI DNR, Rhinelander, WI. June 10, 2019.

McMahon, M.C., M. Ditmer, and J. Forester. Find the moose: Employing unmanned aerial vehicles for the detection of moose in northeastern Minnesota. Annual Meeting of the Minnesota Chapter of The Wildlife Society, Duluth, Minnesota, February 19-21, 2019.

Forester, J. D. 2018. White-tailed deer and moose biology and management in mid-west. Norway Student Exchange, University of Minnesota, Saint Paul, MN. 26 September 2018.

Other Outreach:

McMahon, M.C. 2019. It's a bird, it's a plane, it's a...drone! Cedar Creek: Eyes on the Wild project blog. <https://eyesonthewild.blogspot.com/2019/02/its-bird-its-plane-its-adrone.html>

VI. PROJECT BUDGET SUMMARY:

A. Preliminary ENRTF Budget Overview:

***This section represents an overview of the preliminary budget at the start of the project. It will be reconciled with actual expenditures at the time of the final report.**

Budget Category	\$ Amount	Overview Explanation
Personnel:	\$298,383	1 project manager at 50%FTE for 2y; 1 engineer at 11%FTE for 2y; 1 wildlife biologist at 8%FTE for 2y; 1 graduate research assistant in CS&E at 50% FTE for 2y; 1 FWCB Master's student at 50% FTE for 2y.
Equipment/Tools/Supplies:	\$8,851	Quadcopter UAV, Parts for both fixed-wing and quadcopter UAVs, and cameras/sensors
Capital Expenditures over \$5,000:	\$20,798	1 Fixed wing UAV w/ flight training (\$14,450), combined color/thermal camera for moose calf

		work (\$6,348).
Travel Expenses in MN:	\$9,206	Travel to and between data gathering sites and truck rental .Food and housing for field work.
Other:	\$10,760	Networking and Computer Services for storage to support UMN projects in the CS&E – such as large files provided by the aerial imagery, repairs
TOTAL ENRTF BUDGET:	\$348,000	

Explanation of Use of Classified Staff:

Explanation of Capital Expenditures Greater Than \$5,000:

The UAV and all of the additional equipment utilized for engineering purposes to enhance the UAV will continue to be used for similar projects and purposes by the Forester and Isler Labs at UMN for the life of the instrument. If other researchers, state or tribal agencies are interested in its use, we will provide it for them whenever possible. If the instrument is sold prior to its useful life, proceeds from the sale will be paid back to the Environment and Natural Resources Trust Fund.

Total Number of Full-time Equivalents (FTE) Directly Funded with this ENRTF Appropriation: 4.6

Total Number of Full-time Equivalents (FTE) Estimated to Be Funded through Contracts with this ENRTF Appropriation: 0

B. Other Funds:

Source of Funds	\$ Amount Proposed	\$ Amount Spent	Use of Other Funds
Non-state			
National Science Foundation	\$801,000	\$0	Not Funded
State			
	\$	\$	
TOTAL OTHER FUNDS:	\$	\$	

VII. PROJECT STRATEGY:

A. Project Partners:

Partners receiving ENRTF funding

- Dr. Mark Ditmer, Research Specialist, Univ. of MN - Dept. of Fisheries, Wildlife and Conservation Biology, \$60,549, Project leader – working with graduate students to collect and analyze the data
- Dr. James Forester, Assistant Professor, Univ. of MN - Dept. of Fisheries, Wildlife and Conservation Biology, \$19,444 , Wildlife biologist – advising wildlife, ecological, and statistical aspects of the project
- Dr. Volkan Isler – Associate Professor, Univ. of MN - Dept. of Computer Science, \$40,232, Engineer – assisting with the development of UAV technologies and imagery software

Partners NOT receiving ENRTF funding

- Dr. Joseph Knight, Associate Professor, Univ. of MN – Dept. of Forest Resources, consultant for remote sensing and aerial imagery classification procedures

B. Project Impact and Long-term Strategy:

Our interdisciplinary research team will develop and implement changes to UAV systems that will have lasting benefits for the ongoing monitoring of any wildlife species large enough to be VHF-tagged (e.g. bat species of concern in MN) and will enable managers to collect much finer resolution data in an autonomous fashion to monitor changes in sensitive ecosystems. Initially, our results will lead directly to better understanding of the

conservation and management needs of moose and highlight the ability of our system to identify changes in sensitive ecosystems. Embracing the new capabilities that UAVs have to offer will provide better data, more cost-effective and safer research, while making research less invasive. Our work will not only research these methods but create easy to use systems that make UAV use and analysis of imagery accessible to researchers and managers. We will train and offer processing support for imagery as a means to get the systems more fully integrated into management and research.

We already have support from the UMN’s Institute on the Environment who previously purchased a UAV system for our research on wildlife. The University of Minnesota currently has FAA approval for research in in nearly all areas within the state. Our research team has collaborated extensively with MN DNR researchers and managers in the past. We have access to previously collared animals (bear, bats, and moose), and strong working relationships with researchers throughout the state who have interest in this technology.

C. Funding History:

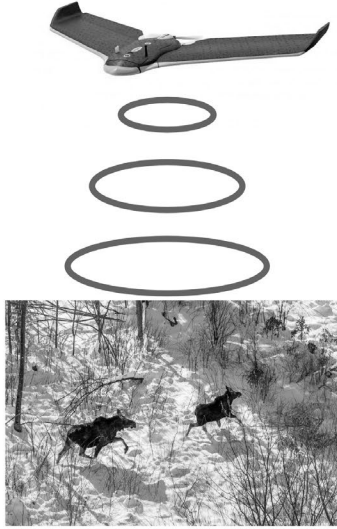
Funding Source and Use of Funds	Funding Timeframe	\$ Amount
University of Minnesota's Institute on the Environment	12/2013-12/2014	\$900
		\$
		\$

VIII. REPORTING REQUIREMENTS:

- The project is for 2 years, will begin on 07/01/2017, and end on 06/30/2019.
- Periodic project status update reports will be submitted 01/01 and 07/01 of each year.
- A final report and associated products will be submitted between June 30 and August 15, 2019.

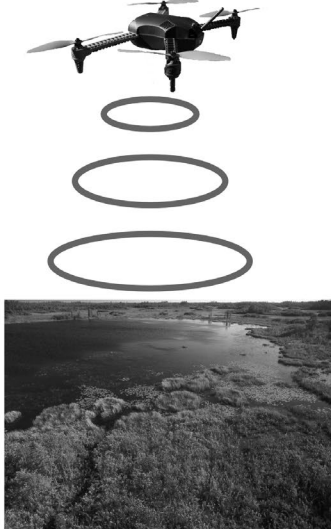
IX. VISUAL COMPONENT or MAP(S):

Action 1



Non-invasive moose calf counts
Estimates of moose calf survival
Fixed-wing flights at high altitudes

Action 2



Monitoring of ecosystems
Fine-scale, frequent imagery
Track changes over time

**Environment and Natural Resources Trust Fund
M.L. 2017 Final Project Budget**

Project Title: Moose Calf Surveys and Monitoring

Legal Citation: M.L. 2017, Chp. 96, Sec. 2, Subd. 03j

Project Manager: James Forester

Organization: *University of Minnesota*

M.L. 2017 ENRTF Appropriation: \$ 348,000

Project Length and Completion Date: 2.5 Years, Jan 30, 2020

Date of Report: 06/03/2021

ENVIRONMENT AND NATURAL RESOURCES TRUST FUND BUDGET	Revised Activity 1 Budget 05/10/2020	Amount Spent
BUDGET ITEM		
Personnel (Wages and Benefits)	\$149,192	\$149,192
Project Manager (Mark Ditmer) - 50 %FTE each year for 1 year (77.6% salary ,22.4% fringe) - Total estimated at: \$30,952		
Wildlife Biologist (James Forester) - 8% FTE each year for 2.5 years (66.3% salary, 33.7% Fringe). - Total estimated at: \$23,919		
Engineer (Volkan Isler) - 11% FTE each year for 2 years (75% salary, 25% fringe). - Total estimated at: \$40,232		
Master's Student - U of M - Dept. of Fisheries Wildlife and Conservation Biology: 50% FTE each year for 2 years: 49.7% salary, 8.7% fringe, 41.6% tuition). - Total estimated at: \$66,925		
PhD student – U of M -Dept. of Forest Research: 50% FTE for one semester to aid in UAS deployment and image analysis (49.7% salary, 8.7% fringe, 41.6% tuition). - Total estimated at: \$17,979		
Undergraduate research technician (12 weeks at \$15/hr) Total estimated: \$9,486. Additional tech help was need to finish project.		
Grad Research Student - UMN Computer Science & Engineering - 50% FTE each year for 2 years (58% salary, 10% fringe, 32% tuition). - Total estimated at: \$103,652		
Equipment/Tools/Supplies		
Unmanned aerial vehicle: quadcopter - selected through competitive bid		
Replacement and spare parts for either (quadcopter or fixed wing) unmanned aerial vehicle as needed, and computer supplies and materials to support unmanned aerial flights.	\$358	\$358

Project Budget_022319

Thermal camera for sighting moose calves. A thermal camera will allow us to pick out their heat signature relative to surrounding cool spring ground and vegetation. A rugged camera that is used by several other studies that utilize thermal imagery to get imagery of wildlife from the air.	\$3,700	\$3,700
High resolution multi-spectral camera for collecting data on vegetation beyond a typical RGB camera - (near-infrared, red-edge, red and green). This data will allow us to discern vegetation types and plant stress far better typical cameras.		
Capital Expenditures Over \$5,000		
Fixed wing unmanned aerial vehicle selected through competitive bid (includes basic RGB camera and flight lessons). This unmanned aerial vehicle will be made available to other researchers and state agencies for future work.	\$14,450	\$14,450
Thermal /color camera with GPS sensors to allow for geotagged simultaneous thermal and RGB surveys with quadcopter. Total estimated at \$6,348.	\$6,348	\$6,348
Travel expenses in Minnesota		
Travel to study areas by research assistants and project management staff and technicians: 1 UMN Fleet Truck Rental at \$834 for 2.5 months a year for 2 years (4* \$834 monthly rate)= \$3,336 + (4 weeks* \$274 weekly rate)= \$1,096, Total vehicle rental = \$4,432; Mileage for fleet vehicle @ \$.037 per mile (UMN fleet rate) * 15,000 miles = \$5,500; Personal vehicle use to get research assistants and technicians to and from Cedar Creek (no vehicle rental) and project management to field sites (no vehicle rental) = \$0.575 per mile (UMN personal vehicle rate) * 3120 miles = 1794. - \$11,726	\$6,950	\$6,950
Room and board for field crew - 1 research assistant + 2 field techs for two month-(\$1000)	\$1,000	\$1,000
Travel expenses out of state		
Travel to and registration for a national conference to discuss the robotics portion of this project.		
Other		

Project Budget_022319

<p>Networking and Computer Services (U of M Computer Science and Engineering). Networking and computer charges are expenses charged to sponsored and non sponsored accounts to support the portion of networking and computer infrastructure used by sponsored and non sponsored research projects. In a formula found to be Uniform Guidance compliant by the Office of Treasury Accounting and Internal/External Sales and Sponsored Projects Administration, research specific computing is separated from general-purpose computing. The networking and computer support charge is based on FTEs and special projects that can be attributed to research-only projects. Project Engineer: (100% - 1 sum mo) 173 hrs * \$2.26/hr = \$392 * 2 years = (\$784 total); Graduate research assistant (Computer Science & Engineering): (50% - 12 mos) 1,040 hrs * \$3.40/hr = \$3,536 * 2 years = (\$7072 total). - \$7,856. Additional Network/Comp service Needed to finish the project.</p>	<p>\$3,928</p>	<p>\$3,928</p>
<p>Service contract and repair costs (including postage and repair fees) for fixed wing and quadcopter</p>	<p>\$1,884</p>	<p>\$1,884</p>
<p>COLUMN TOTAL</p>	<p>\$187,810</p>	<p>\$187,810</p>

Project Budget_022319



Activity 1 Balance	Revised Activity 2 Budget 05/10/2020	Amount Spent	Activity 2 Balance	TOTAL BUDGET	TOTAL BALANCE
\$0	\$149,193	\$149,193	\$0	\$298,385	\$0
	\$1,653	\$1,653	\$0	\$1,653	\$0
\$0	\$140	\$140	\$0	\$498	\$0

Project Budget_022319

\$0				\$3,700	\$0
	\$3,000	\$3,000	\$0	\$3,000	\$0
\$0				\$14,450	\$0
\$0	\$0	\$0	\$0	\$6,348	\$0
\$0	\$486	\$486	\$0	\$7,436	\$0
\$0	\$0	\$0	\$0	\$1,000	\$0
	\$770	\$770	\$0	\$770	\$0

Project Budget_022319

\$0	\$4,948	\$4,948	\$0	\$8,876	\$0
\$0	\$0	\$0	\$0	\$1,884	\$0
\$0	\$160,190	\$160,190	\$0	\$348,000	\$0

1 27 May 2021
2 Michael C. McMahon
3 University of Minnesota
4 2003 Upper Buford Circle
5 Saint Paul, MN 55108
6 (651) 500-6370
7 mcmah231@d.umn.edu

8
9

10 RH: McMahon et al. · UAS for Deer Density Estimation

11

12 **Comparing unmanned aerial systems to conventional methodology for surveying a wild**
13 **white-tailed deer population**

14

15 MICHAEL C. MCMAHON,¹ *Department of Fisheries, Wildlife, and Conservation Biology,*
16 *University of Minnesota, 2003 Upper Buford Circle, Suite 135, Saint Paul, MN, 55108,*
17 *USA*

18 MARK A. DITMER, *Department of Fisheries, Wildlife, and Conservation Biology, University of*
19 *Minnesota, 2003 Upper Buford Circle, Suite 135, Saint Paul, MN, 55108, USA*

20 JAMES D. FORESTER, *Department of Fisheries, Wildlife, and Conservation Biology,*
21 *University of Minnesota, 2003 Upper Buford Circle, Suite 135, Saint Paul, MN, 55108,*
22 *USA*

23

24

25

26

¹ Email: mcmah231@d.umn.edu

27 **Table of contents short summary**

28 Ungulate populations are highly dynamic and require efficient survey methodology to inform
29 management efforts. This study aimed to assess the efficacy of thermal sensor-equipped
30 unmanned aerial systems (UAS) for estimating white-tailed deer densities, and found that UAS-
31 based deer density estimates were comparable to conventional fecal pellet-group count-based
32 density estimates. We find that UAS surveys offer an effective and temporally sensitive method
33 for estimating wild ungulate densities.

34

35 **Abstract**

36 *Context*

37 Ungulate populations are subject to fluctuations caused by extrinsic factors and require efficient
38 and frequent surveying to monitor population sizes and demographics. Unmanned aerial systems
39 (UAS) have become increasingly popular for ungulate research; however, little is understood
40 about how this novel technology compares to conventional methodologies for surveying wild
41 populations.

42 *Aims*

43 We examined the feasibility of using a fixed-wing UAS equipped with a thermal infrared sensor
44 for estimating the population density of wild white-tailed deer (*Odocoileus virginianus*) at the
45 Cedar Creek Ecosystem Science Reserve (CCESR), Minnesota, USA. We compared UAS
46 density estimates to those derived from fecal pellet-group counts.

47 *Methods*

48 We conducted UAS thermal survey flights from March to April of 2018 and January to March of
49 2019. Fecal pellet-group counts were conducted from April to May in 2018 and 2019. We

50 modeled deer counts and detection probabilities and used these results to calculate point
51 estimates and bootstrapped prediction intervals for deer density from UAS and pellet-group
52 count data. We compared results of each survey approach to evaluate the relative efficacy of
53 these two methodologies.

54 *Key Results*

55 Our best-fitting model of certain deer detections derived from our UAS-collected thermal
56 imagery produced deer density estimates ($\bar{X} = 9.40$, 95% prediction interval = 4.32–17.84
57 deer/km²) that overlapped with the pellet-group count model when using our mean pellet
58 deposition rate assumption ($\bar{X} = 7.01$, 95% prediction interval = 4.14–11.29 deer/km²). Estimates
59 from our top UAS model using both certain and potential deer detections resulted in a mean
60 density of 13.77 deer/km² (95% prediction interval = 6.64–24.35 deer/km²); similar to our pellet-
61 group count model that used a lower rate of pellet deposition ($\bar{X} = 10.95$, 95% prediction interval
62 = 6.46–17.65 deer/km²). The mean point estimates from our top UAS model predicted a range of
63 136.68–273.81 deer, and abundance point estimates using our pellet-group data ranged from
64 112.79–239.67 deer throughout CCESR.

65 *Conclusions*

66 Overall, UAS yielded similar results to pellet-group counts for estimating population densities of
67 wild ungulates; however, UAS surveys were more efficient and temporally sensitive.

68 *Implications*

69 We demonstrated how UAS could be applied for regularly monitoring changes in population
70 density. We encourage researchers and managers to consider the merits of UAS and how they
71 could be used to enhance the efficiency of wildlife surveying.

72

73 **Introduction**

74 The ability to collect data on population size and demographic vital rates frequently, accurately,
75 and efficiently is critically important for monitoring wildlife populations undergoing rapid
76 changes. Numerous ungulate populations throughout North America are in flux as a result of
77 hunting pressure (Bonenfant et al. 2009), climatic and land use changes (Plante et al. 2018),
78 disease (Edmunds et al. 2016), and changes to biological communities (Mech et al. 2018).
79 White-tailed deer (*Odocoileus virginianus*), have adapted to and exploited various anthropogenic
80 landscape and climatic changes resulting in a vast expansion of their geographic ranges and
81 population densities (Dawe and Boutin 2016). Measuring the changes in deer populations is
82 important to inform management actions intended to reduce ecological impacts associated with
83 overgrazing (Mysterud 2006) and inter- and intraspecific disease transmission (Jennelle et al.
84 2014; Ditmer et al. 2020).

85 The recent rise in the use of unmanned aerial systems (UAS) for surveying wildlife
86 populations is an especially attractive tool for monitoring dynamic populations because UAS
87 offers a cheaper, safer, and more flexible alternative to conventional aircraft (Sasse 2003; Watts
88 et al. 2010). Hourly operating costs may be reduced by as much as 82% with UAS, as compared
89 to conventional aircraft (Vermeulen et al. 2013) and the logistics and regulations regarding their
90 usage continue to diminish (Werden et al. 2015), especially when compared to manned aircraft
91 flights (Linchant et al. 2015). Importantly, UAS may also increase survey accuracy as compared
92 to traditional ground-based wildlife surveys (Chabot and Bird 2012). Hodgson et al. (2018)
93 demonstrated that UAS data were on average 43% to 96% more accurate than replicated ground-
94 based counts of seabirds within their colonies. When operators follow principles to reduce
95 disturbance to wildlife (Hodgson and Koh 2016), unmanned aerial systems can minimise animal

96 disturbance by removing the need to approach animals on foot (Krause et al. 2017), reducing the
97 time humans spend in close proximity to study species (Weissensteiner et al. 2015), and by
98 creating less noise than conventional aircraft (Bennitt et al. 2019).

99 UAS equipped with forward looking infrared (FLIR) sensors are a promising option for
100 monitoring fluctuations in population size because wildlife surveys using UAS can be repeated
101 frequently (Allan et al. 2018), assuming proper flight conditions, and can reduce operational
102 costs (Elsy and Trosclair 2016) while improving survey accuracy (Lethbridge et al. 2019).
103 Thermal sensors capture thermal radiation (i.e., body heat from animals), and thus increase the
104 detection probability of warm-bodied animals, even at night or with partial obscuration from
105 vegetation (Gill et al. 1997; Mulero-Pázmány et al. 2014; Montague et al. 2017). Aircraft-
106 mounted thermal sensors improved detection of white-tailed deer relative to traditional ground-
107 based spotlight surveys (Naugle et al. 1996). Due to the reduction in size and cost of both FLIR
108 sensors and UAS, many researchers and managers are deploying them for ungulate research and
109 population monitoring (Israel 2011; Lhoest et al. 2015; Chrétien et al. 2016; Witzuk et al. 2018;
110 Beaver et al. 2020; McMahon et al. 2021).

111 Numerous technologies and methods, such as UAS-based approaches, are available for
112 surveying critical population parameters; however, determining which ones provide the best
113 balance of economic and time constraints on wildlife professionals is a constant challenge.
114 Additionally, new methods and technologies may be resisted by agencies because of potential
115 differences with historical baseline estimates; thus, assessing how new approaches compare to
116 previously well-established methods is an active and important process for improving population
117 monitoring. Ireland et al. (2019) found that UAS thermal surveys had greater spatial coverage
118 and increased operational feasibility relative to camera trap surveys for detecting white-tailed

119 deer at night. However, it is also important to understand how estimates from new methodologies
120 compare to established, ‘low-tech’ methods, and to detail the tradeoffs in the costs, efforts, and
121 learning curves among them. For example, Preston et al. (2021) compared the efficacy of UAS
122 surveys to traditional spotlight surveys for deer, and found that spotlight approaches were
123 underestimating deer densities.

124 Here, we compare population density estimates derived from a UAS with a mounted
125 FLIR sensor to estimates based on fecal (pellet-group) surveys, a method frequently used to
126 estimate the density of ungulate populations (Bennett et al. 1940; Eberhardt and Van Etten
127 1956). Pellet-group counts have been used for decades, and are still in use today (Gable et al.
128 2017), because of their cost effectiveness and ease of implementation. A major drawback of the
129 approach is the requirement to estimate deer defecation and pellet decay rates, which can be
130 difficult to obtain due to seasonal variation in diet and environmental conditions (Wallmo et al.
131 1962; Rogers 1987).

132 Our objectives were to: 1) examine the feasibility of using a fixed-wing UAS for
133 detecting wild white-tailed deer (hereafter referred to as deer) in a forest-prairie interface, 2)
134 determine deer population density from counts of deer in FLIR imagery, and 3) compare deer
135 density estimates from UAS-gathered data to deer density estimates from pellet-group counts.
136 We aim to provide information to wildlife professionals about whether UAS technology provides
137 a significant advantage over cheaper and simpler conventional methodology, and how wildlife
138 managers can most efficiently employ UAS technology to achieve research and management
139 goals.

140

141 **Study area**

142 Surveys were conducted at the Cedar Creek Ecosystem Science Reserve (CCESR); located ~50
143 km north of Saint Paul, Minnesota, USA, near Bethel, Minnesota, in Anoka and Isanti counties
144 (Fig. 1). This is a 2,200 ha experimental ecological reserve that the University of Minnesota
145 operates in cooperation with the Minnesota Academy of Science (Cedar Creek Ecosystem
146 Science Reserve 2019). Elevation at the site was consistent and ranged between 270 m to 295 m
147 above sea level. Mean monthly temperatures at CCESR during our study period (March and
148 April of 2018 and January to March of 2019) ranged between -13.11 °C to 0.44 °C, mean
149 minimum temperatures were between -18.72 °C to -6.17 °C, and mean maximum temperatures
150 ranged between -8.0 °C to 7.11 °C. Mean monthly precipitation ranged from 0.91 cm to 5.92 cm
151 in rain and snow water equivalent (SWE). These weather data were collected by the Andover
152 National Weather Service Reporting Station, ~ 19 km southwest of our study site (MNDNR
153 2019).

154 The CCESR property was located within the meeting point of western prairie ecosystems,
155 northern hardwood forests, and eastern deciduous forests (Cedar Creek Ecosystem Science
156 Reserve 2019). Land-cover types at CCESR included deciduous forest, conifer forest, forested
157 wetland, emergent wetland, agriculture, grassland, developed areas, and open water (MN Land
158 Cover Classification, 2013). Common wildlife species included white-tailed deer, coyote (*Canis*
159 *latrans*), black bear (*Ursus americanus*), and wild turkey (*Meleagris gallopavo*), as well as
160 various mesomammals.

161

162 **Methods**

163 *UAS surveys*

164 We conducted UAS thermal surveys across the CCESR property from March to April of 2018
165 and from January to March of 2019. We used a Sentera PHX Pro fixed-wing UAS equipped with
166 a FLIR Vue Pro 640 (640 x 512 pixel resolution, 32° FOV, 19 mm lens, 30 Hz) (FLIR Systems
167 Inc., Wilsonville, OR, USA) thermal sensor to detect white-tailed deer. We selected a fixed-wing
168 UAS in favor of a multi-copter for increased flight endurance (Jiménez López and Mulero-
169 Pázmány 2019) and reduced noise levels (M. McMahon, University of Minnesota, personal
170 observation) to minimise wildlife disturbance. Survey plot locations were selected based on the
171 availability of landing sites and our ability to maintain visual line of sight with the PHX. We
172 identified landing zones across the CCESR property by intersecting areas of the highest relative
173 elevation (Gesch et al. 2002) with areas of open and dry habitat types (NLCD 2011) using
174 program R (R Core Team 2019). Launching from areas of higher relative elevation allowed us to
175 maintain visual line of sight with the UAS during its course of flight (Federal Aviation
176 Regulation 107.31). We considered open and dry areas of at least 335 m long and 30 m wide,
177 depending on wind conditions, to be safe landing areas for the PHX. Flight survey plots were
178 expanded from the landing zones to encompass as much land area as possible, with plot size
179 limited by battery endurance of the PHX and the distance with which we could maintain un-
180 aided visual contact. We originally identified nine survey plots with appropriate launch and
181 landing zones; however, one plot was later removed due to our inability to safely land the UAS
182 at that site. Our resulting eight survey plots ranged in size from 46.29 ha to 119.82 ha and
183 encompassed 30.69% of the CCESR property in total (Fig. 1).

184 We pre-programmed the PHX to fly parallel transects at 121 m above ground level
185 (AGL) over each survey plot using the laptop-based Sentera Ground Control program. We flew
186 each plot at least twice per survey season, for a grand total of 35 survey flights, at various times

187 of day from morning until evening. Parallel transects were used for efficiency and to minimise
188 wildlife disturbance (Mulero-Pázmány et al. 2017), and we did not observe any behavioral
189 reactions during the course of our study. The onboard thermal sensor was automatically triggered
190 by the PHX's flight computer to achieve the pre-programmed image overlap. Thermal imagery
191 was captured as still photos with 70 to 80% front overlap and 30% side overlap. Each image
192 covered an average ground area of 3,948 m² (approximately 60 x 70 m ground distance). Images
193 were geo-referenced from the PHX's GPS system and included data on altitude, speed, and bank
194 angle of the UAS at the time of image capture. Imagery was saved on a mini SD card onboard
195 the UAS, and was transferred post flight to an external hard drive and cloud-based storage
196 system for post-processing.

197

198 *UAS data analysis*

199 We removed any imagery that was captured with UAS bank angles (amount of side-to-side roll)
200 of >10° because imagery captured at greater angles of bank (e.g., during turn-arounds when the
201 UAS was realigning to start new transects) would show inconsistent ground areas depending on
202 bank angle, and would likely include space outside of our defined survey plots. We considered
203 any bank angles of <10° to be products of ordinary wind turbulence during flight, based on
204 observing the flight characteristics of the PHX and the distribution of bank angles in our data.
205 We subsampled our thermal imagery for each plot by randomly selecting starting images and
206 successively keeping any image with a centroid that was ≥ 80 m apart from any previously
207 retained image's centroid, using program R. This process yielded a subsample of thermal
208 imagery with a ground distance of 10 m to 24 m between the edges of thermal images to be
209 analysed. This ensured that we did not analyse overlapping imagery, potentially recounting

210 individual deer, and reduced the workload of reviewing the ~ 22,600 total thermal images
211 collected.

212 We manually reviewed the subsampled imagery from each plot and recorded counts of
213 deer observations that we classified as either ‘certain’ or ‘potential’ detections. Certain
214 detections were recorded when we had no doubt that a deer was in the image based on the shape,
215 size, and relative brightness of the thermal heat signature. Potential detections were less certain
216 detections that may have only met some, but not all of our shape, size, and brightness search
217 criteria. Deer were distinguished from other wildlife by relative size and shape, as they were the
218 only animal of their size present (e.g., bears were in dens, and wolves are rarely found in the
219 study area). Coyotes, which were present in the study area, could potentially be misidentified as
220 deer but are generally smaller and less common than deer. Detection of deer fawns was not a
221 factor since UAS surveys were flown prior to parturition, and young from the previous year
222 would have been of sufficient size to meet the criteria used to detect adult deer. Prior to the start
223 of the study, we recorded thermal imagery from a captive deer farm with a known number of
224 deer. We used the imagery from the deer farm for training observers prior to reviewing field
225 data. Imagery of the captive deer was taken with the same FLIR sensor at varying altitudes,
226 angles, and amounts of vegetative cover to provide examples of how deer might appear in
227 thermal imagery.

228

229 *UAS deer density modeling*

230 We modeled deer counts (i.e., the number of deer observed in a thermal image) using the
231 glmmTMB package (Brooks et al. 2017) in program R because it allowed for the inclusion of
232 zero-inflated models and random effects. This approach also allows for different model

233 structures in the zero inflation and conditional components. Assumptions associated with zero-
234 inflated distributions are similar to general abundance modeling and include; 1) a closed
235 population, 2) independent individuals with equal availability for capture, and 3) applying the
236 correct distribution given the presence of overdispersion in the data (Wenger and Freeman 2008).
237 We believed that these assumptions were met relatively well. Although deer hunting occurs
238 outside of the property boundaries, CCSR is closed to most public hunting, which is a leading
239 cause of adult and fawn mortality (Brinkman et al. 2004). Wolves were not likely in the study
240 area, and coyotes generally prey on fawns (Grovenburg et al. 2011), which would not have
241 greatly impacted population demographics during our late winter to early spring study period.
242 Furthermore, Rhoads et al. (2010) reported that female deer occupied an average seasonally-
243 dependent home range of 21.2 ha for the 50% utilization distribution in an exurban population,
244 which is a smaller area than our smallest UAS plot of 46.29 ha. Sub-sampling thermal imagery
245 ensured independence among individuals by removing the potential to count the same deer more
246 than once. Individual deer were relatively equally available to be detected using thermal imaging
247 technology, and there was minimal conifer cover in the study area which could otherwise
248 decrease detection probability (Dunn et al. 2002). We tested for overdispersion in the data, and
249 appropriately applied zero-inflated negative-binomial models to account for the high number of
250 zeros present in our data.

251 We included in our models the variables of sky cover (0 = clear sky, 1 = overcast sky)
252 and the proportions of habitat cover type as possible fixed effects; a maximum of one cover type
253 proportion was included per model component (i.e., each of the two component models could
254 have at most sky cover and one land-cover proportion as a fixed effect). We used sky cover
255 instead of ambient temperature because sky cover was previously shown to improve models of

256 moose (*Alces alces*) detection over ambient temperature in forested habitats (McMahon et al.
257 2021). Ground area (i.e., the spatial area observed within each thermal picture) was added as an
258 offset to the conditional model based on our a priori reasoning that a greater area observed would
259 result in a greater probability of deer detection. Survey flight ID and survey year (0 = 2018,
260 1=2019) were included as crossed random intercepts to account for variation among survey
261 flights and years.

262 We determined the proportion of cover types within each image by clipping land cover
263 data (MN Land Cover Classification, 2013) with a 35-m buffer around the centroid of each
264 thermal image using ArcMap 10.5.1 (Environmental Systems Research Institute, Inc., Redlands,
265 CA, USA). The radius of 35 m was chosen so that the buffer area around each image centroid
266 equaled the mean ground area captured in the thermal imagery. We calculated the ground area of
267 the thermal imagery for each image from flight altitude data using the Pythagorean Theorem and
268 then averaged across all images. Proportions of each land-cover class (developed, conifer forest,
269 deciduous forest, forested wetland, emergent wetland, grassland, agriculture, and open water
270 [i.e., snow-covered ice]) were considered individually and in meaningful groups: forested upland
271 (conifer + deciduous), open upland (agriculture + grassland), wetland (forested wetland +
272 emergent wetland), non-wetland open area (grassland + agriculture + developed + open water),
273 and no cover (emergent wetlands + grass + water + agricultural + developed). The composite
274 variables were chosen based on the type of resources they might provide in winter (e.g., food,
275 cover) and whether a given vegetation type would likely be tall or dense enough to obscure a
276 deer from aerial thermal detection.

277 Our deer detection data were saturated with 'zero' values so we implemented zero-
278 inflated negative binomial and Poisson hurdle models in the glmmTMB package (Wenger and

279 Freeman 2008; Brooks et al. 2017). We modeled deer numbers separately for high (potential +
280 certain deer detection counts) and low (certain deer detection counts) counts, using the same
281 modeling approach for each set of counts. We ran all possible combinations of covariates and
282 random effects in the conditional and binomial models for high and low deer counts. Candidate
283 models were compared using Akaike's Information Criterion (AIC).

284 To predict the deer population size across the entirety of the CCEsr property using our
285 top-supported models of deer abundance (based on high and low count data), we created a virtual
286 grid in Program R that covered the entire area. Each cell of the grid was 3,948 m² (62.83 m x
287 62.83 m), which equaled the mean ground area captured in the individual thermal images. We
288 calculated the proportion of each land-cover type and composite cover-type variable within every
289 grid cell using the land-cover data set and binning scheme described above. To generate a point
290 estimate of the deer population size, we used the *predict* function in program R to estimate the
291 probability of at least one deer being present (i.e., 1-P(structural zero)) and the expected mean of
292 the conditional model for each grid cell (we assumed overcast sky conditions and random effects
293 set to 0). The product of these two vectors (i.e., the expected number of deer per cell) was
294 summed to provide an estimate of the deer population within the CCEsr property.

295 To quantify uncertainty in our point estimate, we needed to account for uncertainty in our
296 parameter estimates as well as stochasticity in the system. We first generated 10,000 sets of
297 parameter values from a multivariate normal distribution with a mean vector set to the fitted
298 coefficient values and a variance-covariance matrix extracted from the fitted model. These
299 bootstrapped parameter values were then used to calculate expected probability of structural
300 zeros and the conditional mean for each cell; random effects, if present in a given model, were
301 generated from a normal distribution with mean = 0 and standard deviation extracted from the

302 bootstrapped model parameters. We used these values to simulate our model for each grid cell by
303 generating a sample from both the binomial and the conditional (either negative binomial or
304 truncated Poisson) distributions and then calculating their product to yield a simulated number of
305 deer within a given cell. These simulated deer numbers were summed across all cells to provide
306 a simulated population estimate. This was repeated for each of the 10,000 sets of parameter
307 values.

308

309 *Pellet-group count surveys*

310 We arranged pellet-group survey transects within the established UAS survey plots using a
311 stratified random approach. We clipped land-cover data (MN Land Cover Classification, 2013)
312 by the boundaries of the eight UAS survey plots and randomly inserted ~ 20 survey points
313 proportionately with the availability of each cover type within the plot, using ArcMap. Our
314 habitat cover types for conducting pellet-group counts included deciduous forest, forested
315 wetland, emergent wetland, grass, and row crops. Transects were planned prior to fieldwork by
316 using our stratified random points as starting locations and laying out a 100-m line in a direction
317 from the starting point that would allow the surveyors to remain in the same habitat cover type
318 for the entirety of the transect. Adjustments were made in the field as required to remain within
319 the same habitat cover type.

320 Pellet-group counts were conducted during the months of April and May (2018 and
321 2019). We surveyed 133 transects in 2018 and resurveyed 120 of the same transects during 2019.
322 Thirteen of the 2018 transects were not available for resurveying in 2019 due to prescribed
323 burning on the CCECSR property. Deer droppings were considered a pellet-group if there were at
324 least 4 pellets of similar size, shape, and color within close proximity (pellets within 30 cm of

325 each other). Pellet-groups were only counted if $\geq 50\%$ of the pellet-group was within 1 m of the
 326 transect centerline, and they were determined to have been deposited after leaf-off the previous
 327 fall. Deciduous leaf litter falling between survey periods (2018 and 2019) eliminated the need to
 328 age or clear away pellet-groups, as only pellet-groups that had been deposited from fall to spring
 329 would be visible above the leaf litter. Where leaf litter was not present (e.g., open habitat types),
 330 we examined pellet-groups and determined deposition timing based on the presence of weather
 331 exposure, moss, and insect damage (Gable et al. 2017). Pellet-groups deposited post fall leaf-off
 332 would not likely show any such damage from exposure.

333

334 *Pellet-group count data analysis and density modeling*

335 We estimated deer density from pellet count data in two ways. In the first, we used a simple
 336 equation (Gable et al. 2017):

$$337 \text{ Deer density (deer/km}^2\text{)} = \frac{\text{pelletgroupscounted}}{\text{pelletgroupdepositionrate} \times \text{depositionperiod} \times \text{samplingunitarea(km}^2\text{)}}.$$

338 We considered the pellet deposition rate to be 25 pellet-groups/deer/day based on pellet count
 339 surveys from a study near International Falls, MN (Gable et al. 2017). This value is based on the
 340 mean values for deposition rate from two other studies; Rogers (1987) used a deposition rate of
 341 34 and Patterson et al. (2002) used 16. We also calculated a low estimate using the value of 34
 342 pellet-groups/deer/day and a high estimate using 16 pellet-groups/deer/day. Our pellet-group
 343 deposition period (time between mean leaf-off date and mean survey date) was 192 days for
 344 2017–2018 and 209 days for 2018–2019. Density estimates were derived for forested (deciduous
 345 + forested wetland) and non-forested (emergent wetland + grass + row crops) habitat cover types
 346 by pooling count data from specific cover types for calculation, and averaging across survey
 347 years. Point estimates of deer density were predicted across CCEsr by applying density

348 estimates for forested and non-forested land cover to the proportion of forested and non-forested
349 land cover of each grid cell in the virtual grid system described above in the *UAS Deer Density*
350 *Modeling* section.

351 We also took a second approach, in which we fit a Poisson hurdle model to the number of
352 pellet groups found per transect. We used the same potential covariates, random effects, and
353 parametric bootstrapping approach that we used for the UAS models; we divided the total area of
354 each land-cover type in the landscape into 200-m² transect units (i.e., equal in area to our sample
355 transects). The result of predicting this model across each transect unit in the landscape was a
356 “predicted number of pellets,” that we converted to “predicted number of deer” by assuming a
357 192-day deposition period and the same high, low, and average pellet deposition rates used in the
358 above equation.

359

360 **Results**

361 *UAS-based deer density*

362 We conducted either two or three replicate surveys over our eight UAS survey plots at CCESR
363 during winter and spring of both 2018 and 2019, totaling 35 thermal UAS flights with analysable
364 data. Our thermal surveys required a total of 24.7 hours of flight time with the PHX. We
365 captured a total of 22,626 thermal images and analysed a subsample of 3,757 non-overlapping
366 images. Of these images, 96.6% did not contain any potential deer detections. We classified 48
367 thermal images as containing certain deer detections (Fig. 2A) and an additional 95 with
368 potential deer detections (Fig. 2B). Images with deer detections ranged in count from 1 to 9
369 individuals and we detected a total of 96 certain deer and an additional 135 potential deer within
370 all survey images (Fig. 3). Our top performing model for high (i.e., certain + potential) deer

371 detection was a zero-inflated negative binomial model that included the variables of sky cover ($\hat{\beta}$
372 = 3.14, SE = 0.45) and the proportion of wetland habitat cover ($\hat{\beta}$ = 0.66, SE = 0.21) in the
373 conditional formula. The zero-inflated formula contained sky cover ($\hat{\beta}$ = 5.70, SE = 1.67) and the
374 proportion of open upland habitat cover ($\hat{\beta}$ = 2.43, SE = 1.22; Table 1). Our top performing
375 model for low (i.e., certain) deer detection was a truncated Poisson model that included sky
376 cover ($\hat{\beta}$ = 0.90, SE = 0.43), the proportion of wetland habitat cover ($\hat{\beta}$ = 1.26, SE = 0.57), and a
377 random effect for survey flight ID in the conditional formula, with the proportions of non-
378 wetland open habitat cover ($\hat{\beta}$ = 3.46, SE = 1.26) in the zero-inflated formula (Table 1).

379 Our top detection models predicted mean point estimates for deer density of 12.38 and
380 6.18 deer/km² for the high and low detection estimates, respectively. Point abundance estimates
381 were 273.81 deer and 136.68 deer on the CCESR property (22.12 km², Fig. 4, Table 2). Our
382 bootstrapped estimates of deer density had a mean estimate of 13.77 deer/km² for the high
383 detection model, and a mean of 9.40 deer for the low detection model. These density estimates
384 equated to a mean of 304.55 deer on the CCESR property for the high-detection model, and
385 207.90 deer for the low-detection model (Fig. 4, Table 2).

386

387 *Pellet-group count deer density*

388 We surveyed 133 pellet-group count transects covering 26,600 m² in 2018 and recorded 1,085
389 pellet-groups. In 2019, we completed 120 transects equating to 24,000 m² surveyed, recording
390 766 pellet-groups.

391 Our predicted point estimates were 5.13, 6.98, and 10.91 deer/km² based on high (34
392 pellet groups/deer/day), mean (25 pellet groups/deer/day), and low (16 pellet groups/deer/day)
393 deposition rates, respectively. Point estimates of abundance were 112.79 deer for high

394 deposition, 153.39 deer for mean deposition, and 239.67 deer for low deposition on the CCESR
395 property (Fig. 4, Table 2). The bootstrapped predictions resulted in a mean of 5.15 deer/km² for
396 high deposition, a mean of 7.01 deer/km² for mean deposition, and a mean of 10.95 deer/km² for
397 low deposition. The corresponding bootstrapped abundance estimates for CCESR from our
398 bootstrapped prediction intervals were 113.25 deer, 154.02 deer, and 240.66 deer, respectively
399 (Fig. 4, Table 2).

400 Overall, UAS and pellet-count survey-based methods yielded comparable results with
401 overlapping estimates for CCESR. In particular, the bootstrapped abundance estimates from
402 certain UAS detections and mean deposition rate pellet-group surveys had high overlap with a
403 difference of 52.59 more deer estimated by UAS methodology. High (certain + potential) UAS
404 detection estimates and pellet-group survey estimates based on low deposition rates also had
405 large overlap with 61.34 more deer estimated by UAS over pellet-group surveys.

406

407 **Discussion**

408 We successfully applied UAS and FLIR technology to survey a wild population of white-tailed
409 deer and compared the efficacy of this approach to pellet-group count surveys, a widely-used
410 conventional method for surveying ungulate populations. Both of these methodologies yielded
411 similar results for density and abundance estimates, dependent on the pellet model assumptions,
412 yet varied in levels of sampling effort, cost, and time. Despite increasing use of UAS in wildlife
413 research (Jiménez López and Mulero-Pázmány 2019), many studies rely on expensive UAS and
414 sensors and do not assess how well the approach compares with established methods. However,
415 understanding the logistical, financial and practical hurdles of incorporating UAS is especially
416 important for wildlife managers with limited resources. Our findings provide insights into the

417 process and utility of integrating UAS into monitoring ungulate populations in an efficient and
418 temporally sensitive manner.

419 The most notable difference between pellet-group counts and UAS surveys was the
420 amount of time and effort required for each approach. Pellet counts took approximately 160
421 hours (i.e., the time taken to count pellets and hike between survey transects) over both survey
422 seasons, whereas the UAS surveys required only 24.7 hours of flight time in addition to
423 approximately 30 minutes to one hour for set up and take down per launch site, totaling 17.5 to
424 35 hours of non-flight field effort. Time spent driving between UAS launch sites was negligible.
425 An additional 25 to 35 hours of effort was required for manual review of thermal imagery. The
426 physical effort required for pellet count surveys was greater, requiring large amounts of off-trail
427 hiking to reach survey sites, relative to the majority of UAS launch sites off of drivable roads and
428 trails. Pellet-group counts were also temporally restricted to just prior to spring green up, after all
429 snow cover was melted, for maximum detectability of pellet-groups by human observers.
430 Conversely, UAS FLIR surveys could be carried out with far greater flexibility and would have
431 been feasible anytime from late November through April, at the northern latitude of our study
432 site, which corresponded to leaf-off conditions for deciduous trees. Forest-dwelling ungulates
433 can be successfully detected using FLIR-equipped UAS in leafless conditions (Witczuk et al
434 2018), and McMahon et al. (2021) found that increasing deciduous tree canopy hindered moose
435 detection. The window of time for deciduous leaf-off conditions is relatively large at northern
436 latitudes and is irrelevant for ungulate surveys in open grassland habitats. This wide temporal
437 range allows researchers and managers greater operational flexibility for surveying ungulates, as
438 compared to being seasonally restricted by pellet-group counts.

439 In addition to the temporal flexibility provided by the UAS approach, the added potential
440 for frequently repeated surveys can provide managers with a means of rapidly conducting
441 surveys to track how the space use and density of ungulate populations change through time. The
442 ability to accurately, efficiently, and economically track ungulate population dynamics is
443 paramount for management decisions because populations can change swiftly due to disease
444 spread (Ditmer et al. 2020), interspecific competition (Weiskopf et al. 2019), changes in predator
445 communities (Sivertsen et al. 2012), severe periods of weather (Bergman et al. 2015), and human
446 land-use change (Fisher and Burton 2018). Barasona et al. (2014) utilised UAS imagery to model
447 the environmental factors relating to the abundance of host species of tuberculosis in Spain (i.e.,
448 red deer [*Cervus elaphus*], fallow deer [*Dama dama*], and cattle [*Bos taurus*]). In Minnesota,
449 chronic wasting disease is of special concern, where the movement of captive deer presents a risk
450 for transmission to wild populations (Makau et al. 2020); applications of UAS similar to those
451 used by Barasona et al. (2014) could provide important information regarding the presence and
452 movement of wild deer in and around captive facilities. Moose populations have also
453 experienced precipitous declines in northern Minnesota (DelGiudice 2018) and many traditional
454 methods of population monitoring (e.g., capture and collaring) are currently restricted. McMahon
455 et al. (2021) assessed the feasibility of monitoring this population's reproductive success without
456 the need for traditional approaches that require handling of moose calves by using a FLIR-
457 equipped UAS. The authors reported detecting GPS-collared adult moose with 85% success and
458 non-collared moose calves with 79% success. They also were able to determine calf survival
459 status after four separate suspected predation attempts, providing evidence that UAS can be used
460 to monitor wild ungulate population demographics with less researcher-induced disturbance.
461 However, McMahon et al. (2021) were only able to successfully gather data on individual wild

462 moose fit with GPS collars and their calves; demonstrating the drawback of spatial limitations of
463 UAS that prevent their application for extensive, large-scale wildlife surveys.

464 The application of UAS for surveying wild terrestrial species over spatially extensive
465 areas has been largely impossible due to limitations of battery life, communication links, and
466 federal regulations concerning commercial UAS use (Whitehead et al. 2014; Chrétien et al.
467 2016; Beaver et al. 2020). For example, Vincent et al. (2015) describes the regulation prohibiting
468 the use of UAS beyond visual line of sight, and how this limits the ability to survey mobile
469 wildlife over spatially extensive areas. Fixed-wing models of UAS currently offer the greatest
470 solution for expanding UAS range, given their superior flight endurance over multi-copters
471 (Linchant et al. 2015); however, the costs associated with our fixed-wing UAS (~\$14,000) and
472 thermal sensor (~ \$3,200) do present a significant monetary barrier. Thermal sensors can be
473 mounted on a less expensive quadcopter UAS, but times aloft (far slower flight speeds) and
474 survey range for each flight become limited, with the additional prospect of disturbing the study
475 species and non-target species due to quadcopters' much noisier operation (Scobie and
476 Hugenholtz. 2016). We found another difficult tradeoff between multi-copter and fixed-wing
477 UAS to be the extensive landing room required for fixed-wing operation. This is challenging in
478 forested and semi-forested environments where sufficient landing zones are minimal. An
479 additional major consideration for fixed-wing UAS operations is balancing UAS groundspeed
480 (speed of UAS as measured in distance over the ground rather than through the air column) with
481 FLIR sensor shutter speed. We recommend conducting test flights to ensure that images of the
482 desired ground area can be captured with the required amount of image overlap prior to flying
483 UAS for wildlife surveys. We experienced limitations of the amount of overlap we could obtain
484 in our thermal images due to the relatively fast groundspeeds of the fixed-wing UAS; because

485 our thermal sensor's shutter speed could not operate at speeds greater than 1.5 images/sec. We
486 also experienced challenges with unreliable triggering of the thermal sensor during survey
487 flights, which was addressed by debugging our novel pairing between FLIR and the PHX.

488 Accurately identifying deer from UAS-gathered thermal imagery was a challenge for
489 estimating population abundance at CCEsr. We collaborated with computer engineers to
490 determine the feasibility of automating deer detection within our thermal imagery; however, this
491 effort was unsuccessful due to the relatively low resolution of our imagery collected at flight
492 altitudes of 121 m AGL. Automated detection algorithms are computationally complex (Chabot
493 et al. 2018; Kellenberger et al. 2018), requiring either higher resolution sensors (which are
494 substantially more expensive) or lower flight altitudes (which increase the risk of wildlife
495 disturbance). These limitations may prevent wildlife managers and researchers from choosing to
496 pursue automated detection, in favor of manual review (McMahon et al. 2021). However,
497 manual review can be time consuming. Regardless of how detections are made, false positives
498 and misidentification of species are prevalent issues in remote sensing applications (Brack et al.
499 2018; Kays et al. 2018). Conducting UAS surveys when thermal contrast between animal targets
500 and their background environment is maximised (i.e., during early morning hours or overcast sky
501 conditions which limit the amount of solar radiation that the ground absorbs) helps mitigate these
502 issues and allows for greater thermal detection of target animals (Franke et al. 2012; Kays et al.
503 2018; Preston 2021). We modeled deer count data using both certain and potential detections as a
504 sensitivity analysis to quantify how variability in detection influenced our population estimates.
505 Including potential deer detections increased our mean population estimate, based on the
506 bootstrapped prediction distribution, by 95 deer relative to the model only including certain
507 detections (~46% increase). Potential deer detections may have included false positives (i.e.,

508 non-deer objects misidentified as deer) which would result in a higher abundance estimate, yet
509 classifying only certain deer detections could have also mistaken actual deer for ground objects.
510 As a post-hoc analysis we re-assessed 50% of the images that we initially considered to contain
511 potential deer detections by examining the overlapping thermal imagery to quantify potential
512 false negatives and positives. Our more thorough examination of each potential detection
513 resulted in a 16% increase in certain detections and an 11% decrease in uncertain detections.
514 This would result in a smaller difference between our certain and potential UAS deer estimates.
515 While the additional effort would provide slightly more accurate population estimates, the
516 approach is time consuming and may simply be unfeasible when considering larger areal
517 coverage or more frequent flights. However, if researchers are able to overcome the previously
518 mentioned hurdles to implementing accurate automated detection algorithms, the need to classify
519 certainty and conduct the associated sensitivity analyses could be avoided.

520 Our estimates of deer abundance ended up being very similar despite the substantially
521 different methodological approaches. This was especially true when comparing the prediction
522 intervals for the pellet-group count model assuming 25 pellets/deer/day to the UAS model with
523 certain deer only, and the pellet-group count model assuming a deposition rate of 16
524 pellets/day/deer to the more liberal certain + potential UAS model. Our findings highlight the
525 sensitivity to the pellet deposition rate assumption previously described by Gable et al. (2017),
526 and suggest that the highest deposition rate (34 pellets/deer/day) may be overestimated for our
527 study area. Although the UAS models do not require quantifying a pellet deposition rate, a
528 difficult value to validate, properly incorporating all aspects of uncertainty into our prediction
529 intervals from the model structures used here was analytically complex. However, as the red-
530 dashed lines in Figure 4 indicate, the simple mean point estimates from both pellet-group count

531 and UAS models were similar to the bootstrapped mean prediction interval estimates from each
532 model, suggesting that simple prediction methods may be sufficient if monitoring changes using
533 an index of abundance is adequate (e.g., tracking monthly changes to density). Finally, while the
534 upper tails of the distributions in our UAS model prediction intervals were extremely long,
535 uncertainty could be reduced with more frequent surveys, surveying a greater extent of the study
536 area, or any number of actions that reduced uncertainty in the detection process (e.g., flying
537 lower and/or slower).

538 Technological advances, along with new tools and methodologies are increasingly
539 available for wildlife managers, yet few studies consider all of the practical aspects of their field
540 use or how they compare with established methods. Pellet-group counts and other ground-based
541 methodologies are relatively affordable, well-understood and documented in the literature, and
542 require less training than novel technological approaches. However, following an initial financial
543 investment and training period, UAS allows for rapid survey capabilities over areas of rough
544 terrain with few restrictions on time and available human effort that control many other methods.
545 Continued advancement and reduction of costs for UAS, FLIR, and automated image analysis
546 technology will likely continue to expand the applications of UAS in wildlife population surveys,
547 making UAS a more readily applicable tool for wildlife managers to include in their toolbox.
548 Tools that can improve the frequency of data collection and accuracy of population monitoring
549 will be even more essential in the coming decades where wildlife must adapt to numerous
550 environmental changes.

551

552 **Conflicts of interest**

553 There are no conflicts of interest to report.

554

555 **Acknowledgements**

556 We thank Dr. F. Isbell, Dr. C. Potter, T. Mielke, and the rest of the staff at the Cedar Creek
557 Ecosystem Science Reserve for their assistance with project planning and field support. We
558 thank Dr. T. Arnold and Dr. J. Knight of the University of Minnesota Twin Cities for their
559 advisement and input. We thank T. Colten and M. Skelton of Sentera for their technical support
560 and field assistance with deploying the PHX. We thank J. Tillery and D. Brown for their
561 assistance as field technicians. Funding was provided by the Minnesota Agricultural Experiment
562 Station (Project# MIN-41-020), the University of Minnesota Graduate School (fellowship
563 support for M. McMahon), and the Environment and Natural Resources Trust Fund as
564 recommended by the Legislative-Citizen Commission on Minnesota Resources.
565 We also recognise the University of Minnesota Department of Fisheries, Wildlife, and
566 Conservation Biology for its technical support on this project.

567

568 **References**

569 Allan, B. M., Nimmo, D. G., Ierodiaconou, D., VanDerWal, J., Koh, L. P., and Ritchie, E.G.
570 (2018). Futurecasting ecological research: the rise of technology. *Ecosphere* **9**(5), e02163.

571 Barasona, J. A., Mulero-Pázmány, M., Acevedo, P., Negro, J. J., Torres, M. J., Gortázar, C., and
572 Vicente, J. (2014). Unmanned aircraft systems for studying spatial abundance of ungulates:
573 relevance to spatial epidemiology. *PLoS ONE* **9**(12), e115608.

574 Beaver, J. T., Baldwin, R. W., Messinger, M., Newbolt, C. H., Ditchkoff, S. S., and Silman, M.
575 R. (2020). Evaluating the use of drones equipped with thermal sensors as an effective
576 method for estimating wildlife. *Wildlife Society Bulletin* **44**, 434-443.

- 577 Bennett, L. J., English, P. F., and McCain, R. (1940). A study of deer populations by use of
578 pellet-group counts. *The Journal of Wildlife Management* **4**(4), 398-403.
- 579 Bennitt, E., Bartlam-Brooks, H. L. A., Hubel, T. Y., and Wilson, A. M. (2019). Terrestrial
580 mammalian wildlife responses to Unmanned Aerial Systems approaches. *Scientific Reports*
581 **9**, 2142.
- 582 Bergman, E. J., Doherty, P. F., White, G. C., and Holland, A. A. (2015). Density dependence in
583 mule deer: a review of evidence. *Wildlife Biology* **21**, 18-29.
- 584 Bonenfant, C., Pelletier, F., Garel, M., and Bergeron, P. (2009). Age-dependent relationship
585 between horn growth and survival in wild sheep. *Journal of Animal Ecology* **78**, 161-171.
- 586 Brack, I. V., Kindel, A., and Oliveira, L. F. B. (2018). Detection errors in wildlife abundance
587 estimates from unmanned aerial systems (UAS) surveys: synthesis, solutions, and
588 challenges. *Methods in Ecology and Evolution* **9**, 1864-1873.
- 589 Brinkman, T. J., Jenks, J. A., DePerno, C. S., Haroldson, B. S., and Osborn, R. G. (2004).
590 Survival of white-tailed deer in an intensively farmed region of Minnesota. *Wildlife*
591 *Society Bulletin* **32**(3), 726-731.
- 592 Brooks M. E., Kristensen, K., van Benthem, K. J., Magnusson, A., Berg, C. W., Nielsen, A.,
593 Skaug, H. J., Maechler, M., and Bolker, B. M. (2017). glmmTMB Balances speed and
594 flexibility among packages for zero-inflated generalized linear mixed modeling. *The R*
595 *Journal* **9**(2), 378-400.
- 596 Cedar Creek Ecosystem Science Reserve. (2019). History Summary.
597 <www.cedarcreek.umn.edu/about/history>. Accessed 19 Nov 2019.

- 598 Chabot, D., Dillon, C., and Francis, C. M. (2018). An approach for using off-the-shelf object-
599 based image analysis software to detect and count birds in large volumes of aerial
600 imagery. *Avian Conservation and Ecology* **13**(1), 15.
- 601 Chabot, D., and Bird, D. M. (2012). Evaluation of an off-the-shelf unmanned aircraft system for
602 surveying flocks of geese. *Waterbirds* **35**, 170-174.
- 603 Chrétien, L.-P., Théau, J., and Ménard, P. (2016). Visible and thermal infrared remote sensing
604 for the detection of white-tailed deer using an unmanned aerial system. *Wildlife Society*
605 *Bulletin* **40**, 181-191.
- 606 Dawe, K. L., and Boutin, S. (2016). Climate change is the primary driver of white-tailed deer
607 (*Odocoileus virginianus*) range expansion at the northern extent of its range; land use is
608 secondary. *Ecology and Evolution* **6**, 6435-6451.
- 609 Del Giudice, G. D. (2018). 2018 Aerial moose survey. Minnesota Department of Natural
610 Resources, Forest Wildlife Populations and Research Group. Grand Rapids, Minnesota,
611 USA.
- 612 Ditmer, M. A., McGraw, A. M., Cornicelli, L., Forester, J. D., Mahoney, P. J., Moen, R. A.,
613 Stapleton, S. P., St-Louis, V., VanderWaal, K., and Carstensen, M. (2020). Using movement
614 ecology to investigate meningeal worm risk in moose, *Alces alces*. *Journal of Mammalogy*
615 **101**, 589-603.
- 616 Dunn, W. C., Donnelly, J. P., and Krausmann, W. J. (2002). Using thermal infrared sensing to
617 count elk in the southwestern United States. *Wildlife Society Bulletin* **30**(3), 963-967.
- 618 Eberhardt, L., and Van Etten, R. C. (1956). Evaluation of the pellet group count as a deer census
619 method. *The Journal of Wildlife Management* **20**(1), 70-74.

- 620 Edmunds, D. R., Kauffman, M. J., Schumaker, B. A., Lindzey, F. G., Cook, W. E., Kreeger, T.
621 J., Grogan, R. G., and Cornish, T. E. (2016). Chronic wasting disease drives population
622 decline of white-tailed deer. *PLoS ONE* **11**(8), e0161127.
- 623 Elsey, R. M., and Trosclair, P. L. III., (2016). The use of an unmanned aerial vehicle to locate
624 alligator nests. *Southeastern Naturalist* **15**(1), 76-82.
- 625 Fisher, J. T., and Burton, A. C. (2018). Wildlife winners and losers in an oil sands landscape.
626 *Frontiers in Ecology and the Environment* **16**, 323-328.
- 627 Franke, U., Goll, B., Hohmann, U., and Heurich, M. (2012). Aerial ungulate surveys with a
628 combination of infrared and high-resolution natural colour images. *Animal Biodiversity and*
629 *Conservation* **35.2**, 285-293.
- 630 Gable, T. D., Windels, S. K., and Olson, B. T. (2017). Estimates of white-tailed deer density in
631 Voyageurs National Park: 1989–2016. Natural Resource Report NPS/VOYA/NRR—
632 2017/1427. National Park Service, Fort Collins, Colorado.
- 633 Gesch, D., Oimoen, M., Greenlee, S., Nelson, C., Steuck, M. and Tyler, D., (2002). The national
634 elevation dataset. *Photogrammetric Engineering and Remote Sensing*. **68**(1), 5-32.
- 635 Gill, R. M. A., Thomas, M. L., and Stocker, D. (1997). The use of portable thermal imaging for
636 estimating deer population density in forest habitats. *Journal of Applied Ecology* **34**,
637 1273-1286.
- 638 Grovenburg, T. W., Swanson, C. C., Jacques, C. N., Klaver, R. W., Brinkman, T. J., Burris, B.
639 M., DePerno, C. S., and Jenks, J. A. (2011). Survival of white-tailed deer neonates in
640 Minnesota and South Dakota. *Journal of Wildlife Management* **75**(1), 213-220.
- 641 Hodgson, J. C., and Koh, L. P. (2016). Best practice for minimising unmanned aerial vehicle
642 disturbance to wildlife in biological field research. *Current Biology* **26**, 404-405.

- 643 Hodgson, J. C., Mott, R., Baylis, S. M., Pham, T. T., Wotherspoon, S., Kilpatrick, A. D., Raja
644 Segaran, R., Reid, I., Terauds, A., and Koh, L. P. (2018). Drones count wildlife more
645 accurately and precisely than humans. *Methods in Ecology and Evolution* **2018**, 1-8.
- 646 Ireland, A. W., Palandro, D. A., Garas, V. Y., Woods, R. W., Davi, R. A., Butler, J. D., Gibbens,
647 D. M., and Gibbens, J. S. (2019). Testing unmanned aerial systems for monitoring wildlife
648 at night. *Wildlife Society Bulletin* **43**, 182-190.
- 649 Israel, M. (2011). A UAV-based roe deer fawn detection system. *International Archives of the*
650 *Photogrammetry, Remote Sensing and Spatial Information Sciences* **38**, 51-55.
- 651 Jennelle, C. S., Henaux, V., Wasserberg, G., Thiagarajan, B., Rolley, R. E, and Samuel, M. D.
652 (2014). Transmission of chronic wasting disease in Wisconsin white-tailed deer:
653 Implications for disease spread and management. *PLoS ONE* **9**, e91043.
- 654 Jiménez López, J., and Mulero-Pázmány, M. (2019). Drones for conservation in protected areas:
655 present and future. *Drones* **3**, 1-23.
- 656 Kays, R., Sheppard, J., Mclean, K., Welch, C., Paunescu, C., Wang, V., Kravitz, G., and Crofoot,
657 M. (2018). Hot monkey, cold reality: surveying rainforest canopy mammals using drone-
658 mounted thermal infrared sensors. *International Journal of Remote Sensing* **40**(2), 4070-
659 419.
- 660 Kellenberger, B., Marcos, D., and Tuia, D. (2018). Detecting mammals in UAV images: best
661 practices to address a substantially imbalanced dataset with deep learning. *Remote sensing*
662 *of Environment* **216**, 139-153.
- 663 Krause, D. J., Hinke, J. T., Perryman, W. L., Goebel, M. E., and LeRoi, D. J. (2017). An accurate
664 and adaptable photogrammetric approach for estimating the mass and body condition of
665 pinnipeds using and unmanned aerial system. *PLoS ONE* **12**(11), e0187465.

- 666 Lethbridge, M., Stead, M., and Wells, C. (2019). Estimating kangaroo density by aerial survey: a
667 comparison of thermal cameras with human observers. *Wildlife Research* **46**, 639-648.
- 668 Lhoest, S., Linchant, J., Quevauvillers, S., Vermeulen, C., and Lejeune, P. (2015). How many
669 hippos: algorithm for automatic counts of animals with infra-red thermal imagery from
670 UAV. *International Archives of the Photogrammetry, Remote Sensing and Spatial*
671 *Information Sciences* **40**, 355-362.
- 672 Linchant, J., Tech, G. A., and Management, F. R. (2015). Are unmanned aircraft systems (UASs)
673 the future of wildlife monitoring? A review of accomplishments and challenges. *Mammal*
674 *Review* **45**, 239-252.
- 675 Makau, D. N., Vanderwaal, K., Kincheloe, J. and Wells, S. J. (2020). Implications of farmed-
676 cervid movements on the transmission of chronic wasting disease. *Preventative Veterinary*
677 *Medicine* **182**, 105088.
- 678 McMahon, M. C., Ditmer, M. A., Isaac, E. J., Moore, S. A., and Forester, J. D. (2021).
679 Evaluating unmanned aerial systems for the detection and monitoring of moose in
680 northeastern Minnesota. *Wildlife Society Bulletin DOI: 10.1002/wsb.1167*, 1-13.
- 681 Mech, L. D., Fieberg, J., and Barber-Meyer, S. (2018). An historical overview and update of
682 wolf-moose interactions in northeastern Minnesota. *Wildlife Society Bulletin* **42**(1), 40-
683 47.
- 684 Minnesota Department of Natural Resources [MNDNR]. (2019). Climate of Minnesota.
685 <www.dnr.state.mn.us/climate/historical/acis_stn_meta.html>. Accessed 18 Nov 2019.
- 686 Mulero-Pázmány, M., Jenni-Eiermann, S., Strebel, N., Sattler, T., Negro, J. J., and Tablado, Z.,
687 (2017). Unmanned aircraft systems as a new source of disturbance for wildlife: a
688 systematic review. *PLoS ONE* **12**, 1-17.

- 689 Mulero-Pázmány, M., Stolper, R., van Essen, L. D., Negro, J. J., and Sassen, T. (2014).
690 Remotely Piloted Aircraft Systems as a Rhinoceros Anti-Poaching Tool in Africa. *PLoS*
691 *ONE* **9**.
- 692 Mysterud, A. (2006). The concept of overgrazing and its role in management of large herbivores.
693 *Wildlife Biology* **12**, 129-141.
- 694 National Land Cover Database 2011 (NLCD 2011). Multi-Resolution Land Characteristics
695 Consortium (MRLC). [https://data.nal.usda.gov/dataset/national-land-cover-database-](https://data.nal.usda.gov/dataset/national-land-cover-database-2011-nlcd-2011)
696 [2011-nlcd-2011](https://data.nal.usda.gov/dataset/national-land-cover-database-2011-nlcd-2011).
- 697 Naugle, D. E., Jenks, J. A., and Kernoham, B. J. (1996). Use of thermal infrared sensing to
698 estimate density of white-tailed deer. *Wildlife Society Bulletin* **24**(1), 37-43.
- 699 Patterson, B. R., Macdonald, B. A., Lock, B. A., Anderson, D. G., and Benjamin, L. K. (2002).
700 Proximate factors limiting population growth of white-tailed deer in Nova Scotia. *Journal*
701 *of Wildlife Management* **66**, 511-521.
- 702 Plante, S., Dussault, C., Richard, J. H., and Côte, S. D. (2018). Human disturbance effects and
703 cumulative habitat loss in endangered migratory caribou. *Biological Conservation* **224**,
704 129-143.
- 705 Preston, T. M., Wildhaber, M. L., Green, N. S., Albers, J. L., and Debenedetto, G. P. (2021).
706 Enumerating white-tailed deer using unmanned aerial vehicles. *Wildlife Society Bulletin*
707 **45**(1), 97-108.
- 708 Rampi, L. P., Knight, J. F., Bauer, M. (2016). Minnesota land cover classification and
709 impervious surface area by Landsat and Lidar: 2013 Update. Retrieved from the Data
710 Repository for the University of Minnesota, <http://doi.org/10.13020/D6JP4S>.

- 711 Rhoads, C. L., Bowman, J. L., and Eyler, B. (2010). Home range and movement rates of female
712 exurban white-tailed deer. *Journal of Wildlife Management* **74**(5), 987-994.
- 713 Rogers, L. L. (1987). Seasonal changes in defecation rates of free-ranging white-tailed deer. *The*
714 *Journal of Wildlife Management* **51**(2), 330-333.
- 715 Sasse, D. B. (2003). Job-related mortality of wildlife workers in the United States, 1937-2000.
716 *Wildlife Society Bulletin* **31**, 1015-1020.
- 717 Scobie, C. A., and Hugenholtz, C. H. (2016). Wildlife monitoring with unmanned aerial
718 vehicles: Quantifying distance to auditory detection. *Wildlife Society Bulletin* **40**, 781-
719 785.
- 720 Siversten, T. R., Mysterud, A. and Gundersen, H. (2012). Moose (*Alces alces*) calf survival in
721 the presence of wolves (*Canis lupus*) in southeast Norway. *European Journal of Wildlife*
722 *Research* **58**, 863-868.
- 723 Vermeulen, C., Lejeune, P., Lisein, J., Sawadogo, P., Bouché, P. (2013). Unmanned aerial
724 survey of elephants. *PLoS ONE* **8**(2), e54700.
- 725 Vincent, J. B., Werden, L. K., and Ditmer, M. A. (2015). Barriers to adding UAVs to the
726 ecologist's toolbox. *Ecological Society of America* **13**, 74-75.
- 727 Wallmo, O. C., Jackson, A. W., Hailey, T. L., Carlisle, R. L. (1962). Influence of rain on the
728 count of deer pellet groups. *The Journal of Wildlife Management* **26**(1), 50-55.
- 729 Watts, A. C., Perry, J. H., Smith, S. E., Burgess, M. A., Wilkinson, B. E., Szantoi, Z., Ifju, P. G.,
730 and Percival, H. F. (2010). Small unmanned aircraft systems for low-altitude aerial surveys.
731 *Journal of Wildlife Management* **74**, 1614-1619.
- 732 Weiskopf, S. R., Ledee, O. E., and Thompson, L. M. (2019). Climate change effects on deer and
733 moose in the Midwest. *The Journal of Wildlife Management* **83**(4), 769-781.

- 734 Weissensteiner, M. H., Poelstra, J. W., and Wolf, J. B. W. (2015). Low-budget ready-to-fly
735 unmanned aerial vehicles: an effective tool for evaluating the nesting status of canopy-
736 breeding bird species. *Journal of Avian Biology* **46**, 425-430.
- 737 Werden, L. K., Vincent, J. B., Tanner, J. C., and Ditmer, M. A. (2015). Not quite free yet:
738 clarifying UAV regulatory progress for ecologists. *Frontiers in Ecology and the*
739 *Environment* **13**(10), 534-535.
- 740 Whitehead, K., Hugenholtz, C. H., Myshak, S., Brown, O., Leclair, A., Tamminga, A., Barchyn,
741 T. E., Moorman, B., and Eaton, B. (2014). Remote sensing of the environment with small
742 unmanned aircraft systems (UASs), part 2: scientific and commercial applications. *Journal*
743 *of Unmanned Vehicle Systems* **2**, 86-102.
- 744 Witczuk, J., Pagacz, S., Zmarz, A., and Cypel, M. (2018). Exploring the feasibility of unmanned
745 aerial vehicles and thermal imaging for ungulate surveys in forests - preliminary results.
746 *International Journal of Remote Sensing* **39**, 5504-5521.

747

748

749

750 **Figures and tables**

751 **Figure 1:** Cedar Creek Ecosystem Science Reserve (CCESR) study area, Minnesota, USA.

752 Unmanned aerial system (UAS) survey plots are distinguished by the teal, numbered boundaries.

753 Plot 8 was omitted from our study because of our inability to safely land the UAS at that site.

754

755 **Figure 2:** Thermal imagery of certain white-tailed deer (*Odocoileus virginianus*) detections (A)

756 and potential deer detections (B) collected at Cedar Creek Ecosystem Science Reserve,

757 Minnesota, USA during UAS surveys from March to April of 2018 and from January to March
758 of 2019. We distinguished between certain and potential deer detections by shape, brightness,
759 and size of thermal signatures. Figure 2A shows clear thermal signatures of deer based on these
760 factors, while figure 2B contains less certainty based on shape. Such signatures were still
761 counted as potential deer because shape can vary greatly in thermal imagery (e.g., when deer are
762 bedded down versus standing/walking).

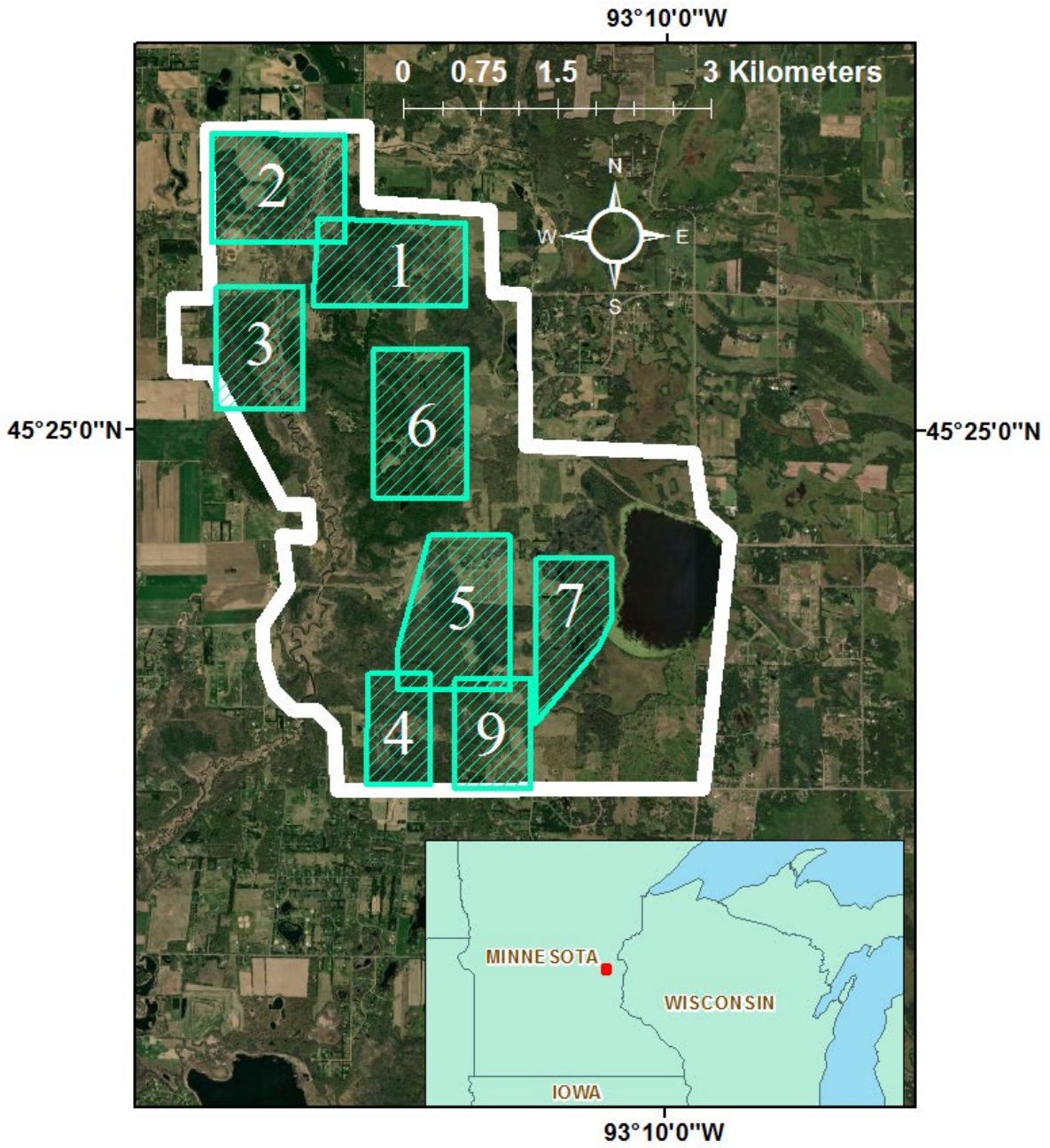
763

764 **Figure 3:** Histogram showing the number of UAS images with 1–9 certain or potential white-
765 tailed deer (*Odocoileus virginianus*) detections from thermal imagery during unmanned aerial
766 system surveys at the Cedar Creek Ecosystem Science Reserve, Minnesota, USA from March to
767 April of 2018 and from January to March of 2019. Overall, deer counts per image ranged from 1
768 to 9 deer, with 3,631 images containing no detection. We distinguished between certain and
769 potential deer detections by shape, brightness, and size of thermal signatures.

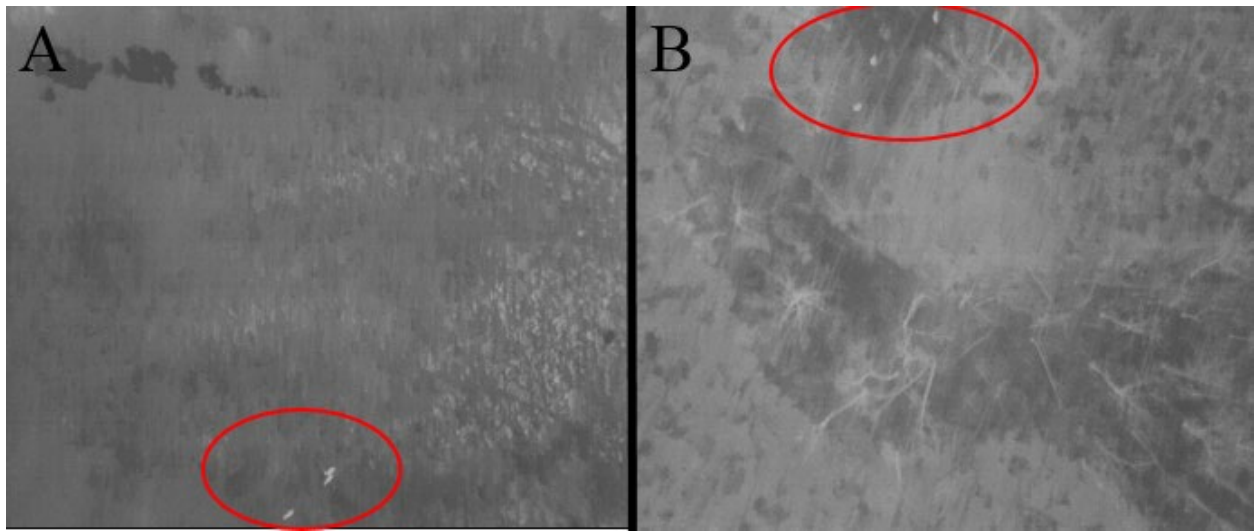
770

771 **Figure 4:** Boxplots of the bootstrapped predictions of the number of estimated deer in the Cedar
772 Creek Ecosystem Science Reserve, Minnesota, USA based on pellet-group count models
773 assuming high, mean, and low rates of pellet deposition (34, 25 & 16 pellets per deer per day,
774 respectively) and UAS models using counts of certain and certain plus potential white-tailed deer
775 in thermal images. Surveys were conducted from March to May of 2018 and from January to
776 May of 2019. Orange points represent the means of the bootstrapped predictions. Red-dashed
777 lines on each pellet-based model show the model-free point estimates. The red dashed-lines over
778 the UAS model estimates represent mean point estimates from the top model for certain and
779 certain plus potential deer detections.

780 Figure 1



782 Figure 2



783

784

785

786

787

788

789

790

791

792

793

794

795

796

797

798

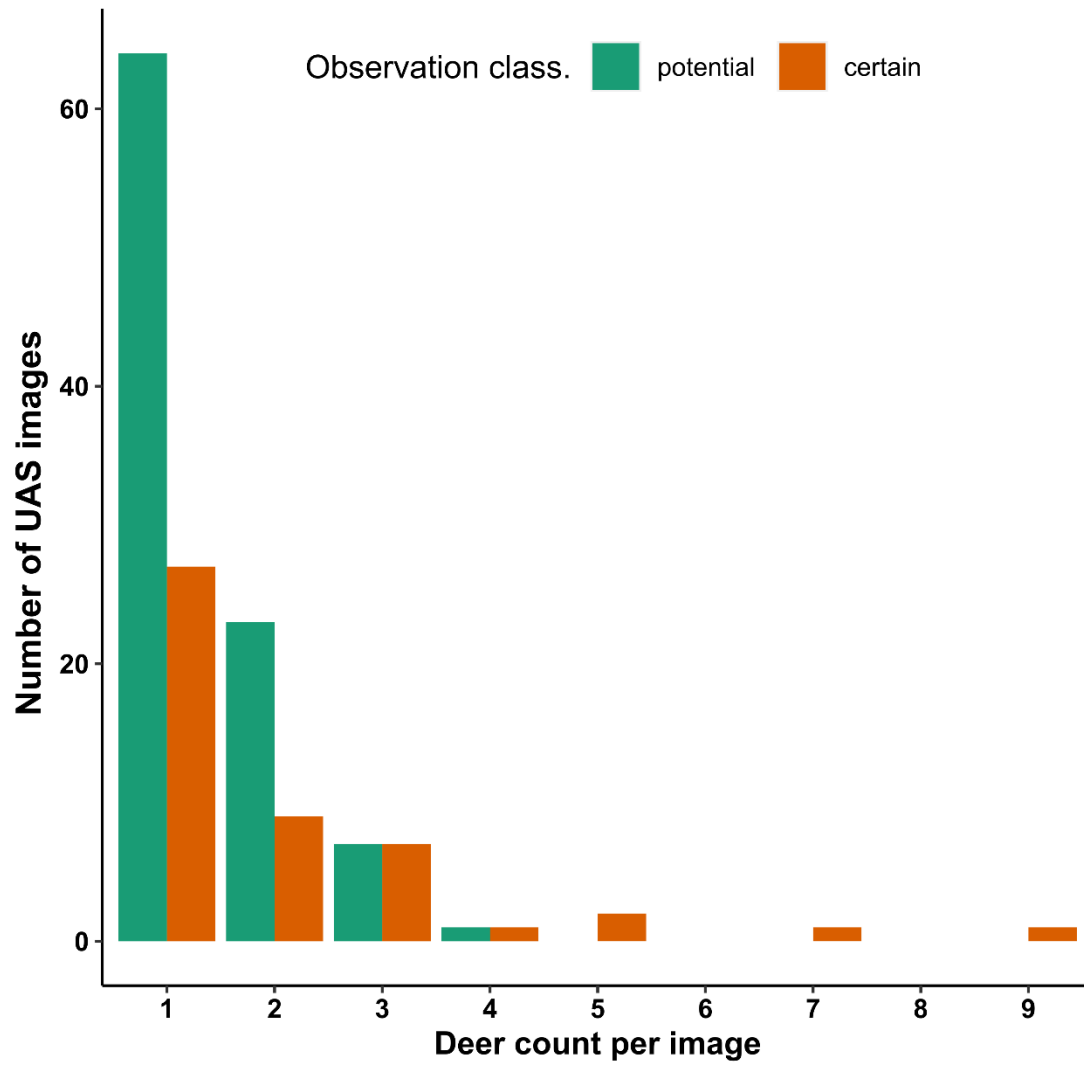
799

800

801

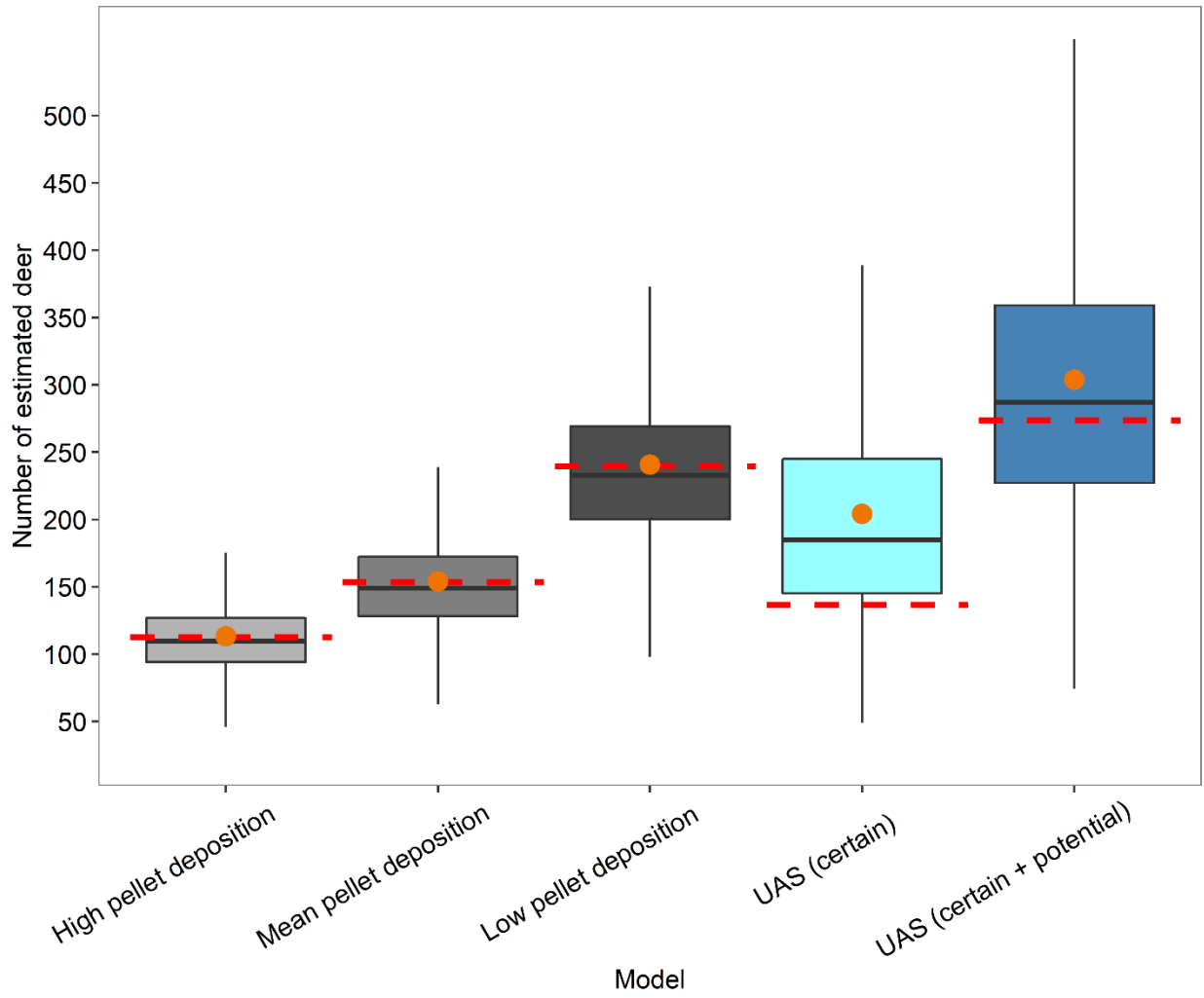
802

803 Figure 3



804
805
806
807
808
809
810
811
812
813
814

815 Figure 4



816

817

818 **Table 1:** The highest-ranking models for estimating deer abundance based on detection data
 819 from unmanned aerial system surveys from March to April of 2018 and from January to March
 820 of 2019 at Cedar Creek Ecosystem Science Reserve, Minnesota, USA. We estimated deer
 821 abundance based on high (certain + potential) deer detections (Response Type = High) and low
 822 (certain) deer detections (Response Type = Low). We considered various distributions (*Family*)
 823 for modeling deer abundance, but show only the top performing distributions for each response
 824 type. All models included an offset for ground area captured in the analysed thermal image.
 825 Model ranking (*Rank*) is based on Δ AIC.

Formula	Family	loglik	Δ AIC	Rank
Response Type = High				
Conditional Formula = \sim Sky Cover + Proportion Wetland*, Zero-Inflated Formula = \sim Sky Cover + Proportion Open Upland**	Zero-inflated Negative Binomial	-694.9	0	1
Conditional Formula = \sim Sky Cover + Proportion Wetland + Random Effect for Survey Flight ID, Zero-Inflated Formula = \sim Sky Cover + Proportion Open Upland	Zero-inflated Negative Binomial	-694.7	1.7	2
Conditional Formula = \sim Sky Cover + Proportion Wetland + Random Effect for Survey Year, Zero-Inflated Formula = \sim Sky Cover + Proportion Open Upland	Zero-inflated Negative Binomial	-694.9	2	3
Response Type = Low				
Conditional Formula = \sim Sky Cover + Proportion Wetland + Random Effect for Survey Flight ID, Zero-Inflated Formula = \sim Proportion Non-Wetland Open***	Truncated Poisson	-306.9	0	1

Conditional Formula = ~ Sky Cover + Proportion Wetland, Zero-Inflated Formula = ~ Proportion Non- Wetland Open	Truncated Poisson	-308.7	1.6	2
Conditional Formula = ~ Sky Cover + Proportion Conifer + Proportion Deciduous, Zero-Inflated Formula = ~ Proportion Non-Wetland Open	Truncated Poisson	-309.2	2.6	3

826 *Wetland habitat is defined as forested wetland + emergent wetland habitats

827 **Open upland habitat is defined as row crops (agricultural) + grass habitats

828 ***Non-wetland open habitat is defined as row crops (agricultural) + grass + developed + open
829 water habitats

830

831 **Table 2:** White-tailed deer density and abundance estimates from unmanned aerial system

832 (UAS) surveys and pellet-group counts from March to May of 2018 and from January to May of

833 2019 at the Cedar Creek Ecosystem Science Reserve (CCESR), Minnesota, USA. UAS high

834 estimates are based on certain + potential thermal detections, and UAS low detections are based

835 on only certain detections. Pellet estimates are from pellet-group surveys with low estimates

836 corresponding to 34 pellet groups per deer per day, mean estimates to 25 pellet groups per deer

837 per day, and high estimates to 16 pellet groups per deer per day. Point estimates do not include

838 estimates of error. 95% prediction intervals were calculated through bootstrapped estimates.

	CCESR Density (deer/km ²)	95% Prediction Interval (deer/km ²)	CCESR (total deer)	95% Prediction Interval (total deer)
UAS High Point Estimate	12.38	-	273.81	-
UAS Low Point Estimate	6.18	-	136.68	-

UAS High Bootstrapped Estimate	13.77	6.64-24.35	304.55	146.88-538.62
UAS Low Bootstrapped Estimate	9.40	4.32-17.84	207.90	95.56-394.62
Pellet Low Point Estimate	5.13	-	112.79	-
Pellet Mean Point Estimate	6.98	-	153.39	-
Pellet High Point Estimate	10.91	-	239.67	-
Pellet Low Bootstrapped Estimate	5.15	3.04-8.30	113.25	66.82-182.48
Pellet Mean Bootstrapped Estimate	7.01	4.14-11.29	154.02	90.88-248.18
Pellet High Bootstrapped Estimate	10.95	6.46-17.65	240.66	142.00-387.78


839


840



Tools and Technology

Evaluating Unmanned Aerial Systems for the Detection and Monitoring of Moose in Northeastern Minnesota

MICHAEL C. McMAHON ¹, Department of Fisheries, Wildlife, and Conservation Biology, University of Minnesota, 2003 Upper Buford Circle, Suite 135, Saint Paul, MN 55108, USA

MARK A. DITMER , Department of Fisheries, Wildlife, and Conservation Biology, University of Minnesota, 2003 Upper Buford Circle, Suite 135, Saint Paul, MN 55108, USA

EDMUND J. ISAAC, Grand Portage Biology and Environment, 27 Store Road, Grand Portage Band of Lake Superior Chippewa, Grand Portage, MN 55605, USA

SETH A. MOORE, Grand Portage Biology and Environment, 27 Store Road, Grand Portage Band of Lake Superior Chippewa, Grand Portage, MN 55605, USA

JAMES D. FORESTER , Department of Fisheries, Wildlife, and Conservation Biology, University of Minnesota, 2003 Upper Buford Circle, Suite 135, Saint Paul, MN 55108, USA

ABSTRACT The use of unmanned aerial systems (UAS) for wildlife surveying and research has widely expanded in the past decade, but with varying levels of success. Applying UAS paired with Forward Looking Infrared (FLIR) technology to survey forest-dwelling species has been particularly challenging because of unreliable animal detection. We describe our application of UAS and FLIR technology to detect GPS-collared moose (*Alces alces*) and their calves in the heavily-forested region of northeastern Minnesota, USA, during 2018 and 2019. We conducted grid-pattern UAS thermal surveys over GPS-collared cows during the calving seasons (April to June) of 2018 and 2019 to determine the feasibility of using a FLIR-equipped UAS for detecting cow moose, and for quantifying the number of calves. We also collected data on environmental and flight characteristic variables to model moose detection. Our best fitting model of moose detection showed increased detection with more cloud cover at the survey site ($\hat{\beta} = 1.13$, SE = 0.43), whereas increased forest canopy ($\hat{\beta} = -1.10$, SE = 0.38), and vegetative greenness (enhanced vegetation index, EVI; $\hat{\beta} = -1.37$, SE = 0.32) both reduced detection success. By adjusting our methodology based on our detection model findings, we increased our adult moose detection success from 25% during our first season, to 85% during our second season, and calf detection from 27% to 79%, respectively. We report on our methodological improvements and identify limitations to UAS-based wildlife research in forested systems. Overall, we found that UAS with FLIR sensing is a promising tool for quantifying moose calving success, twinning rate, and calf survival, and may be effective for monitoring the reproductive success and survival of other wildlife species in densely forested regions. © 2021 The Wildlife Society.

KEY WORDS aerial survey, *Alces alces*, calf survival, detection modeling, drones, FLIR, Minnesota, thermal infrared, unmanned aerial systems (UAS), unmanned aerial vehicles (UAV).

The use of unmanned aerial systems (UAS) in wildlife science has grown rapidly (Jiménez López and Mulero-Pázmány 2019) for their applications in animal surveying and censuses (Vermeulen et al. 2013, Chrétien et al. 2015, Ezat et al. 2018), detection of animal sign (e.g., nests and tracks; Goebel et al. 2015, van Andel et al. 2015), and habitat evaluation (Chen et al. 2017, Olsoy et al. 2018). Studies deploying UAS have covered a range of taxonomic

groups including terrestrial and aquatic mammals (Hodgson et al. 2013, Witczuk et al. 2018), birds (Chabot and Bird 2012), reptiles (Ezat et al. 2018), and fish (Kiszka et al. 2016). Unmanned aerial systems can collect data at fine spatial and temporal resolutions because they can fly at low altitudes and much slower flight speeds relative to conventional manned aircraft (Anderson and Gaston 2013). Operational efficiency of UAS is increased with the ability to launch UAS rapidly on site with user discretion, whereas conventional aircraft often are limited by low cloud cover, require additional flight time to travel to and from refueling sites, and have a considerably higher operating cost (Chabot 2009, Watts et al. 2010, Vermeulen et al. 2013,

Received: 6 April 2020; Accepted: 28 October 2020
Published:

¹E-mail: mcmah231@d.umn.edu

Linchant et al. 2015). Safety is also increased with UAS because they eliminate the need for manned-flight in often hazardous environments (Jones et al. 2006, Watts et al. 2010); low-level flight is a leading cause of job-related mortality for wildlife professionals (Sasse 2003).

Evidence suggests that the presence of UAS can disturb wildlife by eliciting behavioral (Bennitt et al. 2019) and physiological responses (Ditmer et al. 2015). However, UAS reduces the need to approach animals on foot or with ground vehicles for counting or conducting observations, and may ultimately cause less disturbance than traditional aerial counting methods with manned aircraft (Chabot and Bird 2012, Goebel et al. 2015, Weissensteiner et al. 2015, Hodgson et al. 2018) due to less noise from electric UAS motors (Mulero-Pázmány et al. 2017). Consequently, UAS provide a powerful tool for monitoring of populations where repeat visits are required to monitor parameters like nesting success or survival rates (Sardá-Palomera et al. 2012); this is especially valuable when monitoring species that are sensitive to anthropogenic disturbances (Ditmer et al. 2019).

Unmanned aerial systems can be equipped with a large variety of sophisticated sensors, and the use of multiple combinations of sensors are possible with adequate UAS payload capacity. The proliferation of UAS and sensors in a variety of scientific fields and industries has led to reduced sensor and UAS costs and improvements in the spatial resolution of sensors. Color (RGB) cameras are commonly included on UAS and yield high-resolution imagery of ground features and even wildlife (Chabot and Bird 2012; Hodgson et al. 2013, 2018). Forward Looking Infrared (FLIR) sensors are increasingly being deployed in UAS systems to successfully detect and survey homeothermic wildlife species (Witczuk et al. 2018, Ireland et al. 2019). By capturing thermal radiation emitted from animals, FLIR sensors allow for increased detection probability of species that are well camouflaged, partially obscured by vegetation, or at greater distances than could be detected with conventional methods (Dunn et al. 2002, Haroldson et al. 2003, Montague et al. 2017). These advantages reduce perception bias (i.e., failing to detect an animal that was present and available for detection; Marsh and Sinclair 1989) and have provided significant increases in the efficacy of some wildlife surveys (Focardi et al. 2001). Thermal sensing works best when there is high contrast between an animal's temperature and the background environment (i.e., a warm-bodied animal against cool ground; Garner et al. 1995, Chrétien et al. 2016). Rocks, bare ground, logs, and living trees absorb and emit large amounts of thermal radiation, which results in bright returns that can create false-positive detections (Garner et al. 1995, Dunn et al. 2002). Importantly, environments with thick vegetation or dense forest canopy can obscure wildlife from detection thus limiting the effectiveness of UAS-FLIR pairing (Gill et al. 1997, Dunn et al. 2002, Kissell and Nimmo 2011). Thermal sensors have been useful for detecting moose (*Alces alces*) and other ungulates from manned aircraft (Addison 1972, Adams et al. 1997, Bontaites et al. 2000,

Bernatas and Nelson 2004, Millette et al. 2014); similar levels of success have been achieved when affixing FLIR sensors to UAS (Chrétien et al. 2016, Witczuk et al. 2018, Ireland et al. 2019, Beaver et al. 2020), even with smaller bodied target species, such as recently born roe deer (*Capreolus capreolus*) fawns in grass meadows (Israel 2011).

Most studies to date have paired UAS with FLIR technology for wildlife detection in open terrain without a high percentage of forest cover (Israel 2011, Lhoest et al. 2015, Ireland et al. 2019). Indeed, both manned aircraft and UAS surveys using FLIR sensing in forested environments have faced greater challenges due to unreliable animal detection (Potvin and Breton 2005; Chrétien et al. 2015, 2016; Witczuk et al. 2018). Surprisingly, this was true even for large-bodied animals; Dunn et al. (2002) found that aerial FLIR sensing did not aid in detection of elk (*Cervus elaphus*) because: 1) elk were well-insulated and did not have high enough contrast in thermal imagery, 2) emitted thermal radiation from trees and bare ground confounded detection, and 3) heavy tree cover (e.g., dense coniferous forest habitat) physically obscured elk from detection. Further understanding and overcoming these limitations of FLIR-equipped UAS is critical for realizing the full potential of this technology for management and conservation applications.

Moose inhabiting northeastern Minnesota's Grand Portage Indian Reservation, USA, are an important subsistence species used by the Grand Portage Band of Lake Superior Chippewa historically and presently, but harvests have declined in recent years concomitant with significant (~65%) declines in moose populations throughout their range in Minnesota over the last decade (S. A. Moore, Grand Portage Trust Lands, unpublished data; Del Giudice 2018). This has resulted in extensive research and management efforts by the Grand Portage Band of Lake Superior Chippewa and the Minnesota Department of Natural Resources (MNDNR) to understand the drivers of the decline (Severud et al. 2015). Mortality of adult moose in MN has been linked to disease (Wünschmann et al. 2015), increased parasite loads (Verma et al. 2016), and predation (Carstensen et al. 2017). Warming temperatures and decreasing snow depth associated with climate change are also thought to be contributing to their decline by increasing thermal stress (Street et al. 2016) and allowing for the increase of white-tailed deer (*Odocoileus virginianus*) population densities (Weiskopf et al. 2019). Deer pose a threat to moose as they are known to carry transmissible diseases and parasites (Wünschmann et al. 2015). Neonate (i.e., moose calf) birthing, survival, and predation rates are critical for understanding the future population trajectory of moose (Severud et al. 2015, 2019), thus, the Grand Portage Trust Lands Department initiated an intensive study of the northeastern moose population beginning in 2008. Tribal biologists conduct annual aerial counts to monitor population demographics and have fitted moose with GPS collars to examine survival and causes of mortality. These efforts have been undertaken to conserve moose on the landscape and preserve a cultural icon for future generations.

These demographic estimates became more challenging to quantify outside of the reservation after the state of Minnesota banned moose collaring due to initially high capture-induced abandonment rates during studies of calf survival and predation (Del Giudice et al. 2015, 2018). Forward Looking Infrared-equipped UAS may provide a much needed, non-invasive tool to better estimate and track these important demographic rates of moose calves.

In this study we attempted to determine the feasibility of using UAS technology to detect cow moose and quantify the presence of any neonates while minimizing disturbance of cow-calf pairs. Our study aimed to quantify the number of calves born per cow and determine the length of calf survivorship through repeated UAS flights. We also explicitly attempted to determine what factors limited the effectiveness of UAS operations with FLIR technology to detect moose in a heavily forested environment by modeling the detection probability of adult moose during our 92 spring flight missions based on weather conditions, habitat type

and structure, UAS flight characteristics (e.g., flight altitude), and the phenology of vegetation. Our research details how wildlife researchers and managers can more efficiently utilize UAS and FLIR technologies to collect data on large ungulates in northern forested environments.

STUDY AREA

All UAS flights were conducted within the Grand Portage Band of Lake Superior Chippewa Indian Reservation and eastern extents of the Grand Portage State Forest, Minnesota, USA (Fig. 1). Topography was highly varied and ranged from 183 m to 553 m above sea level. Mean monthly temperatures for Grand Portage ranged between 1.89° C to 14.0° C during our study periods (May to June, 2018 and April to May, 2019). The mean minimum temperatures ranged between -2.94° C to 7.94° C, and mean maximum temperatures were between 6.67° C to 20.11° C. Monthly precipitation ranged from 3.86 cm to 11.28 cm

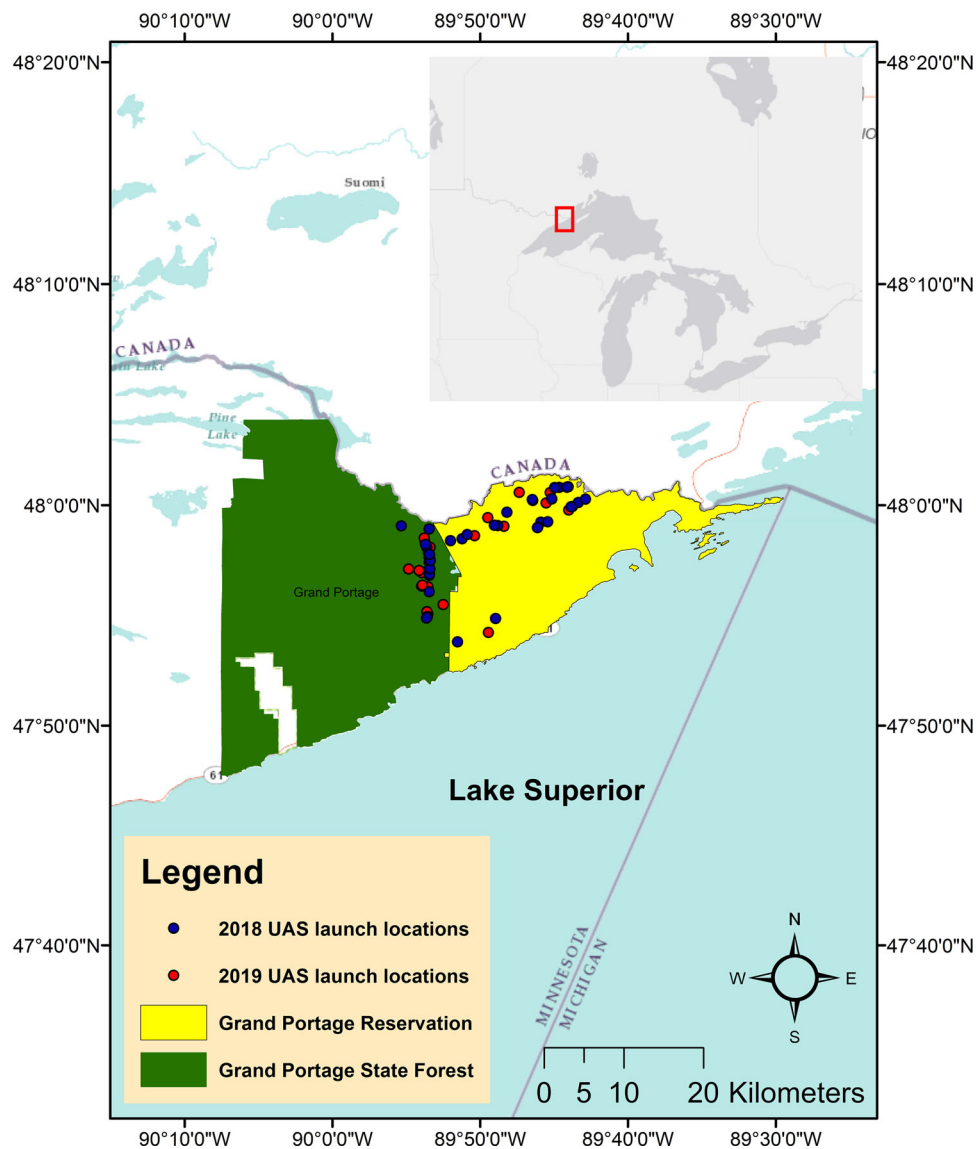


Figure 1. Study area of Grand Portage Reservation and eastern Grand Portage State Forest, in northeastern Minnesota, USA. Unmanned aerial system (UAS) launches are shown across the study area for the 2018 and 2019 field seasons.

with a mean monthly precipitation level of 6.67 cm (NOAA 2019). Snow depth during our study period ranged from 0 cm to ~60 cm (M. C. McMahon, University of Minnesota, personal observation).

Vegetation on the reservation consisted of boreal forest with aspen-birch (55%; *Populus tremuloides* and *Betula papyrifera*), conifer (25%; *Pinus strobus*, *P. resinosa*, *P. banksiana*, *Abies balsamea*, and *Thuja occidentalis*), northern hardwood (6%; *Acer saccharum* and *A. rubrum*), swamp hardwood (3%; *Fraxinus spp.*), and other (11%) communities (E. Isaac, Grand Portage Trust Lands, unpublished data). In addition to moose, white-tailed deer, black bears (*Ursus americanus*), and gray wolves (*Canis lupus*) were present in our study area.

METHODS

Data Collection

Our study population consisted of 22 cow moose fitted with GPS-collars with Iridium-satellite relay capabilities (VECTRONIC Aerospace, Berlin, Germany). Capture and handling of moose was conducted by the Grand Portage Natural Resources Management Department (IACUC Protocol# 1812-36635A). Moose locations were recorded and stored every 30 minutes to GPS collars, with GPS coordinates transmitted to satellites every two hours. Adult moose movement patterns can indicate a variety of critical information such as calving and either successful or attempted predation events (Severud et al. 2015, Obermoller et al. 2019). We analyzed cow moose movements multiple times a day to identify locations and times for safe and efficient UAS deployment to detect cow moose and calves. Prior to conducting flight missions above cow-calf pairs, we conducted initial test flights over GPS-collared bull moose in May of 2018 to gauge levels of disturbance from UAS flights. We would classify a disturbance if there were any erratic movements (i.e., fleeing from an area) that corresponded in time to UAS launch and flight times. Although none of these initial flights led to a behavioral disturbance, we took precautions in our surveys of cow moose and calves to reduce the risk of disturbance (see below), and continued monitoring movement behavior to identify potential disturbance responses (Hodgson and Koh 2016).

We used a DJI Inspire 2 quadcopter (~\$3,000 USD; Shenzhen DJI Sciences and Technologies Ltd., Nanshan District, Shenzhen, China), equipped with a FLIR Vue Pro 640 (640 × 512 pixels, 32° FOV, 19 mm, 30 Hz) (~\$3700 USD; FLIR Systems Inc., Wilsonville, OR, USA) for 2018 surveys and a FLIR Duo® Pro R (640 × 512 pixels, 32° FOV, 19 mm, 30 Hz; ~\$6350 USD) for 2019 surveys. Both thermal sensors were one-band sensors with a spectral interval that measured 7.5 to 13.5 μm. The FLIR Duo® Pro R used in 2019 also featured an RGB sensor (4000 × 3000 pixels, 56° × 45° FOV) that allowed us to capture color imagery simultaneously with thermal imagery. Survey flights were planned and conducted using the Pix4Dcapture app (Pix4D, Prilly, Switzerland). Thermal infrared and RGB footage were recorded and stored onboard the UAS for review post flight.

Flights occurred from 25 May 2018 to 28 June 2018 (n = 44 flights) and 25 April 2019 to 30 May 2019 (n = 48 flights) at varying times between morning and evening civil twilight. Surveys were flown in rectangular grid transects centered over the most recently updated GPS locations of cows. Rectangular grids were used to maximize our coverage in the event that the cow moved off of the last known location prior to launching the UAS, and to minimize the risk of animal disturbance (Mulero-Pázmány et al. 2017). To minimize animal disturbance from our presence on the ground, we launched the UAS from reservation and county roads or trails that were between 300 m and 600 m Euclidean ground distance from updated moose locations. This distance also allowed us to maintain visual contact of the UAS, and sufficient radio communication between the remote and quadcopter. Additionally, we flew at altitudes that were near the maximum allowable 122 m (~400 ft) above ground level; altitudes ranged from 75 m to 121 m depending on terrain elevations relative to launch points.

Moose Demographic Data and Predation Events

Thermal infrared video footage was reviewed manually post flight by human observers. Observers were trained to detect living animals in thermal video by viewing sample footage collected over domestic animals (e.g., domestic bison, cows, and captive deer) of known location and abundance, to develop a sight picture for large-bodied mammals in thermal imagery. The same observers reviewed thermal video footage for both seasons. Adult moose and calves were visually identified from the video footage by their shape and brightness in the footage, the latter also by their proximity with the cow. Detections of target moose (i.e., bright white silhouettes that often resembled a large animal body with a head) were confirmed by updated cow GPS locations collected during and post UAS survey times. We attempted to utilize object-based image analysis (OBIA) to quantify moose detections from our thermal video footage. However, we would have needed to greatly increase the resolution of our FLIR sensors (at an economic expense), or fly the UAS at lower altitudes, increasing the risk of disturbing moose and striking hazards (e.g., tall trees), to effectively apply OBIA methods to discern moose from other objects.

For 2018 flights, moose detections were verified by matching the position of the UAS on the flight transect where a thermal detection was observed (based on flight time) to the location and time stamp from the collared moose that corresponded to that time in the flight. In 2019, detections were verified by matching GPS coordinates of the UAS and of the moose at given flight times. This was possible because the FLIR Duo® Pro R used in 2019 featured geotagged video footage that provided GPS coordinates for the UAS every second of survey time, whereas the FLIR Vue Pro used in 2018 did not. Color (RGB) footage was also reviewed for flights with positive thermal detections as an additional verification throughout the 2019 season. Thermal detections of cows and counts of calves were recorded for each flight.

We investigated suspected calf predation events by flying over known collared cow-calf pairs after large movements occurred in a short period of time, with the cow commonly circling back to the suspected predation location. We considered a predation event to be positively confirmed if we could detect the cow without the previously detected calf. Conversely, we concluded that a predation event was unsuccessful or did not occur by thermally detecting the calf with its mother. Our conclusions about predation events through remote sensing were corroborated by subsequent on-foot investigations.

Moose Detection Variables

To better understand what factors altered our ability to detect moose using UAS with FLIR technology, we developed a detection model that included data on weather conditions, UAS operations, habitat type, and vegetation structure and phenology. Factors that we hypothesized would influence detection included: 1) cloud cover, which was recorded in the field from visual observations; 2) temperature; 3) relative humidity; 4) wind speed; 5) mean altitude; 6) canopy cover; 7) forest composition; and 8) vegetation phenology. Temperature, humidity, and wind speed were collected post flight with archived weather data recorded at the Cook Municipal airport (Cook, MN, USA; 47.82°N, -92.69°W; National Oceanic and Atmospheric Administration 2019). We recorded altitude of the UAS throughout each flight and summarized these data as mean altitude for our detection models. Light Detection and Ranging (LiDAR) was collected throughout the region during May 2011 (a leaf-free period in the study area) at a rate of 1 pulse/meter with a vertical accuracy RMSE of 5.0 cm and a horizontal accuracy of 1.16 m (Minnesota Geospatial Information Office 2018). We estimated percent forest canopy as the percentage of LiDAR returns that were >3 m above the ground, based on subtracting the return values from a Digital Elevation Model (DEM) with a spatial resolution of 3 m, within a 30-m resolution grid that covered the study area. We assigned each flight a canopy cover percentage based on the maximum canopy cover value within 20 m of the moose's GPS-location during the UAS flight (see rationale in the Moose Detection Modeling

section). Because we believed conifer cover would reduce moose detection, even in early spring, we included the total percentage of conifer and mixed conifer-deciduous forest within the same buffer. Land cover was derived from a multitemporal composite of Landsat 8 imagery combined with LiDAR data (Minnesota Geospatial Information Office 2016). To estimate the phenology on a given day at a particular UAS flight area, we used the enhanced vegetation index (EVI) from the MODIS data set collected by the National Aeronautics and Space Administration (NASA). The MODIS dataset provides remotely sensed estimates of vegetative greenness at a 500-m spatial resolution composited over a 16-day period (MODIS/Terra Vegetation Indices 16-day L3 Global 500-m resolution, MOD13A1; Didan 2015); we used the MODIS package (Didan 2015) in program R (v 3.6.1, R Core Team 2019) to download the data. Moose GPS-locations were overlaid on the EVI raster that temporally corresponded with the field data collection.

Moose Detection Modeling

After our first season in 2018, we used effect plots to visualize the relationship between the variables and adult moose detection (Table 1). We were specifically looking for what conditions influenced detection so we could improve our success during the 2019 season. The graphs indicated that decreased temperature and canopy cover, and greater cloud cover all increased detection. When modeling the 2018 data, we did not investigate the influence of EVI. We have provided an example of the effects of cloud cover from flights over a captive bison (*Bison bison*) herd located at the University of Minnesota's Cedar Creek Ecosystem Science Reserve where we tested our UAS and FLIR sensors prior to conducting surveys of wild moose (Fig. 2). Thermal survey flights during clear sky conditions resulted in unclear bison detections (Fig. 2A) relative to overcast sky conditions (Fig. 2B). During our second field season, we maximized detectability of moose by conducting flights earlier in the season (starting 25 April instead of 23 May), earlier in the morning (when ground temperature was at its lowest), and on days with greater cloud cover.

We hypothesized that canopy cover would have a strong influence on our ability to detect moose with our FLIR

Table 1. Detection model covariate names and descriptions with units, mean and SE, and ranges in observations, combined from 2018 and 2019 flight data from northeastern Minnesota, USA.

Variable	Definition	Units	Mean (SE)	Range
Altitude	Mean altitude of the UAV (m above ground)	Meters above ground	106.6 (1.20)	82.3–132.6
MooseDetect	Whether adult moose was detected or not (response variable)	Binary (0 = no, 1 = yes)	0.57 (0.05)	0–1
Canopy	Max. proportion of the canopy >3 m with 20-m buffer of the moose	Proportion	0.50 (0.02)	0.05–0.76
Cloud	Whether cloud cover was considered overcast or not	Binary (0 = no, 1 = yes)	0.16 (0.04)	0–1
Conifer	Proportion of the landcover in a 20-m buffer around the moose that was conifer or mixed forest	Proportion	0.25 (0.04)	0–1
EVI	Enhanced vegetation index—remotely sensed metric of vegetative greenness	Index (possible range: -2000–10000)	4210 (157.4)	2145.0–6843.0
Humid	Relative humidity recorded at nearest airport	Proportion	49.76 (1.71)	19.0–87.0
LaunchTime	UAV launch time (hours and minutes)	Hours	9:35 (00:20)	4:00–17:00
Temp	Temperature	°C	13.52 (0.74)	-1.11–27.22
Wind	Wind speed recorded at the nearest airport	Knots	5.42 (0.29)	0.00–11.3

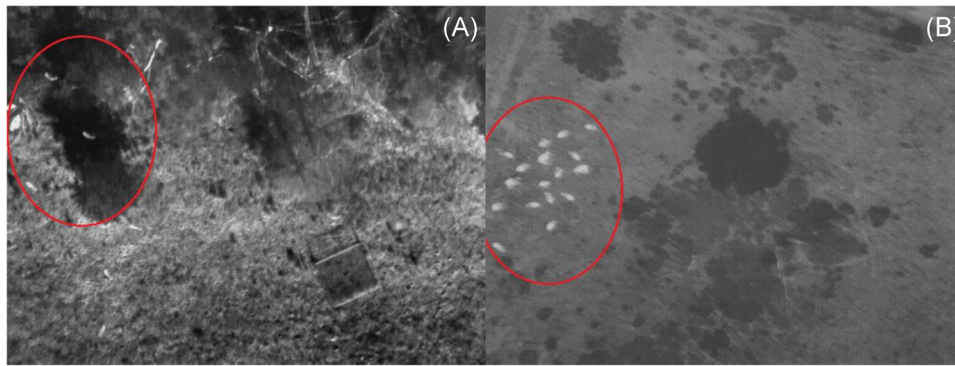


Figure 2. Side-by-side comparison of thermal infrared photos of a captive bison herd captured during clear sky conditions (A) and overcast sky conditions (B). Imagery was collected at the University of Minnesota’s Cedar Creek Ecosystem Science Reserve, USA, during July 2018. This contrast demonstrates the positive effect that overcast sky conditions have on thermal detection.

sensor, so we created a set of univariate models in which we regressed different spatial extents of both the mean and maximum canopy cover around a given moose’s GPS-location during the time of flight with our detection response. Each linear model contained one value for the scaled mean or maximum canopy cover at buffers of 20 m, 25 m, 30 m, 50 m, and 100 m. We used a generalized linear model structure with a binomial distribution in the `glm` function of program R and assessed the fit of each model using Akaike’s Information Criteria adjusted for small sample sizes (AIC_c). The 20-m buffer with the maximum value for canopy cover explained the most deviance in moose detection so we used it in the full model of moose detection (see below) and used a 20-m buffer to create the total percentage of conifer and mixed conifer-deciduous forest.

To formally model moose detection (binary response: 0 = present but not detected, 1 = present and detected) for our combined two spring field seasons, we developed a set of 15 *a priori* models and a null model (intercept only). We restricted the total number of model parameters to 3 such that each model either contained 3 additive covariates or an interaction with additive effects for the 2 associated variables. We used the same generalized linear model structure described above for the canopy-cover buffer analysis. Within each model, all independent variables were centered and scaled by their corresponding standard deviation to improve model convergence, and we assessed relative model fit using AIC_c . Prior to fitting the models, we removed 3 observations due to covariate completeness ($n = 89$ flights).

We determined the strength of influence for each covariate in the top model(s) by creating effect plots using the package `ggeffects` (Lüdtke 2018) in program R. Each plot illustrates the mean and 95% confidence interval of predicted moose detection at each value of the covariate while all other variables are held constant at their mean values. We predicted moose detection across the 2.5% to the 97.5% quantile values to assess the change within the 95% distribution of the values we collected for the given covariate. All covariates used in the effect plots were created at their

original scale (not centered and scaled) to better illustrate the relationships with familiar values (e.g., % of canopy cover, degrees Celsius).

Post Hoc Modeling

We collected sky condition observations from the same weather station that we used for our other weather-based covariates. We created an additional covariate using the National Oceanic and Atmospheric Administration’s (NOAA 2019) cloud coverage classification to compare against our original field-based observation data of cloud cover (Cloud). The weather station-based covariate was binary with the NOAA classification for overcast coded as a 1 while all other observations, including missing, were coded as 0. To determine the relative importance of field vs weather-station derived cloud cover, we fit models with the centered and scaled values for Cloud (field-based) and compared the AIC_c and coefficient estimates to those from models based on the weather station estimates of cloud cover ($n = 89$ flights). We then removed all observations that corresponded to the weather station-based covariate’s classification of missing and repeated the comparison ($n = 82$ flights). When comparing the detection percentages between field and weather station-based sky conditions, we had more flights with weather station-based data because some flights had missing field-based observations.

RESULTS

We conducted 92 total thermal UAS flights over cow moose from 2018 to 2019. Combined detection success over 2018 and 2019 was 57%; however, modifications to flight timing and procedures increased detection success from 25% in 2018 to 85% in 2019. Over the 2 years of our study we detected 18 individual cows, with multiple detections per cow. We had a combined calf detection success of 54% over the 2 study periods, confirming the detection of 18 individual calves. Similar to adult moose, calf detection improved from 27% in 2018 to 79% in 2019 after making adjustments to the timing of flights. During 2019, we confirmed 3 separate suspected predation events of calves with UAS thermal survey flights and disproved one that was

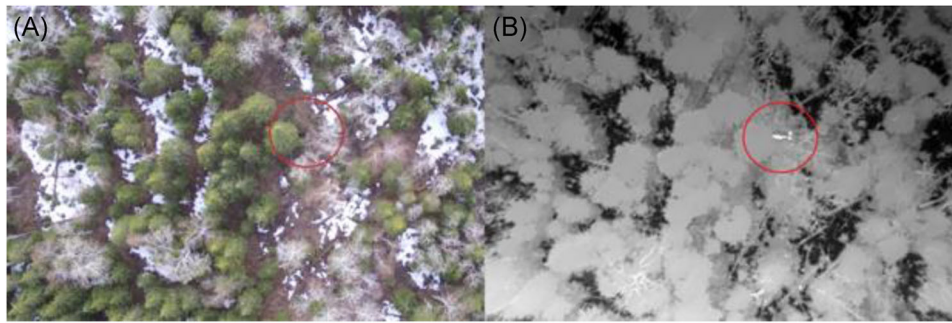


Figure 3. Comparison of UAS-gathered RGB imagery (A) and thermal infrared imagery (B) of a cow moose with two calves in northeastern Minnesota, USA, during spring of 2019. The photos were captured at the same time and location over this cow and her calves, which demonstrates the advantage of increased detection success from thermal infrared technology over RGB photography.

thought to be a successful predation. Only 46% of thermally detected moose in 2019 could be seen in corresponding RGB footage upon visual inspection. Vegetation and dark-colored terrain often obscured moose in RGB footage, whereas FLIR footage allowed for easy detection (Fig. 3).

Detection Analysis

Our top model of adult moose detection included the additive influences of vegetative greenness (EVI; $\hat{\beta} = -1.37$, SE = 0.32), whether cloud cover was considered overcast or not (Cloud; $\hat{\beta} = 1.13$, SE = 0.43), and maximum canopy cover (Canopy; $\hat{\beta} = -1.10$, SE = 0.38; scaled and centered; Table 2, Fig. 4). From the lowest to the highest values of the 95% distribution of observed EVI values (Fig. 4A), our top-fitting model predicted moose detection would decrease from 92.6% (95% CI = 80.7%–97.4%; EVI = 2160) to 18.0% (95% CI = 6.4%–41.3%; EVI = 6512). Detectability increased during flights with overcast skies ($\bar{X} = 96.2\%$, 95% CI = 73.2%–99.6%) relative to flights occurring during conditions without overcast skies ($\bar{X} = 53.7\%$, 95% CI = 38.3%–68.5%; Fig. 4B). Moose detection also decreased with more canopy cover around the moose's

location (20 m buffer) from a prediction of 96.4% (95% CI = 77.2%–99.5%; Canopy = 13.1%) to 29.9% (95% CI = 13.3%–54.2%; Canopy = 70.7%; Fig. 4C). Temperature was not included in the top model; however, it did exhibit a somewhat strong negative effect on moose detection (Temp; $\hat{\beta} = -0.90$, SE = 0.37).

Post Hoc Analysis of Cloud Cover

Weather station-based observations of cloud cover did not explain as much variation in moose detection as field-based observations of cloud cover. Our field-based assessment of overcast (Cloud = 1) was associated with 13 moose detections and only one non-detection (92.9% [13/14]). In comparison, the weather station-based classification of overcast was associated with a positive detection during 16, and a non-detection during 4, flights (80% [16/20]). When our best-supported model (n = 89 flights) included weather station-based data where missing data were considered not to be overcast (coded as 0), AIC_c increased by 7.28; the scaled and centered coefficient value ($\hat{\beta} = 0.58$, SE = 0.30) was smaller than our original covariate estimate for Cloud ($\hat{\beta} = 1.13$, SE = 0.43). Models where all missing values in

Table 2. All 16 models considered when assessing the factors influencing the detection (binary) of adult moose in northeastern Minnesota, USA, using UAS with thermal sensors during the spring of 2018 and 2019. We used generalized linear models with a binomial distribution and restricted the number of parameters to a maximum of three.

Model	logLik	ΔAIC_c	Weight
EVI + Cloud + Canopy	-35.55	0.00	0.86
Canopy + EVI + Temp	-37.66	4.24	0.10
Cloud + EVI + Temp	-39.16	7.22	0.02
Canopy + EVI + Canopy \times EVI	-40.05	9.02	0.01
Cloud + Temp + Cloud \times Temp	-42.17	13.25	0.00
Conifer + Cloud + Temp	-42.64	14.19	0.00
Altitude + LaunchTime + Temp	-42.82	14.56	0.00
EVI + Humid + Wind	-43.87	16.64	0.00
Altitude + Canopy + Altitude \times Canopy	-44.73	18.37	0.00
Altitude + EVI + Altitude \times EVI	-45.21	19.32	0.00
Altitude + Conifer + LaunchTime	-47.00	22.92	0.00
Canopy + Cloud + Humid	-47.33	23.57	0.00
Canopy + Conifer + Canopy \times Conifer	-52.83	34.58	0.00
Cloud + Humid + Wind	-54.98	38.87	0.00
Humid + LaunchTime + Wind	-56.29	41.50	0.00
Intercept only (NULL)	-60.74	43.95	0.00

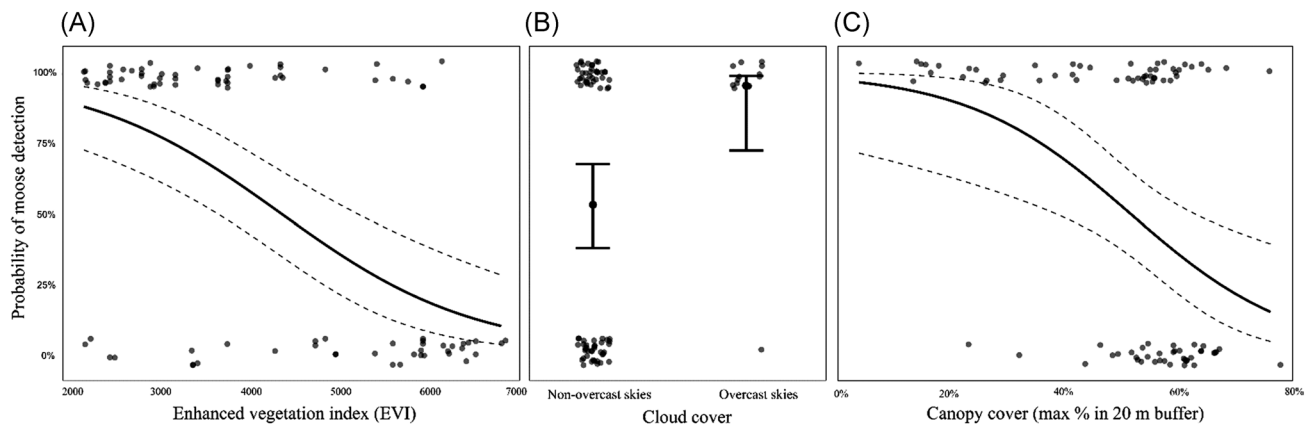


Figure 4. Detection success of GPS-collared adult cow moose in northeastern Minnesota, USA, during spring of 2018 and 2019 using thermal technology mounted on a UAS. Moose detections are plotted as raw values on the y-axis as either 100% (present and detected) or 0% (present but not detected). The predicted mean and 95% confidence intervals are based on the best-supported model for detection. We predicted moose detection for all sampled values of A) the remotely-sensed enhanced vegetation indices (EVI) over the moose's location, B) whether or not the sky was overcast during the flight (field-observation) while holding the other values in the best-supported model at their means, and C) maximum canopy cover around the moose's GPS location during the time of the flight.

the weather station-based data were removed ($n = 82$ flights) resulted in an increased AIC_c of 7.49 compared to the field-based observation cloud cover model; the covariate estimates were again smaller as well (weather station-based cloud cover: $\hat{\beta} = 0.61$, $SE = 0.32$; field observation cloud cover: $\hat{\beta} = 1.17$, $SE = 0.44$).

DISCUSSION

We successfully applied UAS technology and FLIR sensors to detect collared adult cow moose and calves in a heavily forested region of northeastern Minnesota. The increase in detection success from our first to our second field season was a result of developing preliminary relationships between adult moose detection and environmental and temporal covariates. This improvement provides validation that our final detection model (which incorporated both years of flight data) captured useful relationships for researchers planning to conduct ungulate surveys with UAS and FLIR technology. We maximized detection success during our second season by conducting survey flights earlier in the calving season to take advantage of leaf-free conditions. We also concentrated our flight efforts within the early morning hours when temperatures were coolest, and less thermal energy was being emitted from ground objects. Snow cover present in our second season (2019) during the early spring also improved thermal detection by covering ground objects and maximizing the thermal contrast between moose and their environment. Importantly, our research provides a valuable method for determining ungulate reproductive success and calf survival using a less invasive method than handling and collaring calves, which may induce additional stressors (Del Giudice et al. 2015).

Our FLIR-equipped UAS demonstrated clear advantages over conventional methodology for monitoring moose calving success by increasing animal detectability while reducing survey cost and effort. The inclusion of FLIR sensing with UAS was crucial for detecting cow-calf pairs in

forested environments. Moose were often obscured by canopy cover in RGB footage, whereas FLIR footage allowed for easy detection (Fig. 3). Challenges of visual detection without FLIR are also reflected in the state-wide aerial counts conducted by the MNDNR. The MNDNR reported an average estimated detection probability of 61% for their 2018 aerial survey using conventional aircraft and visual observation (Del Giudice 2018), compared to our detection probability of 85% using UAS and FLIR technology. Further, unmanned aerial systems offered a relatively cheap method to collect aerial data (e.g., Vermeulen et al. 2013), and following the initial financial investment for UAS equipment our operating costs were minimal, with ground transportation being our largest field expenditure.

Integrating OBIA methods for detecting wildlife in aerial imagery is a promising approach that can accurately automate detection (Witharana and Lynch 2016, Chabot et al. 2018). Chrétien et al. (2016) applied OBIA to detect ungulates from UAS imagery and reported 100% detection rates in some surveys; this success was accomplished with very high-resolution sensors (Guirado et al. 2017). We employed an economical FLIR sensor with relatively low resolution (640×512), as is common for wildlife research (Witczuk et al. 2018), and experienced challenges using OBIA. Flying the UAS at lower altitudes may have compensated for low resolution but would have increased the potential to disturb moose and have been problematic for terrain avoidance. Dense forest further convoluted the OBIA process because of the many bright returns caused by heated, non-living ground objects among the trees. These objects sometimes resembled moose in brightness and shape (e.g., vegetation would distort the recognizable silhouette of a moose), greatly decreasing the ability of OBIA software to accurately classify objects. Instead, we opted to manually review the video footage, which served to be a simple and efficient way to identify collared moose, and was especially effective for identifying calves present with cows

(distinguishing different sized targets with OBIA adds further complexity). Manual detection required ~16 combined hours per observer over our two seasons, averaging ~10 min per UAS flight for each observer. Until sensors with higher resolution become more economical, or OBIA methods overcome lower resolution limitations, the technical hurdles of implementing OBIA may only be worthwhile for researchers with access to high-resolution sensors and those attempting to detect non-collared animals, especially over large spatial extents.

The accuracy of conventional methodology for monitoring reproduction (e.g., observing calf tracks) can also be questionable (Y. C. Ibrahim, Grand Portage Trust Lands, personal communication). The use of UAS and FLIR sensing enabled us to confirm suspected predation events with greater certainty. While GPS data from collared cows can show movements indicative of predation events, as described by Obermoller et al. (2019), relying solely on this method does not always reliably detect the fate of the calf. For example, after a cow in our study had demonstrated the indicative movements of a predation event, UAS thermal imagery revealed that the calf had survived and was still with the cow after the event. This suggests that repeated UAS flights over collared cows can provide a low-disturbance method to monitor calf survival during the first month of their lives, and again following leaf fall in autumn.

Unmanned aerial systems were less disruptive than typical approaches for monitoring calving success and calf survival. Capturing moose calves and fitting them with GPS or VHF collars is a popular method for examining calf survival (Ballard et al. 1981, Patterson et al. 2013, Severud et al. 2015); however, this approach has an inherent risk of capture-related mortality, with abandonment shown to be the leading cause of capture-induced calf mortality (Livezey 1990). Del Giudice et al. (2015) reported that 18.4% of captured neonate moose were abandoned within 48 hours post capture during an initial study of calf mortality in northeastern Minnesota. Phillips and Alldredge (2000) observed that continued human disturbance of elk from ground approaches during the peak calving season decreased calf-cow ratios in their study population, and it is conceivable that similar impacts may be experienced by moose. Our survey protocols were designed to minimize the chance of UAS-specific moose disturbance, and we gauged levels of disruption by monitoring animal behavior (derived from GPS-collar relocation data) following each flight. We identified one individual cow who made a >1 km movement beginning just 7 min after the UAS was launched. This rate of movement is not unusual for moose (E. Isaac, Grand Portage Trust Lands, personal communication); however, it did not occur with other moose during other flights. Because we approached this site on foot through dense vegetation (for other flights, we limited the noises of our approach by launching from a gravel road accessed by vehicle or from a walking trail), it is possible that our approach, rather than the UAS, ultimately caused the cow to flee the area.

We considered a lack of behavioral response by moose to be evidence of no disturbance from UAS flights, similar to Vermeulen et al. (2013), and Goebel et al. (2015) in their UAS studies of elephants and penguins (*Pygoscelis spp.*), respectively. It is important to keep in mind, however, that disturbance may cause unseen physiological stress in wildlife that do not exhibit any overt behavioral response (Ditmer et al. 2015). Although animals may acclimate to repeated low-altitude UAS flights (Ditmer et al., 2019), we echo the UAS ethical guidelines outlined by Hodgson and Koh (2016) regarding wildlife disturbance: flights should be conducted no lower in altitude than is necessary for data collection and repeat flights over individuals should only be done when it is necessary to collect critical data.

One major challenge of conducting wildlife surveys with FLIR-technology is that solar energy can reduce detection by complicating the identification of target animals. Solar radiation heats the ground and non-target objects (e.g., rocks, stumps, trees), which in turn create noise, or thermal bright spots in an image, leading to potential false-positive detections or masking of target animals (Dunn et al. 2002, Chrétien et al. 2016, Lethbridge et al. 2019). Similar to Millette et al. (2011), who conducted thermal surveys of moose from a manned aircraft, our results for cloud cover and temperature on moose detection demonstrated this phenomenon. Increased cloud cover improved thermal detection probability because clouds blocked some amount of solar energy from reaching objects on the ground, thus maximizing the thermal contrast between moose and their surroundings and reducing the potential for misidentifying a non-moose object as a moose. Localized changes in cloud cover and the resulting thermal heating of ground objects were illustrated by our findings that field-based cloud cover observations explained more variation in detection in our model than weather station-based observations. For example, during preliminary testing of our UAS, thermal imagery collected on different days (clear vs. overcast), but at the same time of day and with similar ambient temperatures (20.0°C and 16.1°C), dramatically altered our ability to visually count the known number of individual bison present (see Fig. 2).

Remotely-sensed data describing forest canopy cover and phenological measures of greenness, such as NDVI or EVI, can greatly enhance UAS operators' understanding of where and when to conduct flights to maximize efficiency in forested environments. Although coniferous cover has been repeatedly shown to limit thermal detection of animals (Garner et al. 1995, Dunn et al. 2002, Potvin and Breton 2005), the impacts of deciduous canopy phenology are less well known. As expected, we found that canopy cover and EVI negatively influenced detection success, since greater closure of deciduous tree canopy and denser green vegetation can block the thermal energy of moose from reaching our FLIR sensor. This was supported by our observation of declining detection success in 2019 as the deciduous tree canopy progressed from leafless towards full leaf-out. Indeed, even when we could detect moose that were partially obscured by vegetation, their thermal image

appeared distorted in both shape and intensity of the heat signature, a phenomenon also reported by Wiggers and Beckerman (1993). Although FLIR technology greatly enhanced our ability to detect moose relative to RGB alone, we still failed to detect moose that were completely obscured by deciduous tree canopy or located within very dense conifer stands.

A limitation to using NASA's MODIS products to assist in planning surveys is the time lag between the median date of the 16-day composite EVI data and when it becomes publicly available (~1 month based on our recent downloads). Using greenness indices from previous years could allow for identifying areas with less vegetative cover (increased detection), but the current lag in data availability is a significant hurdle to successfully incorporating this product into surveys of the same year. Winter and leafless periods of fall and spring clearly yield the greatest potential for successful FLIR detection. The increase in detection success during our second field season was certainly a direct result of our efforts to fly prior to deciduous leaf-out. It is important to remember that our study occurred in a boreal ecosystem near 48° N latitude. Thus, the strong relationships we found in our detection models may only be valid in forested environments and where temperature differentials between target species and ambient temperatures are relatively large (i.e., temperate or cooler environments). When possible, we recommend that researchers conduct test flights with captive animals before initiating extensive studies, to familiarize themselves with the way local vegetation types and structure may hinder detection during field research.

Despite the clear benefits of UAS for wildlife surveys, current regulations still reduce operational efficiency. Although much has improved in the last five years regarding ease of compliance with federal regulations, many of the regulatory hurdles outlined by Vincent et al. (2015) still stand. Most importantly, regulations prohibiting operation beyond visual line of sight (BVLOS) or at night severely limited our ability to efficiently target animals. The BVLOS requirement, which requires the operator to maintain unaided visual contact with the UAS at all times of the flight, was especially burdensome in our forested study area. Likewise, we were prohibited from surveying during the night and early morning before dawn—times when the thermal contrast between wildlife and the ground, as well as other non-living objects, are at their greatest (Mulero-Pázmány et al. 2014, Witczuk et al. 2018). Indeed, Ireland et al. (2019) concluded that conducting white-tailed deer surveys with FLIR-equipped UAS was optimized at night because of maximized thermal contrast. The Federal Aviation Administration can grant waivers to relax some flight restrictions, but approvals are not guaranteed, and the application process can be lengthy and often unrealistic for the temporal demands of field seasons.

Hardware limitations of UAS impact their effectiveness and ease of use for inexperienced UAS pilots and crew. Short battery endurance, as was outlined by Linchant et al. (2015), is one such limitation. Our maximum flight endurance with our payload configuration was ~20 min, which

reduced our survey size and maximum distance the UAS could travel from launch points when visual contact was not an issue. Endurance limitations were not insurmountable for calf monitoring of GPS-collared moose; however, short flight endurance combined with BVLOS restrictions currently limit the potential for UAS to be applied to large-scale population monitoring over extensive forested areas. Manned aircraft still excel in such situations due to greater autonomy.

Weather conditions impacted our ability to operate and successfully detect animals. Precipitation prevented flight operations because of the potential for water damage to equipment (Duffy et al. 2017) and the negative effect on thermal image quality. Burke et al. (2018) described how condensed airborne water droplets, such as fog, will decrease data quality of FLIR imagery due to water vapor readily absorbing longwave radiation (Gordon et al. 2007). Our results from test flights in foggy conditions corroborated this. Heavy winds can impact flight stability and be hazardous for UAS operations in close proximity to trees, thus Weissensteiner et al. (2015) recommended that operations in forested environments only be conducted during calm wind conditions. Flight turbulence also decreased the quality of our thermal data by creating blurred imagery and shaky video footage. Winds greater than 35 km/hr during our study were rare, but these conditions and other inclement weather grounded our flight operations for safety and data quality for ~16% of our attempted field days.

Our reliance on a weather reporting station ~215 km from our flight operations was done to standardize our weather data and was the nearest and most comparable source of historic weather data. However, we recommend a field-based weather meter for future operations to collect measurements at specific flight locations. Field-based meters collect real-time weather conditions, which should be more robust for detection modeling and flight planning than weather station-based data. Findings from our post hoc analysis demonstrated that weather station-based cloud cover data explained less variation in moose detection than our field-based observations due to localized variation in cloud cover. We hypothesized that temperature and relative humidity, which were also collected from the weather station, would be significantly associated with moose detection. However, neither were in our top model; again, potentially due to the different conditions experienced at the flight location versus the weather station.

Our work served to hone UAS methodology for the application of wildlife research. We found that a readily available off-the-shelf UAS equipped with FLIR technology was an effective platform for detecting collared moose and counting and monitoring calves in a densely forested environment. We identified several ongoing environmental challenges and technical limitations, but we also realized significant improvement in detection success from one season to the next. Our efforts to model factors driving moose detectability allowed us to establish best practices for maximizing UAS efficacy with FLIR sensing for surveys of forest-dwelling animals. It is likely that the continued

improvement and reduced costs of UAS (Baxter and Hamilton 2018), and associated sensors, will open new doors to the types of data collection possible and expand on potential target species. We postulate that FLIR sensor-equipped UAS—especially with the capability to collect geo-tagged thermal imagery—could be effective for monitoring reproductive success (e.g., birthing success, twinning rate, and young survival) of other GPS-collared, large-bodied mammals.

ACKNOWLEDGMENTS

We thank the Grand Portage Band of Lake Superior Chippewa for their collaboration on this project. We appreciate Y. C. Ibrahim's support with accessing and managing data on study animals and R. Deschampe Jr.'s technical support in the field. We thank J. Tillery for his assistance as a field technician. We also recognize the University of Minnesota Department of Fisheries, Wildlife, and Conservation Biology for its technical support on this project. Funding was provided by the Minnesota Agricultural Experiment Station (Project# MIN-41-020), the University of Minnesota Graduate School (fellowship support for M. McMahon), and the Environment and Natural Resources Trust Fund as recommended by the Legislative-Citizen Commission on Minnesota Resources. This work could not have been completed without funding from the Great Lakes Restoration Initiative for monitoring moose on the Grand Portage Indian Reservation. We thank A. Rodgers (Associate Editor), A. Knipps (Editorial Assistant), and the anonymous reviewers who provided helpful comments that improved the manuscript.

LITERATURE CITED

- Adams, K. P., P. J. Pekins, K. A. Gustafson, and K. Bontaites. 1997. Evaluation of infrared technology for aerial moose surveys in New Hampshire. *Alces* 33:129–139.
- Addison, R. B. 1972. The possible use of thermal infrared imagery for wildlife census. *Proceedings of the 8th North American Moose Conference and Workshop* 8:301–325.
- Anderson, K., and K. J. Gaston. 2013. Lightweight unmanned aerial vehicles will revolutionize spatial ecology. *Frontiers in Ecology and the Environment* 11:138–146.
- Ballard, W. B., T. H. Spraker, and K. P. Taylor. 1981. Causes of neonatal moose calf mortality in south central Alaska. *Journal of Wildlife Management* 45:335–342.
- Baxter, P. W. J., and G. Hamilton. 2018. Learning to fly: integrating spatial ecology with unmanned aerial vehicle surveys. *Ecosphere* 9.
- Beaver, J. T., R. W. Baldwin, M. Messinger, C. H. Newbolt, S. S. Ditchkoff, and M. R. Silman. 2020. Evaluating the use of drones equipped with thermal sensors as an effective method for estimating wildlife. *Wildlife Society Bulletin* 44:434–443.
- Bennitt, E., H. L. A. Bartlam-Brooks, T. Y. Hubel, and A. M. Wilson. 2019. Terrestrial mammalian wildlife responses to Unmanned Aerial Systems approaches. *Scientific Reports* 9:2142.
- Bernatas, S., and L. Nelson. 2004. Sightability model for California big-horn sheep in canyonlands using forward-looking infrared (FLIR). *Wildlife Society Bulletin* 32:638–647.
- Bontaites, K. M., K. A. Gustafson, and R. Makin. 2000. A Gasaway-type moose survey in New Hampshire using infrared thermal imagery: preliminary results. *Alces* 36:69–75.
- Burke, C., M. Rashman, S. Wich, A. Symons, C. Theron, and S. Longmore. 2018. Optimising observing strategies for monitoring animals using drone-mounted thermal infrared cameras. *International Journal of Remote Sensing* 40:439–467.
- Carstensen, M., E. C. Hildebrand, D. Plattner, M. Dexter, V. St-Louis, C. Jennelle, and R. G. Wright. 2017. Determining cause-specific mortality of adult moose in northeast Minnesota, February 2013–July 2016. Minnesota Department of Natural Resources, Wildlife Health Program. Forest Lake, Minnesota, USA.
- Chabot, D. 2009. Systematic evaluation of a stock unmanned aerial vehicle (UAV) system for small-scale wildlife survey applications. Thesis, McGill University, Montreal, Québec, Canada.
- Chabot, D., and D. M. Bird. 2012. Evaluation of an off-the-shelf unmanned aircraft system for surveying flocks of geese. *Waterbirds* 35:170–174.
- Chabot, D., C. Dillon, and C. M. Francis. 2018. An approach for using off-the-shelf object-based image analysis software to detect and count birds in large volumes of aerial imagery. *Avian Conservation and Ecology* 13:15.
- Chen, S., G. J. McDermid, G. Castilla, and J. Linke. 2017. Measuring vegetation height in linear disturbances in the boreal forest with UAV photogrammetry. *Remote Sensing* 9:1257.
- Chrétien, L., J. Théau, and P. Ménard. 2015. Wildlife multispecies remote sensing using visible and thermal infrared imagery acquired from an unmanned aerial vehicle (UAV). *International Archives of the Photogrammetry, Remote Sensing and Spatial Information Sciences XL-1/W4:241–248*.
- Chrétien, L., J. Théau, and P. Ménard. 2016. Visible and thermal infrared remote sensing for the detection of white-tailed deer using an unmanned aerial system. *Wildlife Society Bulletin* 40:181–191.
- Del Giudice, G. D. 2018. 2018 Aerial moose survey. Minnesota Department of Natural Resources, Forest Wildlife Populations and Research Group. Grand Rapids, Minnesota, USA.
- Del Giudice, G. D., W. J. Severud, T. R. Obermoller, R. G. Wright, T. A. Enright, and V. St-Louis. 2015. Monitoring movement behavior enhances recognition and understanding of capture-induced abandonment of moose neonates. *Journal of Mammalogy* 96:1005–1016.
- Didan, K. 2015. MOD13A2 MODIS/Terra vegetation indices 16-Day L3 global 1km SIN grid V006 [Data set]. NASA EOSDIS Land Processes DAAC. <<https://doi.org/10.5067/MODIS/MOD13A2.006>>. Accessed 3 Jan 2021.
- Ditmer, M. A., J. B. Vincent, L. K. Werden, J. C. Tanner, T. G. Laske, P. A. Iaizzo, D. L. Garshelis, and J. R. Fieberg. 2015. Bears show a physiological but limited behavioral response to unmanned aerial vehicles. *Current Biology* 25:2278–2283.
- Ditmer, M. A., L. K. Werden, J. C. Tanner, J. B. Vincent, P. Callahan, P. A. Iaizzo, T. G. Laske, and D. L. Garshelis. 2019. Bears habituate to the repeated exposure of a novel stimulus, unmanned aircraft systems. *Conservation Physiology* 7:1–7.
- Duffy, J. P., A. M. Cunliffe, L. Debell, C. Sandbrook, S. A. Wich, J. D. Shutler, I. H. Myers-smith, M. R. Varela, and K. Anderson. 2017. Location, location, location: considerations when using lightweight drones in challenging environments. *Remote Sensing in Ecology and Conservation* 4:7–19.
- Dunn, W. C., J. P. Donnelly, and W. J. Krausmann. 2002. Using thermal infrared sensing to count elk in the southwestern United States. *Wildlife Society Bulletin* 30:963–967.
- Ezat, M. A., C. J. Fritsch, and C. T. Downs. 2018. Use of an unmanned aerial vehicle (drone) to survey Nile crocodile populations: a case study at Lake Nyamithi, Ndumo Game Reserve, South Africa. *Biological Conservation* 223:76–81.
- Focardi, S., A. M. De Marinis, M. Rizzotto, and A. Pucci. 2001. Comparative evaluation of thermal infrared imaging and spotlighting to survey wildlife. *Wildlife Society Bulletin* 29:133–139.
- Garner, D. L., H. B. Underwood, and W. F. Porter. 1995. Use of modern infrared thermography for wildlife population surveys. *Environmental Management* 19:233–238.
- Gill, R. M. A., M. L. Thomas, and D. Stocker. 1997. The use of portable thermal imaging for estimating deer population density in forest habitats. *Journal of Applied Ecology* 34:1273–1286.
- Goebel, M. E., W. L. Perryman, J. T. Hinke, D. J. Krause, N. A. Hann, S. Gardner, and D. J. LeRoi. 2015. A small unmanned aerial system for estimating abundance and size of Antarctic predators. *Polar Biology* 38:619–630.
- Gordon, I. E., L. S. Rothman, R. R. Gamache, D. Jacquemart, C. Boone, P. F. Bernath, M. W. Shephard, J. S. Delamere, and S. A. Clough. 2007. Current updates of the water-vapor line list in HITRAN: a new diet for

- air-broadened half-widths. *Journal of Quantitative Spectroscopy and Radiative Transfer* 108:389–402.
- Guirado, E., S. Tabik, D. Alcaraz-Segura, J. Cabello, and F. Herrera. 2017. Deep-learning versus OBIA for scattered shrub detection with Google Earth imagery: ziziphus lotus as case study. *Remote Sensing* 9:1220.
- Haroldson, B. S., E. P. Wiggers, J. Beringer, L. P. Hansen, and J. B. McAninch. 2003. Evaluation of aerial thermal imaging for detecting white-tailed deer in a deciduous forest environment. *Wildlife Society Bulletin* 31:1188–1197.
- Hodgson, A., N. Kelly, and D. Peel. 2013. Unmanned aerial vehicles (UAVs) for surveying marine fauna: a dugong case study. *PLoS ONE* 8:1–15.
- Hodgson, J. C., and L. P. Koh. 2016. Best practice for minimising unmanned aerial vehicle disturbance to wildlife in biological field research. *Current Biology* 26:R404–R405.
- Hodgson, J. C., R. Mott, S. M. Baylis, T. T. Pham, S. Wotherspoon, A. D. Kilpatrick, R. Raja Segaran, I. Reid, A. Terauds, and L. P. Koh. 2018. Drones count wildlife more accurately and precisely than humans. *Methods in Ecology and Evolution* 2018:1–8.
- Ireland, A. W., D. A. Palandro, V. Y. Garas, R. W. Woods, R. A. Davi, J. D. Butler, D. M. Gibbens, and J. S. Gibbens. 2019. Testing unmanned aerial systems for monitoring wildlife at night. *Wildlife Society Bulletin* 43:182–190.
- Israel, M. 2011. A UAV-based roe deer fawn detection system. *International Archives of the Photogrammetry, Remote Sensing and Spatial Information Sciences* 38:51–55.
- Jiménez López, J., and M. Mulero-Pázmány. 2019. Drones for conservation in protected areas: present and future. *Drones* 3:1–23.
- Jones, G. P. IV, L. G., Pearlstine, and H. F. Percival. 2006. An assessment of small unmanned aerial vehicles for wildlife research. *Wildlife Society Bulletin* 34:750–758.
- Kissell, R. E., and S. K. Nimmo. 2011. A technique to estimate white-tailed deer (*Odocoileus virginianus*) density using vertical-looking infrared imagery. *Wildlife Biology* 17:85–92.
- Kiszka, J. J., J. Mourier, K. Gastrich, and M. R. Heithaus. 2016. Using unmanned aerial vehicles (UAVs) to investigate shark and ray densities in a shallow coral lagoon. *Marine Ecology Progress Series* 560:237–242.
- Lethbridge, M., M. Stead, and C. Wells. 2019. Estimating kangaroo density by aerial survey: a comparison of thermal cameras with human observers. *Wildlife Research* 46:639–648.
- Lhoest, S., J. Linchant, S. Quevauvillers, C. Vermeulen, and P. Lejeune. 2015. How many hippos: algorithm for automatic counts of animals with infra-red thermal imagery from UAV. *International Archives of the Photogrammetry, Remote Sensing and Spatial Information Sciences* 40:355–362.
- Linchant, J., G. A. Tech, and F. R. Management. 2015. Are unmanned aircraft systems (UASs) the future of wildlife monitoring? A review of accomplishments and challenges. *Mammal Review* 45:239–252.
- Livezey, K. B. 1990. Toward the reduction of marking-induced abandonment of newborn ungulates. *Wildlife Society Bulletin* 18:193–203.
- Lüdecke, D. 2018. ggeffects: Tidy data frames of marginal effects from regression models. *Journal of Open Source Software* 3:772.
- Marsh, H., and D. F. Sinclair. 1989. Correcting for visibility bias in strip transect aerial surveys of aquatic fauna. *Journal of Wildlife Management* 53:1017–1024.
- Millette, T. L., E. Marciano, and D. Laflower. 2014. Winter distribution of moose at landscape scale in northeastern Vermont: a GIS analysis. *Alces* 50:17–26.
- Millette, T. L., D. Slaymaker, E. Marciano, C. Alexander, and L. Richardson. 2011. Aims-thermal—a thermal and high resolution color camera system integrated with GIS for aerial moose and deer census in northeastern Vermont. *Alces* 47:27–37.
- Minnesota Geospatial Information Office. 2016. Minnesota land cover classification and impervious surface area by landsat and lidar: 2013 update—version 2. <https://gisdata.mn.gov/dataset/base-landcover-minnesota>. Accessed 20 Nov 2019.
- Minnesota Geospatial Information Office. 2018. Phase 3—Arrowhead Region data. http://www.mngeo.state.mn.us/committee/elevation/mn_elev_mapping.html. Accessed 20 Nov 2019.
- Montague, D. M., R. D. Montague, M. L. Fies, and M. J. Kelly. 2017. Using distance-sampling to estimate density of white-tailed deer in forested, mountainous landscapes in Virginia. *Northeast Naturalist* 24:505–519.
- Mulero-Pázmány, M., S. Jenni-Eiermann, N. Strebel, T. Sattler, J. J. Negro, and Z. Tablado. 2017. Unmanned aircraft systems as a new source of disturbance for wildlife: a systematic review. *PLoS ONE* 12:1–14.
- Mulero-Pázmány, M., R. Stolper, L. D. Van Essen, J. J. Negro, and T. Sassen. 2014. Remotely piloted aircraft systems as a rhinoceros anti-poaching tool in Africa. *PLoS One* 9:1–10.
- National Oceanic and Atmospheric Administration [NOAA]. 2019. Climate data online. Local climatological data station details for Cook Municipal Airport, MN, USA. <https://www.ncdc.noaa.gov/data-access/>. Accessed 27 Sep 2019.
- Obermoller, T. R., G. D. Del Giudice, and W. J. Severud. 2019. Maternal behavior indicates survival and cause-specific mortality of moose calves. *Journal of Wildlife Management* 00:1–11.
- Olsoy, P. J., L. A. Shipley, J. L. Rachlow, J. S. Forbey, N. F. Glenn, M. A. Burgess, and D. H. Thornton. 2018. Unmanned aerial systems measure structural habitat features for wildlife across multiple scales. *Methods in Ecology and Evolution* 9:594–604.
- Patterson, B. R., J. F. Benson, K. R. Middel, K. J. Mills, A. Silver, and M. E. Obbard. 2013. Moose calf mortality in central Ontario, Canada. *Journal of Wildlife Management* 77:832–841.
- Phillips, G. E., and A. W. Alldredge. 2000. Reproductive success of elk following disturbance by humans during calving season. *Journal of Wildlife Management* 64:521–530.
- Potvin, F., and L. Breton. 2005. Testing 2 aerial survey techniques on deer in fenced enclosures—visual double-counts and thermal infrared sensing. *Wildlife Society Bulletin* 33:317–325.
- R Core Team. 2019. R: a language and environment for statistical computing. R Foundation for Statistical Computing, Vienna, Austria. <https://www.R-project.org/>
- Sardá-Palamera, F., G. Bota, C. Viñolo, O. Pallarés, V. Sazatornil, L. Brotons, S. Gomáriz, and F. Sardá. 2012. Fine-scale bird monitoring from light unmanned aircraft systems. *Ibis* 154:177–183.
- Sasse, D. B. 2003. Job-related mortality of wildlife workers in the United States, 1937–2000. *Wildlife Society Bulletin* 31:1015–1020.
- Severud, W. J., G. Del Giudice, T. R. Obermoller, T. A. Enright, R. G. Wright, and J. D. Forester. 2015. Using GPS collars to determine parturition and cause-specific mortality of moose calves. *Wildlife Society Bulletin* 39:616–625.
- Severud, W. J., T. R. Obermoller, G. D. Del Giudice, and J. R. Fieberg. 2019. Survival and cause-specific mortality of moose calves in northeastern Minnesota. *Journal of Wildlife Management* 83(5):1131–1142.
- Street, G. M., J. Fieberg, A. R. Rodgers, M. Carstensen, R. Moen, S. A. Moore, S. K. Windels, and J. D. Forester. 2016. Habitat functional response mitigates reduced foraging opportunity: implications for animal fitness and space use. *Landscape Ecology* 31:1939–1953.
- van Andel, A. C., S. A. Wich, C. Boesch, L. P. Koh, M. M. Robbins, J. Kelly, and H. S. Kuehl. 2015. Locating chimpanzee nests and identifying fruiting trees with an unmanned aerial vehicle. *American Journal of Primatology* 77:1122–1134.
- Verma, S. K., M. Carstensen, R. Calero-Bernal, S. A. Moore, T. Jiang, C. Su, and J. P. Dubey. 2016. Seroprevalence, isolation, first genetic characterization of *Toxoplasma gondii*, and possible congenital transmission in wild moose from Minnesota, USA. *Parasitology Research* 115:687–690.
- Vermeulen, C., P. Lejeune, J. Lisein, P. Sawadogo, and P. Bouché. 2013. Unmanned aerial survey of elephants. *PLoS One* 8:e54700.
- Vincent, J. B., L. K. Werden, and M. A. Ditmer. 2015. Barriers to adding UAVs to the ecologist's toolbox. *Ecological Society of America* 13:74–75.
- Watts, A. C., J. H. Perry, S. E. Smith, M. A. Burgess, B. E. Wilkinson, Z. Szantoi, P. G. Ifju, and H. F. Percival. 2010. Small unmanned aircraft systems for low-altitude aerial surveys. *Journal of Wildlife Management* 74:1614–1619.
- Weiskopf, S. R., O. E. Ledee, and L. M. Thompson. 2019. Climate change effects on deer and moose in the midwest. *Journal of Wildlife Management* 83:769–781.
- Weissensteiner, M. H., J. W. Poelstra, and J. B. W. Wolf. 2015. Low-budget ready-to-fly unmanned aerial vehicles: an effective tool for

- evaluating the nesting status of canopy-breeding bird species. *Journal of Avian Biology* 46:425–430.
- Wiggers, E. P., and S. E. Beckerman. 1993. Use of thermal infrared sensing to survey white-tailed deer populations. *Wildlife Society Bulletin* 21:263–268.
- Witczuk, J., S. Pagacz, A. Zmarz, and M. Cypel. 2018. Exploring the feasibility of unmanned aerial vehicles and thermal imaging for ungulate surveys in forests—preliminary results. *International Journal of Remote Sensing* 39:5504–5521.
- Witharana, C., and H. J. Lynch. 2016. An object-based image analysis approach for detecting penguin guano in very high spatial resolution satellite images. *Remote Sensing* 8:375.
- Wünschmann, A., A. G. Armien, E. Butler, M. Schrage, B. Stromberg, J. B. Bender, A. M. Firshman, and M. Carstensen. 2015. Necropsy findings in 62 opportunistically collected free-ranging moose (*Alces alces*) from Minnesota, USA (2003–13). *Journal of Wildlife Diseases* 51:157–165.

Associate Editor: Rodgers.

Technical Report

Department of Computer Science
and Engineering
University of Minnesota
4-192 Keller Hall
200 Union Street SE
Minneapolis, MN 55455-0159 USA

TR 19-008

UAV Landing at an Unknown Location Marked by a Radio Beacon

Nikolaos Stefas, Haluk Bayram, Volkan Isler

July 30, 2019

Revised

UAV Landing at an Unknown Location Marked by a Radio Beacon

Nikolaos Stefas, Haluk Bayram and Volkan Isler
University of Minnesota *

Abstract

We consider the problem of minimizing the time to approach and land near a target radio beacon at an unknown location with an Unmanned Aerial Vehicle (UAV). We show that a cone-like region exists above the target inside of which bearing measurements of a directional antenna lose directionality: signal recordings in all directions yield similar signal strength. We present a geometric model of this region based on antenna simulations and data collected with a real system. Our main contribution is a strategy that takes advantage of a UAV's ability to change altitude and exploits a special structure occurring when approaching the target beacon from above to reduce the flight time required to land near the beacon. We analyze the performance of our strategy and demonstrate through simulations that by exploiting this structure we can achieve shorter flight times than our previous work.

1 Introduction

Landing near the source of radio signal (beacons) with Unmanned Aerial Vehicles (UAVs) has many important applications. In search and rescue applications, beacons can mark the location of an emergency package delivery like rations and medicine [1], defibrillators [2] and flotation devices [3]. In environmental monitoring applications, radio-tagging animals can be used to mark their location [4], [5] and can be a useful wildlife and farm management tool. UAVs equipped with a directional antenna that can track radio beacons are a good fit in such scenarios due to their ability to travel fast, reach difficult to access areas and carry small payloads.

A common technique to locate the area of a target radio beacon using directional antennas is the triangulation of bearing measurements [6, 7, 8]. There are primarily two ways of obtaining bearing measurements (directionality). We can either use a single directional antenna or use omnidirectional, multi-array antennas. In this work we focus on a single directional antenna. Bearing measurements in this case are acquired by rotating the antenna

*This work is supported in part by MnDRIVE, NSF awards #1525045 and #1617718 and MN LCCMR. H. Bayram is also supported by TUBITAK 2232 (#119C008). Stefas and Isler are at the University of Minnesota. Bayram is at Istanbul Medeniyet University. Emails : stefas125@umn.edu, isler@umn.edu, haluk.bayram@medeniyet.edu.tr

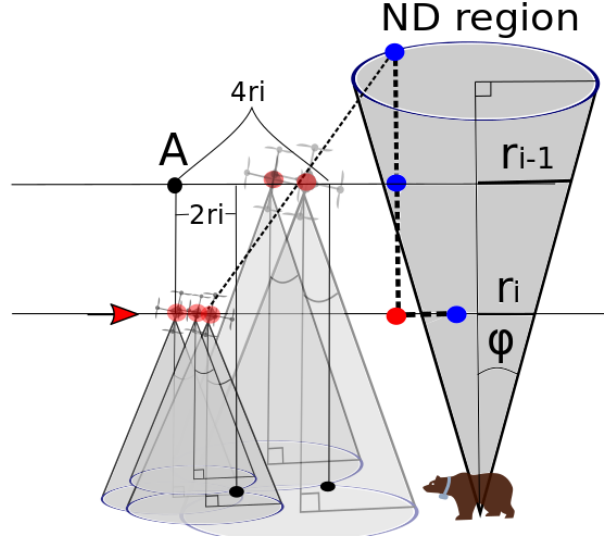


Figure 1: A UAV may be unable to localize a radio beacon with a directional antenna at a high altitude due to the existence of a cone-like region above the target inside of which we lose directionality. We name this region No Directionality (ND) region and present a strategy that utilizes binary measurements to detect it (red if outside, blue if inside). We first detect the ND region by increasing the height and covering an increasing area around the starting location A. Then we reduce the uncertainty area by lowering the height and reducing the size of the ND region so that $r_i < r_{i-1}$ and re-locating it.

in place with a fixed angle step and selecting the direction that recorded the strongest signal [9]. Due to multi-path effects and interference in unknown environments we cannot assume that the signal strength monotonically increases as we approach the beacon and a full rotation is required to normalize the recordings [10]. The duration of a bearing measurement depends on the angle step and the beacon's number of pulses per second. For example, a bearing measurement of angle step 10 deg and a beacon transmitting signals at 0.5 Hz requires over a minute to complete. A UAV able to reach an 18 m/s speed can travel over 1000 m during that time. In many UAV systems the time spent acquiring bearing measurements can be orders of magnitude larger than travel time [11].

In this work we take advantage of a UAV's ability to change altitude and exploit a special structure occurring when approaching the target beacon from above to significantly reduce measurement acquisition time (Figure 1). Many studies have used UAVs with directional antennas in order to determine the area a target beacon lies in [11], [12], [13]. However in most cases the altitude is fixed and the target is not approached from above. Reducing measurement acquisition time has been studied recently in [10] where a directional and omni-directional antennas are used together to remove the need of full rotation bearing measurements for signal strength normalization. However, the authors do not provide any mathematical guarantees for localization time and their approach does not take advantage of a UAV's ability to change altitude. We show that there exists a region above the target inside of which bearing measurements with a directional Yagi antenna lose directionality: signal recordings in all directions yield similar signal strength. We name this region *No Directionality* (ND) region. We also show that we can detect whether a location is inside

the region (binary ND measurement) with only four signal recordings. The authors in [14] mention this region but they explicitly avoid it because their approach can fail when near the region. Using this special structure we provide a strategy for UAVs to land near a target beacon using only one initial bearing measurement and ND measurements.

Our contributions can be summarized as follows:

1. We present a strategy that exploits a special structure occurring when approaching the target beacon from above. Our strategy takes advantage of a UAV's ability to change altitude and utilizes this special structure to reduce the flight time required to land near the beacon.
2. We analyze the strategy performance and show through simulations that in comparison to our previous work it can reduce the time it takes for a UAV to localize and land near the target and validate it on a real system.

2 Problem Statement

Our problem, No Directionality (ND) region-based target landing can be formulated in the following way. We are given an initial measurement angle (bearing) corrupted with an upper bounded noise α and an approximation of the ND region of a stationary signal transmitter as being perceived by the receiver. The goal is for a UAV to land on a target area of radius r^* such that the total (flight) time is minimized:

$$\min_S \text{time}(S) = \frac{1}{\|v\|} \sum_{i=1}^{N-1} \|s_i, s_{i+1}\| + N\tau_m \quad (1)$$

$S = \{s_1, \dots, s_N\}$ is the set of measurement locations, $\|v\|$ is the robot speed which we assume to be constant, $\|s_i, s_{i+1}\|$ is the distance between locations s_i, s_{i+1} and τ_m is the (fixed) time required for taking a single measurement. Since the target beacon is assumed to be stationary, the landing location does not change over time. We also assume that the signal can be sensed at all times, if not we can just search for it.

3 No-Directionality Region Modeling

In this section we model the area around the target beacon based on our antenna radiation field and classify the locations in which we can or cannot obtain reliable directionality measurements. Our antenna operates at the 163 MHz range with a director of 0.84 m length and 0.25 m spacing, an exciter of length 0.88 m and a reflector of 0.93 m length and 0.26 m spacing. Using the Matlab antenna toolbox we obtained the electrical field strength around the antenna for multiple angles corresponding to different locations relative to the target beacon. For each location we obtained the relative field strength by rotating the antenna in place while keeping it horizontal with respect to the ground plane. In Figure 2 we present the electrical field strength for two sample locations. The relative field strength drops as we increase the altitude and it becomes increasingly difficult to determine the direction to the signal source.

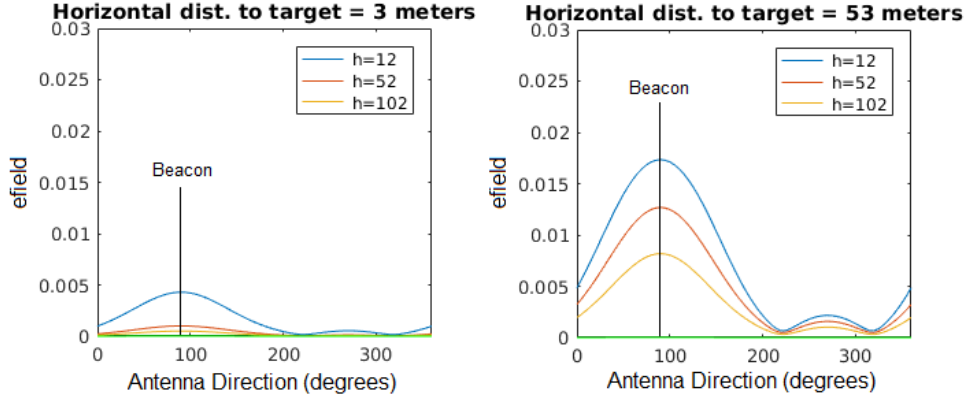


Figure 2: We observe that for a given altitude the normalized ideal signal strength flattens out as we approach the target. The electrical field strength shown is an example from two antenna locations relative to the target beacon for varying altitudes h . We use this observation to detect whether we are close to the target when at a high altitude.

We use this observation and classify locations based on whether direction to the signal source is reliable. In Figure 3 we present the results of this classification for various distances $\in \{1, 3, \dots, 71\}m$ and altitudes $\in \{1, 3, \dots, 109\}m$. For each location we obtain four signal strength values, each with a rotation of 90 deg. A location is labeled “GD” if it provides good directionality, where the difference between maximum and minimum field strength is above $threshold = 0.0054$ chosen empirically based on the real data collection. Otherwise, the location is labeled as “ND” for no directionality. For each location we obtained the results for varying angles between the antenna facing direction and direction to the source $\in \{5, 15, 25, 35, 45\}$ deg. The choice of obtaining four signal strength values results in some of the boundary locations being ambiguous labeled both as ND and GD. We obtain the boundary line(s) by calculating the largest and smallest angles between the target location and these ambiguous boundary locations. The result resembles a cone. We refer to this conic approximation of the ND region as the ND cone with apex angle ϕ . Our modeling concludes that for $SNR = 20$ there is a region (blue) with angle $\phi \in (16.7, 20.3)$ deg inside of which we cannot determine directionality. Furthermore, there exists an ambiguous region (red and blue) with angle $\theta \in (7.1, 15.4)$ deg inside of which the locations can yield both ND and GD measurements.

In order to verify that our ND region modeling is useful we collected data with a real UAV system (described in Section 6). Due to practical limitations we focused on a smaller area and used a larger grid size. The data were collected for distances $\in [9, 25]m$ and altitudes $\in [19, 44]m$. The initial direction between the first recording of each set differed by 40 deg, which yields the highest possible angle difference. The angles calculated using the real data were $\phi = 17.8$ deg, $\theta = 17.4$ deg. These results resemble the noisy simulated case and indicate that our modeling can be of practical use.

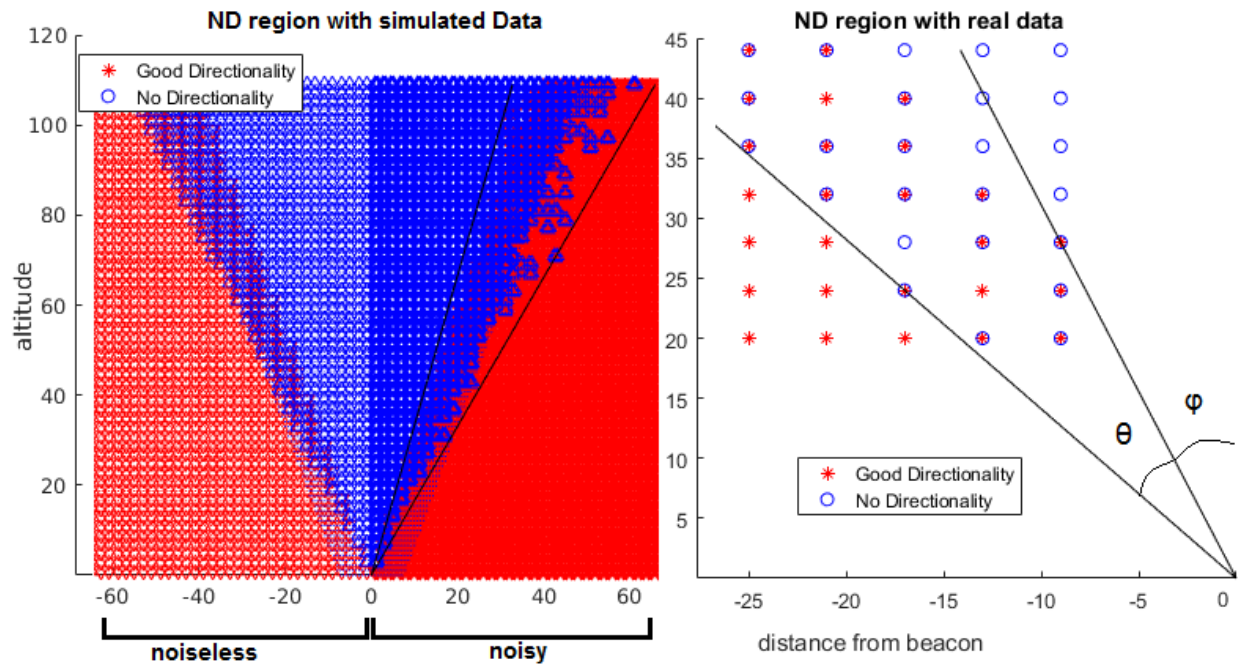


Figure 3: Classifying locations on whether they provide good directional measurements (GD, red) or not (ND, blue) based on expected electrical field strength. The resulting approximation resembles a cone (blue area) of apex angle ϕ . At the boundaries of the cone there exists an ambiguous area of angle θ containing both ND and GD locations. The ND region with simulated data plot represents two cases. First, the noiseless case where $\phi = 20.3$, $\theta = 7.1$ deg. Second, adding white Gaussian noise with $SNR = 20$ results in $\phi = 16.7$, $\theta = 15.4$ deg. The ND region with real data plot was created with data collected with a real UAV system and resulted in $\phi = 17.8$, $\theta = 17.4$ deg.

4 Strategy

The strategy can be seen in Algorithm 1 and relies on the conic approximation of the ND region presented in Section 3. Other than the initial bearing measurement, we only use binary ND measurements that are much faster and can detect whether we are inside the ND region. Taking an ND measurement at height H_i , we can determine whether the target's ground location is within radius $r_i = H_i \tan \phi$ from the measurement ground location.

Our strategy is split into two phases (see Figure 1) : The goal of the first phase is to ensure the ND region is detected. At the beginning of Phase 1 there are two possibilities, either the ND region can be detected at the initial location A or not. If at location A we do not detect the ND region, then we take more ND measurements at locations near A and towards the direction of the initial bearing measurement (blue circles in Figure 4). If the target is not inside the area covered by these measurements, we increase the altitude such that the ND measurement footprint increases and covers a larger area (red circles in Figure 4). This is repeated until the ND region is detected.

The goal of the second phase is to ensure that the radius of the ND region is at most r^* . At the end of Phase 1 we have entered the ND region but its radius at its current height may be larger than r^* . In this case Phase 2 reduces height and follows the boundary of the ND region until its radius reduces to at most r^* . If at any point during Phase 2 we exit the ND region while reducing height, then we re-detect it. Re-detecting the ND region is similar to Phase 1 but since we no longer know its direction, we obtain ND measurements in all directions.

The inputs to Algorithm 1 are desired landing area radius r^* , direction of the initial bearing measurement, initial starting location A , ND cone apex angle ϕ and bearing measurement noise α . In order to provide performance guarantees in terms of task completion we get the competitive ratio with respect to the optimal offline strategy outlined in Section 4.1. The details of the performance analysis for Phase 1 and Phase 2 while $\theta = 0$ is provided in Sections 4.2 and 4.3 and complete proofs are included in the appendix. Then we address the case where $\theta > 0$ in Section 4.4.

Algorithm 1 ND-Region-Landing

Input: r^* , A , ϕ , α , Initial bearing

Output: Landing location s_N

- 1: Call Algorithm 2 to detect the ND region
 - 2: Call Algorithm 3 to reduce ND region radius to r^* and determine the landing location s_N
-

4.1 Lower Bounding the Optimal Offline Strategy

For our analysis we upper bound the cost of the optimal offline algorithm OPT which has access to the target location and use this bound to compute the performance of our strategy with respect to OPT. Let OPT start at location A and have knowledge of the target location C and its corresponding ND region. If A is located outside the ND region then any strategy has to acquire at least one ND measurement to detect the region and determine that it is

inside the desired area of radius r^* and at height H^* . In order to obtain this measurement any strategy has to travel at least $L - r^*$, where $L = \|AC\|$. The total travel cost of OPT is $\leq L - r^*$ which for a constant and normalized travel speed $\|v\| = 1$ is equivalent to total flight time.

4.2 Phase 1: Detect the ND Region

In this section we show that Algorithm 2 is guaranteed to detect the ND region and analyze its performance in Theorem 3. In line 1 we acquire the initial bearing measurement, initialize our travel direction and determine the coverage pattern using Lemma 1. The loop in lines 2-10 doubles the ground and height step sizes and covers the circular sector of the circle centered at A with radius $2r_i$ and angle 2α .

Algorithm 2 Phase 1:ND-Region-Detection

Input: $r_0 = r^*$, $H_0 = \frac{r^*}{\tan \phi}$, A , ϕ , α , Initial bearing
Output: ND region detection location s_i

- 1: Determine the coverage pattern using Lemma 1
- 2: **while** ND region has not been detected **do**
- 3: Double radius r_i and height H_i
- 4: Based on the coverage pattern cover the circular sector of a circle with radius $2r_i$ with angle α
- 5: **end while**

The problem of covering the area of a circle with a number of smaller circles has been studied at [15]:

Lemma 1. *We need at most $q + 1$ circles of radius r to cover a circular sector of radius $2r$ and angle $\leq 30q$ deg, where $q \in \{1, 2, \dots, 6\}$. We need at most seven circles of radius r to cover the entire area of a circle with radius $2r$.*

Using Lemma 1 we can upper bound the cost of each step of the while loop in Algorithm 2 in the following way.

Lemma 2. *Let the approximation of the ND region be a right angular cone with apex angle ϕ and its apex point at C such that at height H_i its cap is a circle with radius $r_i = H_i \tan \phi$. Let the initial bearing measurement location be A outside the ND region, height H_i and upper bounded angle noise $\alpha < 90$ deg. If $AC \leq 2r_i$ then we can get inside the ND region with at most four steps of total length $\leq 8r_i$.*

The proof uses Lemma 1 for covering a 90 deg circular sector (see Appendix 8.1 for details). Now we can upper bound the cost of Algorithm 2.

Theorem 3. *Let the initial bearing measurement location be A outside the ND region, height H_0 and upper bounded angle noise $\alpha < 90$ deg. Let the approximation of the ND region be a right angular cone with apex angle ϕ and its apex point at C such that at height H_i its cap is a circle with radius $r_i = H_i \tan \phi$. Algorithm 2 can detect the ND region with a competitive ratio of $\max \left(\frac{2L(4 + \frac{1}{\tan \phi})}{(L - r^*)}, 4 \log_2 \left(\frac{L}{r^*} \right) \right)$, for $r^* = r_0$ and $L = \|CA\|$.*

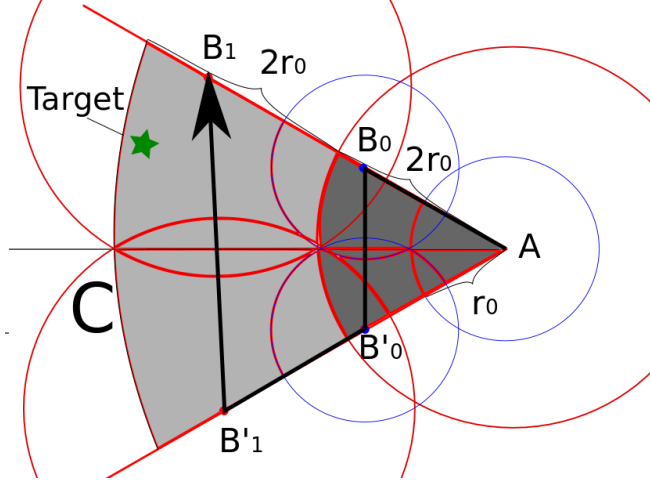


Figure 4: Detecting the ND region when the initial bearing measurement is at location A and height H_0 with bearing measurement upper bounded noise angle $\alpha = \angle B_0AB'_0$. If the target is further away from A than $2r_0$ then the target is inside the black colored area that is the circular sector of the circle centered at A with radius $2r_0$ and angle 2α and we need at most three more ND measurements (blue circles) to cover it. If the target it is not further away than $2^{k+1}r_0$ we increase height until the radius becomes $2^k r_0$.

The proof uses the fact that if the ND region is detected at the k -th iteration then $\|CA\| = L > 2r_{k-1} = 2^k r_0$ and $k \leq \log_2(\frac{L}{r_0})$. The travel distance is upper bounded using Lemma 2 since $8 \sum_{j=0}^k 2^j r_0 + \|H_k\| < r_0 2^k (4 + \frac{1}{\tan \phi})$. Th

4.3 Phase 2: Reduce Area of the ND Region

In this section we show that Algorithm 3 is guaranteed to reduce the ND region radius to r^* and analyze its performance. In line 1 we determine the size of the area that we need to cover and how many circles are required for a complete coverage. We will refer to the number, location and visit order of the circles as a coverage pattern. In lines 2-8 we reduce the altitude and radius of the ND conic region and attempt to detect the ND region again. In lines 4-7 we visit each circle according to the coverage pattern until we detect the ND region again. Once the radius of the ND region drops below the desired we stop and land.

At the end of Algorithm 2 the height is H_k and the last location is ensured to be inside the ND region. The goal of Algorithm 3 is to reduce the radius of the ND region to less than or equal to the desired r^* . We achieve this by lowering the height H_i such that the radius r_i of the ND region at height H_{i-1} is $r_{i-1} = \frac{r_i}{2}$. If we end up outside the ND region at height H_{i-1} then by construction we cannot be further away than $2r_{i-1}$. Since the ND region at height H_{i-1} has radius r_{i-1} we simply need to cover a circle of radius $2r_{i-1}$ with circles of radius r_{i-1} (ND measurement coverage area).

Using Lemma 1 we can upper bound the cost of each iteration of the while loop in Algorithm 3.

Lemma 4. *Let the approximation of the ND region be a right angular cone with apex angle ϕ and its apex point at C such that at height H_i its cap is a circle with radius $r_i = H_i \tan \phi$.*

Let location A be inside the ND region at height H_i . At height $H_{i+1} = \frac{H_i}{2}$ the ND region has radius $r_{i+1} = \frac{r_i}{2}$. If location A at height $\frac{H_i}{2}$ does not lie inside the ND region then we can get inside the ND region with at most six steps (and measurements) of total length $\leq 12r_i$.

The proof is available in Appendix 8.3 and is similar to Lemma 2. Using Lemma 4 we can upper bound the cost of Algorithm 1 as follows.

Theorem 5. *Let the target beacon be at location C , the initial measurement location be A such that $\|CA\| = L$. Let the approximation of the ND region be a right angular cone with apex angle ϕ and its apex point at C such that at height H_k its cap is a circle with radius $r_k = H_k \tan \phi$. Given an initial bearing measurement of upper bounded angle noise $\alpha < 90$ deg Algorithm 1 can land near the target beacon within a circular area of radius r^* with a competitive ratio of $\max(\frac{2L(16+\frac{2}{\tan \phi})}{(L-r^*)}, 9 \log_2(\frac{L}{r^*}))$.*

The proof follows from Theorem 3 and Lemma 4. We note that for a total of m iterations the travel distance is $H_k + \sum_{j=0}^{m-1} \frac{12r_k}{2^j} \leq r_k(12 + \frac{1}{\tan \phi})$.

Algorithm 3 Phase 2:Reduce-ND-Region-Area

Input: r^* , $r_i = r_k$, $H_i = H_k$, ϕ , θ , α

Output: Landing location s_N

- 1: Determine coverage pattern based on ϕ , θ angles
 - 2: **while** $r_i > r^*$ **do**
 - 3: Halve radius r_i and height H_i
 - 4: **repeat**
 - 5: Determine the next measurement location s_j based on the coverage pattern
 - 6: Go to location s_j and take ND measurement m_j
 - 7: **until** $m_j \in$ ND region
 - 8: **end while**
-

4.4 Handling the Ambiguous Region

In this Section we handle the existence of locations at the boundary of the ND region that may result in both good (GD) and bad (ND) directionality measurements (see Section 3). In this case Algorithm 2 may result in an early detection of the ND region. Then Algorithm 3 may miss re-detecting the ND region after reducing the altitude due to the ND region location lying further away than twice the ND region radius (Lemma 4). To address this we increase the radius of the circle we cover in Lemma 1. In other words, we handle these ambiguous locations with a simple modification of the coverage pattern in the first line of Algorithm 3. Due to the difficulty of mathematically determining the smallest number of circles of a fixed radius that cover the area of a circle of an increasing radius [16] we do not handle the general case. We only handle and analyze a few practical cases.

At height H_i the ND region can be detected at most $H_i \tan(\phi + \theta)$ away from the beacon location. This is at most $e_i = H_i \tan(\phi + \theta) - H_i \tan(\phi)$ away from the boundary of the ND cone. If we then halve the height (Algorithm 3) we can be at most $\frac{H_i}{2} \tan(\phi) + e_i = r_{i-1} + e_i$

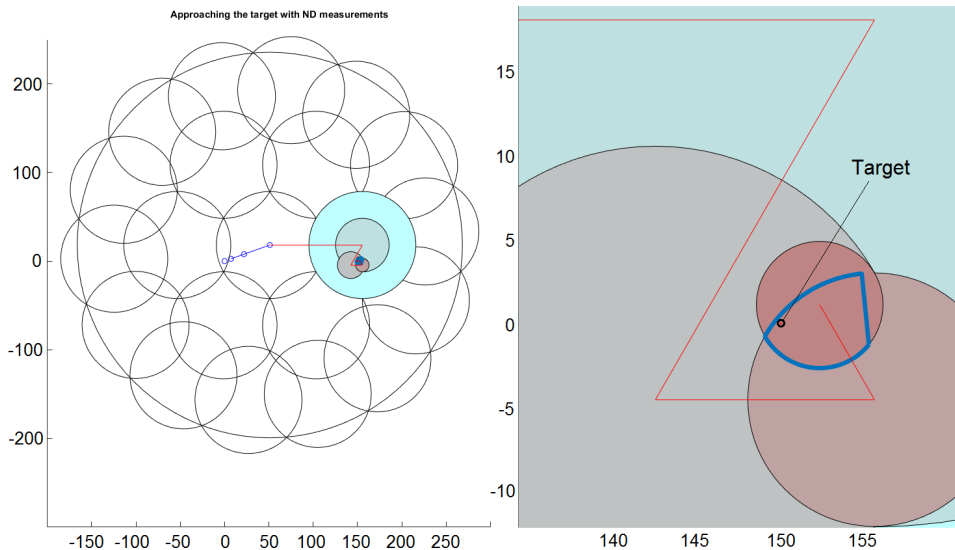


Figure 5: An example of our strategy outlined in Algorithm 1 for $\phi = 15^\circ$ and $\theta = 0$. The desired landing area radius is 3 m and the target beacon is located 150 m away from the starting location. The starting location is at $[0,0]$ with an altitude of 12 m. Phase 1 (blue trajectory) detects the ND region after 4 steps at altitude 450 m. Phase 2 (red trajectory) reduces the ND region area (colored circles) until it achieves a radius of 3 m. The blue bold line is the final area uncertainty.

away from the ND region. Let $ratio = \frac{2(r_i+e_i)}{r_i}$ be the ratio between the large and small circles in the problem of covering the area of a circle with a number of smaller circles. In [17] it is shown that for ratios that are smaller than 2.246, 2.414 and 2.532 we need at most 8, 9 and 10 circles, respectively. Larger ratios are difficult to determine and require numerical evaluation [16]. In our modeling we calculated $ratio = 2$ ($\theta = 0$), $ratio < 2.9$ ($\theta = 10$) and $ratio < 3.7$ ($\theta = 17$). We can evaluate numerically that for $ratio < 2.9$ we need at most 21 circles and for $ratio < 3.3$ we need at most 48 circles. For $ratio < 3.7$ Lemma 4 requires at most 42 additional steps. This results in the cost of each step in Lemma 4 being multiplied by a factor of at most 8.

5 Simulations

In this section we show that **ND-Region-Landing** can provide short flight times when the goal is to localize and land near a target beacon. Since no other strategy considers the concept of no directionality we chose to compare the total flight times achieved by Algorithm 1 against our previously published **Localize-Target-on-Plane** algorithm [11] which chooses the location of bearing measurements during execution so as to localize a radio beacon. In our implementation we used heuristics to improve performance without hurting our theoretical guarantees. We modified Algorithm 3 to keep track of the intersection area of all the measurement locations and avoid taking measurements that do not contain the target. We

also modified Algorithm 2 to take a single ND measurement at a higher altitude that covers the entire area required for each step (we triple the height instead of doubling it). Furthermore, if a measurement lies outside the ND region then it acts as a bearing measurement and we use the resulting area (quadrant) to further reduce the measurement intersection area. In order to achieve the same goal both strategies approach the target after localizing it. Performance evaluation was based on mission time difference over 100 simulations.

We generated 60 sets with varying ND region apex angle $\phi \in \{15, 30, 45, 60\}$ deg, target beacon distance $L \in \{150, 300, 600, 1200, 2400\}m$ and for uniformly distributed measurement bearing noise with varying corruption $\alpha \in \{10, 20, 30\}$ deg. Figure 6 presents how much shorter our strategy is when compared with `Localize-Target-on-Plane` for $r^* = 3$ m. For ambiguous measurement locations that can yield both good and bad directionality we assumed we set $\theta = 0$ (no ambiguity), $\theta = 10$ deg and $\theta = 17$ deg (calculated in Section 3). A location in the ambiguous region has 50% chance to detect the ND region. Our strategy performs better as the initial bearing measurement accuracy increases due to Phase 1 ending closer to the center of the ND region. We also observe a decrease in performance as θ increases, which is expected given the need to cover a larger area in which we need more circles and thus more measurements. An example scenario can be seen in Figure 5. These results show that `ND-Region-Landing` can provide shorter flight times when approaching a target beacon by exploiting the special structure of the ND region and our UAV’s ability to change height and approach the target from above.

6 Field Experiments

We validate our strategy with a real UAV system and radio beacon. The UAV we used was a multi-rotor DJI Matrice 100 with 3.4 kg takeoff weight, about 12 minutes flight time and a maximum travel speed of 22 m/sec. An RTL-SDR (Software Defined Radio) USB signal receiver was connected to a 3-element Yagi antenna that can sense and record the signal emitted by our beacon. Our radio beacon was the ATS F1800 which transmits a pulse approximately once every two seconds. In Section 3 we calculated the ND region angles with the real data to be $\phi = 17.8$ deg, $\theta = 17.4$ deg.

We placed the beacon 75 m away from the UAV and used the implementation in Section 5 to get the measurement locations. The input values were $\alpha = 15$ deg and $r^* = 7$ m which for $\phi + \theta = 34$ deg requires a minimum altitude of 10 m (chosen for safety). The resulting trajectory (chosen for visualization purposes) and measurement locations can be seen in Figure 7. The UAV detected the ND region at the third measurement at an altitude of 100 m. Then the altitude was reduced and the ND region was re-detected until it was reduced to a radius $\leq r^*$. The final measurement and landing location was 2 m away from the beacon.

7 Conclusion and Future Work

In this work we studied the problem of landing near the source of a radio signal (beacons) with UAVs. Our main contribution is a strategy that exploits a special structure occurring when a UAV approaches a target beacon from above to reduce the flight time required to land

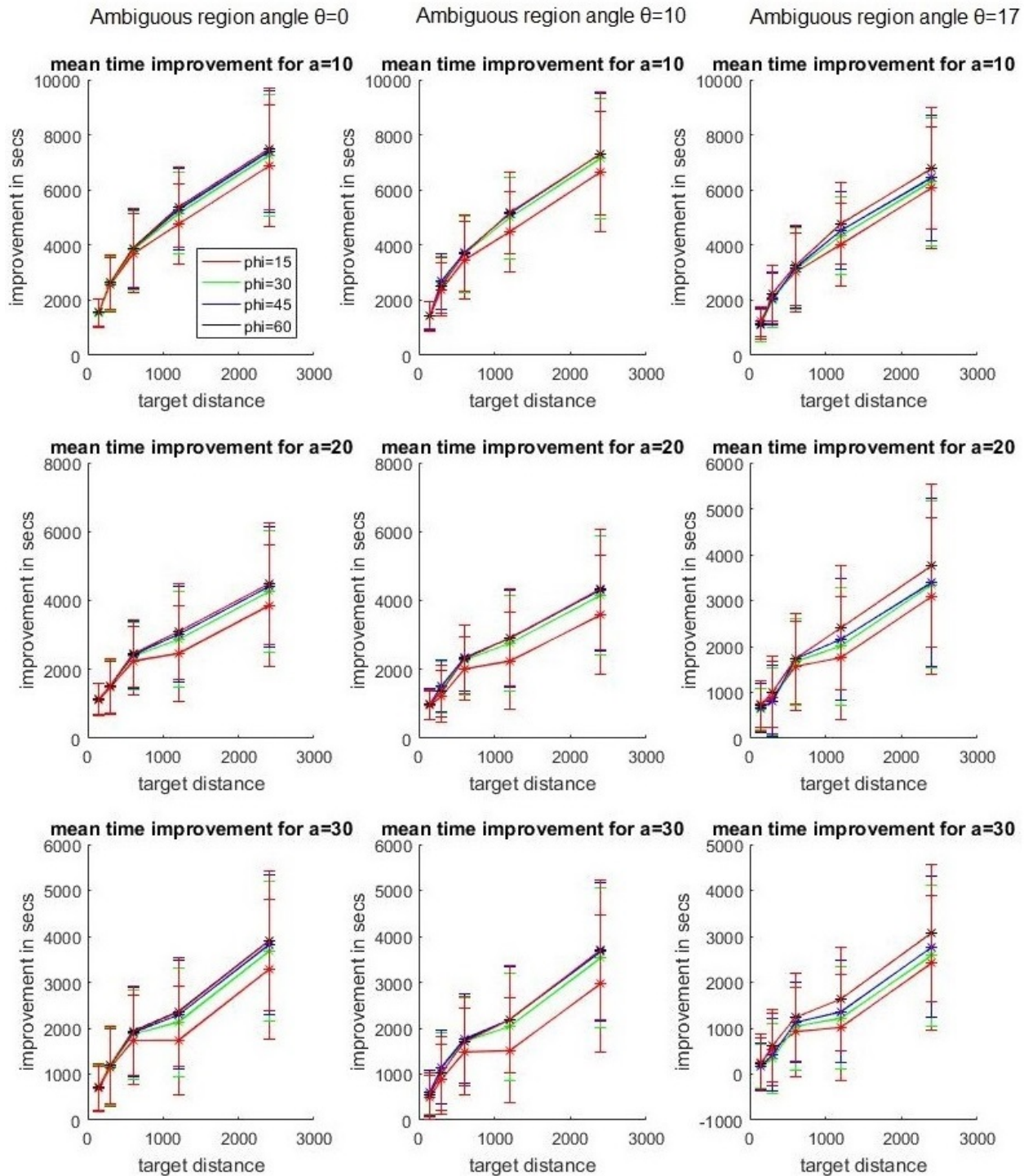


Figure 6: Average mission time improvement of our strategy over Localize-Target-on-Plane [11] for varying ND region apex angle ϕ , target beacon distance L (x-axis), bearing measurement noise α . The ambiguous region has size θ and 50% to produce the ND region.

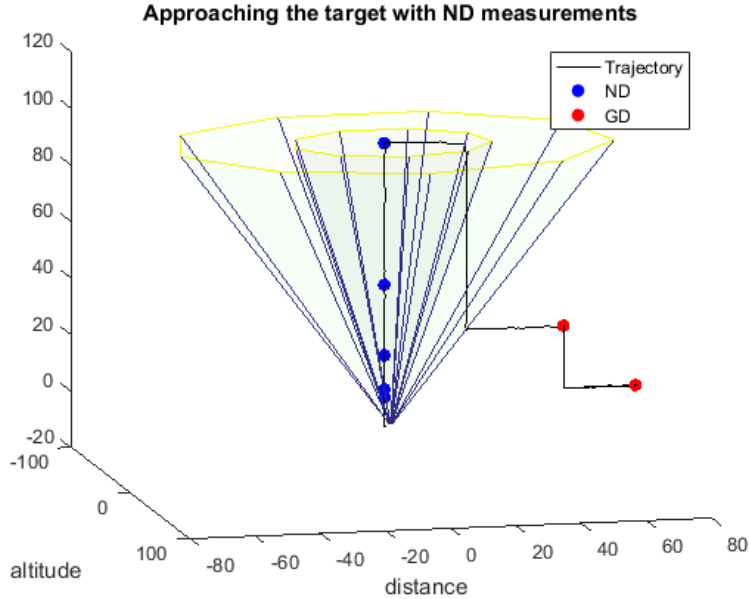


Figure 7: Results from the field experiment for $r^* = 7 \text{ m}$, $\phi = 17.8 \text{ deg}$, $\theta = 17.4$. The conic region represents our conic approximation of the ND region. The measurements outside the ND region are colored red (GD) and the measurements inside the ND region are colored blue (ND). The target beacon was at 75m distance away from the initial location.

near it. This is important because current approaches can fail when attempting to localize a target using bearing measurements at a high altitude due to the existence of a conic region above the target inside of which bearing measurements lose directionality: signal recordings in all directions yield similar signal strength (ND region). This way we can detect whether a location is inside the region and the region ground footprint is guaranteed to contain the target. Then we reduce the uncertainty area by decreasing height and re-locating the region. Through simulations comparison with our previous work we demonstrate that we produce shorter localization times and we validate our strategy with a real UAV system.

For our future work there are many venues we can explore. One of the main assumptions of this work is that the target is stationary. What if the target is dynamic and the ND region can move during the measurement acquisition stage? In such cases it may be more advantageous to obtain more measurements at a higher altitude where the ND region is larger. Depending on the distance between the initial starting location and the beacon location Algorithm 1 can result in an altitude that may be undesirable for a practical implementation. Similarly, the desired uncertainty area may require the UAV to fly at very low altitudes which may, again, not be desirable. We would like to provide alternative strategies that can approach and localize the target while reducing the maximum/minimum altitude that needs to be reached. Finally, we would also like to explore alternative strategies to handle the ambiguous region and improve the competitive ratio which can become large.

References

- [1] M Heutger and M Kückelhaus. Unmanned aerial vehicle in logistics: a dhl perspective on implications and use cases for the logistics industry. *DHL Customer Solutions & Innovation, Troisdorf, Germany*, 2014.
- [2] Alec Momont. Ambulance drone. *Delft University of Technology*, 2016.
- [3] Celia Seguin, Gilles Blaquière, Anderson Loundou, Pierre Michelet, and Thibaut Markarian. Unmanned aerial vehicles (drones) to prevent drowning. *Resuscitation*, 127:63–67, 2018.
- [4] Jarrod C Hodgson, Shane M Baylis, Rowan Mott, Ashley Herrod, and Rohan H Clarke. Precision wildlife monitoring using unmanned aerial vehicles. *Scientific reports*, 6:22574, 2016.
- [5] Matthew Dunbabin and Lino Marques. Robots for environmental monitoring: Significant advancements and applications. *IEEE Robotics & Automation Magazine*, 19(1):24–39, 2012.
- [6] Pratap Tokekar, Joshua Vander Hook, and Volkan Isler. Active target localization for bearing based robotic telemetry. In *Intelligent Robots and Systems (IROS), 2011 IEEE/RSJ International Conference on*, pages 488–493. IEEE, 2011.
- [7] Haluk Bayram, Joshua Vander Hook, and Volkan Isler. Gathering bearing data for target localization. *IEEE Robotics and Automation Letters*, 1(1):369–374, 2016.
- [8] L David Mech. *Handbook of animal radio-tracking*. U of Minnesota Press, 1983.
- [9] Kurt VonEhr, Seth Hilaski, Bruce E Dunne, and Jeffrey Ward. Software defined radio for direction-finding in uav wildlife tracking. In *Electro Information Technology (EIT), 2016 IEEE International Conference on*, pages 0464–0469. IEEE, 2016.
- [10] Louis Dressel and Mykel J Kochenderfer. Pseudo-bearing measurements for improved localization of radio sources with multirotor uavs. In *2018 IEEE International Conference on Robotics and Automation (ICRA)*, pages 6560–6565. IEEE, 2018.
- [11] Haluk Bayram, Nikolaos Stefas, and Volkan Isler. Aerial radio-based telemetry for tracking wildlife. In *2018 IEEE/RSJ International Conference on Intelligent Robots and Systems (IROS)*, pages 4723–4728. IEEE, 2018.
- [12] Oliver M Cliff, Robert Fitch, Salah Sukkarieh, Debbie Saunders, and Robert Heinsohn. Online localization of radio-tagged wildlife with an autonomous aerial robot system. In *Robotics: Science and Systems*, 2015.
- [13] Haluk Bayram, Nikolaos Stefas, Kazim Selim Engin, and Volkan Isler. Tracking wildlife with multiple uavs: System design, safety and field experiments. In *Multi-Robot and Multi-Agent Systems (MRS), 2017 International Symposium on*, pages 97–103. IEEE, 2017.

- [14] Adrien Perkins, Louis Dressel, Sherman Lo, and Per Enge. Antenna characterization for uav based gps jammer localization. In *Proceedings of the 28th International Technical Meeting of The Satellite Division of the Institute of Navigation (ION GNSS+ 2015)*, 2015.
- [15] Richard Kershner. The number of circles covering a set. *American Journal of mathematics*, 61(3):665–671, 1939.
- [16] CT Zahn and CT Zahn. *Black box maximization of circular coverage*. US Department of Commerce, National Institute of Standards and Technology, 1962.
- [17] Hans Melissen. Loosest circle coverings of an equilateral triangle. *Mathematics Magazine*, 70(2):118–124, 1997.

8 Appendix

8.1 Proof of Lemma 2

Proof. From Lemma 1 we need at most 4 circles of radius r_i to cover the entire sector area of a circle with radius $2r_i$ and angle $\alpha < 90$ deg. But note that at the previous step $i - 1$ we have already covered the area that is covered by the circle center at A and we do not need to cover it again. Thus we only need 3 circles of radius r_i to cover the remaining sector area. Thus, if the center of the ND region is not further away than $2r_i$ visiting the centers of all 3 circles guarantees that we visit at least one point of the ND region. Traveling to the center of each circle requires less than $2r_i$ distance since the circles overlap. Thus, we require at most 3 measurements and 4 steps each of length $\leq 2r_i$ for a total length of $8r_i$. \square

8.2 Proof of Theorem 3

Proof. Let the ND region be detected at the k-th step. In order to bound the number of steps k note that detecting the ND region at the k-th step means that $\|CA\| = L > 2r_{k-1} = 2^k r_0$ which implies that $k \leq \log_2(\frac{L}{r_0})$. Thus, during Phase 1 we take at most $3k \leq 4 \log_2(\frac{L}{r_0})$ ND measurements. Using Lemma 2 Phase 1 travels at most $8 \sum_{j=0}^k 2^j r_0 + \|H_k\| = 8r_0(2^{k-1} - 1) + \frac{2^k r_0}{\tan \phi} < r_0 2^k (4 + \frac{1}{\tan \phi}) < 2L(4 + \frac{1}{\tan \phi})$. Since the optimal strategy OPT takes at least one measurement and travel $L - r^*$ (see Section 4.1) the competitive ratio (in terms of travel distance and number of measurements) is $\max\left(\frac{2L(4 + \frac{1}{\tan \phi})}{L - r^*}, 3 \log_2(\frac{L}{r^*})\right)$ for $r^* = r_0$. \square

8.3 Proof of Lemma 4

Proof. We define a circle C' centered at A with radius $2r_i$. From Lemma 1 we need at most 7 “small” circles of radius r_i to cover the entire area of a circle with radius $2r_i$. By construction, the ND region cannot be further away than r_i and thus C' contains the center of the ND region. Thus, visiting the centers of all 7 “small” circles guarantees that we visit at least one point of the ND region. The centers of the 6 perimeter “small” circles yield a

hexagon that is inscribed inside the center circle. The length of each side of this hexagon is less than the length of the side of the hexagon inscribed on C' (with radius $2r_i$) which is $4r_i \sin(30^\circ)$. \square

8.4 Proof of Theorem 5

Proof. Lemma 4 gives us the cost of each step and for a total of m steps we travel a total travel distance of $H_k + \sum_{j=0}^{m-1} \frac{12r_k}{2^j} \leq H_k + 12r_k = r_k(12 + \frac{1}{\tan \phi}) \leq 2L(12 + \frac{1}{\tan \phi})$. The analysis for the number of ND measurements follows from Theorem 3 and Lemma 4 and results in $6k \leq 6 \log_2(\frac{L}{r^*})$. Thus the competitive ratio for this strategy is $\max(\frac{2L(16 + \frac{2}{\tan \phi})}{L - r^*}, 9 \log_2(\frac{L}{r^*}))$, where $r_0 = r^*$. \square



Approximation algorithms for tours of orientation-varying view cones

The International Journal of
Robotics Research
2020, Vol. 39(4) 389–401
© The Author(s) 2020
Article reuse guidelines:
sagepub.com/journals-permissions
DOI: 10.1177/0278364919893455
journals.sagepub.com/home/ijr


Nikolaos Stefas , Patrick A Plonski  and Volkan Isler

Abstract

This article considers the problem of finding a shortest tour to visit viewing sets of points on a plane. Each viewing set is represented as an inverted view cone with apex angle α and height h . The apex of each cone is restricted to lie on the ground plane. Its orientation angle (tilt) ϵ is the angle difference between the cone bisector and the ground plane normal. This is a novel variant of the 3D Traveling Salesman Problem with Neighborhoods (TSPN) called Cone-TSPN. One application of Cone-TSPN is to compute a trajectory to observe a given set of locations with a camera: for each location, we can generate a set of cones whose apex and orientation angles α and ϵ correspond to the camera's field of view and tilt. The height of each cone h corresponds to the desired resolution. Recently, Plonski and Isler presented an approximation algorithm for Cone-TSPN for the case where all cones have a uniform orientation angle of $\epsilon = 0$. We study a new variant of Cone-TSPN where we relax this constraint and allow the cones to have non-uniform orientations. We call this problem Tilted Cone-TSPN and present a polynomial-time approximation algorithm with ratio $O\left(\frac{1 + \tan \alpha}{1 - \tan \epsilon \tan \alpha} \left(1 + \log \frac{\max(H)}{\min(H)}\right)\right)$, where H is the set of all cone heights. We demonstrate through simulations that our algorithm can be implemented in a practical way and that by exploiting the structure of the cones we can achieve shorter tours. Finally, we present experimental results from various agriculture applications that show the benefit of considering view angles for path planning.

Keywords

Path planning, view planning, approximation algorithms, geometric algorithms, euclidean traveling salesman problem, traveling salesman problem with neighborhoods

1. Introduction

Consider the task of an aerial vehicle charged with collecting images of a given set of locations. Such tasks arise in many applications such as crop monitoring, animal tracking, and road inspection. In this article, we study a novel coverage problem inspired by this scenario. We associate each measurement with an inverted cone apexed at the location of interest. The height of the cone is associated with the desired resolution and the apex angle corresponds to the camera's field of view (FOV). In other words, each cone encodes the set of view points from which a target can be imaged at a desired location. See Figure 1. The task is to visit a given set of cones so as to ensure that all locations are covered.

Coverage is a fundamental problem in robotics and has been studied extensively (Choset, 2001; Galceran and Carreras, 2013). A coverage tree structure was proposed in Sadat et al. (2014) allowing for online, non-uniform adaptive coverage with an unmanned aerial vehicle (UAV). However, this strategy cannot provide any guarantees on the trajectory length which coupled with the UAV's limited battery might result in an incomplete tour. The work of

Cheng et al. (2008) provides a constant factor solution for a UAV covering an urban building with a camera sensor. In contrast to our work, the orientation angle of the camera was fixed to look downwards. Complete coverage of a tree surface using right angular cones was used by Stfas et al. (2016) for a UAV flying at a low altitude inside an orchard. However, non-uniform tilt angle views were not considered. A sampling-based methodology to generate trajectories for coverage of 3D objects with unmanned underwater vehicles was presented by Englot and Hover (2013). Similar to our work, the authors achieved short trajectories and applied their method to underwater ship hull inspection. More recently, informative path planning problems in which mobile robots aim to maximize an objective function

University of Minnesota, Minneapolis, MN, USA

Corresponding author:

Nikolaos Stfas, Department of Computer Science and Engineering,
University of Minnesota, 200 Union Street SE, Minneapolis, MN 55455,
USA.

Email: stefal25@umn.edu

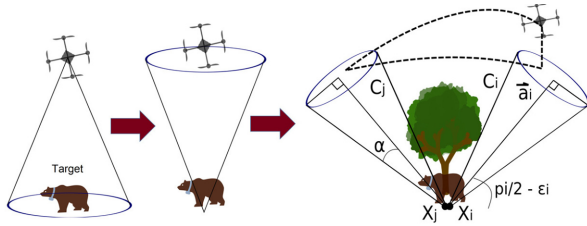


Fig. 1. In order for a UAV to capture images of a target animal it needs to enter an inverted view cone C_i , positioned at X_i with orientation vector \vec{a}_i and apex angle $\alpha \leq \frac{\text{cameraFOV}}{2}$. The height h_i of the cone is relative to the desired resolution. If visibility is occluded, the view cone C_i may need to be tilted by an angle ϵ_i .

related to information gain were studied by Singh et al. (2009) and Low et al. (2008). When the locations to be covered are known ahead of time, we can compute an optimal trajectory to visit them.

The basic task of visiting a given set of locations is the Traveling Salesman Problem (TSP) which admits a polynomial-time approximation scheme (PTAS) for the Euclidean version (Arora, 1998; Mitchell, 1999). If we incorporate sensor footprint as a set of given areas instead of points we wish to visit, then we have the Traveling Salesman Problem with Neighborhoods (TSPN), which is APX-hard (de Berg et al., 2005; Safra and Schwartz, 2006). TSPN in two dimensions is a well-studied problem and many researchers have provided approximation algorithms for various cases (Reinelt, 1994). Euclidean TSPN has been shown to admit a PTAS if the neighborhoods have a well-defined structure (Dumitrescu and Mitchell, 2001; Mitchell, 2007). A constant factor approximation was shown in Dumitrescu and Tóth (2015) for arbitrary, planar disks. TSPN in three dimensions is a more difficult problem. A PTAS was provided by Bodlaender et al. (2009) for disjoint polygons of comparable size and a quasipolynomial-time approximation scheme (QPTAS) was provided by Chan and Elbassioni (2011) for α -fat, weakly disjoint neighborhoods. Dumitrescu and Tóth (2016) presented a constant factor approximation when the neighborhoods take the form of unit balls, lines, or planes. Recently, in Plonski and Isler (2019), we presented a polynomial-time approximation algorithm for the 3D TSPN with intersecting neighborhoods when the neighborhoods take the form of right angular (non-tilted) cones and their apex points lie on a planar surface. We called this problem Cone-TSPN. Our approach was based on the idea that by intersecting the cones with a set of horizontal planes we can reduce the problem to that of equal size disks on the plane with a number of upper bounded detours. There are instances when it is desirable to have tilted cones. For example, carefully chosen tilted views might be required if visibility of the target area is limited (see Figure 1) or when covering reflective surfaces (see Figure 2). In Section 2, we demonstrate with quantitative results that in such cases we can obtain more visual information (i.e., better views) if we introduce cones with different tilt angles. We address this problem in this article.

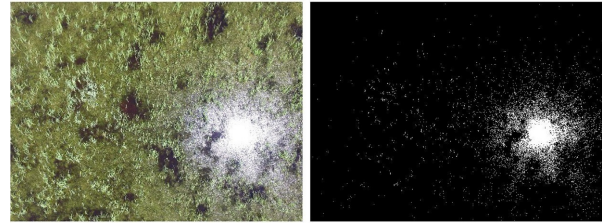


Fig. 2. When covering watery fields such as wild rice (left image), sunlight reflection can be a problem (right image). By choosing our view angles carefully we can reduce sunlight specularities.

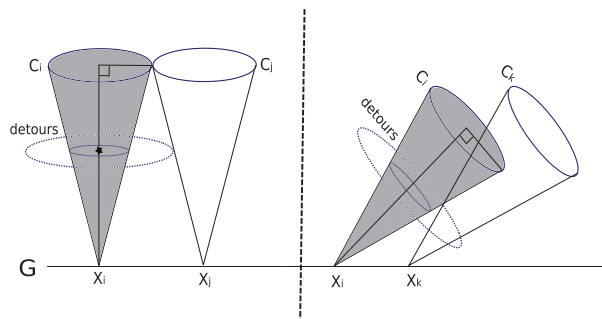


Fig. 3. When using the non-Tilted Cone-TSPN strategy we plan two detours, an inner and outer concentric circular path to ensure all cones that intersect cone C_i are visited. This is illustrated with cones C_i and C_j (left). However, if cone C_i tilts, these two detours can no longer guarantee that all cones intersecting it will be visited because the relative arrangement of the cones can change. This is illustrated with cones C_i and C_k (right). Cone C_k can be placed such that it intersects cone C_i but lies in between the two previously planned detours and is not covered by them.

The Cone-TSPN strategy presented in Plonski and Isler (2019) is not directly applicable for input view cones of varying orientation (or tilt) and cannot provide theoretical guarantees. Removing the assumption that the cones are right angular (not tilted) requires addressing a number of challenges. When the cones are allowed to tilt, their intersection with a horizontal plane is no longer a disk but an ellipse. This means that we can no longer use a PTAS TSPN tour for disks to visit the cones on the plane. Instead, we use a PTAS TSP on their center and bound the length of this tour with respect to the optimal solution. More importantly, the relative arrangement of the cones change as they tilt and the previously planned detours cannot guarantee complete coverage of all cones (see Figure 3 for an example). We need to modify and possibly add additional detours (see Section 6 for details). These challenges arise when the cones have uniform orientation angles. The problem becomes even more challenging if we let the cones have non-uniform orientation angles. We address this challenge by grouping the cones by similar angles and further modifying the detour strategy to guarantee coverage of all cones in the same group (see Section 7). In this work, we

extend Cone-TSPN and provide a polynomial-time approximation algorithm for tilted input view cones.

The rest of the article is organized in the following way. The problem statement is presented in Section 3. Our analysis starts with disjoint cones of similar height and identical (uniform) orientation in Section 4. Then, we study the cases where the cones do not have similar heights in Section 5 and are not disjoint in Section 6. We conclude our analysis with non-disjoint cones with varying (non-uniform) orientation in Section 7 and evaluate the performance of our algorithm in Section 8. Complete proofs for the analyses of Sections 4, 5, 6, and 7 are included in the appendix. Finally, in Section 2, we show our quantitative results for two different agriculture applications with different view angles and discuss future work in Section 9.

We conclude this section with a summary of our contributions.

1. We present a polynomial-time approximation algorithm that solves the Cone-TSPN problem for input view cones of varying orientation (or tilt).
2. We provide an implementation and a detailed analysis of its performance.
3. We demonstrate that tilted cone views are useful in different agriculture applications for which top-down views (non-tilted cones) may not be sufficient.

2. Motivating field applications

Currently, most applications that perform visual coverage of an area with a UAV are restricted to right angle (non-tilted), uniform, top-down views. However, this can result in significant loss of information. To demonstrate this we consider two different scenarios. First, we consider the problem of visual coverage of reflective surfaces. We demonstrate that by choosing our angle views carefully we can reduce sunlight specularities. Second, we consider the problem of visual inspection of a target in difficult to see areas. We show a scenario where tilted view angles can successfully obtain visual information of a target object or area even if it lies below another object blocking the top-down views (e.g. bridges, trees).

2.1. Reflective surface coverage

We performed a set of experiments that verify our claim that coverage of reflective areas requires tilted view cones to avoid direct sunlight reflection. We covered a 30×30 m² area over a lake at an altitude of 10 m with three different view angles. We will refer to the view angle with the least amount of sunlight reflection in the camera as the best view angle. Similarly, the worst view angle is that with the greatest amount of sunlight reflection. Using the 0°, non-tilted views as baseline (top-down views), we compared the amount of sunlight in the images using pixel intensities for over 1,000 images (see Figure 4).

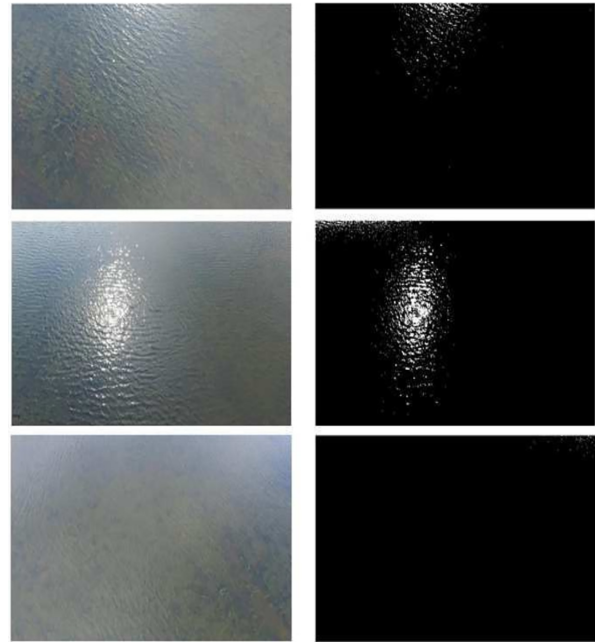


Fig. 4. Reducing sunlight specularities in images using tilted view cones. We covered a lake area with a UAV taking images (left column) and used pixel intensities to quantify the amount of sunlight on the images (right column). The top-down views were used as a baseline (top row). The worst view angles had 671.75% more sunlight than the top-down views (middle row). The best view angles had 81.57% less sunlight than the top-down views (bottom row).

At the time of the experiments, the Sun polar angle was 35° and the Sun azimuthal angle was 250° (from the magnetic north). By using the law of reflection, we calculated the Sun angles and identified that the best view angle was the one with a polar angle of 55° and azimuthal angle of 70°. The worst view angle had a polar angle of 55° and azimuthal angle of 250°. By covering the area with the best view angles, the average amount of sunlight specularities in the images was reduced by 81.57%. However, coverage with the worst view angles increased the average amount of sunlight specularities in the images by 671.75%. These results validate our claim that we can reduce sunlight specularities when covering reflective surfaces by choosing our coverage views carefully.

2.2. Visual inspection of a target

We performed a set of experiments to verify our claim that tilted view cones can provide more visual information of a target object if its occluded by other objects and visibility is limited. During this set of experiments we chose a red ball as our target object under a tree cluster that blocks visibility. The tree cluster could fit on a cylinder of about 20 m in diameter and 25 m in height. We generated two coverage plans. The first was top-down view coverage. The second was tilted view coverage. The center of the cluster on the ground

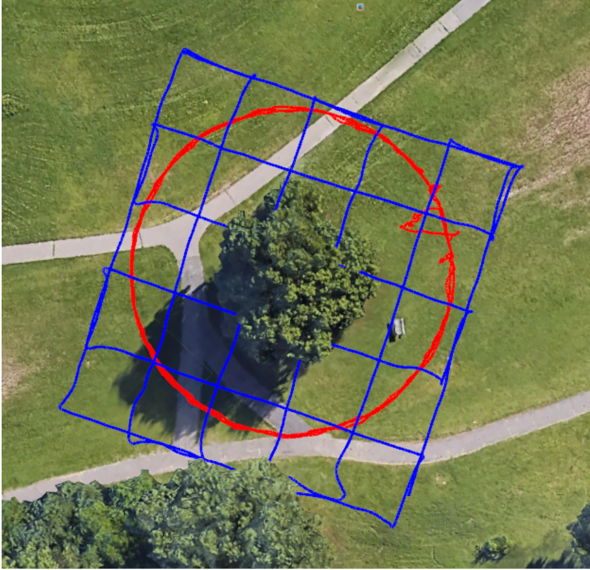


Fig. 5. GPS trajectories of the two coverage plans. Top-down coverage was performed with a double grid (blue) with 50 m edges and at 25 m altitude. Tilted coverage was performed with a circular pattern at radius 12.5 m, altitude of 12.5 m, and camera tilt of 60° .

was chosen as the reference point for both coverage plans. In order to quantify how much visual information we obtain, we placed a red ball of 1 m diameter at the center of the cluster and counted the number of views that detected it.

Top-down views were acquired with a square double grid coverage pattern. The altitude chosen was 25 m to avoid hitting the tree (see Figure 5). Our camera had a 90° FOV and at an altitude of 25 m the square grids edge was about 50 m. Pixel resolution was $3,000 \times 3,000$ and, thus, we cover 1 m^2 with 60^2 pixels (the ball area). We chose an overlap of 80% and for each 50 m line we took 10 images every for a total of 120 images. For every image acquired we performed simple color segmentation to detect the red ball and counted the number of pixels. If we counted more than 1,500 pixels (equivalent to seeing over 41% of the ball) in a single image, we successfully detected the red ball. Out of all the images acquired with the top-down view coverage plan the red ball was present in only 1 (see Figure 6). It is worth noting that in both views the ball was not fully visible.

Tilted views were acquired uniformly on a circle around the tree with a tilt of 60° . For a camera tilt of 60° and a distance of 25 m (with respect to the red ball) altitude was chosen to be 12.5 m. Similarly, the radius of the circle pattern was 12.5 m. We chose an 87.5% overlap (with respect to the bounding circle) and acquired 32 views uniformly. Using the same procedure as before, we detected the red ball in five images acquired from the tilted view coverage plan (see Figure 6). The ball was almost fully visible in two of the images. These results validate our claim that we can obtain more visual information in certain scenarios when using tilted side views.

3. Problem statement

Our problem, Tilted Cone-TSPN, can be formulated in the following way. We are given $C = (C_1, \dots, C_n)$, $\vec{A} = (\vec{a}_1, \dots, \vec{a}_n)$, $X = (X_1, \dots, X_n)$, $H = (h_1, \dots, h_n)$ where C is a set of cones C_1, \dots, C_n with fixed apex angle α . Cone C_i has apex point X_i on the ground plane G with normal \vec{n} and orientation vector \vec{a}_i of length h_i such that $\vec{n} \angle \vec{a}_i = \epsilon_i$. The goal is to compute a minimum length trajectory T which intersects all cones in C (see Figure 7).

We present a strategy called Orientation-Visit (Algorithm 5), which has an approximation factor

$$O\left(\frac{1 + \tan \alpha}{1 - \tan \epsilon \tan \alpha} \left(1 + \log \frac{\max(H)}{\min(H)}\right)\right) \quad (1)$$

with $|\epsilon| + |\alpha| < \frac{\pi}{2}$, which means that the cones (and by extension the UAV) do not touch the ground.

The tangent terms in Equation (1) behave well in practical situations. A camera has usually around $\frac{\pi}{2}$ FOV, which translates to $\alpha \leq \frac{\pi}{4}$ and $\tan \alpha \leq 1$. If we set $\epsilon = \alpha - \frac{\pi}{30}$, which means that the view cones will almost touch the ground, we have $\tan \epsilon \leq 0.9$ and, thus, $\frac{1 + \tan \alpha}{1 - \tan \epsilon \tan \alpha} \leq 20$. Note that if we have non-uniform orientations $\epsilon = \arg \max_{a_i} \vec{n} \angle \vec{a}_i$.

4. Disjoint cones of similar height and identical orientation

In this section, we present the strategy for the case where the cones are disjoint, have similar heights, and identical orientation. We first present a method to obtain upper and lower bounds of the swept area of a tour using conic volumes. These bounds help us remove dependence on the number of cones when computing the performance of our strategy. The strategy is outlined in Algorithm 1. Tilted Slice-Visit solves Tilted Cone-TSPN for disjoint cones of similar height and identical orientation angle ϵ by fixing a coverage plane P_{h_i} at height h_i and visiting the cone bisectors on that plane with a TSP tour. Finally, if the optimal tour T^* achieves maximum height h^* , we assume that there exists an estimate height \hat{h} in the direction of the cone orientation vector \hat{a} such that $h^* \leq \hat{h} \leq 2h^*$ (its existence is proven in Plonski and Isler (2019)).

Lemma 1. *Let the optimal tour T^* have length L^* and maximum height h^* . Let its projection onto plane G with normal \vec{n} be T_G^* . For maximum cone height h_{max} and an estimate height \hat{h} such that $\hat{h} \geq h_{max}$, $\hat{h} \leq 2h^*$, the Minkowski sum sweep volume $f(T_G^*, \hat{h})$ of a cone C with apex and orientation angles α and ϵ such that $|\epsilon| + \alpha \in (0, \frac{\pi}{2})$ traveling along T is upper bounded by $f(T_G^*, \hat{h}) \leq L^* \hat{h}^2 \tan \alpha (1 + \frac{5\pi}{6} \tan \alpha)$.*

Proof. The volume swept by a cone C with apex angle α , orientation angle ϵ , and height h along a path of length $L_G^* \in G$ can be split into three parts (see Figure 8). First,

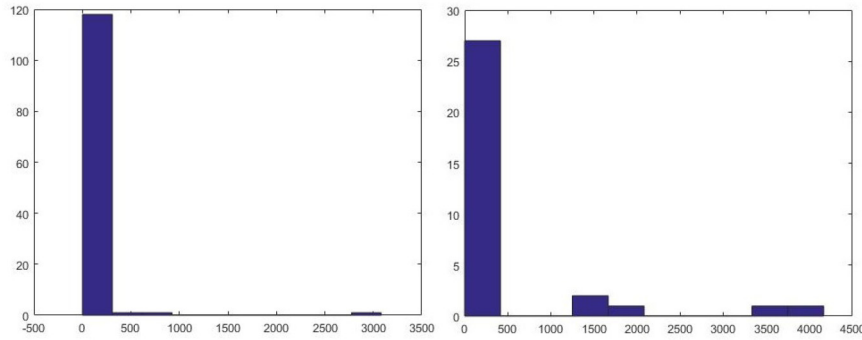


Fig. 6. Number of red ball pixels detected for top-down coverage views (left) and tilted coverage views (right).

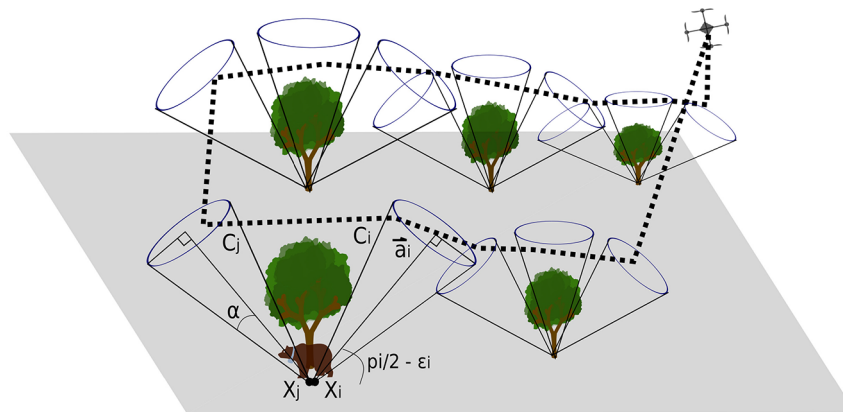


Fig. 7. Given a set of inverted view cones C with apex angle α , heights H , tilts E , orientation vectors \vec{A} , and apex points X located at points of interest the goal is to find the shortest tour to visit them.

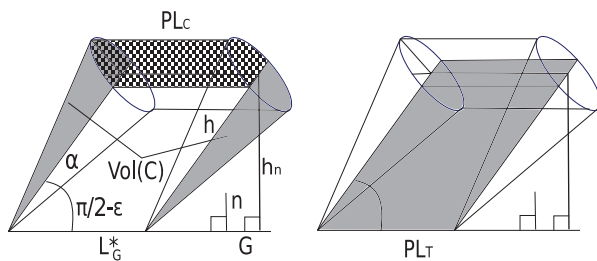


Fig. 8. The sweep volume of a cone C along a path of length L_G^* can be split into three parts. The checkered pattern area of a semicircle swept by the upper half base of the cone. The triangle area PL_T is swept by the largest inscribing triangle on cone C . The gray area $Vol(C)$ includes the points covered by two half cones located at the start and end of L_G^* .

we have $vol(C)$ as two halves of the volume of a cone covering the points at the starting and ending locations of L_G^* not covered by any other cone along L^* . Second, we have PL_C , the area of a semicircle along the path L_G^* . Here PL_C is the area swept by the upper half base of the cone in the direction of the normal of G . If L_G^* is a straight line, its volume looks like that of a slanted half cylinder. Third, we have PL_T , the area of a triangle along L_G^* . Here PL_T is the

area swept by the largest inscribing triangle on cone C . Finally, we note that $\hat{h} \geq h_n = \vec{a} \cdot \vec{n}$. \square

Lemma 2. Let the optimal tour T^* have length L^* and maximum height h^* . Let its projection onto plane G with normal \vec{n} be T_G^* . For maximum cone height h_{max} and an estimate height \hat{h} such that $\hat{h} \geq h_{max}$, $\hat{h} \leq 2h^*$, there exists a constant C_v such that the Minkowski sum sweep volume $f(T_G^*, \hat{h})$ of a cone C with apex and orientation angles α and $\epsilon = 0$ such that $|\epsilon| + \alpha \in (0, \frac{\pi}{2})$ traveling along T is lower bounded by $f(T_G^*, \hat{h}) \geq C_v \tan^2 \alpha \sum_{h_i \in H} h_i^3$.

Proof. The volume of a cone swept out by a tour visit can be represented as the intersection between two cones C_i , C_j of equal height h_i and apex angle α , with their apex points at distance $h_i \tan \alpha$. The volume of this intersection is proportional to the volume of C_i , say by a constant number C_v . For a single cone visit we have $\frac{\pi r_i^2 h_i}{3} = \frac{\pi h_i^3 \tan^2 \alpha}{3}$ and the tour visits all cones with heights $h_i \in H$ (see Figure 9). \square

Now that we have obtained the bounds for the swept area of a tour, we study how they change as the cones tilt. The following two lemmas show how the cone orientation angle ϵ affects the lower bound. The upper bound remains the same.

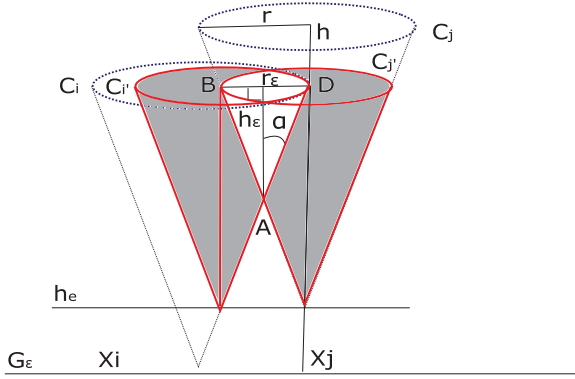


Fig. 9. The volume of intersection between two cones C_i, C_j of equal height is proportional to the volume of C_i by a constant number C_v .

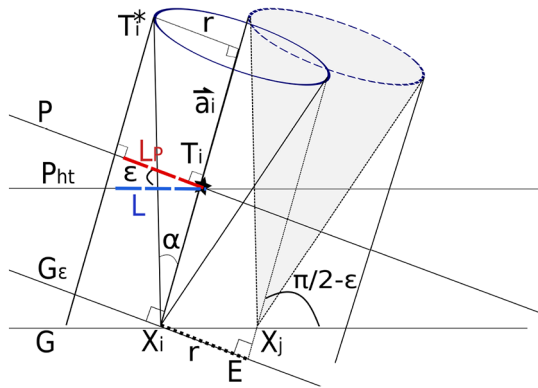


Fig. 10. Tilted Slice-Visit. TSP will visit the cone at T_i , with $|X_i T_i| = h_i$. Here T_i is not further away than $h_i \tan \alpha$ from T_i^* projected along \vec{a} onto P_{h_i} .

Lemma 3. Let cones C_i, C_j have apex and orientation angles α and ϵ , height h_i , cap radius $r = h_i \tan \alpha$, and apex points $X_i, X_j \in$ plane G with normal \vec{n} . Let G_ϵ be a 2D plane with normal \vec{n}_ϵ passing through X_i such that $\vec{n} \perp \vec{n}_\epsilon = \epsilon$ and $\vec{a}_i \perp \vec{n}_\epsilon = 0$. The relative arrangement of two cones tilted by angle ϵ with \vec{a}_j intersecting the cap of c_i is identical to that of two non-tilted cones with their apex points $X_i, X_j \in G_\epsilon$ and one of them elevated from G_ϵ by $h_e = r \tan \epsilon$.

Proof. In Figure 10, $\Delta X_i E X_j$ is a right triangle with $\hat{E} = \frac{\pi}{2}$: $\tan \epsilon = \frac{|EX_j|}{|X_i E|} = \frac{|EX_j|}{r} \Leftrightarrow |EX_j| = r \tan \epsilon$. \square

Lemma 4. Let the optimal tour T^* have length L^* and maximum height h^* . Let its projection on plane G with normal \vec{n} be T_G^* . For maximum cone height h_{max} and an estimate height \hat{h} such that $\hat{h} \geq h_{max}$, $\hat{h} \leq 2h^*$, there exists a constant C_ϵ such that the Minkowski sum sweep volume $f(T_G^*, \hat{h})$ of a cone C with apex and orientation angles α and ϵ such that $|\epsilon| + \alpha \in (0, \frac{\pi}{2})$ traveling along T is lower bounded by $f(T_G^*, \hat{h}) \geq C_\epsilon \tan^2 \alpha \sum_{h_i \in H} h_i^3$, where $C_\epsilon = C_v(1 - \tan \alpha \cdot \tan \epsilon)^3$.

Algorithm 1. Tilted Slice-Visit

- Input:** $x_0, C, H, \hat{A}, X, \epsilon, \alpha$
Output: Tilted Cone-TSPN tour T
- 1: Define a plane P_{h_i} that is parallel to G and elevated by coverage height $h_i = h_{min}$ in the direction of \vec{a}
 - 2: Intersect all orientation vectors with P_{h_i} , the result is a number of points on P_{h_i}
 - 3: Approximate TSP tour T_{h_i} that visits all points on P_{h_i} with starting point x_0 (using, e.g., a PTAS for Euclidean points)
 - 4: Connect P_{h_i} with G using a vertical double line segment at x_0

Proof. Given two tilted by ϵ cones C_i, C_j , by Lemma 3 this is equivalent to two non-tilted cones where C_j is elevated by $h_e = r \tan \epsilon$. Create a new cone C_j' with apex point X_j , apex angle α , height $h_j - h_e = h(1 - \tan \alpha \tan \epsilon)$, and radius $r_\epsilon = h \tan \alpha(1 - \tan \alpha \tan \epsilon)$ (see Figure 9). Create a new cone C_i' with apex point X_i lying at the intersection between h_e and $|X_i D|$, with radius r_ϵ , apex angle α and height $h_i - h_e$. The volume of intersection between C_i, C_j is larger than the volume of intersection between C_i', C_j' . Applying Lemma 2 on C_i', C_j' and noting that $C_\epsilon = C_v(1 - \tan \alpha \tan \epsilon)^3$ produces the desired lower bound. \square

Now that we have obtained the bounds for the swept area of a tour relative to the orientation angle, we can compute the performance of our strategy in Algorithm 1.

Lemma 5. Let an input set C of n disjoint cones have orientation and apex angles ϵ and α , heights H , and coverage height h_i . If Tilted Cone-TSPN tour T is computed with algorithm Tilted Slice-Visit using an $(1 + \beta)$ approximation, then $\frac{L}{1 + \beta} \leq 2h_i + \frac{L^* + 2n \tan \alpha}{\cos \epsilon} \text{mean}(H)$.

Proof. Let the optimal tour T^* with length L^* visit cone C at point T_i^* , lying at cone height h_i . Here T_i^* cannot be further than $r = h_i \tan \alpha$ from the orientation vector \vec{a} (see Figure 10). Our strategy T with length L visits the cone at point T_i , which is a point on the orientation vector \vec{a} . Define plane P such that its normal is parallel to \vec{a} and it passes through X_i . Project T_i^* along \vec{a} onto P and call the resulting point $T_{i,p}^*$. On P $|T_{i,p}^* T_i| \leq h_i \tan \alpha$, then

$$L_P - L_P^* \leq \sum_{\forall c_i \in C} h_i \tan \alpha \tag{2}$$

The projection of a tour with length L^* onto P cannot make it longer than

$$L_P^* \leq L^* \tag{3}$$

Furthermore, the projection of tour on P with length L_P onto P_{h_i} such that $P \perp P_{h_i} = \epsilon$ cannot get longer than a factor of $\cos \epsilon$:

$$L \leq \frac{L_P}{\cos \epsilon} \tag{4}$$

Combining Equations (2), (3), and (4), we obtain

$$L \leq \frac{L^* + \sum_{\forall c_i \in C} h_i \tan \alpha}{\cos \epsilon} \tag{5}$$

Connecting $x_0 \in G$ to P_{h_i} requires two additional line segments of length at most $2h_i$. Finally, note that $\sum_{h_i \in H} h_i = n \text{mean}(H)$. \square

Theorem 6. *Let an input set C of n disjoint cones have orientation and apex angles ϵ and α and heights H . For an estimate height $\hat{h} \geq h_{max}$, $h^* \leq \hat{h} \leq 2h^*$ and $|\epsilon| + \alpha \in (0, \frac{\pi}{2})$, if the strategy Tilted Slice-Visit solves Tilted Cone-TSPN using a $(1 + \beta)$ approximation, then it has an approximation factor*

$$(1 + \beta) \left(\frac{1}{\cos \epsilon} \left(\frac{\hat{h}}{\text{mean}(H)} \right)^2 \left(1 + \frac{5\pi}{6} \tan \alpha \right) \right)$$

Proof. From Lemmas 1 and 4 and noting that $\sum_{h_i \in H} h_i^3 \geq n \cdot \text{mean}(H)^3$, we have

$$n \tan \alpha \leq \frac{L^* \hat{h}^2 (1 + \frac{5\pi}{6} \tan \alpha)}{C_\epsilon \text{mean}(H)^3} \tag{6}$$

Substituting with Lemma 5, we obtain

$$\frac{L}{1 + \beta} \leq 2h_i + \frac{L^*}{\cos \epsilon} + 2 \frac{\text{mean}(H) L^* \hat{h}^2 (1 + \frac{5\pi}{6} \tan \alpha)}{\cos \epsilon C_\epsilon \text{mean}(H)^3} \tag{7}$$

Noting that $h_i \leq \hat{h}$, $h_i \leq 2h^* \leq L^*$ gives the resulting bounds.

5. Disjoint cones of identical orientation

In this section, we present the strategy for the case where the cones are disjoint, have different heights, and identical orientation. If the cones have different heights, then Algorithm 1 may perform poorly owing to being restricted to a coverage height of h_{min} . This is addressed by splitting the cones into a number of height bins such that the requirements of Lemma 1 are met and perform Tilted Slice-Visit on each. The strategy is outlined in Algorithm 2.

Theorem 7. *Let an input set C of n disjoint cones have orientation and apex angles ϵ and α and heights H . For an estimate height $\hat{h} \geq h_{max}$, $h^* \leq \hat{h} \leq 2h^*$ and $|\epsilon| + \alpha \in (0, \frac{\pi}{2})$, if the strategy Tilted Height-Visit solves Tilted Cone-TSPN using a $(1 + \beta)$ approximation, then it has an approximation factor*

$$(1 + \beta) \left(\frac{1}{\cos \epsilon} \left(1 + \frac{5\pi \tan \alpha}{6} \right) \left\lceil 1 + \log_2 \frac{\hat{h}}{h_{min}} \right\rceil \right)$$

Proof. Given coverage height h_i , and the approximation factor from Theorem 6, we have $\left\lceil 1 + \log_2 \frac{\hat{h}}{h_{min}} \right\rceil$ height bins

Algorithm 2. Tilted Height-Visit

Input: $x_0, C, H, \epsilon, \alpha$
Output: tiltedCone-TSPN tour T

- 1: $i = 0$
- 2: **repeat**
- 3: Create bin with height range $B_i = [2^i h_{min}, 2^{i+1} h_{min})$
- 4: For all cones with height $\in B_i$ call Algorithm 1 and find tour T_{B_i} with starting point x_0
- 5: $i = i + 1$
- 6: **until** $2^i h_{min} > h_{max}$
- 7: Connect all tours T_{B_i} with a vertical line segment at x_0

Algorithm 3. Tilted Height-Select

Input: C, H, ϵ, α
Output: Tilted Cone-TSPN tour T

- 1: Sort cones into a set C_{sort} from shortest to tallest based on cone height h
- 2: $MIS = \emptyset$
- 3: **repeat**
- 4: Select the first cone $C_1 \in C_{sort}$, this is the shortest cone in the set
- 5: $MIS = MIS \cup C_1$
- 6: Remove from C_{sort} cone C_1 and all cones intersecting with it
- 7: **until** $C_{sort} = \emptyset$
- 8: Call Algorithm 4 with input MIS

and we compute a subtour for each bin. Finally, note that $\hat{h} \leq 2h_i$ and $\text{mean}(H) \leq \frac{3}{2}h_i$. \square

6. Non-disjoint cones of identical orientation

In this section, we present the strategy for the case where the cones are not disjoint, have different heights, and identical orientation. As we already have a method for the disjoint case, we can handle intersections of cones with identical orientation simply by selecting their maximal independent set (MIS) (Dumitrescu and Mitchell, 2001; Elbassioni et al., 2006). The cones in the MIS intersect all cones $\in C$. The strategy is outlined in Algorithm 3, which is an extension of Algorithm 2 for the case where the cones are not disjoint. Tilted Height-Select constructs the MIS by selecting cones greedily based on height. Then it computes a tour to visit the cones in the MIS and adds the necessary detours to ensure all cones are visited.

Lemma 8. *Given an input set C with orientation and apex angles ϵ and α let the MIS be a subset of C such that the cones $\in MIS$ do not intersect one another and collectively intersect all cones $\in C$. If the MIS is selected using Tilted Height-Select, then Algorithm 6 adds $k = \left\lceil \frac{2}{1 - \tan \alpha \tan \epsilon} \right\rceil$ detours of length $\leq (8k\pi + 4)h_i \tan \alpha$ that visit every cone.*

Proof. At the coverage height h_i , the maximum distance between the orientation vectors \vec{a}_i, \vec{a}_j of a cone $c_i \in MIS$ and a cone intersecting it $c_j \notin MIS$ is $4h_i \tan \alpha$, because

Algorithm 4. Tilted Height-Visit Intersect

Input: $C, H, x_0, \epsilon, \alpha, \vec{A}$
Output: Tilted Cone-TSPN tour T

- 1: Truncate all cones to not be taller than $\hat{h} = h_{max}$
- 2: $i = 0$
- 3: **repeat**
- 4: Create bin with height range $B_i = [2^i h_{min}, 2^{i+1} h_{min})$
- 5: For all cones with height $\in B_i$ call Algorithm 1 and find tour T_{B_i} with starting point x_0 .
- 6: **for** each cone c_i visited in T_{B_i} **do**
- 7: Add $k = \lceil \frac{2}{1 - \tan \alpha \tan \epsilon} \rceil$ circumference detours perpendicular to \vec{a} such that detour $j \in [1, k]$ is centered at T_i and has radius $j2(h_i - h_e) \tan \alpha$
- 8: **end for**
- 9: $i = i + 1$
- 10: **until** $2^i h_{min} > h_{max}$
- 11: Connect all tours T_{B_i} with a vertical line segment at x_0

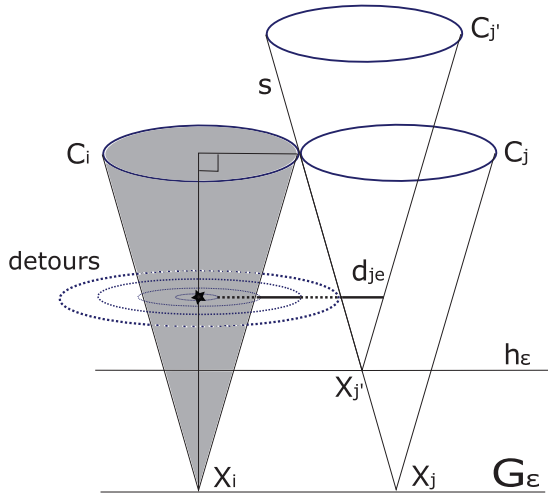


Fig. 11. The furthest cone C_j can be from C_i while still intersecting it results in have a single intersection point lying along the straight line s originating from its apex X_i .

$2h_i \leq h_i$. If the cones are tilted by ϵ , then from Lemma 3 the relative arrangement of two such cones is identical to that of two non-tilted cones with one of them $\notin MIS$, say c_j' , elevated from the plane by $h_e = h_i \tan \alpha \tan \epsilon$. The maximum distance between the orientation vectors \vec{a}_i, \vec{a}_j is $4h_i \tan \alpha$. At height h_i , cone c_j' has diameter $d_{je} = 2(h_i - h_e) \tan \alpha$, thus we can guarantee coverage from \vec{a}_i by adding circumference paths at a right angle, originating at T_i and having radii that are increments of d_{je} . The total length is less than $k8\pi h_i \tan \alpha + 4h_i \tan \alpha$, where k is a constant integer such that $k = \lceil \frac{4h_i \tan \alpha}{2(h_i - h_e) \tan \alpha} \rceil = \lceil \frac{2}{1 - \tan \alpha \tan \epsilon} \rceil$ (see Figure 11). \square

Now that we have computed the cost of the additional detours we can calculate the performance of Algorithm 3.

Theorem 9. Let an input set C of n disjoint cones have orientation and apex angles ϵ and α and heights H . For an

estimate height $\hat{h} \geq h_{max}, h^* \leq \hat{h} \leq 2h^*$ and $|\epsilon| + \alpha \in (0, \frac{\pi}{2})$, if the strategy Tilted Height-Select solves Tilted Cone-TSPN using a $(1 + \beta)$ approximation, then it has an approximation factor

$$(1 + \beta) \left(\frac{18k}{\cos \epsilon} \left(1 + \frac{5\pi \tan \alpha}{6} \right) \left[1 + \log_2 \frac{\hat{h}}{h_{min}} \right] \right)$$

where $k = \lceil \frac{2}{1 - \tan \alpha \tan \epsilon} \rceil$.

Proof. Similar to Theorem 6 we can add the new detours to the length of the detour in Lemma 5:

$$\frac{L}{1 + \beta} \leq 2h_t + \frac{L^*}{\cos \epsilon} + 2 \frac{\text{mean}(H) + h_k(8\pi + 4)}{\cos \epsilon} \frac{L^* \hat{h}^2 (1 + \frac{5\pi}{6} \tan \alpha)}{C_e \text{mean}(H)^3}$$

Similar to Theorem 7, we have $\left[1 + \log_2 \frac{\hat{h}}{h_{min}} \right]$ such tours. \square

7. Non-disjoint cones of varying orientation

In this section, we present the strategy for the case where the cones are disjoint, have different heights, and different orientation. In order to handle the case where the cones have different orientation angles, we split them into different orientation sets. We create a number of orientation sets such that all cones have orientation angle difference θ such that $\epsilon_i \angle \epsilon_j = \theta \leq \frac{\alpha}{2}, \forall i, j, \theta + \alpha \in (0, \frac{\pi}{2})$. For each such set, we show that we only need to add one additional circumference detour to our previous strategy. The strategy is outlined in Algorithm 5. Note that we now have different orientation angles so $\epsilon = \arg \max_{a_i} \vec{n} \angle \vec{a}_i$.

Lemma 10. Let two intersecting cones $C_i \in MIS, C_j \notin MIS$ have apex angle α , heights h_i, h_j and orientation angles ϵ_i and ϵ_j , with $\theta = \epsilon_i \angle \epsilon_j \leq \frac{\alpha}{2}$. If coverage height $h_t \geq h_i \frac{\sin \theta}{\sin(2\alpha + \theta)} + r \tan \epsilon$, we only need to add one additional circumference detour to the strategy outlined in Algorithm 3 centered at the center of the cone at height h_t , at a right angle with respect to \vec{a}_i and at distance $4h_t \tan \alpha + 2(h_t - r \tan \epsilon) \tan \alpha$ to guarantee coverage of all cones intersecting those $\in MIS$ (see Algorithm 5 and Figure 12).

Proof. First we note that if the cones are tilted by ϵ , then from Lemma 3 the relative arrangement of two such cones is identical to that of two non-tilted cones with one of them $\notin MIS$, say c_j' , elevated from the plane by h_e . Thus, without loss of generality we can assume that on the relative arrangement between cones C_i and $C_j, \epsilon_i = \frac{\pi}{2}$. In Figure 12, applying law of sines on $\Delta X_k X_j$ gives $|X_k X_j| = |X_k| \frac{\sin \theta}{\cos(\alpha + \theta)} = \frac{r_i}{\sin \alpha} \frac{\sin \theta}{\cos(\alpha + \theta)}$. Applying the law of sines on $\Delta X_k M X_j$, gives $|X_k M| = \frac{r_i}{\sin(2\alpha + \theta)} \frac{\sin \theta}{\sin \alpha}$. Triangle $\Delta X_k H M$ is a right-angled triangle, thus $|H X_k| = h_i \frac{\sin \theta}{\sin(2\alpha + \theta)}$, where $r_i = h_i \tan \alpha$. Now, if X_k and X_j are elevated by h_e , then we have $|H X_k| = h_i \frac{\sin \theta}{\sin(2\alpha + \theta)} + h_e$.

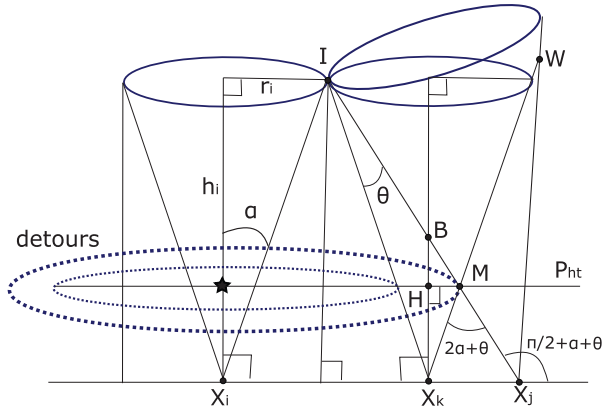


Fig. 12. If two cones C_j, C_k both intersect a third cone C_i , then they also intersect one another after a certain height h_i .

Thus, if coverage height $h_i \geq h_i \frac{\sin \theta}{\sin(2\alpha + \theta)} + h_e$, then these detours guarantee coverage of all cones intersecting C_i .

Lemma 10 implies that if two cones C_j, C_k with maximum orientation difference $\frac{\alpha}{2}$ both intersect a third cone C_i , then they also intersect one another after a certain height h_i (see Figure 12).

Lemma 11. *The additional detour from Algorithm 5 (Lemma 10) visits all cones not visited from Algorithm 3.*

Proof. In Figure 12, let cone c_k have the same height h_i and intersect cone $c_i \in MIS$ at its right-most cap point. The added detour from Lemma 10 visits c_k at its left-most and right-most cap points at coverage height h_i . Let cone c_j be tilted at an angle θ with respect to c_i and intersect c_i at its right-most cap point. Let W be the point of intersection between the two right-most rays of c_k and c_j . Triangle $\Delta X_k W X_j$ has $\hat{W} = \theta$ and $\hat{X}_k = \frac{\pi}{2} - \alpha$. From the law of sines we have $|X_j W| = |X_k X_j| \frac{\cos \alpha}{\sin \theta}$. From the proof of Lemma 10 we know $|X_k X_j| = \frac{r_i}{\sin \alpha \cos(\alpha + \theta)}$. Combining the two we have $|X_j W| = \frac{h_i}{\cos(\alpha + \theta)}$. As $\frac{\pi}{2} > \theta > 0$, then $|X_j W| > \frac{h_i}{\cos(\alpha)}$ which is the length of the right-most ray of cone c_k . Also note that point $M \in c_i \in c_j$ and point $W \notin c_i \in c_j$ for $\theta > 0$. As points M, W belong to the same line $[MW] \in c_j$, it follows that the right-most ray of cone c_k above height $h_i \frac{\sin \theta}{\sin(2\alpha + \theta)} + h_e$ is fully contained in cone c_j . Thus, the outermost detour always visits a tilted cone at distance greater than $4h_i \tan \alpha$ from the apex of c_i . We know from Lemma 8 that the innermost detours visit every other cone at distance $[0, 4h_i \tan \alpha]$, which includes any cone tilted at an angle θ closer to the apex of c_i than c_j .

In order to compute the performance of Algorithm 5 we need to revisit the lower bound from lemma 4. The following lemma shows how the different cone orientation angles affect the lower bound.

Lemma 12. *Let two cones C_i, C_j have the same height h_i , apex angle α , and orientation angle difference $\epsilon_i \angle \epsilon_j = \theta \leq \frac{\alpha}{2}$. A constant C_θ exists (similar to Lemma 4) such that the Minkowski sum sweep volume $f(T_G^*, \hat{h})$ is*

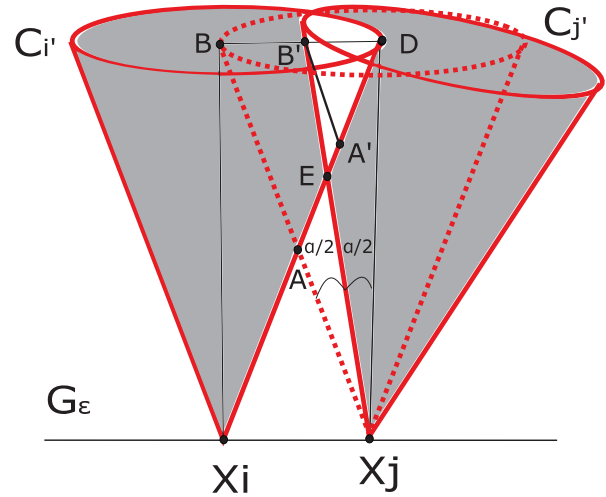


Fig. 13. Computing the volume of intersection between two cones C_i', C_j' with apex angle α , orientation angle difference $\theta = \epsilon_i \angle \epsilon_j \leq \frac{\alpha}{2}$, height h , and radius r . The volume of intersection between C_i', C_j' exists (gray area) and is always smaller than the volume from Lemma 4 by a constant factor.

lower bounded by $f(g(T^*), h) \geq C_\theta \tan^2 \alpha \sum_{h_i \in H} h_i^3$ where $C_\theta = C_\epsilon \frac{\tan^2 \frac{\alpha}{2}}{(1 - \tan \alpha \tan \theta)^5}$.

Proof. In Figure 13, let line $B'A'$ originate from point B' and be parallel to BA . Let the area of $\Delta A'B'D$ be A_3 , the area of ΔABD be A_1 and the area of $\Delta EB'D$ be A_2 . The area of triangles ΔABD and $\Delta A'B'D$ are related by $\frac{A_3}{A_1} = \frac{|BD|^2}{|B'D|^2} = \frac{\tan^2 \frac{\alpha}{2}}{(1 - \tan \alpha \tan \theta)^2}$. As $A_3 \leq A_2$ it follows $\frac{A_2}{A_1} \geq \frac{\tan^2 \frac{\alpha}{2}}{(1 - \tan \alpha \tan \theta)^2}$. Finally, note that the ratios of the volume between two cones C_1, C_2 and the areas of their maximum inscribed triangles T_1, T_2 is related by $\frac{\text{vol}(C_1)}{\text{vol}(C_2)} = \frac{1}{(1 - \tan \alpha \tan \theta)^3} \frac{\text{area}(T_1)}{\text{area}(T_2)}$. Thus, the volume of intersection of cones C_i', C_j' compared with the volume of intersection of cones C_i, C_j from Lemma 4 is not smaller than $\frac{\tan^2 \frac{\alpha}{2}}{(1 - \tan \alpha \tan \theta)^5}$. \square

Theorem 13. *Let h^* be the maximum height the optimal strategy achieves. For any set of input cones C with a given a coverage height \hat{h} such that $\hat{h} \geq h_{\max}, h^* \leq \hat{h} \leq 2h^*$ and orientation and apex angles ϵ and α such that $\epsilon \angle \epsilon_j = \theta \leq \frac{\alpha}{2}, \forall j, \theta + \alpha \in (0, \frac{\pi}{2})$, if the strategy Orientation-Visit solves Tilted Cone-TSPN using a $(1 + \beta)$ approximation, then it has an approximation factor $(1 + \beta) \left(\frac{18k}{\cos \epsilon} \left(1 + \frac{5\pi \tan \alpha}{6} \right) \left[1 + \log_2 \frac{\hat{h}}{h_{\min}} \right] \right)$, where $k = \lceil \frac{2}{1 - \tan \alpha \tan \epsilon} \rceil$.*

Proof. The proof is similar to Theorem 9. The added detours from Lemma 10 result in $k + 1$ circumference paths each with length less than $8\pi h_i \tan \alpha$. These paths can be connected with a double line segment of size less than $4h_i \tan \alpha$. \square

These bounds apply to cones having orientation angle difference $\theta \leq \frac{\alpha}{2}$. In case we have a wider range of cones

Algorithm 5. Orientation-Visit

Input: $C, x_0, H, \vec{A}, \epsilon, \alpha$
Output: Tilted Cone-TSPN tour $T_{\vec{A}}$

- 1: **for** each orientation vector $\vec{a}_k \in \vec{A}$ **do**
- 2: Create cone orientation set O_k with representative orientation \vec{a}_k
- 3: Put all cones with orientation $\vec{a} \in \vec{A}$ such that $(\vec{a} \angle \vec{a}_k) \leq \frac{\alpha}{2}$ into set O_k
- 4: Call Algorithm 3 with input O_k and perform $k + 1$ detours
- 5: **end for**

with a larger orientation angle difference, we simply bin them into sets and perform the same strategy for each such set. Noting that $\hat{h} \leq \max(H)$ and $\epsilon < \frac{\pi}{2} - \frac{\alpha}{2}$, we can simplify the approximation and obtain the result in Equation (1).

Lemma 14. *Given a set of orientation vectors \vec{A} , we need at most $\lceil 8(\frac{\pi}{\alpha})^2 \rceil$ bins to separate them into sets of maximum angle difference of α .*

Proof. We will create a number of bins on the surface of a unit sphere such that for any pair of unit vectors \vec{a}, \vec{b} on the same bin the condition $\vec{a} \angle \vec{b} \leq \alpha$ is satisfied. If \vec{a} and \vec{b} belong on a unit circle, they can be at most α away from each other and we need at least $\frac{2\pi}{\alpha}$ bins to cover all points of the circle. If \vec{a} and \vec{b} belong on a unit sphere, then we can divide it into a number of strips of width α , each centered around a circle that is equal to or smaller than the unit circle. As each strip is α away from each other, we can split the surface of the sphere into $\frac{2\pi}{\alpha}$ strips. We can cover each strip in its entirety with $2\frac{2\pi}{\alpha}$ bins and the entirety of the sphere with $8\frac{\pi^2}{\alpha^2}$ bins. \square

8. Simulations

In Sections 4–7, we presented our strategy for the Tilted Cone-TSPN and its analysis for the worse-case performance. In this section, we present an implementation of our strategy and show through simulations that it can compute practical tours.

8.1. Implementation

We implemented our strategy along with heuristics that improve performance while keeping the theoretical guarantees. Instead of performing the entirety of all ellipsoidal detours on every cone in the MIS , we select a subset of them and only perform the part of the detour that visits another cone. In addition, we plan a tour with multiple orientation directions (azimuth angles). As performance depends on the relative cone arrangement, we consider multiple coverage heights and select the best. After identifying a set of points p_{tour} that cover all cones, we use the Concorde TSP solver (Applegate et al., 2006) in order to compute an optimized tour (see Figure 14 for an example tour).

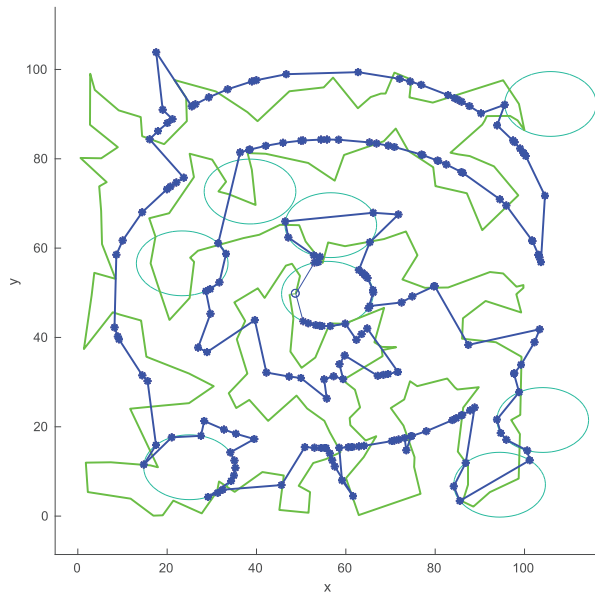


Fig. 14. An example of a computed tour, colored blue. For a set of randomly generated cones with apex angle $\pi/5$, tilt angle $\pi/4$ at coverage height 10 m. The ellipsoids represent the cones $\in MIS$. The computed tour (blue) is 26.94% better than the apex tour (green).

Our implementation is described in Algorithm 6. For each height guess h_t we define a horizontal plane P_{h_t} and compute the Tilted Cone-TSPN tour based on the ellipses resulting from the intersection of the cones with P_{h_t} . For each cone $c_i \in MIS$ we compute two ellipses $el1$ and $el2$ which correspond to the detours at radius $2h_t \tan \alpha$ and $2(k+1)(h_t - h_e) \tan \alpha$ on P_{h_t} (lines 4, 11). Then we identify the intersections between $el1, el2$ and the ellipses of cones $c_j \notin MIS$ (lines 7–14). We obtain at most two points for each cone c_j intersecting either $el1$ or $el2$ prioritizing the shorter detour $el1$. We keep the intersection point that has the closest neighbor among the currently selected set of points to be visited p_{tour} (lines 21–23). If a cone ellipse does not share any intersection points, then it is either on the MIS and does not intersect any cone or is not on the MIS . If it is not on the MIS , then it lies inside one of the ellipsoidal detours. In both cases, we choose to visit the cone at the point on its ellipse that is closest to another point $\in p_{tour}$ (lines 17–19). The optimal tour T_{h_t} visiting all points $\in p_{tour}$ is then computed using the Linkern module from the Concorde TSP solver (line 27). Finally, we select the best coverage height according to tour length (line 30).

8.2. Evaluation

We performed simulations for two representative applications (see also Section 2).

- The first application is coverage of reflective surfaces (see Figure 16). In this application, we select a number of view cones that cover a given square area and select a tilt angle ϵ that avoids direct sunlight (see also

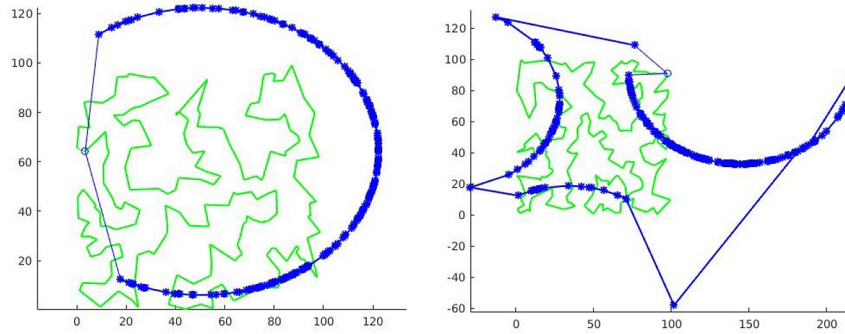


Fig. 15. The performance of Orientation-Visit-Practical depends on the cone arrangement. For 200 cones over a $100 \times 100 \text{ m}^2$ area with an apex angle of $\frac{\pi}{5}$, cone tilting angle $\frac{\pi}{5}$, and azimuth angles $\{0, \pi/2, \pi, -\pi/2\}$, at a height of 80 m the computed tour on the left is 18.71% better than the apex tour (worse than any other coverage height). For a different cone arrangement the computed tour on the right is 63.05% better than the apex tour (best among all coverage heights).

Table 1. Average performance improvement of our strategy over the cone apex tour for sets of varying coverage heights $h_t = \{10, 20, 40, 80\}$ and cone tilting angles $\{\pi/4, \pi/5, \pi/10\}$. The second column of each tilt angle adds the cost of reaching coverage height h_t for the same tour as the first column. Cones have the same orientation vector direction (azimuth angle).

Coverage heights	Tilting angles & height cost					
	$\pi/4$ rad		$\pi/5$ rad		$\pi/10$ rad	
	+ $0h_t$	+ $2h_t$	+ $0h_t$	+ $2h_t$	+ $0h_t$	+ $2h_t$
10 m	27.60%	25.74%	25.99%	24.12%	24.70%	22.84%
20 m	42.01%	39.28%	43.58%	39.84%	41.53%	37.81%
40 m	61.80%	54.38%	61.72%	54.25%	59.60%	52.15%
80 m	63.05%	48.18%	65.90%	50.96%	68.90%	54.01%

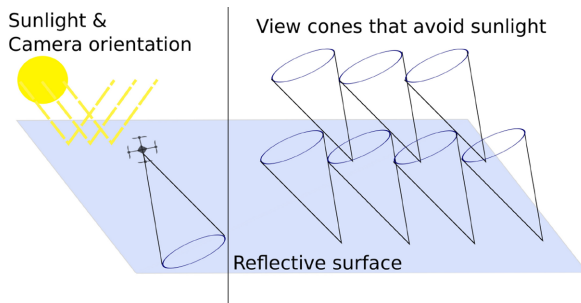


Fig. 16. Illustration of reflective surface coverage application. Given the sunlight direction we can calculate the camera orientation with the least amount of sunlight in the images. This results in view cones with uniform orientation.

Section 2.1). All cones have uniform tilt angle ϵ and orientation vector \vec{a} direction (azimuth angle). The results can be seen in Table 1.

- The second application is visual inspection of a target area (see Figure 17). In this application, we select a number of side view cones that inspect a target area from all angles (see also Section 2.2). All cones share uniform tilt angle ϵ . However, the orientation vector \vec{a}

direction (azimuth angle) varies (non-uniform). The results can be seen in Table 2.

For both scenarios, we generated sets of 200 view cones with an apex angle of $\frac{\pi}{5}$. The apex points were positioned uniformly with $U(0, 100)$ over a $100 \times 100 \text{ m}^2$ area. In total, 12 sets were generated with varying coverage heights $\in \{10, 20, 40, 80\}$ and cone tilt angles $\in \{\frac{\pi}{4}, \frac{\pi}{5}, \frac{\pi}{10}\}$. The azimuth angles for the first and second application were chosen $\in \{0, \frac{\pi}{2}, \frac{-\pi}{2}, \pi\}$, respectively. To evaluate the efficiency of our implementation we compare it with the TSP tour T_G that covers all the apex points on the ground. This tour, the cone apex tour, does not use any information about the cones and can be used as an upper bound on the length of any TSPN tour on our view cone problem.

The performance evaluation was based on the average tour length ratio between our implementation and the cone apex tour over 100 simulations. Tables 1 and 2 present how much shorter our tour is when compared with the cone apex tour for different coverage heights (columns) and cone tilt angles (rows). As the coverage height h_t increases the tour tends to get shorter owing to the increase in the ellipse area (first column for each tilt angle). However, the cost of reaching this height + $2h_t$ can make the total tour long and, thus,

Table 2. Average performance improvement of our strategy over the cone apex tour for sets of varying coverage heights $h_t = \{10, 20, 40, 80\}$ and cone tilting angles $\{\pi/4, \pi/5, \pi/10\}$. The second column of each tilt angle adds the cost of reaching coverage height h_t for the same tour as the first column. Cones have varying orientation vector directions (azimuth angles) $\in \{0, \pi/2, \pi, -\pi/2\}$.

		Tilting angles & height cost					
		$\pi/4$ rad		$\pi/5$ rad		$\pi/10$ rad	
		+ $0h_t$	+ $2h_t$	+ $0h_t$	+ $2h_t$	+ $0h_t$	+ $2h_t$
Coverage heights	10 m	21.79%	19.93%	21.86%	19.99%	22.89%	21.03%
	20 m	31.12%	27.38%	32.39%	28.66%	37.08%	33.36%
	40 m	33.05%	25.59%	41.34%	33.84%	55.91%	48.47%
	80 m	41.56%	26.62%	50.44%	35.51%	62.24%	47.35%

Algorithm 6. Orientation-Visit-Practical

Input: $C, x_0, H, \vec{A}, E, \alpha, X$
Output: Tilted Cone-TSPN tour T

- 1: Compute the TSP cone apex tour T_G visiting the apex points X
- 2: **for** each height guess h_t described in Algorithm 2 **do**
- 3: Define horizontal plane P_{h_t} for height h_t as in Algorithm 1
- 4: Intersect all cones $\in C$ with P_{h_t} and obtain the associated ellipse set ELC_{h_t}
- 5: Sort ellipses into a set ELC_{sort} from shortest to tallest based on cone height
- 6: $MIS_1 = MIS_2 = \emptyset$
- 7: **repeat**
- 8: Select the first ellipse $el1 \in ELC_{sort}$ (shortest cone in the set)
- 9: $MIS_1 = MIS_1 \cup el1$
- 10: Remove from ELC_{sort} ellipse $el1$ and all ellipses intersecting with it
- 11: Create another ellipse $el2$ corresponding to the $k+1$ detour on P_{h_t}
- 12: $MIS_2 = MIS_2 \cup el2$
- 13: Remove from ELC_{sort} ellipse $el2$ and all ellipses intersecting with it
- 14: **until** $ELC_{sort} = \emptyset$
- 15: $p_{tour} = x_0$
- 16: **for** each ellipse $el_i \in MIS_1 \cup MIS_2$ **do**
- 17: **if** el_i does not intersect any other ellipse **then**
- 18: Select the point $p_i \in el_i$ that is closest to another point $\in p_{tour}$
- 19: Add p_i to p_{tour}
- 20: **else**
- 21: **for** each ellipse $el_j \in ELC_{h_t}$ intersecting el_i **do**
- 22: Select the intersection point p_{ij} that has the closest neighbor $\in p_{tour}$
- 23: Add p_{ij} to p_{tour}
- 24: **end for**
- 25: **end if**
- 26: **end for**
- 27: Compute the TSP tour T_{h_t} visiting all points $\in p_{tour}$
- 28: Add to T_{h_t} a vertical line segment of length $2h_t$ connecting P_{h_t} with G at x_0
- 29: **end for**
- 30: Select the best tour among all T_{h_t} and T_G

we need to consider multiple coverage heights and choose the best (second column for each tilt angle). The performance of each individual tour depends on the relative cone arrangement. The maximum performance difference was 44.34% (see Figure 15). These results show that our algorithm can be used in a practical way and provide shorter tours by exploiting the structure of the cones.

9. Conclusion and future work

In this work, we have studied the optimization problem Tilted Cone-TSPN, which is an extension of Cone-TSPN. We have demonstrated through field experiments that tilted view cones are necessary in real-world applications. Our main contribution is a polynomial-time approximation algorithm that solves Tilted Cone-TSPN and guarantees a solution that only depends on the cone apex angle α , tilt angle ϵ , and the ratio between the shortest and tallest cone. In addition to presenting the mathematical bounds, we implemented our strategy with heuristics that improve performance without sacrificing the theoretical guarantees. Simulations over large numbers of cones indicated that our strategy produced a tour that was shorter than the tour on the cone apex points that did not exploit the cone structure.

There are multiple venues for future work. One of the main assumptions of this work is that the conic regions are given ahead of time. What if the cone heights are known, but the apex positions can change (e.g., coverage of a moving target)? Furthermore, the current strategy does not consider prioritization of the conic regions. What if some regions are preferred over others? It may be advantageous to first perform a quick, high-altitude coverage and then a more detailed, lower-altitude coverage of points of interest. Similarly, if changing the tilt angle of the camera is slow, then different angles may be preferred over others. We would also like to explore the extreme case where the cones touch the ground. A different method and analysis might be required for this case, and a ground robot collaborating with a UAV might be a more appropriate option. In

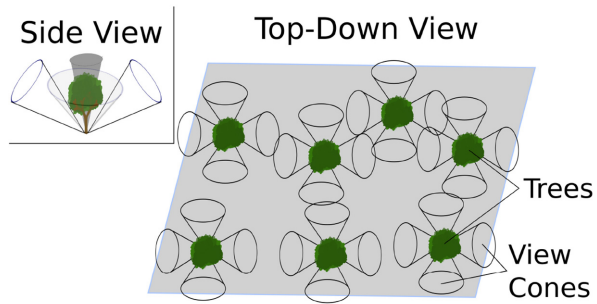


Fig. 17. Illustration of visual inspection of a target area application. In order to capture image footage of an occluded area (e.g., under trees), we require tilted view cones. This results in view cones that face in different directions (different azimuthal angles).

addition, multiple UAVs may be able to cover different height and orientation sets at the same time improving the coverage speed. Finally, we would like to determine whether a UAV can autonomously decide on the best coverage resolution for a given target and choose the best coverage height and orientation online.


Acknowledgements

A preliminary version of this article, was presented at the International Conference on Robotics and Automation (ICRA 2018). This submission extends the conference version by presenting the full details of the proofs, a revised implementation and field experiments. We thank Dr. Forest Isbell for allowing us to perform experiments at Cedar Creek Ecosystem Science Reserve.

Funding

The author(s) disclosed receipt of the following financial support for the research, authorship, and/or publication of this article: This work was supported in part by the NSF (award numbers 1525045, 1617718 & 1849107) and a grant from Minnesota State LCCMR Program.

ORCID iDs

Nikolaos Stefas  <https://orcid.org/0000-0002-4940-1716>

Patrick A Plonski  <https://orcid.org/0000-0002-7978-4586>

References

- Applegate D, Bixby R, Chvatal V and Cook W (2006) Concorde TSP solver. Available at: <http://www.tsp.gatech.edu/concorde/>.
- Arora S (1998) Polynomial time approximation schemes for Euclidean traveling salesman and other geometric problems. *Journal of the ACM* 45(5): 753–782.
- Bodlaender HL, Feremans C, Grigoriev A, Penninx E, Sitters R and Wollé T (2009) On the minimum corridor connection problem and other generalized geometric problems. *Computational Geometry* 42(9): 939–951.
- Chan THH and Elbassioni K (2011) A QPTAS for TSP with fat weakly disjoint neighborhoods in doubling metrics. *Discrete & Computational Geometry* 46(4): 704–723.

- Cheng P, Keller J and Kumar V (2008) Time-optimal UAV trajectory planning for 3D urban structure coverage. In: *IEEE/RSJ International Conference on Intelligent Robots and Systems, 2008 (IROS 2008)*. IEEE, pp. 2750–2757.
- Choset H (2001) Coverage for robotics—a survey of recent results. *Annals of Mathematics and Artificial Intelligence* 31(1): 113–126.
- de Berg M, Gudmundsson J, Katz MJ, Levcopoulos C, Overmars MH and van der Stappen AF (2005) TSP with neighborhoods of varying size. *Journal of Algorithms* 57(1): 22–36.
- Dumitrescu A and Mitchell JS (2001) Approximation algorithms for TSP with neighborhoods in the plane. In: *Proceedings of the 12th Annual ACM-SIAM Symposium on Discrete Algorithms*. Philadelphia, PA: Society for Industrial and Applied Mathematics, pp. 38–46.
- Dumitrescu A and Tóth CD (2015) Constant-factor approximation for TSP with disks. *arXiv preprint arXiv:1506.07903*.
- Dumitrescu A and Tóth CD (2016) The traveling salesman problem for lines, balls, and planes. *ACM Transactions on Algorithms* 12(3): 43.
- Elbassioni K, Fishkin AV and Sitters R (2006) On approximating the TSP with intersecting neighborhoods. In: *International Symposium on Algorithms and Computation*. Berlin: Springer, pp. 213–222.
- Englot B and Hover FS (2013) Three-dimensional coverage planning for an underwater inspection robot. *The International Journal of Robotics Research* 32(9–10): 1048–1073.
- Galceran E and Carreras M (2013) A survey on coverage path planning for robotics. *Robotics and Autonomous Systems* 61(12): 1258–1276.
- Low KH, Dolan JM and Khosla P (2008) Adaptive multi-robot wide-area exploration and mapping. In: *Proceedings of the 7th International Joint Conference on Autonomous Agents and Multiagent Systems, Vol. 1*. International Foundation for Autonomous Agents and Multiagent Systems, pp. 23–30.
- Mitchell JS (1999) Guillotine subdivisions approximate polygonal subdivisions: A simple polynomial-time approximation scheme for geometric TSP, k-MST, and related problems. *SIAM Journal on Computing* 28(4): 1298–1309.
- Mitchell JS (2007) A PTAS for TSP with neighborhoods among fat regions in the plane. In: *Proceedings of the eighteenth annual ACM-SIAM symposium on Discrete algorithms*. Philadelphia, PA: Society for Industrial and Applied Mathematics, pp. 11–18.
- Plonski PA and Isler V (2019) Approximation algorithms for tours of height-varying view cones. *The International Journal of Robotics Research* 38(2–3): 224–235.
- Reinelt G (1994) *The Traveling Salesman: Computational Solutions for TSP Applications*. Berlin: Springer-Verlag.
- Sadat SA, Wawerla J and Vaughan RT (2014) Recursive non-uniform coverage of unknown terrains for UAVs. In: *IEEE/RSJ International Conference on Intelligent Robots and Systems, 2014 (IROS 2014)*. IEEE, pp. 1742–1747.
- Safra S and Schwartz O (2006) On the complexity of approximating TSP with neighborhoods and related problems. *Computational Complexity* 14(4): 281–307.
- Singh A, Krause A, Guestrin C and Kaiser WJ (2009) Efficient informative sensing using multiple robots. *Journal of Artificial Intelligence Research* 34: 707–755.
- Stefas N, Bayram H and Isler V (2016) Vision-based UAV navigation in orchards. *IFAC-PapersOnLine* 49(16): 10–15.